UAB
Universitat Autònoma de Barcelona

Department of Telecommunications and Systems Engineering

Advanced Synthesis Techniques for Parallel-Connected and Cross-Coupled Filters Based on Acoustic Wave Technologies

An Innovative Methodological Approach

Ph.D. Dissertation in Electrical and Telecommunications Engineering by

Ángel Triano Notario
E-mail: Angel.triano@uab.cat

Thesis Advisor: Prof. Pedro de Paco Sánchez
E-mail: Pedro.DePaco@uab.cat
Universitat Autònoma de Barcelona (UAB)
Escola d'Enginyeria

February, 2020

"A journey of a thousand miles begins with a single step"

<div align="right">Lao Tzu</div>

Abstract

The increasing demands of the market are the stimulus that spurs on technological improvement and innovation in the telecommunication sector. The recent arrival of 5G wireless technology promises better communication services with data rates 20 times faster than 4G, providing a level of connectivity never seen before. The fulfillment of 5G goals is imposing a great challenge on every building block of mobile handsets and cellular networks. The services in the new generation require more bandwidth, and the wireless devices will coexist in a complex environment that includes more components with better performance and smaller size.

That is a reality, especially for filtering systems. The best-suited technology for resonators in mobile communications filters is the acoustic wave. The stringent technological constraints are pushing this technology to be more reliable, achieve better performance, and improve higher interference mitigation in an already overcrowded spectrum. Due to the complexity of the filter design process, a vital part of it is entrusted to optimization software tools. However, It is a time-consuming task that may prolong the process for too long before obtaining the final network.

The main objective of this thesis is to offer mathematical tools to provide the required topology straightforwardly and also to obtain the best initial design, a starting point that facilitates the optimization software to find the filtering solution easily.

The most common filter topology is the ladder network. To the date, synthesis methodologies allow defining their fundamental characteristics during the design process with a very low computational cost. To obtain filter responses that fulfill technological and performance design, it is often necessary to modify the classic ladder structure by adding reactive elements or creating couplings between some blocks of the filter that a ladder structure does not contemplate, and no synthesis method can provide. In other circumstances, those couplings may appear due to manufacturing defects, causing severe deterioration of the filter response. The aim of this work is to develop advanced synthesis techniques to generate topologies that include cross-couplings and external elements to address the most useful non-standard filter network configurations. Leveraged on these methodologies, new topologies are proposed to cope with technological limitations.

Another aspect of the filter design process is the phase control network. With it, it is possible to modify the network element values, adapt standalone filters for multiplexer configurations, and assure the feasibility of the filter after bandpass denormalization. Such control is crucial for acoustic wave technology, which is very sensitive to any phase variations introduced with respect to the originally designed. This document describes an effective method to control the network phase to achieve the mentioned goals adequately.

v

Resumen

Las crecientes demandas del mercado son el acicate para las mejoras tecnológicas y la innovación en el sector de las telecomunicaciones. La reciente llegada de la quinta generación de móvil 5G promete mejores servicios de comunicación, con velocidades de datos 20 veces más rápidas que la 4G, proporcionando un nivel de conectividad nunca antes visto. El cumplimiento de los objetivos de 5G están suponiendo un gran desafío para cada componente de los dispositivos y redes de telefonía móvil. Los servicios de la nueva generación necesitan más ancho de banda para unos dispositivos inalámbricos que han de coexistir en un entorno complejo, en el que habrá un mayor número de componentes, con mejor rendimiento y menor tamaño.

Esa es la realidad de los sistemas inalámbricos, especialmente, los sistemas de filtrado. La tecnología más adecuada para los filtros de comunicaciones móviles es la basada en resonares acústicos. Las estrictas limitaciones tecnológicos están empujando a esta tecnología a alcanzar nuevas cotas de fiabilidad, lograr un mayor rendimiento y mejorar la supresión de interferencias en un entorno con un espectro radioeléctrico saturado. Debido a la complejidad del proceso de diseño de filtros, una parte crucial es confiada a herramientas de optimización. Sin embargo, es una tarea que necesita una cantidad de tiempo considerable, y puede prolongar demasiado el proceso de diseño.

El principal objetivo de esta tesis es ofrecer un conjunto de herramientas matemáticas para proporcionar la topología necesaria directamente, y también para obtener el mejor diseño inicial, un punto de partida que facilite al software de optimización la búsqueda de una solución adecuada.

La topología de filtros más común es la ladder. Hoy en día, las metodologías de síntesis permiten definir las características fundamentales de un filtro con un coste computacional muy bajo. Para obtener diseños que cumplan con los requisitos tecnológicos y de rendimiento, a menudo es necesario modificar la estructura clásica del ladder agregando elementos reactivos o creando acoplamientos internos que un filtro ladder no contempla, y que ningún método de síntesis es capaz de proporcionar. Dichos acoplamientos también podrían aparecer debido a defectos de fabricación, provocando un grave deterioro de la respuesta del filtro. El objetivo de este trabajo es desarrollar técnicas de síntesis avanzadas con las que crear topologías que incluyan acoplamientos cruzados y elementos externos para crear configuraciones de filtros no convencionales más útiles. Aprovechando estas metodologías, se han propuesto nuevas topologías para hacer frente a las limitaciones tecnológicas.

Otro aspecto del proceso de diseño de filtros es el control de la fase. Con él, es posible modificar los valores de los elementos de la red, adaptar filtros para ser capaces de trabajar en configuraciones de multiplexores, y asegurar su viabilidad después de la desnormalización paso banda. Debido a la gran sensibilidad a cualquier variación de la fase introducida sobre el filtro original, tal control es crucial para tecnologías acústicas. Este documento describe un método para controlar de forma efectiva la fase de la red a fin de lograr adecuadamente los objetivos marcados para un filtro determinado.

Acknowledgements

I would like to take this occasion to express my deepest gratitude to all people that have helped me through this Ph.D. I am very much obliged to my advisor Professor Dr. Pedro de Paco, for guiding me throughout the research work. His knowledge, motivation, and patience have given the inspiration to excel in this thesis.

I am also indebted to the rest of the Antenna and Microwave Systems research group, Especially Dr. Jordi Verdú for his support and casting a critical eye over my results and reports. I also want to thank Dr. Josep Parrón and Dr. Gary Junkin for their help and counsel. Moreover, I am also grateful to Ernesto Díaz for his helpful technical assistance in the laboratory.

In addition, I would like to thank my current and past office mates Alfred, Iuliia, Patricia and Eloi, for all the good moments and laugh. I want to extend my gratitude to my other colleges Sergi, Giulio, Edith, Edward, Ivan and Guillén, for the unforgettable time spent together.

Work apart, I am eternally grateful to my parents María Teresa and Rafael, for their unconditional support and encouragement in all my life decisions and aspirations, without whom I would not have come this far. I also want to thanks Elena, who has provided me through moral and emotional support at difficult times.

Last but not least, I would like to thank my friends and everybody who influenced my life and research activity that made me possible to become who I am today.

Ángel Triano

Contents

List of Figures

List of Tables

Acronyms

AIN	Aluminium Nitride
AW	Acoustic Wave
BAW	Bulk Acoustic Wave
BVD	Butterworth-Van Dyke
BW	BandWidth
EB	ExaByte
EMF	Electromagnetic Feedthrough
FBAR	Film Bulk Acoustic Resonator
FBW	Fractional BandWidth
FIR	Frequency Invariant Reactance
GLI	Ground-Loop Inductor
IDT	InterDigital Transducer
I.H.P.	Incredible High Performance
IL	Insection Loss
IoT	Internet of Things
k_{eff}^2	Effective piezoelectric coupling coefficient
LCC	L-C inter-resonator Coupling
LiNbO$_3$	Lithium Niobate
LiTaO$_3$	Lithium Tantalite
mBVD	modified Butterworth-Van Dyke
MIMO	Multiple-Input Multiple-Output
NRN	Non-Resonant Node
OoB	Out Of Band
Q	Quality factor
QAM	Quadrature Amplitude Modulation
RL	Return Loss

RN	Resonant Node
RX	Reception
RZ	Reflection Zero
SAW	Surface Acoustic Wave
ScAlN	Scandium-doping of aluminum nitride
SiO$_2$	Silicon dioxide
SMR	Solidly Mounted Resonator
TC	Temperature-Compensated
TCF	Temperature Coefficient of Frequency
TX	Transmission
TZ	Transmission Zero
UWB	Ultra-Wide Bands
V2X	Vehicle-to-everything
XBAR	laterally eXcited Bulk Acoustic Resonator
2G	Second Generation
3G	Third Generation
4G	Fourth Generation
5G	Fifth Generation

Introduction

Microwave filters are indispensable building blocks in modern telecommunication systems and one of the critical parts of the RF front-end. Their main purpose is to reduce dramatically the noise and interference of the external signals that could affect the correct operation of any communication system. A subpar performance of these devices could compromise the quality and integrity of the transferred signal frequencies to the following blocks by reducing the communication range, or increasing the power consumption to keep the same range of coverage, and even causing a temporary interruption of the communications.

Nowadays, mobile communications have become an essential part of our society in all environments with a myriad of services, but this is none but stating the obvious. The insatiable demand for better communication services with higher data rates, reliable communications with reduced energy consumption in networks and devices are spurring the telecommunications industry to create innovative technological solutions with ubiquitous high-speed connectivity. In this continuously evolving scenario, the filter requirements are more and more stringent.

In every generation from 2G to the currently mature 4G, mobile technologies have improved considerably to meet the ever-increasing market demands. The data traffic in 2018 was around 40 Exabytes (EB) per month, and according to Ericsson report [1] the increment of data traffic is expected to be 160 EB per month in 2025 with an estimation of 8.9 billion of active smartphones. The already in deployment 5G claims to be able to deal with these challenges, providing connectivity everywhere, all the time in any kind of framework such as buildings, industrial environments, highly dense areas, remote locations or high-speed transports like planes and trains [2]. It is not meant to be just an incremental improvement over 4G but to become a major evolution of communication technology with several orders of magnitude to perform tasks that 4G networks cannot provide effectively. Another differential characteristic is that it brings together other promising communication services that are expected to be relevant in the near

future of an hyper-connected information society like IoT, V2X in the automotive industry, healthcare or mission-critical systems [3–6] among others.

With the arrival of these new applications and changes, 5G must face the challenge of networks with a frequency spectrum that has become more and more crowded. To make real the goals of 5G, it has been done great efforts in different areas [7]. Other innovations aim to increase the network speeds like carrier aggregation, MIMO antennas or QAM modulation techniques [8, 9].

With respect to mobile filters, the challenge in the present and upcoming generation is to provide high-performance filtering in the smallest footprint possible while keeping a low manufacturing cost and increasing the power handling capabilities at the same time [10]. High performance is attained by designing filters with low insertion losses and high interference protection, that is, excellent out-of-band rejection from the most damaging bands of the filter they have to coexist with. Currently, small size and low realization cost can be achieved only by the acoustic wave technology [11–13]. The most used resonators are Surface Acoustic Wave (SAW) and Bulk Acoustic Wave (BAW) [14–16]. The characteristics of this technology set a frequency range limited to 2.5 GHz for conventional SAW and an operation range over 2 GHz for BAW. From the technological point of view, many advances have been done to extend the range of AW filters up to 6 GHz [17–20] with a high-quality factor.

Material science innovation enables the technology to achieve higher levels of performance, but they alone are not enough. The design tools to exploit the technology improvements properly are an essential part of making the best use of it. The analytic filter design procedure generally consists of a four stages process. The first step is the definition of the filtering function to be implemented, followed by the generation of a lowpass prototype of the network. In the third stage, the bandpass network is obtained by the frequency denormalization of the lowpass prototype. Finally, the network is evaluated to check the fulfillment of the frequency mask, and the factors that influence the feasibility of the filter are validated: power density level of each resonator, quality factors and achievable bandwidth among other parameters. If the design is suitable, it is ready for further electromagnetic simulations and optimization process that provide a more realistic simulation of the future physical device.

In this work, the focus is set on the filter design from a synthesis approach, a mature field in which revolutionary methods do not seem probable to appear, but there is plenty of room for improvement. Using the already existing modern synthesis techniques, this work provides robust and systematic methods oriented toward AW technology that introduces new topologies, along with the ladder-type networks, for standalone filters that may help to meet real design necessities and structures to outperform traditional filter designs, usually based on ladder filters. The objective of this thesis is to define a systematic method to create a wide range of fully canonical filters leveraged on the lowpass prototype, providing robust general methods that require a low computational cost to produce the exact parameters of a network.

1.1   Thesis Outline

The current chapter is dedicated to reviewing the present and future challenges of mobile communications at the dawn of 5G. Especially filters based on acoustic wave filters and their importance in the communication systems.

Chapter 2 presents the acoustic wave technology based on SAW and BAW, main characteristics, basic performance and modeling. The purpose of the chapter is to serve as a bridge between the AW technology and modeling in the lowpass domain, from the single resonator to the ladder filter. The nomenclature and symbology of the lowpass AW filters representation are thoroughly described. The main technological constraints are also presented together with recommendations of how to incorporate them into the synthesis procedure.

Chapter 3 presents the synthesis methodology for ladder-type acoustic filters. It describes the definition of the Chebyshev polynomials of the filtering function and includes a detailed explanation for the parameter extraction procedure of the network elements. The information presented in this chapter is taken into account to guide the design and synthesis methods presented in the following chapters.

Chapter 4 proposes a method based on the phase correction of the characteristic polynomials to address a recurrent inconvenient that suffer asymmetrical filter. In these type of configurations, one the admittance inverter of the network is not unitary, compromising the correct circuital transformation of the resonators that requires serializations. This chapter provides an understanding on the origin of the non-uniformity of the admittance inverters in the main-line path and the necessity of correcting them for filters in AW technology. By a careful analysis is shown how all suitable phase values can be predicted. Finally, several examples of standalone filters are presented in order to demonstrate the method effectiveness.

In chapter 5, it is presented a general synthesis method for fully canonical filters based on mixed-topology networks, which has been created to accommodate AW technology for new configurations beyond the classic ladder network. The design approach is leveraged on the lowpass prototype using a combination of inline and parallel-connected networks. Based on the described theory, two new topologies are fully explained, with synthesis examples to validate the methodology. To guide the synthesis toward a lowpass network that results in feasible filters in AW Technology, a comprehensible description of the consideration to be taken into account is included.

Complementary, Chapter 6 focused on the synthesis of ladder-type filters with reactive elements coupling parts of the structure of the filters. Three kinds of mixed-topologies filters are presented. The first two describe cross-coupled topologies with reactive elements coupling resonators, providing the synthesis method of already known useful structures for which no systematic synthesis method has not yet been developed. The third is based on source-load couplings that serve to model and explain the origin of undesired couplings like electromagnetic feedthrough that may bypass the package ports in the design of filter based on acoustic wave resonators. To validate the presented topologies, several synthesis

examples are provided.

Finally, the conclusions and future work recommendations are drawn in Chapter 7. The reader should note that the synthesized and manufactured filters in this thesis do not pursue to provide designs suitable for commercial use or final design with outstanding performances. They aim to illustrate and validates the powerful capabilities of the synthesis methodologies for ladder filters and the rest of the topologies presented in the document.

1.2   Research Contributions

Throughout the Ph.D. program, a number of papers have been elaborated which have taken part in this dissertation. The list of scientific contributions includes:

- A. Triano, P. de Paco,"A Nodal Bandpass Coupling Matrix Representation Tool for Acoustic Wave Ladder Filters," *IEEE MTT-S International Microwave Symposium , Los Angeles, CA, USA, June 21-26, 2020.* (submitted)

- E. Guerrero, P. Silveira, A. Triano, J. Verdú and P. de Paco,"Synthesis Considerations for Shunt-Starting Acoustic Wave Ladder Filters and Duplexers," *IEEE MTT-S International Microwave Symposium , Los Angeles, CA, USA, June 21-26, 2020.* (submitted)

- A. Triano, J. Verdú, and P. de Paco,"Synthesis of Acoustic Filters Based On Mixed-Topology With Parallel-Connected Structures," *International Journal of Microwave and Wireless Technologies (EuMCE extended)*, 2020 . (submitted)

- A. Triano, P. Silveira, J. Verdú, E. Guerrero and P. de Paco,"Phase Role in the Non-Uniformity of Main-Line Couplings in Asymmetric Extracted-Pole Inline Filters," IEEE *Transactions on Microwave Theory and Techniques*, 2020. (submitted)

- A. Triano, J. Verdú and P. de Paco, "A General Synthesis Technique of Mixed-Topology Including Parallel-Connected Structures for Fully Canonical Ladder-Type Acoustic Filters," IEEE *Transactions on Microwave Theory and Techniques*, 2019.

- A. Triano, P. Silveira, J. Verdú , P. de Paco, "A synthesis Methodology of Mixed-Topology filters with Coupling Reactive Elements," in 2019 IEEE *International Ultrasonics Symposium (IUS)*, Oct. 2019, pp. 1-4.

- P. Silveira, A. Triano, J. Verdú, P. de Paco, "Complex Terminating Impedances for AW Filters: the key for Power Amplifier Co-design," in 2019 IEEE *International Ultrasonics Symposium (IUS)*, Oct. 2019, pp. 1-4.

- A. Triano, J. Verdú and P. de Paco, "Novel Synthesis Technique of Mixed-Topology Extracted-Pole Resonators with Parallel-Connected Structures for Ladder-Type Acoustic Filters," IEEE *MTT-S International Microwave Symposium , Boston, MA, USA, June 2-7, 2019.*

- A. Triano, P. Silveira, J. Verdú and P. de Paco, "Phase Correction of Asymmetrical Chebyshev Polynomials for Extracted-Pole Fully Canonical Filters,"IEEE *MTT-S International Microwave Symposium, Boston, MA, USA, June 2-7, 2019.*

- P. Silveira, A. Triano, J. Verdú, P. de Paco, "Metodología de Síntesis para el Diseño de Filtros en Escalera, Duplexores y Multiplexores en Tecnología Acustica," *International Union of Radio Science (URSI), Sevilla, Spain, Sept. 2019.*

- A. Triano, J. Verdú and P. de Paco,"Synthesis of Acoustic Filters Based On Mixed-Topology With Parallel-Connected Structures," *European Microwave Week of Central Europe(EuMCE), Prague, Czech Republic, May, 2019.*

- A. Triano, J. Verdú, P. de Paco, T. Bauer, and K. Wagner, "Relation between electromagnetic coupling effects and network synthesis for aw ladder type filters," in 2017 IEEE *International Ultrasonics Symposium (IUS)*, Sept. 2017, pp. 1-4.

- J. Verdú, A. Gimenez, A. Triano, I. Evdokimova, P. Silveira and P. de Paco, "Distortion of the bandpass filter response under heterogeneous temperature distribution," *Microwave Technology and Techniques Workshop*, Noordwijk (The Netherlands), April 2017.

Acoustic Wave Filters in the Lowpass Domain

Acoustic wave technology is ubiquitous in filters for mobile communication systems. The basic building block of an acoustic wave filter is the resonators. They can be implemented with two different main families of technology: SAW and BAW. The methodology for ladder-type acoustic filter design, explained in the following chapter, is based on a lowpass synthesis approach. Before delving into it, it is necessary to establish a link between the bandpass network and the lowpass domain equivalent representation of resonators and ladder filters.

This chapter aims to provide an overview of the acoustic wave technology and modeling of the resonators in the lowpass domain. First, a description of the basic operation principles of SAW and BAW resonators are presented. The Butter-Worth Van Dyke model (BVD) is a simple circuital representation made of reactive lumped elements, but it is a useful tool to predict the behavior of the filtering circuit. Its simplicity is a great advantage that makes it suitable for the parameter extraction procedure of synthesis methodology.

After the synthesis, the network must be denormalized in frequency and impedance to provide the bandpass network. At this stage, physical characteristics, that the synthesis does not consider, come into play like the electromechanical coupling coefficient k_{eff}^2, the quality factor of the resonator and power handling capabilities, among others. To guide the design toward feasible filters, these design considerations are taken into account in Section 2.3.

2.1   Acoustic Wave Technology Fundamentals

The key elements of acoustic wave technology are piezoelectric materials; they operate by converting electrical energy into acoustic or mechanical energy. The mechanical waves propagate at a speed around 3000 and 11000 m/s [21, 22], depending on the substrate material. In general terms, the resonance fre-

7

quency is $f_r = V_p/2T$, where V_p is the propagation velocity and T is the thickness of the piezoelectric materials. The area is inversely proportional to the frequency. Thus, an individual resonator can be very small. These characteristic makes the AW filters very attractive for mobile systems where a high degree of miniaturization is paramount.

2.1.1 SAW Resonators

The main difference between SAW and BAW comes from the acoustic wave propagation way through the piezoelectric substrate. In SAW devices, the wave propagates along the surface from one terminal to the other through interdigital transducers (IDTs) as depicted in Figure 2.1. The IDTs are interleaved metal electrodes on each end of the device. They convert an electrical signal that excites one terminal into an acoustic wave that is turned back to an electrical signal when the other terminal is excited by the incoming wave. The acoustic wave amplitude traveling along the surface of the piezoelectric crystal decays into the substrate material, the accumulative decay of each resonator causes the insertion loss (IL) in SAW Filters.
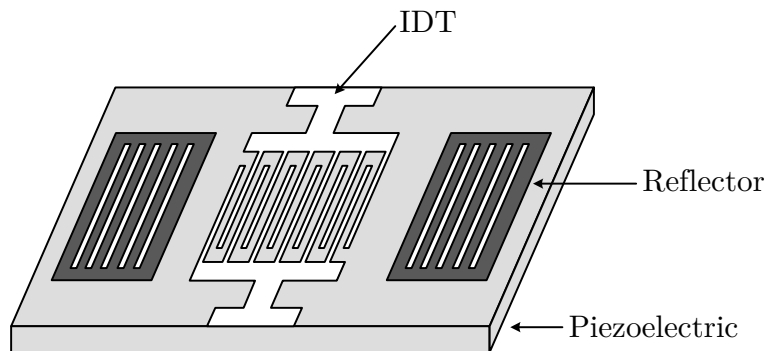
Figure 2.1: Structure of a SAW resonator.

The resonance frequency is limited by the gap of each IDT "finger", and the most suitable are up to 1.5 GHz. For frequencies higher than 2.5 GHz, there exist manufacturing limitations because the requirements for line width and gap separation in the IDTs necessitate a lithography resolution lower than 0.25 μm [22]. The most widely common crystal substrate material for SAW are lithium tantalite (LiTaO$_3$) and lithium niobate (LiNbO$_3$) [21], obtaining a Q factor around 1000 for conventional resonators for this technology.

In SAW filters the performance variation is dominated by the temperature drift. For this reason, they are required to have good temperature stability, and it must be considered for the SAW resonators design [21]. To improve the temperature performance of SAW devices, in [23] was presented the Temperature Compensated SAW (TC-SAW) that increase the effective range of operation up to 2 GHz. The TC-SAW includes additional layers of SiO$_2$ on top of the IDT gaining great temperature stability and Higher Q factor [24–28].

A more recent innovation is the Incredible High Performance SAW (I.H.P. SAW), made of a multi-layer substrate material. It was presented in [19] and released by Murata Co. LTd., this kind of resonators not only improves temperature stability but also increase the Q factor up to 4000 and reduce significantly the transmission losses in multiplexer designs [29].

Recently, the Longitudinal Leaky Surface Acoustic Wave (LLSAW) [30] is emerging as a feasible alternative. LLSAW is a resonator that suffers from leakage of energy through coupling with unnecessary displacement component through surface boundary [21]. Recent improvements have achieved a considerable reduction of the losses to lower propagation loss than non-leaky SAW [31].

In [32] it was investigated the applicability of LLSAW and I.H.P. SAW for frequencies from 3 GHz up to 5 GHz. Although there is no LLSAW with these characteristics in the market yet, it would be possible to see SAW devices at higher frequencies than the current commercial resonators and filters in the near future. In another attempt to elevate the usable frequency range, the Scandium-doping of aluminum nitride (ScAlN) material has been proposed for SAW technology [33]. Although it has shown promising results in terms of higher piezoelectric coefficients for 3-10 GHz frequency range than other technologies at such frequencies, the Q factor is still below 500 [34].

2.1.2 BAW Resonators

BAW resonators are made of a piezoelectric substrate with metal electrodes on top and bottom sides. The term bulk acoustic wave refers to acoustic waves that primary propagates within the bulk of the substrate, traveling vertically through the bulk between the metallic terminals. The most common substrate material is Aluminium Nitride (AIN). The thickness of the slab and the mass of the electrodes defines the resonance frequency [22]. There are two types of BAW resonators used in telecommunication systems, two different approaches that apply different strategies keep the waves from escaping into the substrate: Film Bulk Acoustic Resonator (FBAR) and Solidly Mounted Resonator (SMR).
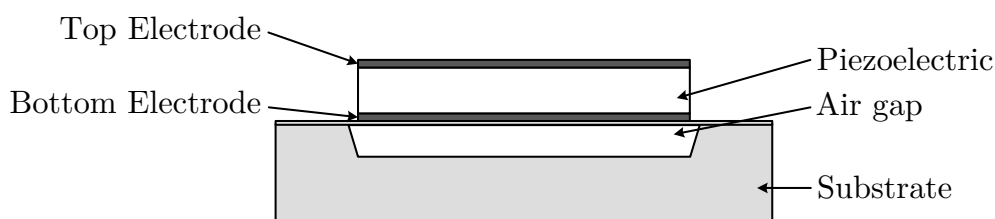
Figure 2.2: Sample structure of an FBAR.

The fundamental difference between FBAR and SMR is the mechanism whereby acoustic energy is trapped within the resonator. In FBAR, an air cavity is etched between the bottom electrode an the substrate to prevent the acoustic energy from propagating through the substrate, as shown in Figure 2.2. SMR opts to implement an acoustic Bragg reflector, a structure formed by multiple layers of alternating materials with low and high acoustic impedance [35], to keep the waves confined into the substrate as

shown in Figure 2.3.

In SMR, the Bragg reflector works by reflecting a percentage of the acoustic energy back into the resonator. The reflected wave will be approximately shifted in phase $180°$ in relation to the incident wave. The destructive interference resulting from transmitted and reflected waves make the Bragg stack looks like a mirror, reflecting the acoustic energy back into the resonator [36]. Imperfections in the manufacturing process of the layers may cause part of the acoustic energy to be stored in each layer of the Bragg reflector. This impacts negatively the Q factor and k_{eff}^2 of the resonator, reducing the achievable bandwidth of the filter.
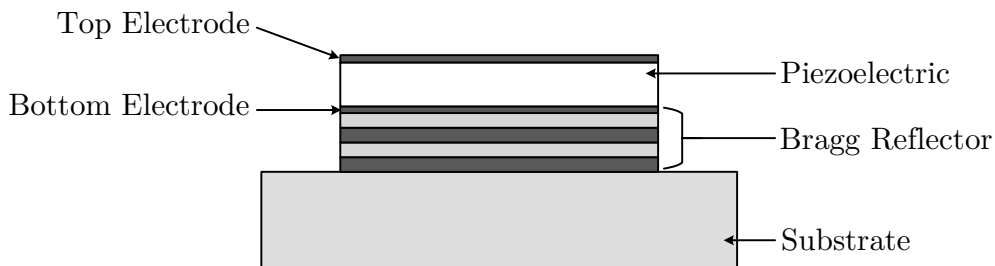
Figure 2.3: Sample structure of an SMR.

A major difference between FBAR and BAW-SMR is the thermal path for the heat generated in the device. The SMR is attached directly to the substrate, giving the ability to dissipate heat more efficiently [37]. FBAR consists of a resonator suspended over an air gap, a poor heat conductor. Thus, the heat generated by the resonators cannot escape so easily. This characteristic causes poorer power handling, higher temperature drifts and less mechanical robustness than the SMR. Although piezoelectric attached directly to the substrate in SMR may cause the appearance of parasitic modes in the resonator and mechanic losses. Yet, both types of resonators provide low loss and higher Q factor than SAW at frequencies over 2 GHz. The Q factor depends mostly on the material choice, but FBAR is the alternative with Q factors up to 4000 [38]. On the other hand, SMR has shown Q factors up 2000 [22] and over 2500 experimentally [39].

The 5G new radio (5G NR) standard defines ultra-wide bands (UWB) that spans bandwidths up to 600 MHz and 900 MHz with bands n79 and n77, respectively. These frequencies are a challenge for both design and technology. In 2019, a new resonator structure called laterally excited bulk acoustic resonators (XBAR) was presented [40,41]. This new type of AW technology can offer high k_{eff}^2 with Q factors over 1000. In [42] was presented the first XBAR filter, an n79 band with low insertion loss. Although it is only a prototype, it seems a promising solution for the new 5G UWB filters in AW technology.

Clearly, BAW technology has better performance than SAW. Nevertheless, instead of predating SAW in communication devices, both complement each other. BAW resonators offer good performance and higher Q factors for their frequency range of practical application, especially LTE bands that have very difficult out-of-band requirements where SAW displays a poorer performance, while SAW is preferable

in lower frequency applications for which its characteristics, good performance, and easier manufacturing make then unbeatable.

2.2 Circuital Equivalence and Lowpass Modeling

An equivalent lowpass network of the ladder filter suitable for AW technology has to be formulated to obtain a link between the synthesis techniques and the real devices. For such purpose, the lowpass equivalent model of bandpass filters with AW resonators must be defined. In this section, a model for acoustic wave resonators and ladder filters in AW technology for lowpass-to-bandpass transformation are discussed.

2.2.1 Acoustic Wave Resonator Model

Resonators may be modeled with the Butterworth-Van Dyke (BVD) equivalent circuit with lumped elements depicted in Figure 2.4. The model is suitable for both, SAW and BAW resonators [21,43,44]. The acoustic path is represented by a series resonator composed of L_a and C_a, and the static capacitance C_0 corresponds to parallel electrode plates of BAW resonators or the IDT of SAW resonator.
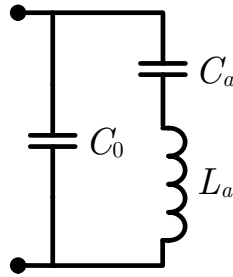
Figure 2.4: Butterworth-Van Dyke equivalent model of an acoustic wave resonator with lumped elements.

The BVD circuit only characterizes the first mode of the resonator, i.e., the fundamental resonance, neglecting higher order harmonics. Although it is a simple approach, it provides a good similitude to the behavior of the geometry and physical performance of the resonators. Besides, by having only three elements, it simple enough to be suitable for a parameter extraction synthesis and optimization with a low computational cost. The input impedance expression is

$$Z_{in}(\omega) = \frac{j\left(\omega L_a - \dfrac{1}{\omega C_a}\right)}{1 - \omega^2 C_0 L_a + C_0/C_a},$$ (2.1)

where ω is the bandpass frequency variable. The series and parallel resonances can be calculated by setting the input impedance to zero and infinite, respectively. They can be defined as

$$f_s = \frac{1}{2\pi\sqrt{L_a C_a}},$$ (2.2)

and

$$f_p = \frac{1}{2\pi}\sqrt{\frac{C_a + C_0}{L_a C_a C_0}} = f_s\sqrt{1 + \frac{C_a}{C_0}}. \tag{2.3}$$

Acoustic Wave Resonator Lowpass Domain Model

To apply the lowpass synthesis techniques for acoustic wave filter design, an equivalent prototype in lowpass domain must be created. The lowpass BVD model is achieved by a proper frequency transformation of the bandpass one. The resulting circuit is shown in Figure 2.5, where the static capacitance C_0 is substituted by a Frequency Invariant Reactante (FIR), a mathematical tool firstly introduced in [45] employed in the formulation of the lowpass prototype filter. The FIR becomes physically realizable after the filter transformation from lowpass to bandpass, in this case, as the capacitor C_0.
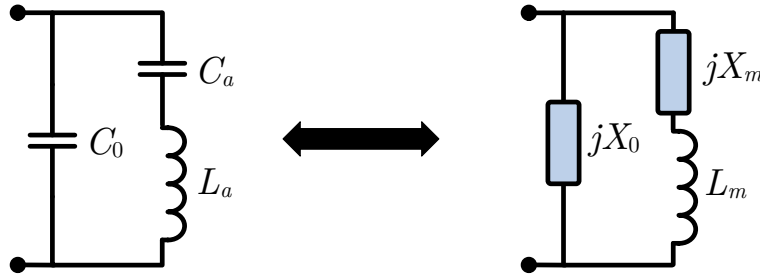
Figure 2.5: Bandpass and lowpass Butterworth-Van Dyke equivalent model of an acoustic wave resonator.

This element introduces a frequency shift from the center frequency of the filters enabling the realization of asymmetric filter response [46]. The input impedance of the lowpass model from Figure 2.5 is

$$Z_{in}(\Omega) = \frac{jX_0 \left(\Omega L_m + X_m\right)}{\Omega L_m + X_m + X_0}, \tag{2.4}$$

where X_0 and X_m are frequency invariant reactances and L_m and lowpass inductor. The variable Ω is the normalized frequency in the lowpass domain. For a bandpass filter type, it defines a bandwidth between ± 1 with a center frequency at zero and is given by

$$\Omega = \alpha\left(\frac{\omega}{\omega_0} - \frac{\omega_0}{\omega}\right), \tag{2.5}$$

where $\omega_0 = \sqrt{\omega_1\omega_2}$ is the center frequency of the filter passband computed as the geometric mean of the frequencies of the lower edge ω_1 and upper edge ω_2 of the band. The parameter α is the inverse relative bandwidth, expressed as

$$\alpha = \frac{\omega_0}{\omega_2 - \omega_1}. \tag{2.6}$$

To obtain the relationship between the bandpass and lowpass elements [47] is necessary to set them equal to each other, the input impedances in (2.1) and (2.4). The circuit comprises three elements. To fully determine the equivalences, the first and second derivative of the impedance are necessary. The bandpass

circuit elements evaluated at the center frequency ω_0 can be expressed in function of the lowpass equivalents as

$$L_a = \frac{Z_0}{2}\left(\frac{2\alpha L_m + X_m}{\omega_0}\right), \tag{2.7}$$

$$C_a = \frac{2}{Z_0}\frac{1}{\omega_0(2\alpha L_m - X_m)}, \tag{2.8}$$

$$C_0 = -\frac{1}{Z_0}\frac{1}{\omega_0 X_0}. \tag{2.9}$$

Note that the evaluation at ω_0 provides a circuit that behaves equally in both, lowpass and bandpass domain, at that frequency. This implies that the validity of bandpass transformation is limited to narrow bandwidth solution [45, 48]. The equivalent lowpass resonator described in this section is the basic cell of the filter. In further analysis of the filter synthesis in chapter 3, a nodal representation of the lowpass BVD model is employed, namely, the dangling resonator.
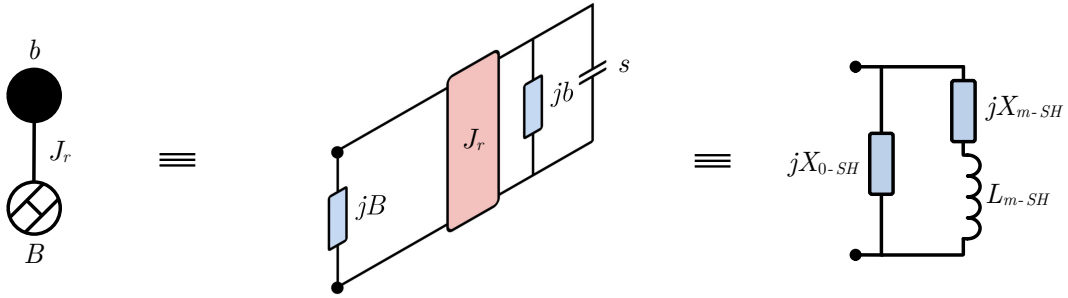
Figure 2.6: Equivalence between the dangling structure and the circuital representation of a BVD shunt resonator in lowpass.

The Dangling Resonator

The nodal model derived from the extracted-pole section [49] that provides with a TZ at finite frequency. The dangling resonator shown in Figure 2.6 is a three-component structure that consists of a Resonant Node (RN), made of a unit capacitor in parallel with a frequency-independent reactance b. The other elements are a Non-Resonating Node (NRN) implemented with an FIR B internally connected to ground and an admittance inverter J_r that represents the coupling between the former nodes. The meaning of the symbols for each node is specified in Figure 2.7, this representation is based on the symbology firstly described at [50] for the description of the lowpass prototype for the synthesis of microwave filters with reactive nodes. The input admittance of the whole dangling resonator is

$$Y_{in}(s) = \frac{J_r^2}{s + jb}. \tag{2.10}$$

When $s = -jb$, the input admittance (2.10) becomes infinite, creating a short circuit to ground through the NRN and producing a TZ at $j\Omega = -jb$. The constant reactance b of the RN performs a frequency shift to produce a TZ. This element is directly associated with the TZ implemented by the acoustic wave
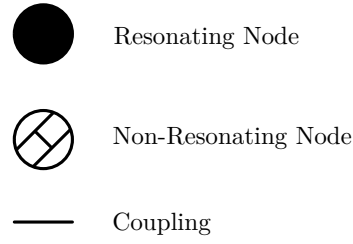
Figure 2.7: Nodes symbols of the dangling resonator.

resonator. They can be interpreted as the resonance frequency of shunt resonators of the anti-resonance frequency for the series resonators. Figure 2.6 shows the equivalence for shunt resonators. By analyzing the input admittance expressions of dangling and BVD circuits, the relationship between them results in:

$$L_{m-SH} = \frac{1}{J_r^2},$$
(2.11)

$$X_{m-SH} = \frac{b}{J_r^2},$$
(2.12)

$$X_{0-SH} = \frac{1}{B}.$$
(2.13)

The series resonator is obtained from serializing the shunt model with a dangling structure by placing an admittance inverter at each side, as depicted in Figure 2.8. To maintain the magnitude and phase characteristics of the resonator, it is a mandatory condition that both admittance inverters J have the same value and opposite sign. Establishing the relationship between the lowpass BVD and the series dangling structure [47] provides the following results:

$$L_{m-SE} = \frac{B^2}{J_r^2 J^2},$$
(2.14)

$$X_{m-SE} = \frac{B}{J^2}\left(\frac{bB}{J_r^2} - 1\right),$$
(2.15)

$$X_{0-SE} = \frac{B}{J_r^2}.$$
(2.16)

In both configurations, the NRN is a direct representation of the static capacitance of the BVD model. To guarantee a positive capacitor C_0 after the bandpass denormalization, the FIR B must be positive for series resonators and negative for shunt resonators. The constant susceptance b is the lowpass normalized TZ introduced by a resonator. The sign of the element has to considered to provide a realizable filter. In case of shunt resonators, b must be positive to introduce a TZ in the lower side of the band and negative for series resonators, placing a TZ above the passband.
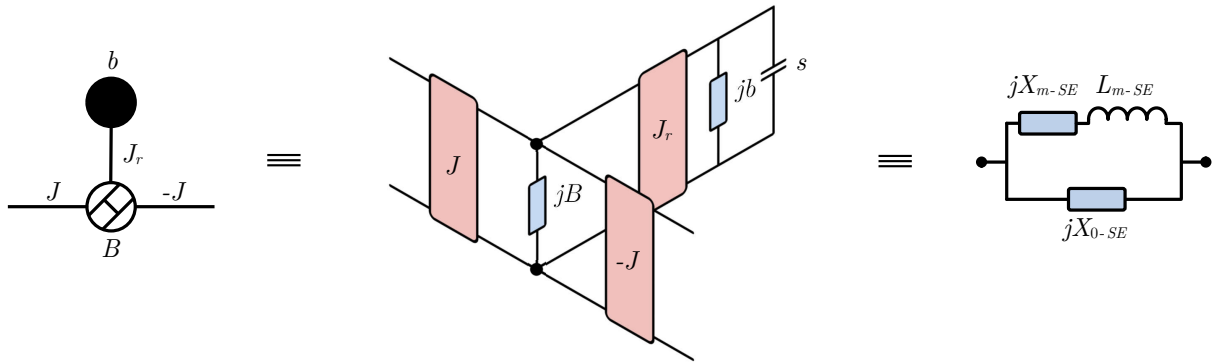
Figure 2.8: Equivalence between the dangling structure and the circuital representation of a BVD series resonator in lowpass domain.

2.2.2   Acoustic Wave Ladder Filter

A ladder topology consists of cascaded resonators alternating series and shunt connected. In acoustic wave, each transmission zero is controlled by an independent resonator. This characteristic provides modularity in the design as the main feature. Therefore, the ladder filter based on acoustic wave technology is always a fully canonical network. This condition made them suitable for the use of the extracted-pole synthesis technique [51].

In Figure 2.9, a generic ladder filter and its lowpass prototype are shown. In this example, the network is made of electrically coupled resonators and also shunt inductors at both ports. These lumped elements usually result from the extraction procedure as phase-matching elements. The lowpass prototype is an in-line network made of dangling resonators. Those in shunt configuration are made of a dangling structure, and the series are made of the same configuration but placed between admittance inverter as described in the previous section.

2.3   Design Considerations and Technological Accommodation

To produce feasible filters, there are some restrictions of acoustic wave technology that the designer must be concerned about before initiating fabrication procedure. Some technological requirements are different depending on whether the technology of the filter is SAW or BAW. Even within the same technology family, different implementations and materials of the resonators impose other conditions linked to the manufacturing process. Other restrictions are motivated by the required reliability, performance, power handling or chip size. The designer also has to be able to provide filters with high selectivity, low IL level along with the defined bandwidth, high rejection level at stop-band, temperature operation range, electrostatic discharge stability and nonlinear effects that may have an significant impact in the filter operation. Some of the above-mentioned requirements can be taken into account during the synthesis process, and it is essential that the designer guides the synthesis of the network to facilitate its realizability.
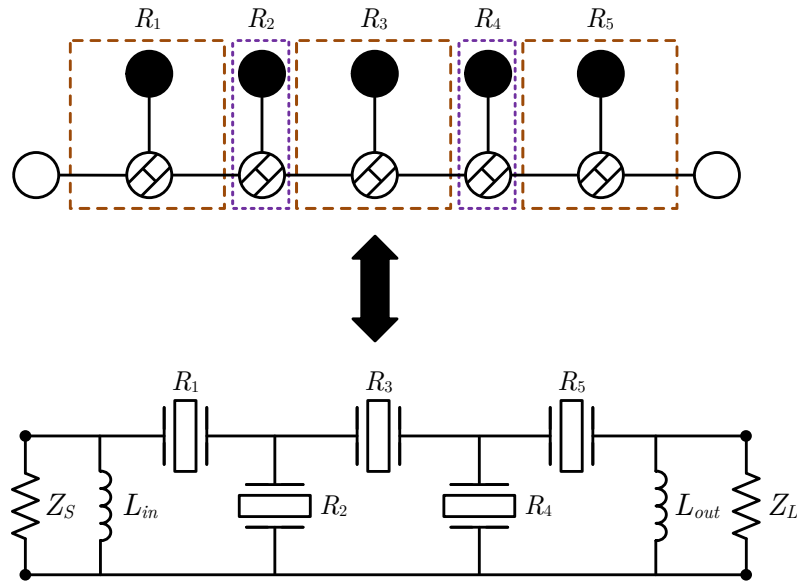
Figure 2.9: Equivalence between a 5th-order filter in acoustic wave and the lowpass inline network made of dangling resonators.

Several fundamental technological considerations are described in this section to provide a better understanding of the constraints for BAW and SAW resonators.

2.3.1 Piezoelectric Coupling Coefficient and Achievable Bandwidth

The energy conversion efficiency of a resonator at resonance frequency is a great concern for the designers. The electromechanical coupling factor in a resonator is, along with the quality factor, a parameter that describes the efficiency of energy conversion processes. In AW technology we can distinguish two different types of electromechanical coupling factors: K^2 that belongs exclusively to the piezoelectric material used in the resonator which only depends on the material properties, and k_{eff}^2, a property of the resonator that depends on the implementation of the resonator, including the metallic terminals.

Table 2.1: List of the most used piezoelectric materials for resonators fabrication and its coupling coefficient K^2.

Material	AIN	ZnO	PZT	LN	LiNbO$_3$	LiTaO$_3$
K^2 (%)	6.5	8.5	23	23	5.5	0.75

The piezoelectric coupling factor K^2 is a dimensionless quantity used to evaluate the efficiency of a piezoelectric material in mutually converting electrical energy to mechanical energy. The nominal maximum piezoelectric coupling factor for the most used materials in the fabrication of resonators are listed in Table 2.1 [52, 53]. In AW resonators, the material choice set the limit of the achievable k_{eff}^2. This parameter is related to the series and parallel resonance frequencies, and consequently, the fractional bandwidth

(FBW) for filters applications. For wide bandwidths, it is necessary to have resonators with high effective coupling coefficients. In BAW technology the maximum achievable k_{eff}^2 is around 9% [38] and can be calculated by

$$k_{eff}^2 = \frac{\pi^2}{4} \left(\frac{f_p - f_s}{f_p} \right), \tag{2.17}$$

where f_p and f_s are the anti-resonance and series resonance frequency of a resonator, respectively. In SAW technology the maximum achievable $k_{eff}^2 \sim 11\%$ [38, 54], although a common factor to measure a resonator performance is the capacitance ratio r [55] which is defined as

$$r = \frac{C_0}{C_a} = \frac{1}{(f_p/f_s)^2 - 1}. \tag{2.18}$$

Both, r and K_{eff}^2 can be related by the following equation [56]:

$$k_{eff}^2 = \frac{\pi^2}{8} \left(\frac{1}{r} \right) \left(1 - \frac{1}{r} \right). \tag{2.19}$$

To have a viable filter, the manufacturing process requires all resonators to have the same k_{eff}^2 or r factor where only a small variation range is acceptable. Customarily, the designs may require some resonators with coupling coefficients out of the practicable range. In such cases, reactive elements can be added to series and shunt resonator to increase or decrease the k_{eff}^2 value if necessary [57]. Despite adjusting the coupling coefficient, the reactive elements modify the resonance frequencies of the affected resonators. Moreover, if their quality factor Q is low, the performance of the passband and insertion loss (IL) may be deteriorated significantly. Therefore, the use of reactive element should be minimized as much as possible for a good design.

In [58], a hybrid approach is proposed that consists in adding an LC resonator in series or parallel to resonator in the acoustic wave technology to increase k_{eff}^2. They show a potential application for wide-band filter designs. However, the low Q factor of the lumped elements may reduce its applicability.

From the synthesis point of view, the required k_{eff}^2 can be configured with the return loss (RL) and the TZs set that defines the filtering function. AW filters are usually fully canonical; hence, the resonance frequencies meet with the prescribed TZs. Their values can be changed and rearrangement along the resonators to find the k_{eff}^2 values to satisfy the required conditions. However, there is limited leeway to maneuver with the input parameters of the filtering function alone. Complementary, this limitation can be overcome with the definition of mixed-topology filters that combines parallel-connected and ladder networks in which some of the prescribed TZs are disassociated from the resonance frequencies of the resonators. This characteristic provides a more flexible assignation of TZs and resonance frequencies to the resonators. The synthesis of these topologies are thoroughly described in chapter 5 and 6.

2.3.2 Insertion Loss and Quality Factor

The insertion loss is one of the most relevant specifications of the filter. The requirements for IL are usually between 1.8 and 3 dB. Its value has a direct impact on the noise figure, which delimits the

efficiency of the receiver chain. For instance, greater values than 3 dB imply that more than 50% of the power is dissipated in the filter. The waste of energy forces to use more power to amplify the signal, reducing the battery life. In other cases, it may cause call interruptions if the received signal is too weak to be processed. Even complying with the IL range, the maximum acceptable variation in the passband or ripple is also limited as this ripple distorts the signal in magnitude and phase.

Insection loss in AW filters has several sources [22], resistive losses, material losses, thermal effects, the order of the filter, signal leakages between the elements that form a filter such as electromagnetic feed-through due to internal couplings or imperfect grounding [59] among others. Although many loss sources have its origin in the material properties, the electromagnetic feed-through in particular and its effects on the filter performance can be addressed from the synthesis point of view, a complete discussion of the matter can be found in Chapter 6.

The quality factor of the resonators is strongly related to IL. With low Q, the losses increase dramatically. With lower Q values, the losses at passband edges are more pronounces than in the middle of the band, and they become more rounded, narrowing the passband as a consequence. Along with the K_{eff}^2 and the characteristic impedance, the quality factor is the most important figure of a resonator. The unloaded Q is defined as the ratio of the stored energy divided by the power dissipated over one cycle [60]. This parameter establishes the upper limit for the overall resonator performance.
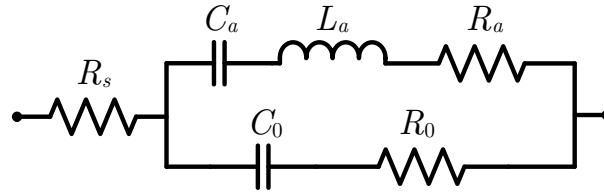
Figure 2.10: Modified BVD equivalent circuit of an acoustic wave resonator considering losses.

The BVD model and synthesis procedure described in the following chapter is a lossless methodology and considers infinite Q. To include the resonator losses in the circuital model, the modified BVD (mBVD) is a more accurate representation of an acoustic resonator [56]. The network is depicted in Figure 2.10, R_s models the metal electrode resistance, R_a is responsible for the acoustic losses in the resonator, and R_0 is associated to the losses introduces by the dielectric material.

The quality factor depends on the frequency. It is typically characterized at two frequencies, Q_s at the resonance frequency f_s and Q_p at the parallel resonant frequency f_p [61]:

$$Q_s = -\frac{1}{2} f_s \frac{\partial \varphi}{\partial f}\bigg|_{f=f_s} \approx \frac{2\pi f_s L_a}{R_a + R_s}, \tag{2.20a}$$

$$Q_p = -\frac{1}{2} f_p \frac{\partial \varphi}{\partial f}\bigg|_{f=f_p} \approx \frac{2\pi f_p L_a}{R_a + R_0}, \tag{2.20b}$$

where φ is the phase angle of the impedance. To aggregate the lossy characteristic of the resonator to

the synthesized filters, the poles and zeros of the transfer function have to be detuned by shifting the real part of complex frequency variable s with $s \longleftarrow s + \tan\delta$, where $\tan\delta$ is the loss tangent. The unloaded quality factor is given by

$$Q = \frac{1}{\tan\delta}. \tag{2.21}$$

In the lowpass domain, the frequency variable can be transformed as [46]

$$\Omega = \Omega - \frac{j}{Q_{LP}}. \tag{2.22}$$

The transformation includes the shifted frequencies and losses. The lowpass quality factor Q_{LP} is computed as

$$Q_{LP} = Q\frac{\Delta\omega}{\omega_0}. \tag{2.23}$$

This quality factor estimation shows a good agreement with the filter response in bandpass domain. Although it should be noted that the quality factor is linear in the frequency range. The approximation could make the simulation to fail in matching the real filter response accurately in some cases. A more precise simulation needs to take into account Q_s and Q_p and R_s to calculate the mBVD model. Usually, these parameters are conditioned by the technology and the manufacturing process. The remaining resistors of the model can be obtained from (2.20) with

$$R_a = \frac{2\pi f_s L_a}{Q_s} - R_a, \tag{2.24a}$$

$$R_0 = \frac{2\pi f_p L_a}{Q_p} - R_a. \tag{2.24b}$$

2.3.3 Power Handling and Temperature Effects

The acoustic wave filters used in communication devices receive powers between 29-30 dBm at the input port from the antenna, and TX filters usually work at higher power levels. Part of the applied power will dissipate and cause a self-heating of the filter. A phone is designed to work properly at an ambient temperature range between -30°C and +55°C. Although being in the working range, temperature increments reduce the lifetime of a filter. It is expected durability longer than 5000 hours at an average temperature of +55°C at maximum power [52].

Many new bands for 5G extend up to 6 GHz for mobile communication devices and even over 24 GHz for other applications. In the new frequency bands, the shrinking of the chipsets is not only a possibility but an imposition to achieve greater levels of integration. Smaller size and higher frequencies lead to more power density in the device, which magnifies the self-heating of the resonators, affecting the filter performance. BAW resonators have a clear comparative advantage over SAW in terms of power handling. In BAW technology, the power density is better uniformly distributed over the filter area [14] and both SMR and FBAR can stand more power due to the better heat removal through the substrate, especially in SMR because of the higher thermal conductivity of the Bragg reflector. On the contrary, the

narrow space between the IDT fingers in SAW resonators makes them prone to exhibit lower tolerance to high power due to electromigration and stress migration damages.

In this regard, the Temperature Coefficient of Frequency (TCF), measured in parts per million (ppm) per degree, has become an important parameter to evaluate the temperature sensitivity and performance. Due to the thermal behavior of the filter, temperature variation diminishes the nominal bandwidth and provokes a shift in frequency [62, 63]. Insertion loss also increases, especially at the upper cut-off frequency, where the effect is more critical.

TC-SAW and TC-BAW devices use an additional SiO_2 layer to minimize the TCF. This material has inverse thermodynamic behavior to the substrate used in standard BAW and SAW technology. A conventional SAW resonator exhibits TCF variation of -35 to -45 ppm/$^\circ$C. Meanwhile, BAW shows a TCF between -22 and -31 ppm/$^\circ$C [17]. The positive temperature coefficient in SiO_2 provides partial temperature compensation, reducing the drift up to -22 and -17 ppm/$^\circ$C for TC-SAW and TC-BAW respectively. The most recent devices like No-drift^{TM} technology from Qorvo [64] reaches TCF between ± 2 ppm/$^\circ$C for BAW and SAW resonators, and the I.H.P. technology by Murata can reduce the TCF to zero by an appropriate design [19].

The network synthesis may yield resonators which power density is more than resonator alone can withstand. A common practice to deal with these situations consists in replacing the single resonator by a cascading some resonators [16, 65]. The solution is effective but, consequently, the impedance and static capacitance changes, the insertion loss increase, and the required die area is bigger. The power density and area estimation can be done as described in [66]. The power density distribution over the resonators depends on the RL and TZs. As ladder filters are fully canonical, the resonance frequency of each resonator is one of the TZs of the filtering function. The TZs assignation to each resonator will change the values of the synthesized filter. That is, the power density of each resonator. A design with a careful selection of the filter parameters and TZs arrangement along the network is crucial to provide a good balance between power handling, size and performance.

2.4   Chapter Summary

In this chapter, it has been presented the acoustic wave technology and the fundamentals for the two main technology families, SAW and BAW. The first is an already mature technology that provides good performance at frequencies below 2 GHz. On the other hand, BAW characteristics outmatch SAW counterpart's performance but, its complicated geometry results in high costs for massive manufacturing in comparison with SAW. Despite these drwabacks, it is the best-suited technology for frequencies over 2 GHz.

The design of fully canonical ladder acoustic filters is based on the lowpass domain synthesis of a filtering function. The nodal lowpass equivalent of an acoustic wave resonator is the dangling structure.

A ladder-type filter is made by cascading N dangling resonators where N represents the filter order and number of transmission zeros. The frequency and impedance transformation of the lowpass prototype to the bandpass network is based on the BVD model of the acoustic resonators.

Although further physic behavior of the resonator is not taken into account by the synthesis techniques, some technological requirements have to be considered for better accommodation of the synthesized network to the acoustic technology at this stage of the design process. A good understanding of the technological constraints is crucial to obtain a good design.

Synthesis Fundamentals of Lowpass Filters

The methodology for the design of ladder-type acoustic filters is typically based on a lowpass synthesis approach. The procedure generally consists of a four stages process. The first step is the definition of the filtering function to be implemented, followed by the generation of a lowpass prototype network. This prototype must be able to accommodate the characteristic frequencies of the filtering function under consideration. In the third stage, the bandpass network is obtained by the frequency denormalization and impedance scaling of the lowpass prototype. Finally, the network is evaluated to check the fulfillment of the frequency mask. Also, the factors that influence the filter feasibility are validated: power density level of each resonator, quality factors, achievable bandwidth, and the fulfillment of the acoustic wave technology constraints, among other parameters.

In the previous chapter, the AW resonators and the technological constraints have been presented. It has been also described how to obtain the equivalence between the acoustic wave resonator and a lowpass circuit based on the BVD model. Furthermore, a link between the ladder filter and the equivalent lowpass prototype as an inline network made of extracted-pole section has been established.

In order to address the filter definition and design from a bottom-up approach, this chapter focuses mainly on the first and second stages. It aims to introduce the synthesis of the general Chebyshev filtering function that defines the transmission and reflection response of the network, and the synthesis procedure to extract the lowpass filter parameters is described in detail. Finally, the coupling matrix representation of the filter in both bandpass and lowpass domain, is introduced as a tool to describe the transfer function and analyze the network.

3.1 Matrix Representation of Chebyshev Polynomials for Two-Port Filtering Networks

The filtering function is a mathematical description of a linear network frequency response that ultimately must satisfy a particular set of electrical specifications. Several filtering functions can be found in the literature, such as the Butterworth, Cauer, or Bessel. Nevertheless, the most adequate is the generalized Chebyshev [67] filtering function, which provides equiripple passband, transmission zeros at infinity, and finite frequencies with a minimum impedance variation in the network.

By considering the filters as passive and lossless networks, they can be generically described with any equivalent two-port network matrix representation. In this section, the ABCD transfer matrix and the scattering parameters matrix [68] are considered. From the latter, the network can be defined in a general polynomial form:

$$[S] = \begin{bmatrix} S_{11} & S_{12} \\ S_{21} & S_{22} \end{bmatrix} = \frac{1}{E(s)} \begin{bmatrix} F(s)/\varepsilon_R & P(s)/\varepsilon \\ P(s)/\varepsilon & (-1)^N F(s)^*/\varepsilon_R \end{bmatrix}, \tag{3.1}$$

where $s = j\omega$ is the frequency variable and N identifies the filter order that, therefore, decides the resonators number. $E(s)$ and $F(s)$ are polynomials of Nth degree with complex coefficients. $E(s)$ is the common polynomial denominator and it is strictly Hurwitz; it implies that its roots are located in the left half-plane of the complex plane or lying along the imaginary axis [69]. In other words, the real part of every root must be zero or negative, this is a necessary condition to guarantee the system stability. $F(s)$ polynomial is the numerator of $S_{11}(s)$, and its roots define de reflection zeros (RZ) of the filtering function. The real constant ε_R normalizes $F(s)$ to turn it monic. The numerator of the transmission parameter $S_{21}(s)$ is the polynomial $P(s)$, which is calculated from normalized TZs at the prescribed finite frequencies at the beginning of the design process. Its coefficients alternate from purely real and purely imaginary values, and it is normalized by the real constant ε.

From the equation of energy conservation for a lossless reciprocal network can be proven the relationship between each polynomial as follows,

$$E(s)E(s)^* = \frac{P(s)P(s)^*}{\varepsilon^2} + \frac{F(s)F(s)^*}{\varepsilon_R^2}. \tag{3.2}$$

Besides, an important orthogonality condition derives from the S-parameters for these kinds of networks:

$$S_{11}(s)S_{12}(s)^* + S_{11}(s)S_{22}(s)^* = 0. \tag{3.3}$$

By expressing equation (3.3) in a polar form, the relationship of $S_{11}(s)$, $S_{22}(s)$ and $S_{21}(s)$ phases is obtained by

$$-\theta_{21}(s) + \frac{\theta_{11}(s) + \theta_{22}(s)}{2} = \frac{\pi}{2}(2k \pm 1). \tag{3.4}$$

The equation states that the right-hand side must be an odd multiple of $\pi/2$ radians, that is, the difference between the phase of $S_{21}(s)$ and the average of phases of the $S_{11}(s)$ and $S_{22}(s)$ is orthogonal. A further

development of (3.3) to express it in terms of the filter order N and the number of TZs at finite frequencies n_{fz}, as in [46], yields

$$(N - n_{fz})\frac{\pi}{2} - k_1\pi = \frac{\pi}{2}(2k \pm 1), \tag{3.5}$$

where k_1 is an integer value. Equation (3.3) implies that the integer quantity $(N - n_{fz})$ must be odd in order to satisfy the right-hand side. From this result, the following conclusion can be drawn: in case of fully canonical networks, where $(N - n_{fz}) = 0$, thus always even, an extra $\pi/2$ radians must be added to the left hand of the equation (3.5), which is equivalent to multiply polynomial $P(s)$ by j.

Alternatively to S-parameters, the filter can be expressed as an ABCD transfer matrix using the classic two-port matrix transformation relations with normalized characteristic impedance. In turn, the scattering parameters can also be expressed in terms of the polynomials $E(s)$, $F(s)$ and $P(s)$ as [46]:

$$A(s) = \frac{(E(s) + F(s)/\varepsilon_R) - (-1)^N(E(s) + F(s)/\varepsilon_R)^*}{2P(s)/\varepsilon} = \frac{A_n(s)}{P(s)/\varepsilon}, \tag{3.6a}$$

$$B(s) = \frac{(E(s) + F(s)/\varepsilon_R) + (-1)^N(E(s) + F(s)/\varepsilon_R)^*}{2P(s)/\varepsilon} = \frac{B_n(s)}{P(s)/\varepsilon}, \tag{3.6b}$$

$$C(s) = \frac{(E(s) - F(s)/\varepsilon_R) + (-1)^N(E(s) - F(s)/\varepsilon_R)^*}{2P(s)/\varepsilon} = \frac{C_n(s)}{P(s)/\varepsilon}, \tag{3.6c}$$

$$D(s) = \frac{(E(s) - F(s)/\varepsilon_R) - (-1)^N(E(s) - F(s)/\varepsilon_R)^*}{2P(s)/\varepsilon} = \frac{D_n(s)}{P(s)/\varepsilon}. \tag{3.6d}$$

Polynomials in (3.6) have a common denominator $P(s)/\varepsilon$, hence, the matrix form may be defined as

$$[ABCD] = \frac{1}{jP(s)/\varepsilon}\begin{bmatrix} A_n(s) & B_n(s) \\ C_n(s) & D_n(s) \end{bmatrix}, \tag{3.7}$$

where polynomials $A_n(s)$, $B_n(s)$, $C_n(s)$, $D_n(s)$ are the numerators of their respective ABCD polynomials. It must be also considered that $P(s)$ have to be multiplied by j when $(N - n_{fz})$ is even according to (3.5). Although the S-parameter matrix is entirely equivalent to the ABCD transfer matrix, the last is more suitable to perform the network synthesis process considered in this chapter.

3.1.1 Relationship Between ε and ε_R

The three polynomials are normalized so that their highest-degree coefficients are unit. That is, the parameters $|S_{11}(s)|$ and $|S_{21}(s)|$ are bounded to ≤ 1 at any value of the frequency variable s, a required to condition to be the functions that define a passive network. The real constants ε and ε_R are the normalizing coefficients for the characteristic polynomials necessary to guarantee the condition fulfillment.

The real constant ε is obtained by evaluating $P(s)/E(s)$ to a frequency where the values of $|S_{11}(s)|$ or $|S_{21}(s)|$ are known. For instance, $\pm j$ where the equiripple for Chebyshev filters is easily determined. The normalizing constant is defined by

$$\varepsilon = \frac{1}{\sqrt{1 - 10^{RL/10}}}\left|\frac{P(s)}{E(s)}\right|_{\pm j}. \tag{3.8}$$

By the evaluation of $|S_{11}(s)|$ and $|S_{21}(s)|$, the relation of both constants can be determined by

$$\frac{\varepsilon}{\varepsilon_R} = \frac{1}{\sqrt{1 - 10^{RL/10}}} \left| \frac{P(s)}{F(s)} \right|_{\pm j}. \tag{3.9}$$

The chosen frequency $s = \pm j$ sets that the maximum level for $|S_{21}(s)|$ at 1. For non-fully canonical network, that is, $n_{fz} < N$, the transmission parameter $|S_{21}(s)| = 0$. Then, by the principle of conservation of energy, the evaluation at infinity results in

$$S_{11}(s) \Big|_{\pm j\infty} = \frac{1}{\varepsilon_R} \left| \frac{F(s)}{E(s)} \right|_{\pm j\infty} = 1, \tag{3.10}$$

where ε_R is unity because polynomials $F(s)$ and $E(s)$ monic. For fully canonical network, where $n_{fz} = N$, the attenuation level at $\pm j\infty$ is finite. Thus, ε_R can be computed from the energy conservation equation (3.2) as

$$\varepsilon_R = \frac{\varepsilon}{\sqrt{\varepsilon^2 - 1}}. \tag{3.11}$$

Given that ε is greater than 1, the resulting factor ε_R is slightly higher than 1.

3.1.2 General Chebyshev Polynomials Synthesis

The Chebyshev filtering function provides the definition of filters with even and odd degree, TZs at a finite frequency and/or infinitive with asymmetric or symmetric characteristics. This section describes a recursive technique for generating the characteristic Chebyshev polynomials [46, 70] with a given set of prescribed transmission zeros and a return loss level as the only necessary parameters to define it. The general filtering function for a N degree network is described by [71]

$$C_N(\omega) = \cosh \left[\sum_{n=1}^{N} \cosh^{-1}\left(x_n\left(\omega \right) \right) \right], \tag{3.12}$$

where term $x_n(\omega)$ is a function of the real frequency variable related to the complex frequency $s = j\omega$ that contains N both RZs and TZs, the latter can be either at a finite frequency or infinite. The functions require the following properties:

- At $\omega = \omega_n$, where ω_n is either a transmission zero at a finite frequency or infinity, $x_n(\omega) = \pm\infty$.

- At the passband edges, defined at $\omega = \pm 1$, $x_n(\omega) = \pm 1$.

- Between $\omega = -1$ and $\omega = 1$, $1 \geq x_n(\omega) \geq -1$.

Satisfying the above-listed constraints, the expression $x_n(\omega)$ is defined as

$$x_n(\omega) = \frac{\omega - 1/\omega_n}{1 - \omega/\omega_n}. \tag{3.13}$$

The filtering function $C_N(\omega)$ can be also be expressed in function of the characteristic polynomials such as

$$C_N(\omega) = \frac{\varepsilon F(\omega)}{\varepsilon_R P(\omega)}. \tag{3.14}$$

The transmission zeros at finite frequencies n_{fz} are the roots of polynomial $P(\omega)$. In case of fully canonical network, $N = n_{fz}$ and the polynomial can be derived by

$$P(\omega) = \prod_{n=1}^{N} \left(1 - \omega/\omega_n\right). \tag{3.15}$$

The roots of $F(\omega)$ polynomial are the reflexion zeros of the filter, and its coefficients are computed by a recursive technique where the solution for the nth degree polynomial is built up from the results of the $(n-1)$th degree from the equation (3.12). The filtering function $C_N(\omega)$ may be rewritten as

$$C_N(\omega) = \frac{1}{2} \left[\frac{\prod_{n=1}^{N} (c_n + d_n) + \prod_{n=1}^{N} (c_n - d_n)}{\prod_{n=1}^{N} (1 - \omega/\omega_n)} \right], \tag{3.16}$$

the denominator is the definition of $P(\omega)$ in (3.15), meanwhile c_n and d_n are

$$c_n = \left(\omega - \frac{1}{\omega_n}\right), \tag{3.17a}$$

$$d_n = \omega' \sqrt{1 - \frac{1}{\omega_n^2}}. \tag{3.17b}$$

where $\omega' = \sqrt{\omega^2 - 1}$. To apply the recursive technique, only the $C_N(\omega)$ numerator is necessary. It may be expressed as

$$Num\left[C_N(\omega)\right] = \frac{1}{2} \left[G_N(\omega) + G'_N(\omega)\right], \tag{3.18}$$

where the terms $G_N(\omega)$ and $G'_N(\omega)$ are

$$G_N(\omega) = \prod_{n=1}^{N} \left[c_n + d_n\right], \tag{3.19a}$$

$$G'_N(\omega) = \prod_{n=1}^{N} \left[c_n - d_n\right]. \tag{3.19b}$$

And in turn, $G_N(\omega)$ can be rearranged as the sum of two polynomials

$$G_N(\omega) = U_N(\omega) + V_N(\omega), \tag{3.20}$$

where the roots of polynomial $U_N(\omega)$ are the ones that belong to $F(\omega)$. The recursive procedure commences by considering the first TZ ω_1 setting $N = 1$ such as

$$U_1(\omega) = \omega - \frac{1}{\omega_1}, \tag{3.21a}$$

$$V_1(\omega) = \omega' \sqrt{\left(1 - \frac{1}{\omega_1^2}\right)}. \tag{3.21b}$$

The result after the first recursion cycle is multiplied by the rest of TZs terms one by one until all of them, including those located at infinite, are used. The general expression for steps $n > 1$ are derived by

$$U_n(\omega) = \omega U_{n-1}(\omega) - \frac{U_{n-1}(\omega)}{\omega_n} + \omega' \sqrt{\left(1 - \frac{1}{\omega_n^2}\right)} V_{n-1}(\omega), \qquad (3.22a)$$

$$V_n(\omega) = \omega V_{n-1}(\omega) - \frac{V_{n-1}(\omega)}{\omega_n} + \omega' \sqrt{\left(1 - \frac{1}{\omega_n^2}\right)} U_{n-1}(\omega). \qquad (3.22b)$$

After the last recursion step, polynomial $F(\omega)$, is defined by $U_n(\omega)$. Finally, the remaining polynomial $E(\omega)$ can be calculated from the equation of energy conservation (3.2). Thus, the filtering function is completely described by polynomials $P(\omega)$, $F(\omega)$, $E(\omega)$ and the normalizing constants ε and ε_R.

3.2   General Description of the Synthesis Method

In this section, the general synthesis procedure for cross-coupled filters prototypes with resonant and non-resonant nodes proposed by Tamiazzo and Macchiarella in [72] is analyzed in detail. This work covers the fundamental theory required for the extraction of every parameter of a filtering network for the diverse types of topologies. The synthesis procedure described in the following chapters focuses on mixed-topology filters combining inline with transversal networks. The analysis presented in this chapter provides a general description of the method for inline networks, and it also supports a good understanding of the method to be integrated with the transversal network.

As an addition to the method, the susceptance of the first and last node extraction of the network is covered in two different ways. The conventional extraction yields a shunt FIR connected to ground, but in some designs could be useful to extract them as a series element, providing more flexibility to the definition of the ladder filter.

3.2.1   Sub-Network Definition

The synthesis method is based on a recursive extraction procedure from an overall network H_k that requires N steps. At each k step, a two-port sub-network is extracted, which scheme is depicted in Figure 3.1. The sub-network comprises a frequency invariant susceptance B_k, an admittance inverter J_k, an admittance Y_k, and a cross admittance inverter J_{ck} between the input and output nodes. The last element, the block H_{k+1}, contains the rest of the sub-networks to be extracted after the kth step.
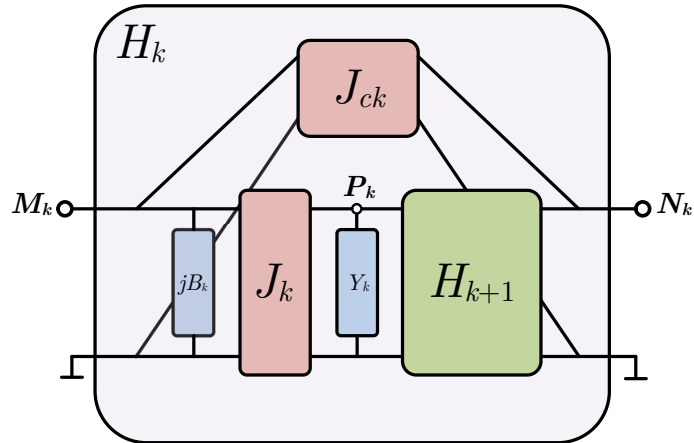
Figure 3.1: Recursive network and sub-network H_k scheme. This figure has been adapted from [72], © 2015 IEEE.
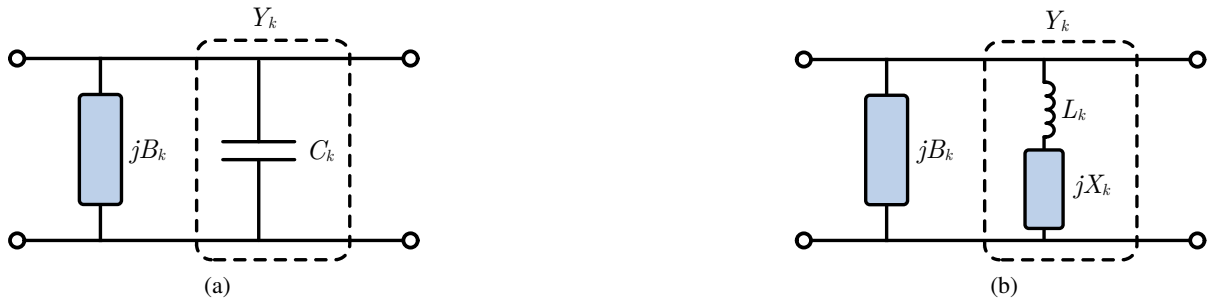
Figure 3.2: Sub-network admittance Y_k scheme of (a) a resonant node and (b) an NRN-RN pair.

One of the capabilities of the synthesis method is the definition of different network topologies for the same filtering function. To identify the location of the parameters to be extracted in a specific topology, three nodes are identified. The node M_k establishes where the extraction begins at each kth step. The second node N_k represents the input or output node, depending on the extraction direction. The third is the inner node P_k and indicates where the admittance Y_k is extracted. This element can be defined as either capacitance or inductance in series with an FIR. Thus, together with B_k, it can configure an RN or an RN-NRN pair as shown in Figure 3.2. Notice the equivalence with the lowpass BVD circuit presented in Figure 2.5.

Additionally, a binary word W is introduced to control the extraction process. The variable must be initially specified, and it defines both the topology and the extraction order, from the source side to load or vice versa. If $W_k = 0$, the extraction is carried out from source to load, and, conversely, $W_k = 1$ inverts the direction of extraction from load to source. Consequently, the values of the three nodes at the kth step are determined by W_k. When $W_k = 0$, the inner node P_k is

$$P_k = M_k + 1 \qquad (3.23)$$

and, if $W_k = 1$,

$$P_k = M_k - 1. \tag{3.24}$$

At the beginning of the process, the outer nodes are initialized as $M_1 = 0$ and $N_1 = N + 1$ for $W_1 = 0$, or as $M_1 = N + 1$ and $N_1 = 0$ if $W_1 = 0$. The value of zero represents the source node and $N + 1$ is the load node. In the subsequent steps, the outer nodes of the H_{k+1} block are defined as

$$M_{k+1} = \min(P_k, N_k), \tag{3.25a}$$

$$N_{k+1} = \max(P_k, N_k), \tag{3.25b}$$

if $W_{k+1} = 0$, and

$$M_{k+1} = \max(P_k, N_k), \tag{3.26a}$$

$$N_{k+1} = \min(P_k, N_k), \tag{3.26b}$$

if $W_{k+1} = 1$.

3.2.2 Realizable Topologies

The number of achievable topologies is determined by the length of the word W. Any filter synthesized with this method is made of an inline structure of N sub-networks. Thus, the total number of possible topologies is 2^N, the number of W combinations. However, not all combinations of W produce different topologies.

For a Nth-order filter, there are groups made of 4 combinations of W that form a topological family, that yields topologies structurally equal. Therefore, the number of distinct topologies is reduced to $2^{(N-2)}$. Among a family, two topologies yield the same result, and the other two are mirrored. That is, the extraction procedure has been carried out inversely with respect to one another. Every topology can be classified as

$$[T] = \begin{bmatrix} T_{1,1} & T_{2,1} & \cdots & T_{2^{(N-2)},1} \\ T_{1,2} & T_{2,2} & \cdots & T_{2^{(N-2)},2} \\ T_{1,3} & T_{2,3} & \cdots & T_{2^{(N-2)},3} \\ T_{1,4} & T_{2,4} & \cdots & T_{2^{(N-2)},4} \end{bmatrix}, \tag{3.27}$$

where T is a matrix that contains all possible topologies and $T_{i,j}$ is a binary word that defines a specific topology. This word is just a configuration of the binary term W that is used only for the sake of the analysis for the different topologies. The subindex i denotes the topological family, which takes values from 1 to $2^{(N-2)}$, and the subindex j indicates a topology within a family, which is a number between 1 and 4. The binary words $T_{i,1}$ in the first row of $G_{i,j}$ defines the initial value of each topology. They can take the values

$$T_{i,1} = 2[0, 1, 3, \cdots, 2^{(N-2)} - 1], \tag{3.28}$$

the values in (3.28) have been expressed in decimal for simplification. The corresponding value has to be converted to a binary word of length N. Within a topology, the four possibilities are

$$T_{i,j} = \begin{bmatrix} T_{i,1} \\ T_{i,2} \\ T_{i,3} \\ T_{i,4} \end{bmatrix} = \begin{bmatrix} T_{i,1} \\ T_{i,1}+1 \\ \overline{T_{i,1}+1} \\ \overline{T_{i,1}+1}+1 \end{bmatrix}, \tag{3.29}$$

where the capping line represents the NOT Boolean binary operator.

The first element is defined as shown in (3.28). The second, $T_{i,2}$, is the previous one incremented by 1. $T_{i,3}$ is obtained by inverting the binary word $T_{i,2}$ or applying the binary operation one's complement. Finally, $T_{i,4}$ is computed by adding 1 to $T_{i,3}$ or two's complement to $T_{i,2}$. For example, let us consider an arbitrary network of order $N = 3$. The total number of topologies is 8, but the distinct topologies are reduced to 2. The matrix T is

$$[T] = \begin{bmatrix} T_{1,1} & T_{2,1} \\ T_{1,2} & T_{2,2} \\ T_{1,3} & T_{2,3} \\ T_{1,4} & T_{2,4} \end{bmatrix} = \begin{bmatrix} 000 & 010 \\ 001 & 011 \\ 110 & 100 \\ 111 & 101 \end{bmatrix}. \tag{3.30}$$

The nodal schemes of all topologies, if they were extracted considering only resonant nodes, can be seen in Figure 3.3. As mentioned above, it can be noted that $T_{i,1}$ is equal to $T_{i,2}$. Topologies $T_{i,3}$, $T_{i,4}$ are equal too and the mirrored version of $T_{i,1}$.

3.3 Synthesis Procedure

The synthesis process is carried out by means of iterative extractions of the lowpass prototype filter elements from an ABCD transfer matrix that represents a network. This matrix is created from the characteristic polynomials of the generalized Chebyshev filtering function in (3.7).

The parameter extractions at step k can be done in three ways, at infinity, at a root of $P_k(s)$ or an arbitrary finite frequency. Thus, the extracted node type is specified by its extraction frequency. An RN is defined when the extraction is realized at infinity. Meanwhile, an NRN-RN pair is extracted at finite frequency. To identify the kind of extraction, a vector Λ is introduced, whose entries are defined as follows:

- $\Lambda_k = 0$:   Extraction at infinity.

- $\Lambda_k = -1$: Extraction at a root of $P_k(s)$.

- $\Lambda_k = j\Omega_k$: Extraction at an arbitrary frequency $j\Omega_k$.

At the beginning of every step k, the first extracted element of the sub-network H_k is the cross inverter J_{ck}. The second element of the network to be extracted is the FIR b_k, which is necessary to prepare the
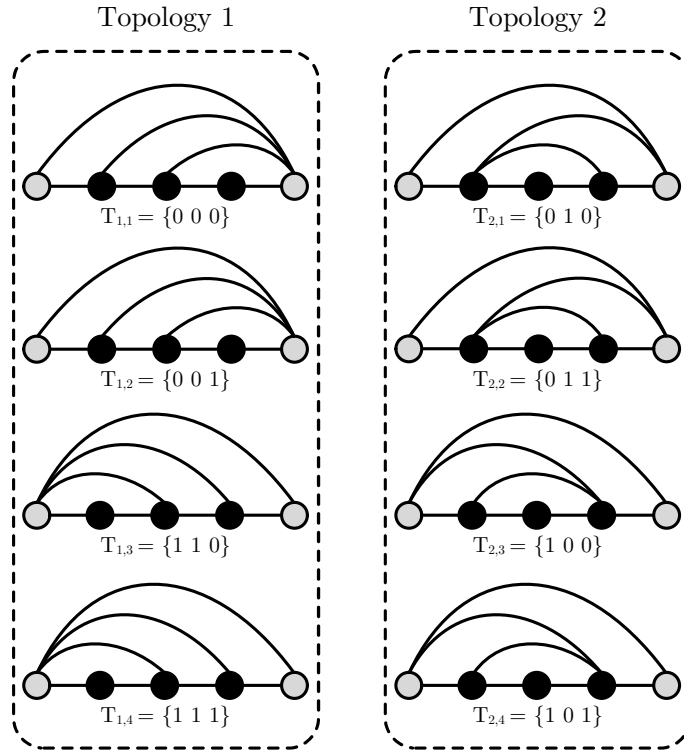
Figure 3.3: Nodal diagram schemes of all possible topologies of a filter of order 3. The resonating nodes are represented in black, the gray nodes are the source/load nodes and the black lines are the coupling between nodes.

removal of the TZ upon the extraction of Y_k after the extraction of a unitary admittance inverter. The procedure for each type of extraction is detailed in the following sections.

3.3.1   Extraction at Infinity

This type of extraction is done by selecting $\Lambda_k = 0$. The elements extracted from H_k in this iteration are the susceptance B_k, a unitary admittance inverter J_k, and the admittance of a resonating node $Y_k = sC_k$. When the degree of $P_k(s)$ is equal to the degree of $B_{nk}(s)$ a cross inverter J_{ck} is necessary. This circumstance occurs when the number of $P_k(s)$ roots to be removed is equal to the remaining sub-networks to be extracted. The cross inverter J_{ck} is computed as

$$J_{ck} = -\lim_{s \to \infty} \frac{jP_k}{B_{nk}}, \tag{3.31}$$

then, it has to be removed from the ABCD transfer matrix before continuing the extraction process as follows:

$$[ABCD]_k' = \frac{1}{jP_k'} \begin{bmatrix} A_{nk}' & B_{nk}' \\ C_{nk}' & D_{nk}' \end{bmatrix} = \frac{1}{j(P_k + J_{ck}B_k)} \begin{bmatrix} A_{nk} & B_{nk} \\ j(C_{nk} + 2J_{ck}P_k + J_{ck}^2 B_{nk}) & D_{nk} \end{bmatrix}. \tag{3.32}$$

The only updated polynomials are C_{nk} and P_k. Note the frequency variable s has been omitted from the polynomials intentionally for the sake of clarity, and the normalization constant ε has been incorporated

to polynomial $P \equiv P(s)/\varepsilon$.

The roots of polynomial $P_k(s)$ represent the TZs at finite frequencies, and the roots of $B_k(s)$ are the eigenmodes of the whole network [73]. Therefore, $B_{nk}(s)$ is a polynomial of degree N, being N the filter order. Meanwhile, $P_k(s)$ is a polynomial of degree N in case of a fully canonical filter or lower degree in the rest of possible cases. As mentioned above, the cross inverter is only required when the degree of $P_k(s)$ and $B_{nk}(s)$ are equal, otherwise $J_{ck} = 0$. That is, only when the network is fully canonical.

The next element to be extracted is the FIR B_k[1]. The extraction of this element is necessary to prepare the circuit for removing the TZ at infinity in the next step. The value is calculated evaluating the polynomials D'_{nk} and B'_{nk} at infinite.

$$B_k = -\lim_{s \to \infty} \frac{D'_{nk}}{B'_{nk}}. \tag{3.33}$$

After (3.33), the element must be removed from the ABCD matrix as follows:

$$[ABCD]''_k = \frac{1}{jP''_k} \begin{bmatrix} A''_{nk} & B''_{nk} \\ C''_{nk} & D''_{nk} \end{bmatrix} = \begin{bmatrix} 1 & 0 \\ -B_k & 1 \end{bmatrix} \frac{1}{jP'_k} \begin{bmatrix} A'_{nk} & B'_{nk} \\ C'_{nk} & D'_{nk} \end{bmatrix}$$
$$= \frac{1}{jP'_k} \begin{bmatrix} A'_{nk} & B'_{nk} \\ C'_{nk} - B_k A'_{nk} & D'_{nk} - B_k B'_{nk} \end{bmatrix}. \tag{3.34}$$

Next, the unitary admittance inverter is extracted and $[ABCD]'''_k$ is updated as

$$[ABCD]'''_k = \frac{1}{jP'''_k} \begin{bmatrix} A'''_{nk} & B'''_{nk} \\ C'''_{nk} & D'''_{nk} \end{bmatrix} = \begin{bmatrix} 0 & -j \\ -j & 0 \end{bmatrix} \frac{1}{jP''_k} \begin{bmatrix} A''_{nk} & B''_{nk} \\ C''_{nk} & D''_{nk} \end{bmatrix}$$
$$= \frac{1}{jP''_k} \begin{bmatrix} -jC''_{nk} & -jD''_{nk} \\ -jA''_{nk} & -jB''_{nk} \end{bmatrix}. \tag{3.35}$$

The extraction of this element implies an interchange of the polynomials between the first and the second row in the ABCD matrix. Finally, the extraction of the admittance $Y_k = sC_k$ is performed by removing a shunt capacitance as follows:

$$C_k = -\lim_{s \to \infty} \frac{D'''_{nk}}{sB'''_{nk}}, \tag{3.36}$$

and $[ABCD]_{k+1}$ matrix is updated as

$$[ABCD]_{k+1} = \frac{1}{jP_{k+1}} \begin{bmatrix} A_{nk+1} & B_{nk+1} \\ C_{nk+1} & D_{nk+1} \end{bmatrix} = \begin{bmatrix} 1 & 0 \\ -sC_k & 1 \end{bmatrix} \frac{1}{jP'''_k} \begin{bmatrix} A'''_{nk} & B'''_{nk} \\ C'''_{nk} & D'''_{nk} \end{bmatrix}$$
$$= \frac{1}{jP'''_k} \begin{bmatrix} A'''_{nk} & C'''_{nk} \\ C'''_{nk} - sC_k A'''_{nk} & D'''_{nk} - sC_k B'''_{nk} \end{bmatrix}. \tag{3.37}$$

The remaining ABCD matrix after updating the polynomials in (3.37) is the network in H_{k+1}. After the complete extraction of H_k, polynomials C_{k+1} and D_{k+1} have been reduced one degree after removing a TZ at infinity. The iterative extraction process continues with H_{k+1}.

---

[1]The variable B_k identifies a frequency invariant susceptance within the network, it should not be mistaken with the ABCD polynomials $B(s)$ and its numerator $B_n(s)$. The latter is also found as B_{nk} in this chapter.

It must be kept in mind that when $W_{k+1} \neq W_k$ the remaining ABCD matrix must be rotated before the extraction of H_{k+1}. In that case, polynomials A_{nk+1} and D_{nk+1} have to be interchanged. Hence, the extraction would proceed from the other side.

3.3.2 Extraction of a Root of $P_k(s)$

At the beginning of the extraction, $P_0(s)$ contains only the prescribed TZs finite frequencies of the filtering function. In general, the roots of $P(s)$ polynomial represents the resonance frequencies that will implement the resonators. Therefore, this kind of extraction requires $P_k(s)$ to be, unless, of degree one.

The procedure sequence is similar to the previous section. The extraction of a cross-inverter J_k is not required this time. If we evaluate (3.31) at a root of $P_k(s)$ instead of infinite, the result will be always zero. Then, the first non-zero element to be extracted is B_k, as a preparation of the circuit for the removal of the $P_k(s)$ root. It is calculated by

$$B_k = -\lim_{x \to j\Omega_k} \frac{D_{nk}(j\Omega_k)}{B_{nk}(j\Omega_k)}. \tag{3.38}$$

Once B_k has been obtained, it must be removed from the ABCD matrix with (3.34), defining the updated matrix as $[ABCD]'_k$. The following element to be extracted from the sub-network H_k is the unitary inverter J_k and the $[ABCD]''_k$ is updated as in (3.34). In the last step, the admittance Y_k has to be obtained. The former corresponds to the input admittance of $[ABCD]''_k$, and it can be defined by

$$Y_k = \left.\frac{D''_{nk}(s)}{B''_{nk}(s)}\right|_{s=s_k} = \left.\frac{b_{0k}}{(s-s_k)}\right|_{s=s_k} = \left.\frac{1}{sL_k + jX_k}\right|_{s=s_k}, \tag{3.39}$$

where the admittance it is compound by an inductance L_k, related to the residue b_{0k}, in series with an FIR jX_k that is related to both, b_{0k} and the pole $s_k = j\Omega_k$ as can be seen in Figure 3.4. The parameter b_{0k} can be obtained as

$$b_{0k} = \left.\frac{D''_{nk}(s)(s-s_k)}{B''_{nk}(s)}\right|_{s=s_k}. \tag{3.40}$$

Finally, the polynomials of the remaining ABCD matrix is defined as follows:

$$[ABCD]_{k+1} = \frac{1}{jP_{k+1}} \begin{bmatrix} A_{nk+1} & B_{nk+1} \\ C_{nk+1} & D_{nk+1} \end{bmatrix} = \frac{(s-j\Omega_k)}{jP''_k} \begin{bmatrix} \dfrac{A''_{nk}}{(s-j\Omega_k)} & \dfrac{B''_{nk}}{(s-j\Omega_k)} \\ \dfrac{C''_{nk}}{(s-j\Omega_k)} & \dfrac{D''_{nk}}{(s-j\Omega_k)} \end{bmatrix}. \tag{3.41}$$

With the last step, every element of H_k has been extracted, and all polynomials have been reduced one degree. The extraction process continues with H_{k+1}. However, as mentioned in the previous section, if $W_{k+1} \neq W_k$ the polynomials A_{nk+1} and D_{nk+1} has to be interchanged prior any element extraction.
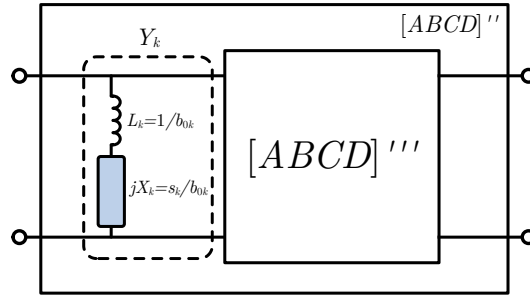
Figure 3.4: Impedance Y_k within $[ABCD]''_k$.

3.3.3 Extraction at an Arbitrary Finite Frequency

The elements extraction from the sub-network H_k at an arbitrary finite frequency $\Lambda = j\Omega_k$ that does not belong to polynomial $P_k(s)$ is carried out following the same steps of the previous section. However, the cross inverter J_{ck} must be extracted. Such step is a requirement to have the remaining network with a pole at $j\Omega_k$. This element is extracted as a parallel admittance inverter as follows:

$$J_{ck} = -\frac{P_k(j\Omega_k)}{B_{nk}(j\Omega_k)}. \tag{3.42}$$

Once the cross inverter value has been calculated, the element must be removed from the ABCD matrix. The updated matrix is defined as

$$[ABCD]'_k = \frac{1}{jP'_k}\begin{bmatrix} A'_{nk} & B'_{nk} \\ C'_{nk} & D'_{nk} \end{bmatrix} = \frac{1}{j(P_k + J_{ck}B_k)}\begin{bmatrix} A_{nk} & B_{nk} \\ j(C_{nk} + 2J_{ck}P_k + J_{ck}^2 B_{nk}) & D_{nk} \end{bmatrix}. \tag{3.43}$$

Now, one of the roots of $P'_k(s)$ is $j\Omega_k$. It must be noticed that as a consequence of the evaluation to a root that does not belong to P_k, the roots of the updated polynomial are not the same as before anymore. This effect causes the resonant frequency of the following resonators, the ones embraced by a cross inverter, will not match with the TZs of the filtering function. Besides, the new roots of $P'_k(s)$ might not necessarily be pure imaginary values; complex roots in conjugate pairs value may appear. As AW resonators can not implement complex resonant frequencies, these cases should be avoided. The management of complex roots is thoroughly detailed in Chapter 6.

The remaining extraction proceeds as in Section 3.3.2. First, the FIR B_k is determined using (3.38) and then, it is removed from the current ABCD matrix with (3.34). Next, the unitary admittance inverter J_k is removed with (3.34). Then, the elements of the dangling resonator in Y_k are calculated with (3.39) and (3.40). In the last step, the ABCD matrix of the following sub-network H_{k+1} is computed as in (3.41). Finally, if $W_{k+1} \neq W_k$ the polynomials A_{nk+1} and D_{nk+1} has to be exchanged before continuing with the next iteration.

3.3.4   Completion of the Synthesis Process

The extraction procedure involves an additional step after the completion of the Nth step of the recursive method, the residual H_{N+1} comprises an admittance J_{N+1} and two susceptances B_{P_N} and B_{N_N} in parallel at input and output ports represented by the contiguous nodes P_N and N_N, respectively as shown in Figure 3.5. The ABCD sub-network matrix is defined as

$$[ABCD]_{N+1} = \frac{1}{jP_{N+1}} \begin{bmatrix} A_{nN+1} & B_{nN+1} \\ C_{nN+1} & D_{nN+1} \end{bmatrix} = \frac{1}{J_{N+1}} \begin{bmatrix} -B_{N_N} & j \\ j(J_{N+1}^2 - B_{P_N}B_{N_N}) & -B_{P_N} \end{bmatrix}. \quad (3.44)$$

The coupling J_{N+1} is extracted as the cross inverter (3.31), but considering that all polynomials are of degree zero, it can be calculated by

$$J_{N+1} = -\frac{P_{N+1}}{B_{nN+1}}. \quad (3.45)$$

Finally, the last FIR elements that remain to be extracted can be obtained by

$$B_{P_N} = -j\frac{D_{nN+1}}{B_{nN+1}}, \quad (3.46)$$

and

$$B_{N_N} = -j\frac{A_{nN+1}}{B_{nN+1}}. \quad (3.47)$$

In ladder topologies, it is desirable that the main-line admittance inverters can be obtained or scaled to the same value; for convenience, they usually are set to ± 1 alternately. Depending on the TZs values and arrangement along the topology, from the input and output point perspective, one admittance inverter may result in an uneven value. When the extraction is carried out from source to load, the uneven one will be J_{N+1}. The even distribution is requisite for a correct series resonator serialization, like shown in Figure 2.8, where the admittance inverters at each side of the dangling resonator have the same value and opposite sign. This event is analyzed in-depth and solved in Chapter 4.
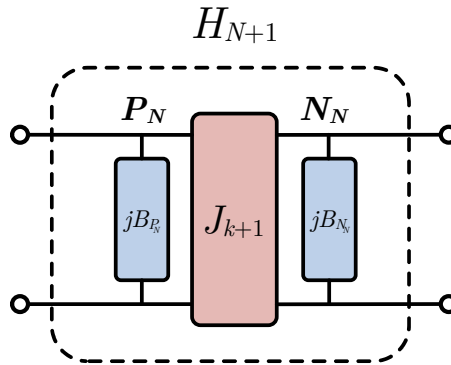
Figure 3.5: The last elements to extract from the network after the Nth step.

3.4   Extraction of Non-Shunt FIR at Input and Output Nodes

The first and last FIRs extracted are the external elements of the filter. They are connected to source and load and coupled to the rest of the network by admittance inverters. In ladder configurations, the inverters

are required to serialize the dangling resonators between them when the first resonator from source or load is series. Therefore, they are just a tool for the circuital transformation and do not exist physically. If the external resonators are shunt, a leftover admittance inverter that cannot be associated with any dangling resonator will remain. In such cases, it can be neglected after the circuital transformation because the filter response would not be affected, although a 90° shift will be applied to the phase response in regard to the lowpass prototype. However, if the normalized source and load terminals of the network are complex instead of unity, they can not be ignored. The filter response depends now on the input and output phase, and the omission of remaining admittance inverter may affect it severely. To avoid its physical implementation, a compatible option with the described extraction method is considered for the definition of the source and load FIR element.
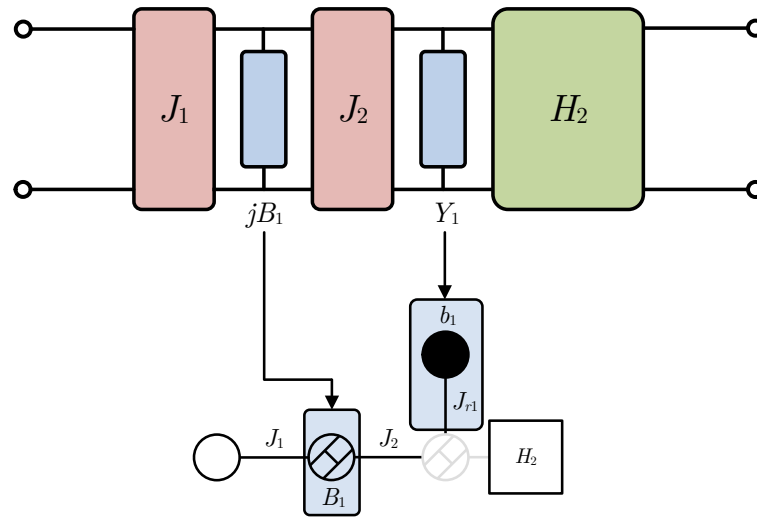
Figure 3.6: Extraction scheme of the first network element as an FIR between admittance inverters and its equivalent nodal diagram, the light gray parts in the nodal schemes are non-extracted elements yet.

This alternative consists in extracting the input/output element between admittance inverter in such a way that they will be serialized as a series impedance. The extraction procedure may begin from source or load, and the first step is the extraction of a cross inverter as in (3.42). Next, a unitary admittance inverter is obtained, updating the network as in (3.35). The following steps are carried out as in Section 3.3.3 to extract b_1 and Y_1. The result can be seen in Figure 3.6. After that, the extraction of the network can continue using the conventional methodology.

Again, the process also may end at source or load elements. The extraction of the last element as an FIR between admittance inverter involves the last two iterations, H_N and H_{N+1}. First, the network is turned by interchanging polynomial A_{nk} and D_{nk} by setting $W_N = 1$ in order to continue the extraction from the output terminal. Now, an admittance inverter J_{N+2} is extracted, followed by the extraction of source/load element b_{N+1} at the $j\Omega_N$ as in (3.38). Next, another unitary admittance inverter J_{N+1} and Y_N are extracted. Finally, the last two FIRs and the last admittance inverter of the main path J_N is obtained following the steps described in Section 3.3.4, where the susceptances b_{N-1} and b_N are the

NRNs of resonators $N-1$ and N, respectively. The resulting network is depicted in Figure 3.7. Following these sequences when needed, the input and output terminals can be serialized so that none of the main path admittance inverters are required to be implemented physically.
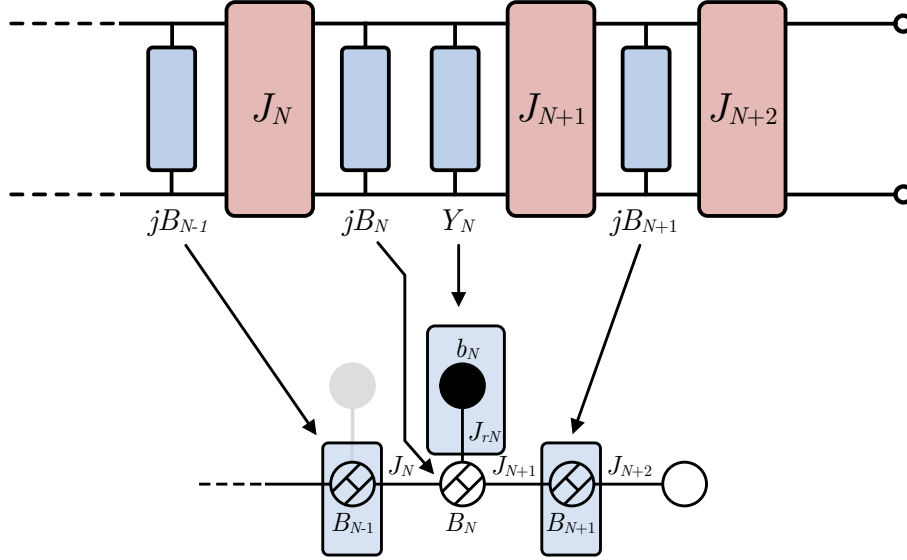
Figure 3.7: Extraction scheme of the last element of the network as an FIR between admittance inverters and its equivalent nodal diagram, the light gray parts in the nodal schemes are non-extracted elements in this iteration.

3.5   Coupling Matrix Representation of the Network

A coupling matrix is a useful tool for modeling any kind two-port networks that contains all relevant information of the filter lowpass prototype, where the matrix entries emerge from the synthesis procedure. The coupling matrix is not only used for representation purposes but also simplifies the reconfiguration of the topology by taking advantage of the matrix operations, like inversions, similarity transformations, or partitioning the network [74]. In the present work, the main utility is for lowpass and bandpass simulation of the filter response for ladder or any other topology. Besides, it is employed for the electric characteristic computation of each element, such as the power that a resonator has to withstand [75].

The common descriptions include the conventional NxN and the extended $N+2$ version of the coupling matrix [46] for N coupled resonators. The synthesis technique presented in this work is adequate for this kind of representational tool. However, the classical coupling matrix has to be expanded in order to hold the NRNs too, leading to a $(2N+2) \times (2N+2)$ square matrix. A general coupling matrix is symmetric around the main diagonal as can be seen in Figure 3.8, where we can distinguish four types of elements:

- **Source and load**: they are located in the first two positions of the main diagonal (M_{11} and M_{22}). They are the matching elements B_S and B_L at input and output ports, respectively.
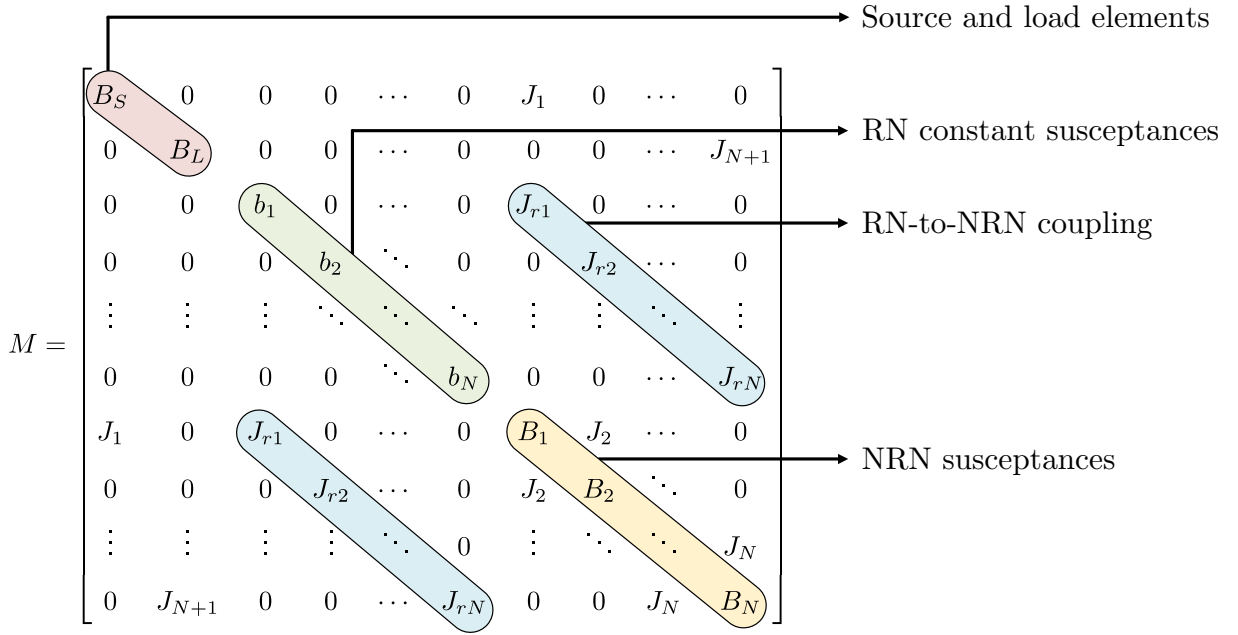
Figure 3.8: General coupling matrix representation.

- **Resonant nodes**: a set of N diagonal elements that are distributed from M_{33} to $M_{(N+2)(N+2)}$. They are the self-coupling of the resonators, represented by the FIRs b_i in parallel with unity capacitors.

- **Non-Resonanting Nodes**: a set of N diagonal elements that are distributed from $M_{(N+3)(N+3)}$ to $M_{(2N+2)(2N+2)}$. The elements are the susceptance of the NRN of the dangling resonator, coupled to their respective RN b_i by J_{ri}.

- **Couplings**: admittance inverters J_{ri} and J_i that connect all the diagonal nodes. They are the RN-to-NRN coupling and the admittance inverter in the main path, respectively.

3.5.1 Analysis Based on the Coupling Matrix

To perform a full analysis of the network, the coupling matrix by itself does not provide all the information required. We need to incorporate two additional matrices, one for the unitary parallel capacitors of the resonant nodes and another for the conductance of each port. In order to analyze the two-port network, the input port is excited through an internal conductance G_S, and the second port is loaded with a conductance G_L as depicted in Figure 3.9. Then, the expression of the network using a matrix notation is defined as

$$-j\,[i] = [A]\,[v] = [\Omega W + M - jG]\,[v], \tag{3.48}$$

where the current array only excites the source node, resulting in column vector $i_s = [1, 0, \ldots, 0]^T$.
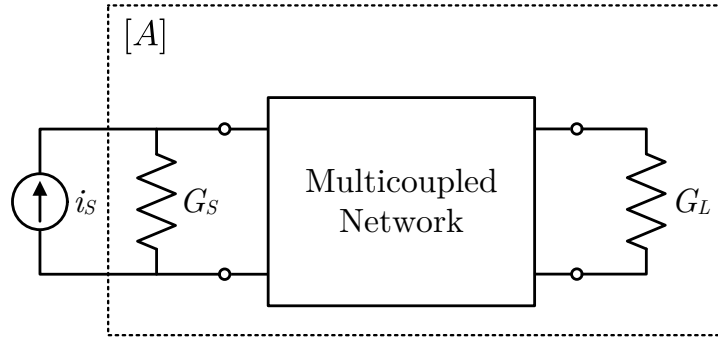
Figure 3.9: Multicoupled network connected to a current source of conductance G_s and loaded with G_L.

Matrices G and W have the same size of M. G is the matrix of conductances in whose all elements are zero except for the $G_{11} = G_S$ and $G_{22} = G_L$, and they reflect conductances of the ports. In our case, the reference admittance is normalize to 1, that is, $G_S = G_L = 1$. On the other hand, W is a diagonal matrix which entries are the unit capacitance of the resonator node. Therefore, the elements of the diagonal between W_{33} and $W_{(N+2)(N+2)}$ are unity, and the rest are set to zero to provide frequency dependency only to the resonating nodes. As the W entries are frequency variant elements, they have to be multiplied by the normalized lowpass frequency variable Ω (3.48). The lowpass S-parameter of the network in Figure 3.9 can be computed as

$$S_{11} = 1 - 2jG_S \left[A^{-1}\right]_{11} \tag{3.49a}$$

$$S_{12} = -2j\sqrt{G_S G_L} \left[A^{-1}\right]_{12} \tag{3.49b}$$

$$S_{21} = -2j\sqrt{G_S G_L} \left[A^{-1}\right]_{21} \tag{3.49c}$$

$$S_{22} = 1 - 2jG_S \left[A^{-1}\right]_{22} \tag{3.49d}$$

In the presented network matrix representation and the scattering parameters definition in (3.49), the input and output ports are at the first and second position of the diagonal, respectively.

3.5.2   Bandpass Transformation of the Coupling Matrix

A frequency transformation of the lowpass prototype yields the BVD bandpass parameters of the resonator as described in Chapter 2. Alternatively, the bandpass coupling matrix offers an equivalent tool to simulate the behavior of the filtering network.
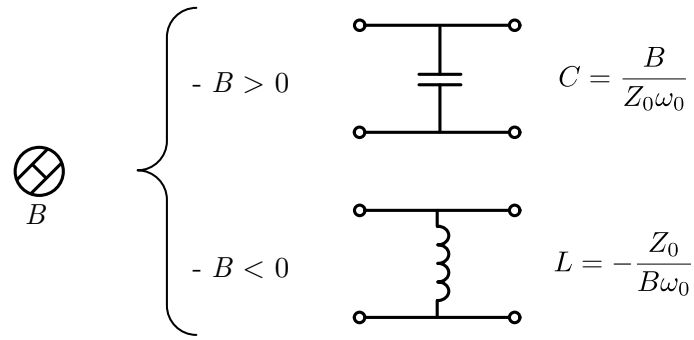
Figure 3.10: NRN and its bandpass equivalent elements according to its value.

Analyzing the energy in each node, simulating the S-parameter and optimizing the ladder filter parameters may become complicated and time-consuming. These negative traits are even more pronounced in complex networks with cross-couplings and additional reactive elements. The solution based on the coupling matrix facilitates the task. To extend the advantages to bandpass domain, the coupling matrix bandpass transformation is presented in this section.

The transformation of each element must be done considering its corresponding bandpass equivalent of the nodal scheme. For example, the source and load nodes are usually shunt FIRs, the bandpass elements equivalence may be a shunt capacitor or an inductor, the result depends directly on the values's sign as shown in Figure 3.10, where Z_0 is the characteristic impedance of the network, and ω_0 is the central frequency of the band.

Alternatively, the FIR placed between admittance inverters is turned into a series reactive element like the depicted in Figure 3.11. Notice that for an exact transformation, the admittance inverters must be of equal value and opposite sign. Although a dangling structure can model the lowpass AW resonator, we can distinguish different configurations for series and shunt resonators, and their respective transformation must be analyzed separately. The NRN of a shunt resonator is positive value, according to Figure 3.10 their bandpass equivalent is a shunt capacitor, which represents the static capacitance C_0 of the BVD. The resonating node is substituted by an inductor in parallel to a 1 pF capacitor coupled to the NRN through J_{rx}.

The bandpass nodal equivalence is shown in Figure 3.12. The equations that relate the nodal scheme in lowpass and bandpass are derived by

$$b_x = \frac{3 + 2\eta_{sh}}{2\eta_{sh} - 1} \frac{1}{\omega_0^2 C_x}, \tag{3.50a}$$

$$J_{rx} = \left(1 - \frac{2\eta_{sh} - 1}{3\eta_{sh} + 2}\right) \sqrt{\frac{\omega_0 C x (\lambda - \alpha)}{2}}, \tag{3.50b}$$

$$B_x = \frac{1}{\omega_0} \left[\alpha + \frac{\lambda - \alpha}{2}\left(1 - \frac{2\eta_{sh} - 1}{3\eta_{sh} + 2}\right)\right], \tag{3.50c}$$
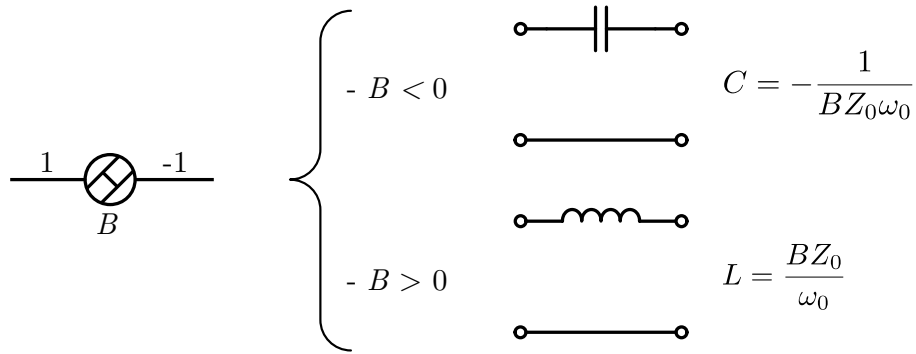
Figure 3.11: NRN between admittance inverts and its bandpass equivalent elements according to its value.

where the variables C_x, η_{sh}, α and σ, are

$$C_x = 1\text{pF}, \tag{3.51a}$$

$$\sigma = B - \frac{J_r^2}{b}, \tag{3.51b}$$

$$\alpha = \frac{2J_r^2 FBW}{b^2}, \tag{3.51c}$$

$$\eta_{sh} = \frac{\xi}{\alpha - \sigma}, \tag{3.51d}$$

$$\xi = \frac{2FBW}{b}\left(2\alpha + \frac{J_r^2}{b}\right), \tag{3.51e}$$

and $FBW = \omega_0/(\omega_2 - \omega_1)$ is the fractional bandwidth, the variables ω_1 and ω_2 are the upper and lower cut-off frequencies of the band, respectively. The detailed proof of the transformation is provided in the Appendix A.
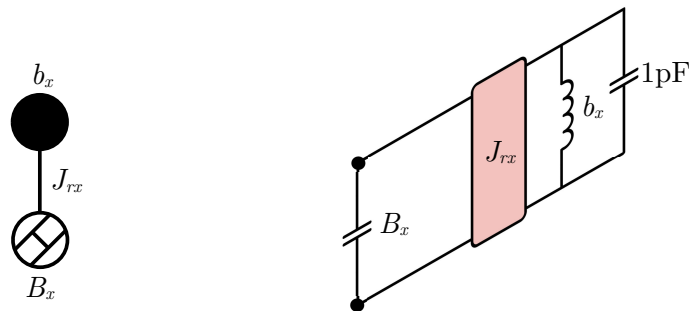
Figure 3.12: Nodal shunt resonator model in BP domain and its equivalent circuital bandpass prototype.

Figure 3.13 illustrates the equivalent circuit for series resonators. The NRN has a negative value. Therefore, it is transformed into a shunt inductor. Given that the element is placed between admittance inverters, it will turn into a series capacitor (Figure 3.11) after circuital the transformation, representing the also C_0 in the BVD of a series acoustic.
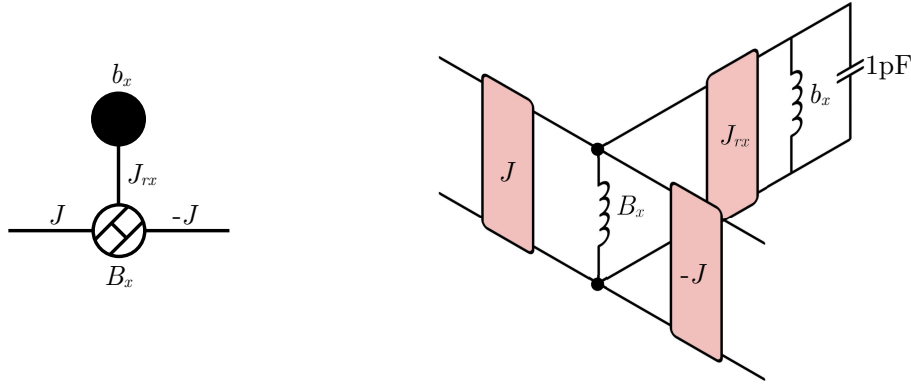
Figure 3.13: Nodal series resonator model in bandpass domain and its equivalent circuital bandpass prototype.

The equations that relate the nodal scheme in lowpass and bandpass are

$$b_x = \frac{1 + 2\eta_{se}}{2\eta_{se} - 3} \frac{1}{\omega_0^2 C_x}, \tag{3.52a}$$

$$J_{rx} = \left(\frac{1 + 2\eta_{se}}{2\eta_{se} - 3} - 1\right) \sqrt{\frac{(\lambda + \alpha)(2\eta_{se} - 3)\omega_0 C_x}{2(1 + 2\eta_{se})}}, \tag{3.52b}$$

$$B_x = \frac{1}{\omega_0} \frac{2\eta_{se} - 3}{\alpha(1 - 2\eta_{se}) - 2\lambda}, \tag{3.52c}$$

where variables η_{se} is

$$\eta_{se} = \frac{\xi - \lambda}{\lambda + \alpha}. \tag{3.53}$$

Finally, the bandpass coupling matrix M_{BP} is

$$M_{BP} = \begin{bmatrix} B_{mS} & 0 & 0 & 0 & \cdots & 0 & J_1 & 0 & \cdots & 0 \\ 0 & B_{mL} & 0 & 0 & \cdots & 0 & 0 & 0 & \cdots & J_{N+1} \\ 0 & 0 & b_{m1} & 0 & \cdots & 0 & J_{rm1} & 0 & \cdots & 0 \\ 0 & 0 & 0 & b_{m2} & \ddots & 0 & 0 & J_{rm2} & \cdots & 0 \\ \vdots & \vdots & \vdots & \ddots & \ddots & \ddots & \vdots & \vdots & \ddots & \vdots \\ 0 & 0 & 0 & 0 & \ddots & b_{mN} & 0 & 0 & \cdots & J_{rmN} \\ J_1 & 0 & J_{rm1} & 0 & \cdots & 0 & B_{m1} & J_2 & \cdots & 0 \\ 0 & 0 & 0 & J_{rm2} & \cdots & 0 & J_2 & B_{m2} & \ddots & 0 \\ \vdots & \vdots & \vdots & \vdots & \ddots & 0 & \vdots & \ddots & \ddots & J_N \\ 0 & J_{N+1} & 0 & 0 & \cdots & J_{rmN} & 0 & 0 & J_N & B_{mN} \end{bmatrix} \tag{3.54}$$

The coupling matrix entries can not be directly the transformed ones because the final value in the matrix depends on their location. According to Figure 3.10, the source and load parameters B_{mS} and B_{mL} are defined generically as

$$B > 0 \longrightarrow B_{mS/L} = C = \frac{B}{Z_0 \omega_0}, \tag{3.55a}$$

$$B < 0 \longrightarrow B_{mS/L} = -\frac{1}{L} = \frac{B \omega_0}{Z_0}. \tag{3.55b}$$

The entries for the susceptance b_{mi} of resonator are defined as

$$b_{mi} = -\frac{1}{b_{xi}}. \tag{3.56}$$

For the rest of the resonator parameters, the entries are introduced differently. In series resonator, J_{rmi} and B_{mi} are given by

$$J_{rmi} = J_{rxi} \sqrt{Z_0}, \tag{3.57a}$$

$$B_{mi} = \frac{-Z_0}{B_{xi}}, \tag{3.57b}$$

and for shunt is given by

$$J_{rmi} = \frac{J_{rxi}}{\sqrt{Z_0}}, \tag{3.58a}$$

$$B_{mi} = \frac{B_{xi}}{Z_0}. \tag{3.58b}$$

As well as the lowpass matrix representation (3.48), the two-port network to be completely analyzed in bandpass requires additional matrices. The nodes equations resulting from Kirchhoff's law for the circuit depicted in Figure 3.9 can be expressed in matrix notation as

$$-j\,[i] = [A]\,[v] = [\omega W_{BP} + (\omega_m \circ M_{BP}) - jG_{BP}]\,[v], \tag{3.59}$$

where G_{BP} is the conductances matrix, with all elements are set to zero except for the port entries G_{BP11} and G_{BP22}, which value are $1/Z_0$, the characteristic admittance of the system. The matrix W_{BP} has the diagonal entries $W_{(N+3)(N+3)}$ to $W_{(2N+2)(2N+2)}$, set to 10^{-12}, the resonator's parallel capacitor ($C_x = 1$ pF), the rest of the matrix are zero. The matrix is multiplied by the frequency scalar variable ω in rad/s.

In contrast to the lowpass coupling matrix, the diagonal elements M_{BP} are frequency dependent, the denormalizing factors are applied by the operation $(\omega_m \circ M_{BP})$, where the symbol $\circ$ is the Schur product or the entrywise matrix product [76]. The matrix ω_m has to apply the frequency dependency only to de diagonal elements. Thus, the rest of the entries are set to one. The diagonal elements at the position of input and output port W_{BP11} and W_{BP22} are

$$B > 0 \longrightarrow W_{BP11/22} = \omega, \tag{3.60a}$$

$$B < 0 \longrightarrow W_{BP11/22} = \frac{1}{\omega}. \tag{3.60b}$$

The diagonal entries W_{BP33} to $W_{BP(N+2)(N+2)}$ (the position of the resonant nodes) are $1/\omega$. The NRNs are defined between $W_{BP(N+3)(N+3)}$ and $W_{BP(2N+2)(2N+2)}$. The correspondent factors are $1/\omega$ and ω for series and shunt resonators, respectively. Finally, the S-parameters of the network are calculated with (3.49).

3.5.3 Extended Coupling Matrix

The coupling matrix can be extended to any kind of 2-port network like the topologies presented in Chapters 5 and 6. For cross-coupled and mixed-topologies that may require FIRs to play the role of reactive lumped elements, the size of the coupling matrix needs to increases to $(2N + 2 + X_l)$, where X_l is the number of FIR elements. For instance, B_k in Figure 5.2 will be turned into capacitors or inductors after the circuital transformation. The equivalent between the FIR and the bandpass element is depicted in Figures 3.10 and 3.11. The extended coupling matrix is built upon the general one described for the ladder topology. To simplify the management, it is divided into three sub-matrices:

- M_C: $(2N + 2 \text{ x } 2N + 2)$ sub-matrix that contains the ladder coupling elements, and it is built like in Figure 3.8.

- M_{X_l}: $(X_l \text{ x } X_l)$ sub-matrix with the extra FIRs that are not part of the dangling resonators nor input/output elements. They are located in the diagonal like the NRN and RN nodes.

- M_{CX_l}: sub-matrix with the connections between the FIRs from M_{X_l} and the sub-matrix M_C.

The extended coupling matrix M_e built by the sub-matrices defined above is

$$M_e = \begin{bmatrix} M_C & M_{CX_l} \\ M_{CX_l} & M_{X_l} \end{bmatrix}. \tag{3.61}$$

The network analysis by M_e and the bandpass transformation follow the same procedure than the previously described for the plain ladder network.

3.6 Synthesis Example

In this section, a numerical example of a synthesized filter is elaborated to illustrate the synthesis method. The example covers the whole process from the definition of the characteristic polynomials, the extraction procedure and the bandpass transformation.

In this example we consider a 7th-order symmetric filter in band 1 Tx with a passband from 1.920 to 1.980 GHz (relative bandwidth 3.07%). The effective coupling coefficient k_{eff}^2 considered is 8%. The filter specifications to calculate the characteristic polynomials are $RL = 20$ dB and $\Omega_{tz} = \{2.60, -2.46, 2.26, -2.28, 2.26, -2.46, 2.60\}$ rads/s. The Chebyshev polynomials synthesis yields the polynomials $F(s)$, $E(s)$, $P(s)$ listed in Table 3.1.

Table 3.1: Synthesized characteristic polynomial coefficients of the 7th-order filter.

Degree	$F(s)$	$E(s)$	$P(s)$
7	1	1	j
6	$-0.2107j$	$1.9668 - 0.2107j$	2.5200
5	1.8109	$3.7449 - 0.4221j$	$17.3432j$
4	$-0.3312j$	$4.1270 - 0.7538j$	43.5018
3	0.9522	$3.6963 - 0.7905j$	$100.0275j$
2	$-0.1341j$	$2.2377 - 0.6297j$	249.6853
1	0.1294	$0.9285 - 0.3179j$	$191.7886j$
0	$-0.0087j$	$0.1963 - 0.0885j$	476.3966

Table 3.2: Extracted elements of the 7th-order filter prototype.

	B_k	b_k	J_{rk}
Res. 1	-2.1136	-2.60	2.2198
Res. 2	3.6636	2.46	2.9063
Res. 3	-3.3970	-2.26	2.7723
Res. 4	3.8267	2.28	2.9456
Res. 5	-3.3970	-2.26	2.7723
Res. 6	3.6636	2.46	2.9063
Res. 7	-2.1136	-2.60	2.2198
B_S	-0.4233		
B_L	-0.4233		
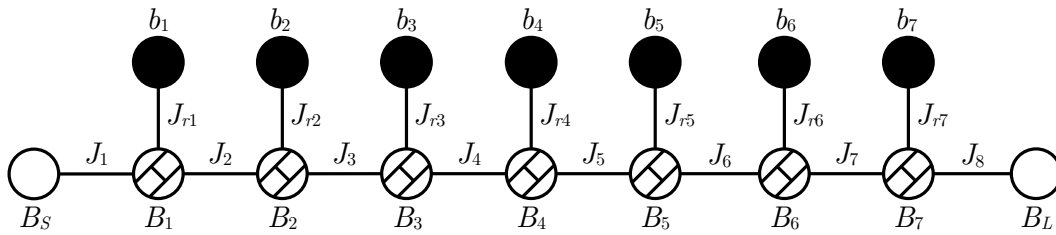
Figure 3.14: Nodal diagram of the synthesized 7th-order filter.

Given that the filter is fully canonical, the extraction procedure is done at the $P(s)$ roots every iteration. The extraction order is from source to load, that is $\Lambda = \{-1 \ -1 \ -1 \ -1 \ -1 \ -1 \ -1\}$ and $W = \{0 \ 0 \ 0 \ 0 \ 0 \ 0 \ 0\}$. Following the procedures described in Section 3.3.3 and Section 3.3.4 yield the lowpass prototype depicted in Figure 3.14 after the last iteration. The parameter values are listed in Table 3.2. The b_k parameters are the FIRs that tune each resonator to its resonance frequency. Notice that the admittance of the resonator node is $(s + jb_k)$ and, therefore $b_k = -\Omega_{tzk}$ to introduced the TZs at the prescribed frequency.

The transformation to bandpass domain of the coupling matrix results in the nodal parameters in Table 3.3. The simulation in both lowpass and bandpass domain, using the coupling matrix, can be compared in Figure 3.15. In addition, the simulation of the filter using the BVD has been included in Figure 3.16. Note that, except minor differences, the simulation with the bandpass coupling matrix and the BVD are equivalent.

Notice that the admittance inverters in the main-line are chosen unitary, with the same value and alternating sign and, therefore, the network is directly transformable to the BVD model like explained in Section 2.2. Their values, the resonance frequencies, and K_{eff}^2 are listed in Table 3.4.
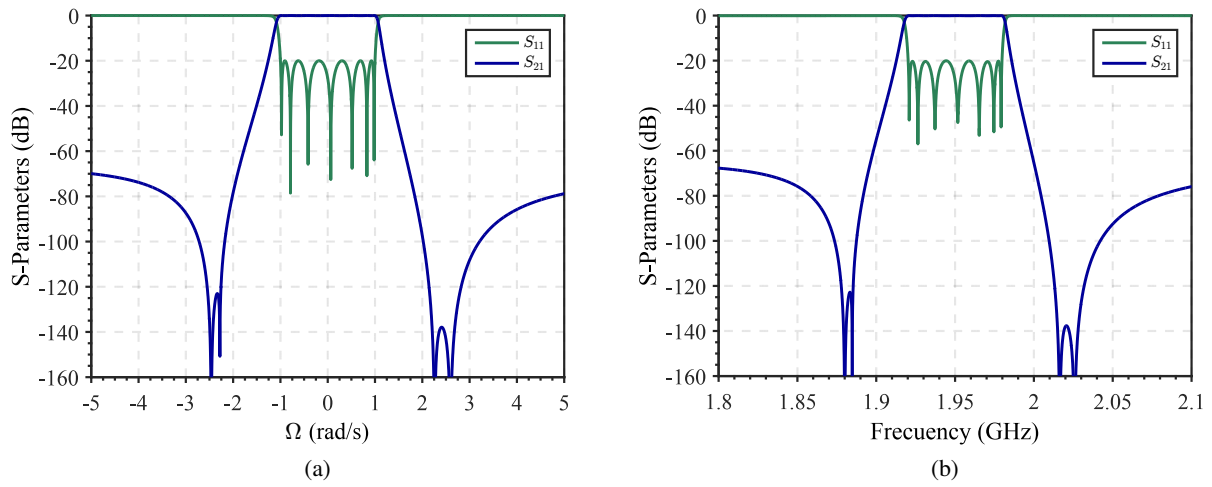
Figure 3.15: S-parameters of (a) the lowpass coupling matrix and (b) bandpass coupling matrix response.
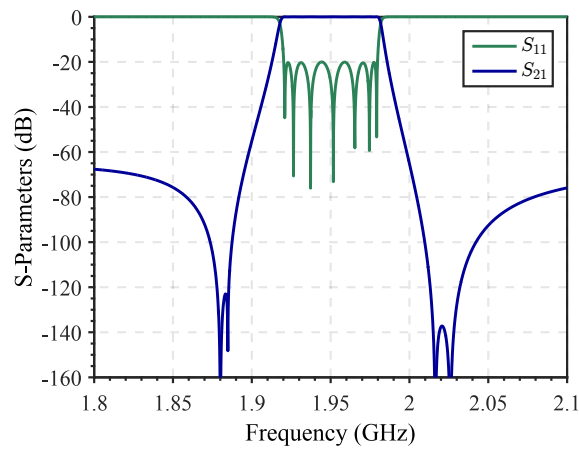
Figure 3.16: S-parameters of the bandpass filter using the BVD model of the resonators.

Table 3.3: Elements of the 7th-order filter prototype in bandpass domain.

	B_{mk}	$b_{mk}(10^{-9})$	J_{mrk}
Res. 1&7	-1.1966×10^{-12}	-0.1620	0.2906
Res. 2&6	5.5699×10^{12}	-0.1395	0.0074
Res. 3&5	-1.9438×10^{-12}	-0.1605	0.3679
Res. 4	5.8439×10^{12}	-0.1402	0.0076
$B_{mS}(10^{-9})$	-0.1037		
$B_{mL}(10^{-9})$	-0.1037		

Table 3.4: BVD elements of the synthesized 7th-order ladder filter.

	Res. 1&7	Res. 2&6	Res. 3&5	Res. 4
L_a (nH)	119.96	18.25	198.99	1.9579
C_a (pF)	0.0551	0.3926	0.0334	0.4076
C_0 (pF)	0.7806	5.5699	0.4809	5.8439
$K_{eff}^2(\%)$	8	8	8	8
f_s (GHz)	1.9579	1.8800	1.9497	1.8848
L_S	9.64 nH			
L_L	9.64 nH			

3.7 Chapter Summary

In this chapter, the procedure of synthesis and design of ladder filters based on acoustic wave resonators have been presented. The theoretical content of the chapter is the cornerstone not only for the design of ladder filters but to create more advanced topologies that may result advantageous in acoustic wave technology that is fully described in the following chapters.

From the very beginning, with the TZs set and RL level as filter specifications, a general class Chebyshev function is introduced to describe the mathematical expression of the transmission and reflection response of the acoustic wave filter.

The lowpass network parameters are obtained by using a synthesis technique based on a recursive extraction method from a transfer matrix of the network computed from characteristic polynomials. The synthesis methodology is a versatile tool capable of providing different topologies. Nevertheless, the extraction procedure is employed in this chapter for the realization of fully canonical filters, which lowpass prototype is N cascaded dangling resonators. An interesting characteristic of the methodology is the capability to create ladder-like cross-coupled topologies by the extraction of cross inverters. The advantages of this characteristic have been exploited to model parasitic effects in Chapter 6.

The lowpass prototype frequency transformation yields the bandpass parameters of the BVD model of the resonators as described in Chapter 2. For the analysis and simulation of the network, a coupling matrix arrangement in his nodal representation has been introduced in both lowpass and bandpass. The coupling matrix has been presented for the ladder-type filters, but it is an agile representational tool that can be expanded to any topology configuration, specially for cross-coupled and parallel-connected topologies covered in Chapters 5 and 6.

In general, this chapter has aimed to describe a robust methodology that provides a fast software tool to define a filtering network inclined to ladder networks in AW technology, in a short time with a low computational cost. The implementation of the real device requires further steps, including electromagnetic simulations, physical layout, package design, etc. Nevertheless, the solution obtained with methodology settles a good starting point for the following stages of the whole design steps.

Phase Adjustment for Ladder-type Acoustic Wave Filters in Lowpass Domain

In the previous chapter, a synthesis methodology for the design of ladder filters has been presented. It was shown that they could be modeled with an inline filter topology, allowing the use of the extracted-pole synthesis technique. The equivalent lowpass model corresponds to a series of dangling resonators between admittance inverters, and such networks are adequate to accommodate a fully canonical filtering function, defined by a set of transmission zeros and return loss level. The circuital extraction procedure yields a nodal scheme like the one depicted in Figure 4.1, where *N* corresponds to the filter order.

It is interesting to notice that during the extraction process, it is not possible to determine both the main-line admittance inverter and the RN-to-NRN coupling, respectively J_k and J_{rk}, but only their ratio [51]. This fact leads to multiple solutions suitable for different technologies providing the same transmission and reflection responses [46]. In the particular case of ladder topologies, very common with acoustic wave technology, the admittance inverters in the main-line are employed in pairs as an instrument to serialize shunt connected resonators, as explained in Section 2.2.1, that is, they do not exist physically. For simplicity, all J_i can be set to a common value with alternation in sign along the source-to-load path. This is a necessary condition for further lowpass-to-bandpass transformation [77] of the network elements.

Regarding the filter specifications, it may occur that one admittance inverter in the main-line path cannot be scaled to the common value conveniently, and it is required to take a different one than the rest [51]. When extraction procedure is performed from source to load, the uneven inverter is located closest to the output port, e.g., J_{N+1} in Figure 4.1. Even when one admittance inverter is not equal to the others, the serialization can be carried out assuming that it has the same value, ignoring the real one. However, it should be expected degradation of the reflection coefficient in such case. The effects will be more severe the more different is the uneven admittance inverter.
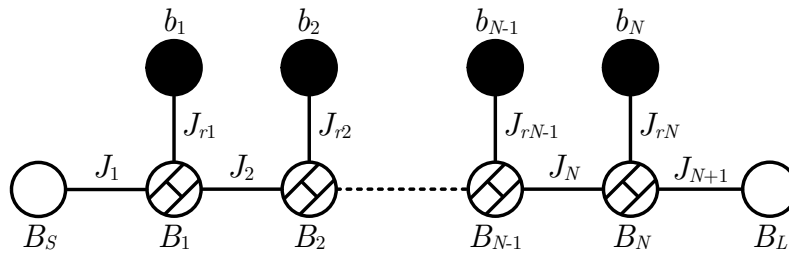
Figure 4.1: Lowpass nodal scheme of an inline prototype filter with N transmission zeros.

The most common solution to equalize the inverter is to apply an admittance redistribution of the output elements of the network. However, despite its simplicity and utility, it may not be appropriated for every case. Depending on the filter specifications, the redistribution may require to change the output port impedance, which produces a mismatch that will affect the filter response up to a certain degree. Moreover, in other cases it is not applicable, like in cross-coupled topologies described in Chapter 6, where there are ladder networks with a source-to-load coupling embracing the whole main-line inverters. In such scenario, the redistribution method has to be discarded as it is not possible to scale the network without changing the value of the cross-coupling.

To overcome its limitations, the origin and effects are thoroughly studied in this chapter. It is also proposed an alternative method based on the phase correction of the characteristic polynomials of the filtering function $F_{11}(s)$, $F_{22}(s)$ and $E(s)$. The phase modification method attains the same result as the admittance redistribution by changing the phases of the input and output port simultaneously in other to equalize the admittance inverters in a fully canonical lowpass prototype. Unlike the admittance redistribution, this new method achieves a unity terminating output admittance G_L in every case, and it also provides a myriad of suitable phase values. Although the chapter focus is only on the advantages of standalone filters, the differentiated phase correction of $F_{11}(s)$, $F_{22}(s)$ may also be useful for duplexer design, where one of the most important features is the isolation between transmitter and receiver filters. In [77, 78], it is described that the loading effects in both filters can be minimized by modifying the input phase of each filter at the antenna port for having $0°$ input phase at the central frequency of the counter band. Thereby, by a proper phase correction, both conditions, uniform admittance inverter in the main-line and the phase match for duplexers, can be achieved simultaneously.

Part of the content of this chapter has been published by thesis author in [79], where the method is particularized to a specific distribution in odd-order filters. In addition to the previous publication, this chapter discusses all possible cases and a more detailed explanation of the problem statement.

4.1   Uneven Admittance Inverters in Inline Fully Canonical Filters

Generically, when the nodes in the main-line of the network are surrounded by admittance inverters, it is possible to scale the impedance at each node to arbitrary values, once the characteristic immittances of

the inverters are set to the desired value. This is equivalent to adjust the transformer ratios of the input and output coupling transformers such that the total energy transferring through the node remains the same [46].

In ladder topologies, it may be desirable that main-line admittance inverters can be obtained or scaled to the same value. For the sake of simplicity, all admittance inverter J_k can be set to ± 1, where the sign alternation of side inverters along the source and load path is a necessary condition for further lowpass-to-bandpass elements transformation [77]. The unitary condition in ladder filters is dependent on the filter function specifications. When the TZs are allocated symmetrically over the ladder topology, e.g., $\Omega_{Ak} = \{\Omega_1, \Omega_2, \Omega_3, \Omega_2, \Omega_1\}$, where they are the same at both sides of Ω_3, all the main-line admittance inverters can be scaled to ± 1 successfully during the extraction procedure. However, if another type of TZs distribution is used, hereafter asymmetrical TZs distribution, like $\Omega_{Bk} = \{\Omega_1, \Omega_2, \Omega_1, \Omega_2, \Omega_3\}$, an uneven admittance inverter in the main-line path with a different value than the rest will be required.

Table 4.1: Extracted elements of the 5th-order filter prototype with Ω_{Ak} TZs distribution.

	B_k	b_k	J_{rk}
Res. 1	-1.0927	-1.8	1.1768
Res. 2	3.4897	2.0	2.4193
Res. 3	-2.6930	-2.5	2.6548
Res. 4	3.4897	2.0	2.4193
Res. 5	-1.0927	-1.8	1.1768
B_S	-0.7388		
B_L	-0.7388		

Table 4.2: Extracted elements of the 5th-order filter prototype with Ω_{Bk} TZs distribution.

	B_k	b_k	J_{rk}
Res. 1	-1.0927	-1.8	1.1768
Res. 2	3.3440	2.0	2.4193
Res. 3	-1.8121	-1.8	1.7911
Res. 4	3.5215	2.0	2.4946
Res. 5	-1.4090	-2.5	1.7951
B_S	-0.7388		
B_L	-0.4553		

For instance, let us consider a filter with TZs at $\Omega_{Ak} = \{1.8, -2, 2.5, -2, 1.8\}$ rad/s and $RL = 20$ dB. The resulting network scheme is depicted in Figure 4.1, and the filter elements are listed in Table 4.1. In this case, the admittance inverters are $J_k = \{1, -1, 1, -1, 1, -1\}$. Because all TZs are symmetrically distributed at each side of $\Omega_{A3} = 2.5$, their values are all one with the alternated sign. However, with a TZs distribution like $\Omega_{Bk} = \{1.8, -2, 1.8, -2, 2.5\}$ rad/s, in which Ω_{A3} and Ω_{A5} have been interchanged, the admittance inverters are $J_k = \{1, -1, 1, -1, 1, -0.8689\}$, where the $|J_6|$ value differs from the others. The rest of the network parameters are shown in Table 4.2. Different TZs sorting yields other network parameters. However, as they implement the same filtering function, the S-Parameters for both networks coincide (Figure 4.2).

To adequately accommodate the network to a given topology, a simple solution consist in applying a circuital transformation approach where the real and imaginary parts of the admittance of the last elements of the network are redistributed. That is, by re-accommodating the output port elements, a unitary value is attained.
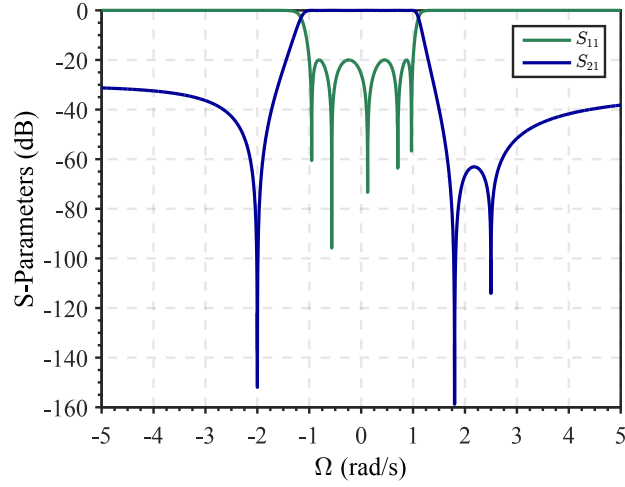
Figure 4.2: S-parameters of the extracted filter using TZs distributions Ω_{Ak} and Ω_{Bk}.
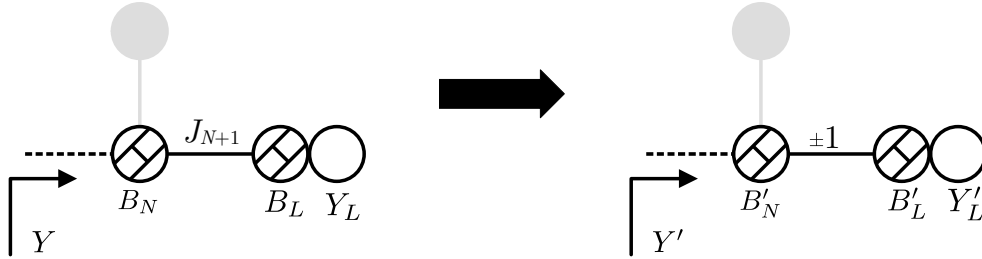
Figure 4.3: Network nodal diagram of the last three elements before (left) and after (right) the admittance redistribution. The grey elements are actually part of the network, but they are irrelevant in this situation.

In the scenario depicted in Figure 4.3, the admittance expression Y comprises the last NRN B_N, the load element B_L and the coupling admittance inverter between them, where J_{N+1} is assumed a non-unity inverter. The admittance before and after the redistribution can be defined as

$$Y = jB_N + \frac{J_{N+1}^2}{jB_L + Y_L} = \frac{Y_L J_{N+1}^2}{Y_L^2 + B_L^2} + j\left(B_N - \frac{B_L J_{N+1}^2}{Y_L^2 + B_L^2}\right) = Y_r + jY_i, \qquad (4.1a)$$

$$Y' = \frac{Y_L'}{Y_L'^2 + B_L'^2} + j\left(B_N - \frac{B_L'}{Y_L'^2 + B_L'^2}\right) = Y_r' + jY_i'. \qquad (4.1b)$$

Notice that $J_{N+1}'^2$ has been substituted by 1 in the equation. By equaling the real parts $Y_r = Y_r'$ of both expression, B_L' can be derived as

$$B_L' = \pm\sqrt{\frac{Y_L'}{Y_r} - Y_L'^2}. \qquad (4.2)$$

The NRN B_N' can be obtained by equaling the imaginary parts of the admittance with

$$B_N' = Y_i + \frac{B_L' Y_r}{Y_L'}. \qquad (4.3)$$

Usually, Y_L' is expected to be 1. However, it can be observed in (4.2) that it is only possible if the condition $Y_L' \leq 1/Y_r$ is satisfied, i.e., $Y_r \leq 1$. Otherwise, B_L would be imaginary and, therefore, non-realizable. To avoid this result, Y_L' can be modified, but a mismatch will be produced in the output port for not been unitary terminated. For example, in the network obtained with Ω_{Bk} TZs set, Y_{rB} and Y_{iB} are

$$Y_{rB} = 0.6254, \tag{4.4a}$$

$$Y_{iB} = -1.1243. \tag{4.4b}$$

The real part of the admittance Y_r is lower than one. Therefore, $Y_L' = 1$ can be assured. The redistributed element values can be calculated with (4.2) are (4.3) as

$$B_L' = \pm\sqrt{\frac{1}{Y_{rB}} - 1} = \pm 0.7739, \tag{4.5a}$$

$$B_5' = Y_{iB} + B_L' Y_{rB}. \tag{4.5b}$$

Notice that the admittance redistribution offers two solutions. The FIR B_L' can be either positive or negative depending on the chosen sign. Both results are valid but yield different values of B_L' and B_5'. As mentioned in Section 2.2.1, the NRN must be negative to transform the dangling resonator into a series one or positive in case of being shunt. Thus, B_L' sign must be decided considering the nature of the Nth resonator upon the bandpass transformation of the filter prototype.

Table 4.3: 5th-order filter prototype elements with a Ω_{Ck} TZs distribution.

	B_k	b_k	J_{rk}
Res. 1	-0.6489	-1.80	1.1761
Res. 2	1.1085	1.16	0.5833
Res. 3	-2.9532	-1.80	2.3379
Res. 4	2.0059	2.00	1.8959
Res. 5	-2.5918	-2.50	2.4198
B_S	-0.7353		
B_L	-0.4519		

In contrast, if the TZs are $\Omega_{Ck} = \{1.8, -1.16, 1.8, -2, 2.5\}$ rad/s, the extraction procedure yields the network parameters in Table 4.3, and the admittance inverters are $J_k = \{1, -1, 1, -1, 1, -1.1693\}$. The real and imaginary parts of the admittance are $Y_{rC} = 1.1353$ and $Y_{iC} = -2.0787$, respectively. The real part is greater than one, and this forces an impedance mismatch at the output port. To minimize it, the closest value to unity that can be chosen is $Y_L' = 1/Y_{rC} = 0.8808$. In this case, the FIR at load port will be zero, thus, the new element values are $B_L' = 0$ and $B_5' = -2.0787$. Although the admittance inverter J_{N+1} is now equalized, and the circuital transformation can be done flawlessly, the return loss and in-band response may present a severe deterioration because of the impedance mismatch.

In any case, this method forces the non-equal inverter to be the same as the rest, at the expense of indirectly modifying the output phase of the network, which is $\theta_{22}(s)$. This involves that a phase shifter
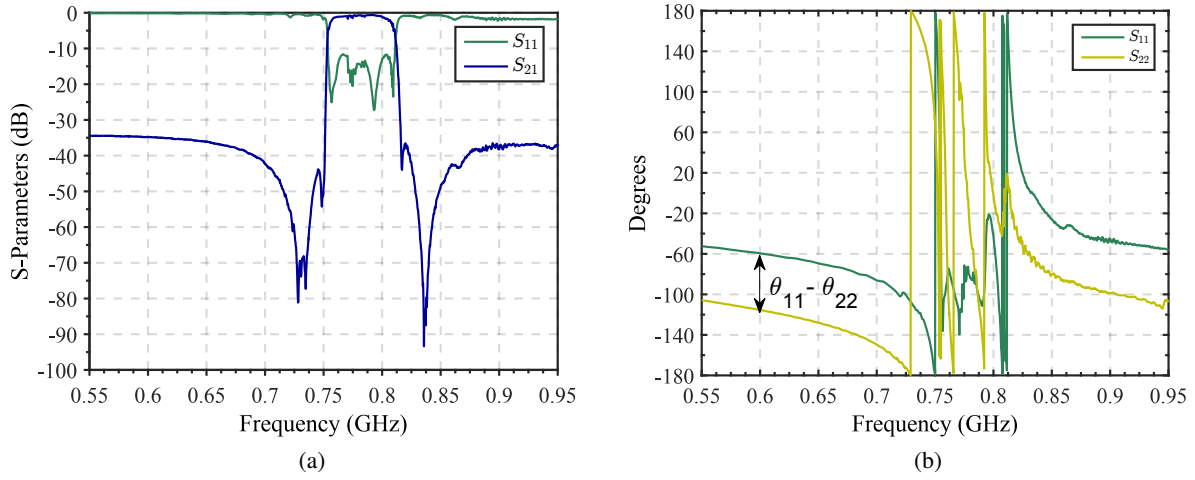
Figure 4.4: S-parameters (a) and (b) phase response of a 7th-order B28Rx filter.

is necessary to achieve a fully synthesized filter. The works [80, 81] show how the filter response is affected when this phase shifter is neglected. Of course, this solution is useful with stand-alone inline configurations, but it requires external reactive elements to compensate for the extra phase, for example, when parallel-connected configurations are involved [81, 82]. In a sense, the non-unitary inverter in the given topology can be understood as a phase reconditioning issue that the filtering function does not provide for a specific TZs distribution among the resonators.

The general polynomial synthesis method for the Chebyshev filtering function is generated from the filter order, an arbitrary set of TZs and RL. The filtering function and the transfer matrix is built assuming $F_{11}(s) = F_{22}^*(s) = F(s)$. If their roots are coincident upon the imaginary axis or they are symmetrically arranged about it, then, the ith root of $F_{11}(s)$ is related to the corresponding root of $F_{22}(s)$, where the polynomial numerator of $F_{22}(s)$ is the complex conjugate of $F_{11}(s)$. In terms of reflection coefficient phase, it is known that $\theta_{11}(s) = \theta_{22}(s)$.

However, if the prescribed TZs are distributed asymmetrically along the network in a ladder topology, the phase terms $\theta_{11}(s)$, $\theta_{22}(s)$ should be expected to be different in order to comply with the even distribution of admittance inverter's values in the network. In other words, if the resonators of the filter are asymmetrically distributed, asymmetric characteristic polynomials are needed. For instance, there is a measure of a B28Rx 7th-order filter with an asymmetrical TZs distribution in Figure 4.4a. It is observable in Figure 4.4b that the input and output phase are not equal. This occurrence can be clearly seen in the OoB regions, where the difference between $\theta_{11}(s)$ and $\theta_{22}(s)$ are directly the offset between both traces.

In this chapter, the phenomenon is addressed from the polynomials that define the filtering function to avoid the addition of reactive elements, producing the same effect by changing the characteristic polynomial phases. In the following sections, the generation of asymmetric polynomials is explained. Through observation of the uneven admittance inverter values in function of the additive phase terms, two

mathematical models and the method followed to implement them are discussed. It is also demonstrated that the solution provided by the method based on the circuital transformation is only a particular result that belongs to the solutions map provided by the models described in this work.

4.2 Asymmetrical Polynomial Definition

The procedure for the definition of the asymmetrical polynomials to deal with asymmetric filter networks is based on the work in [83]. The relationship between modified scattering parameters and Chebyshev characteristic polynomials is given by

$$S_{11}(s) = \frac{F_{11m}(s)}{E_m(s)}, \quad S_{22}(s) = \frac{F_{22m}(s)}{E_m(s)},$$

$$S_{21}(s) = S_{12}(s) = \frac{P_m(s)}{E_m(s)}. \tag{4.6}$$

where the subscript m refers to modified characteristic polynomials that are defined as follows:

$$F_{11m}(s) = \frac{F(s)}{\varepsilon_R}\sqrt{\Psi/\Phi}, \quad F_{22m}(s) = \frac{(-1)^N F^*(s)}{\varepsilon_R}\sqrt{\Phi/\Psi},$$

$$E_m(s) = \frac{E(s)}{\sqrt{\Psi\Phi}}. \tag{4.7}$$

The parameters Ψ and Φ are complex constants which absolute value is $|\Psi| = |\Phi| = 1$. With the angles associated to these new variables (ψ, ϕ)(4.8), the phase of F_{11m} and F_{22m} can be modified. Both phase terms are bounded together and linked to the phase of $E_m(s)$.

$$\Psi = e^{j\psi}, \qquad\qquad \Phi = e^{j\phi}. \tag{4.8}$$

By using the classic two-port [S] matrix to [ABCD] matrix transformation formulas, the polynomials $A_n(s)$, $B_n(s)$, $C_n(s)$, and $D_n(s)$ in (3.7) may be directly expressed in terms of the coefficients of modified characteristic polynomials $F_{11m}(s)$, $F_{22m}(s)$ and $E_m(s)$:

$$A_n(s) = \frac{(E_m(s) + F_{11m}(s))(E_m(s) - F_{22m}(s)) + P_m^2(s)}{2E_m(s)},$$

$$B_n(s) = \frac{(E_m(s) + F_{11m}(s))(E_m(s) + F_{22m}(s)) - P_m^2(s)}{2E_m(s)},$$

$$C_n(s) = \frac{(E_m(s) - F_{11m}(s))(E_m(s) - F_{22m}(s)) - P_m^2(s)}{2E_m(s)},$$

$$D_n(s) = \frac{(E_m(s) - F_{11m}(s))(E_m(s) + F_{22m}(s)) + P_m^2(s)}{2E_m(s)},$$

$$\tag{4.9}$$

where the $P(s)$ polynomial is

$$P(s) = \frac{Pm(s)}{\varepsilon}. \tag{4.10}$$

Adopting the equations in (4.9), as a substitute for (3.6), the extraction process can be carried out as usual. If Ψ and Φ are properly defined, it is expected that the extraction process will yield the last J_{N+1} to a unitary value. However, the definition of the asymmetrical polynomials depends directly on the chosen value for Ψ and Φ.

4.3   Phase Determination

Initially, the shape of each case has been unveiled by performing a sweep in ψ and ϕ. The resulting space map of input and output phase correction parameters, that yields all the inverters in the main-line unitary after the extraction procedure, are explored to identify their geometric patterns. They depend on the network order into consideration. For odd-order filters, the suitable phase values are like an equilateral hyperbola, and for even-order filters, the phase values describe an ellipse. Although both are different, they belong to the same group of geometric shapes, conic sections. They can be defined as non-degenerate curves shape that can be obtained when a plane intersects one or two right circular cones [84]. The attribute that differentiates them is the eccentricity e, a constant value that characterizes the shape of a curve. When it is greater than 1, the geometric shape corresponds to a hyperbola, conversely if $0 < e < 1$, the result is an ellipse. In the following, the method to find all suitable phase values for both cases is described.

4.3.1   Odd-Order Ladder Filters

To fully characterize a network, for each TZs array Ω_{tzi}, a double phase sweep has been conducted doing $n\psi \times n\phi$ complete circuital extractions from the network ABCD matrix where the effect is located to the last admittance inverter. The evolution of J_{N+1} value is obtained as a function of (ψ, ϕ). Both parameters have been swept in a range from $-180°$ to $180°$. Although the obtained outcome depends on the filter TZs and RL specifications, a large number of realizations have been done obtaining consistent results. In all of them, the pair (ψ, ϕ) describes a map that can be fitted with the parametric equation of a conjugate hyperbola, as shown in Figure 4.5a and Figure 4.5b, respectively. For illustration purpose the only considered J_{N+1} values are those within a tolerance of 0.1% ($J_{N+1} = 1 \pm 0.001$).

   A hyperbola can be completely defined by four parameters: the hyperbola type (horizontal or vertical), the two slant asymptotes, the origin locus and the distance from it to the vertex of one branch (α). Whereas it is equilateral in any case, its slant asymptotes have a slope 1 at $\psi = \pm\phi$. Through observation, it has been discerned that unitary $J_{N+1}(\phi, \psi)$ describes an equilateral hyperbola-like shape which origin
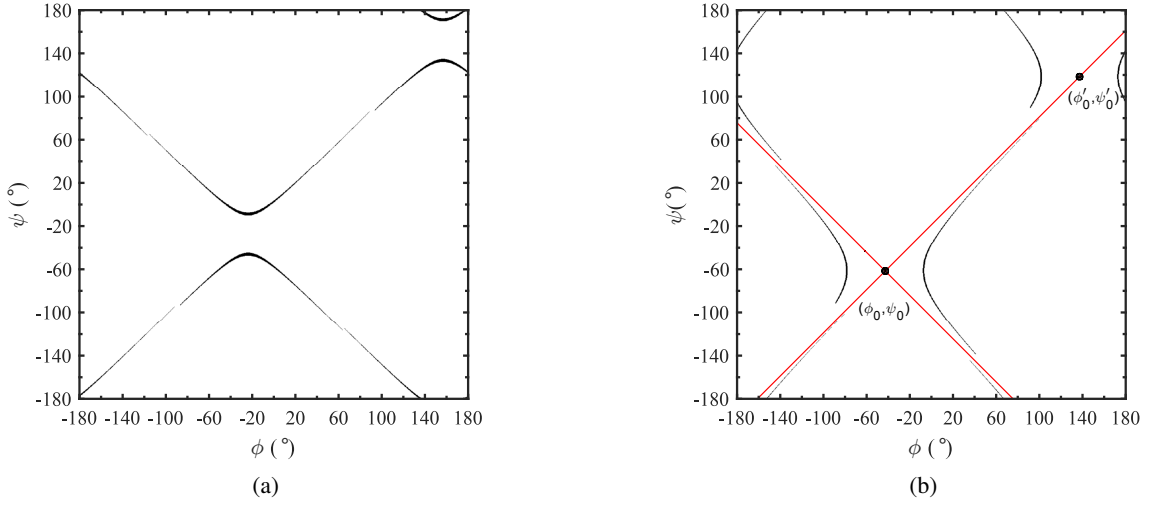
Figure 4.5: (a) Horizontal hyperbola and (b) vertical hyperbola representation. The black trace represents those combinations of ϕ, ψ that yields $|J_{N+1}| = 1$. For illustration purpose all $|J_{N+1}|$ values that fit in 1 ± 0.001 have been plotted. The red traces correspond to the asymptotes. The point (ϕ_0, ψ_0) is the origin and (ϕ'_0, ψ'_0) the origin of another hyperbola with a $180°$ in both directions.

location coincides with $\psi_0 = \theta_{11}$, $\phi_0 = \theta_{22}$, given by

$$\theta_{11} = \left. \frac{F(s)}{E(s)} \right|_{s=j\omega_1} \qquad \text{and} \qquad \theta_{22} = \left. \frac{F(s)}{E(s)} \right|_{s=j\omega_N}, \qquad (4.11)$$

where θ_{11}, θ_{22} are the phases of $S_{11}(s)$ and $S_{22}(s)$ evaluated at first and last TZ respectively.

The general equation for equilateral hyperbolas is

$$\frac{(\phi - \phi_0)^2 - (\psi - \psi_0)^2}{\alpha^2} = \pm 1. \qquad (4.12)$$

If the LHS of equation (4.12) is negative, the hyperbola aperture is vertical, and horizontal otherwise. The hyperbola type is determined by the $|J_{N+1}|$ value that results from the network synthesis considering $\psi = 0°$, $\phi = 0°$. If $|J_{N+1}| < 1$ the hyperbola is vertical and horizontal when $|J_{N+1}| > 1$, as it is stated in (4.12). The $|J_{N+1}|$ value determines the orientation of the hyperbola, but it can be only known after performing a whole network extraction. In filters which TZs distribution presents internal symmetry and different outer TZs like $\Omega_{tz} = \{\Omega_1, \Omega_2, \Omega_3, \Omega_2, \Omega_4\}$, the hyperbola type could be recognized a priori from the absolute value of the input and output phases $|\theta_{11}|$ and $|\theta_{22}|$. If $|\theta_{11}| > |\theta_{22}|$, the hyperbola is vertical and horizontal if $|\theta_{11}| < |\theta_{22}|$. However, this behavior is only observable in such case. These phase terms are obtained with (4.11) using the normalized frequency of the first and last TZs of the network. A phase term is greater as the TZ is closer to the center frequency and vice versa. It also should be noted in both, Figure 4.5a and Figure 4.5b, that the hyperbola-like shapes present periodicity every $\pm 180°$ degrees in ψ_0 and ϕ_0 directions regardless its aperture.

Apart from these two orientation types, there is also a third possibility, filters with TZs distribution

in such a way that it is achieved $|J_{N+1}| = 1$ before correcting the polynomial phases. Here, the vertex of both branches is located in the origin of the hyperbola, as shown in Figure 4.6. This situation is given, but not exclusively, when the TZs are symmetrically allocated over the network. As expected, the asymptote with positive and negative slope are given by $\psi = (\phi - \phi_0) + \psi_0$ and $\psi = -(\phi - \phi_0) + \psi_0$, respectively.

However, the vertices cannot be inferred directly from the function representation. The calculation is carried out by an indirect approach that will be described in Section 4.4.1. In the following, they are going to be under discussion to illustrate in more detail the three possible results. In the first two cases, the horizontal and vertical hyperbolas are shown; the third case explores filters with TZs distribution which $|J_{N+1}| = 1$ directly with the initial starting set-up ($\psi = \phi = 0$). Finally, the method used to obtain the vertex location V_h is described.

Hyperbola Types

The analysis of the three cases has been done following the same procedure. First, a network synthesis is done without modifying the polynomials to obtain the J_{N+1} used to identify the hyperbola type. Then, the phase sweep is carried out, and the results are plotted.

Let us consider first a 5th-order lowpass fully canonical filter with a TZs set $\Omega_{tz1} = \{2.6, -1.6, 2.6, -2.5, 3\}$ rad/s and $RL_1 = 10$ dB. An initial network synthesis yields $|J_{N+1}| = 1.005503$. As the admittance inverter is greater than one, the hyperbola is horizontal. Such property can be seen in Figure 4.5a. The center, calculated using (4.11), is located in $\phi_0 = \theta_{22} = -23.7531°$, $\psi_0 = \theta_{11} = -27.8209°$.

For the vertical case, a 5th-order lowpass fully canonical filter with a set of TZs $\Omega_{tz2} = \{1.4, -1.7, 2.6, -2, 1.8\}$ rad/s and $RL_2 = 10$ dB is considered. An initial network synthesis yields $|J_{N+1}| = 0.878566$, the admittance inverter is lower than 1, meaning that the hyperbola is vertical as shown in Figure 4.5b. The center is located in $\phi_0 = \theta_{22} = -42.7635°$, $\psi_0 = \theta_{11} = -61.5988°$.

As seen in Figure 4.5b, the continuity in the function is interrupted at some points. This discontinuity occurs when traces cross the asymptotes of the hyperbolic response. It was mentioned before that the hyperbolas show periodicity every $±180°$. The traces that appear after the end of the interrupted traces belong to another hyperbola on the map. A large number of realizations have been carried out, obtaining a margin of $±45°$ for ψ and ϕ around the origin point where the continuity is assured.

Considering the absolute value of the uneven admittance inverter as a measure of the values asymmetry in a specific TZs distribution, as $|J_{N+1}|$ tends to move away from unity, the further the hyperbola branches are from each other.

The third case occurs in filters with symmetric TZs distribution. Let us consider a 5th-order lowpass fully canonical filter with a TZs set $\Omega_{tz3} = \{1.8, -2, 2.6, -2, 1.8\}$ rad/s and $RL_3 = 10$ dB. An initial network synthesis yields $|J_{N+1}| = 1$. As shown in Figure 4.6, the sweep yields two slopes that cross in
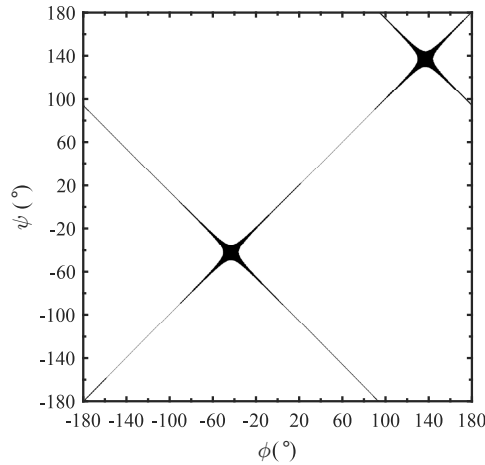
Figure 4.6: Phase sweep plot when the distance to the vertex is zero. The black trace represents those combinations of ψ, ϕ that yields $|J_{N+1}| = 1$. For illustration purpose all $|J_{N+1}|$ values that fit in 1 ± 0.001 have been plotted.

the center point. That is, the valid pairs ϕ, ψ are those that lie directly over the asymptotes. It must also be highlighted that in this case, the area in which $|J_{N+1}| = 1\pm0.001$ is more extensive than previous cases. That occurrence leads to less sensitive networks from the input/output phase shifts perspective. This special case corresponds to a degenerate conic section that is described as two intersecting lines [85], which mathematical expression is

$$\frac{(\phi - \phi_0)^2 - (\psi - \psi_0)^2}{\alpha^2} = 0. \tag{4.13}$$

Effectively, it can be observed in Figure 4.6 that there are identified pairs of angles (ϕ, ψ) suited to correct the input/output phase of the network. Moreover, as the solution is not unique, the designer has the chance to select that phase pair of values which lead to obtain $|J_{N+1}| = 1$. But at the same time, it is possible to consider other phase requirements as it could be the case of avoiding loading effects in the design of duplexers or multiplexers [78]. When the network is synthesized applying the phase correction using (ϕ, ψ) corresponding to one of the vertices, one of the reactive input/output elements will be zero because one of the phase terms cancels the input or output phase. If the hyperbola is vertically-orientated $\psi = \psi_0$, which is θ_{11}, the new input phase will be zero and no reactive element B_S at source port is necessary [51]. Conversely, if the hyperbola is horizontal, the reactive element at the output port will be zero. Besides, if different valid (ϕ, ψ) pairs are used, none of the input/output reactive elements will be null.

Relationship Between the Phase Map and the Admittance Redistribution Method

Section 4.1 describes a method to equalize the inverter values in the main-line by an admittance redistribution of the last three elements of the network. The solution changes $\theta_{22}(s)$ in the process without

altering $\theta_{11}(s)$. Hence, this is equivalent to pre-modify the characteristic polynomials before the circuital extraction with $\psi = 0$ and certain value for ϕ.

The filter used in Section 4.1 to exemplify the admittance redistribution with Ω_{Bk} TZs, which network parameters are in Table 4.2, showed two solutions for B_L, positive or negative depending on the sign of the square root. These solutions lead to two different circuit elements or equivalently, two additive output phase terms, ϕ_{B1} and ϕ_{B2}. They can be computed from the difference between the phase of the reflection coefficients before and after the admittance redistribution. The calculation is made at the output port when the S-parameters are evaluated at Ω_{B5}, that is, the resonance frequency of the closest resonator to the output port. Under such condition, the only circuit element from the output port is B_L. Before the admittance redistribution the FIR is $B_L = -0.4553$ and the phase term is $\phi_0 = -48.96°$. The redistributed FIR is (4.5) $B'_L = \pm 0.7739$, that yields $\phi'_0 = \pm 75.4726°$. Thus, the phase terms ϕ_{B1} and ϕ_{B2} are

$$\phi_{B1} = \phi_0 + |\phi'_0| = 26.51°, \tag{4.14a}$$

$$\phi_{B2} = \phi_0 - |\phi'_0| = -124.43°. \tag{4.14b}$$

In the original synthesized filter, the last admittance inverter is $|J_6| = 0.8689$, lower than one. Thus, a double phase sweep of the characteristic polynomials describes the vertical hyperbola shown in Figure 4.7a. It can be noted that two points are cutting the ψ axis at $\psi = 0°$. These two values correspond with ϕ_{B1} and ϕ_{B2}. This result reveals that the circuital transformation done by the admittance redistribution is actually a particular case within the hyperbola.
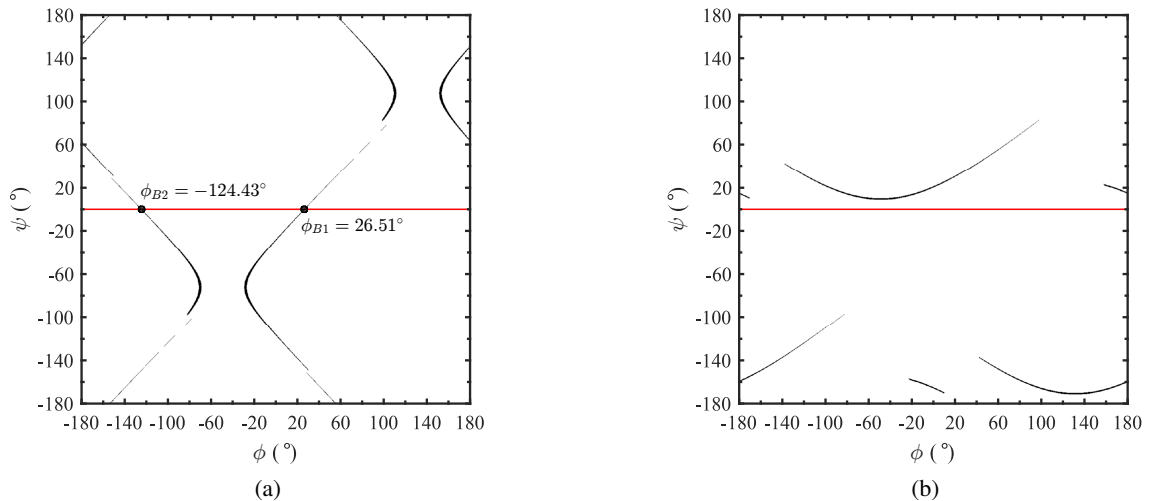
Figure 4.7: (a) Horizontal hyperbola of the filter with Ω_{Bk} TZs and (b) vertical hyperbola of the filter with Ω_{Ck} TZs. The black trace are those combinations of ϕ, ψ that yields $|J_{N+1}| = 1 \pm 0.001$. The red line cross the ϕ axis is at $\psi = 0$.

However, it was demonstrated in Section 4.1 the existence of filter specifications that produce networks for which the admittance distribution can not be done unless an impedance mismatch is forced, what kind of information the phase map can provide to clarify such circumstance?

The case has been illustrated with a network with TZs $\Omega_{Ck} = \{1.8, -1.16, \ 1.8, -2, \ 2.5\}$ rad/s, which network parameters are listed in Table 4.3. The double phase sweep of this filter yields the phase map in Figure 4.7b. It can be observed that no point is cutting $\psi = 0°$. In other words, there is no additive output phase ϕ that can correct the last admittance inverter if the input phase term ψ is zero. This brings to light the cause of the applicability limitations for redistribution method, and reinforce the necessity of the asymmetrical polynomial definition in such cases.

From both phase maps in Figure 4.7, it can be concluded that in all networks which phase maps describe vertical hyperbolas ($|J_{N+1}| < 1$), the redistribution is always possible because there exist cutting point at $\psi = 0$ in both branches. However, for those networks with horizontal hyperbolas ($|J_{N+1}| > 1$), it may occur that no branches cross the line at $\psi = 0$. To equalize the uneven inverter is necessary to change, unless, the input phase with a non-zero ψ.

4.3.2 Even-Order ladder filters

In odd-order filters, the symmetric distributions can be achieved by having the same resonance frequencies at both halves of the network, considering the central resonator as an axis of symmetry. Hence, even-order filters do not possess symmetry under these terms, and the unitary admittance inverters can only be achieved, without any phase correction, by a careful selection of TZs and RL values. For example, with the network with TZs $\Omega_{Dk} = \{2.5, -1.3, \ 1.5, -2.64, \ 2, -1.86\}$ rad/s and $RL = 20$ dB, which network parameters are listed in Table 4.4, the admittance inverters are $J_k = \{1, -1, \ 1, -1, \ 1, -1, \ 1\}$.

In any event, the unique geometric shape that defines the input and output phases (Ψ, Φ) providing an unitary admittance inverter for even-order filters is an ellipse. To illustrate the phenomenon, let us

Table 4.4: Extracted elements of the 6th-order filter prototype with a Ω_{Dk} TZs distribution.

	B_k	b_k	J_{rk}
Res. 1	-1.6233	-2.50	2.0910
Res. 2	1.2539	1.30	0.9785
Res. 3	-2.4661	-1.50	1.8270
Res. 4	3.1101	2.64	2.9667
Res. 5	-3.4831	-2.00	2.4392
Res. 6	1.2111	1.86	1.2928
B_S	-0.4460		
B_L	0.6775		

Table 4.5: Extracted elements of the 4th-order filter prototype with a Ω_{Ek} TZs distribution.

	B_k	b_k	J_{rk}
Res. 1	0.9234	1.80	1.1080
Res. 2	-2.3310	-1.60	1.6192
Res. 3	1.8854	2.00	1.8385
Res. 4	-2.4007	-2.50	2.3224
B_S	0.7782		
B_L	-0.4700		
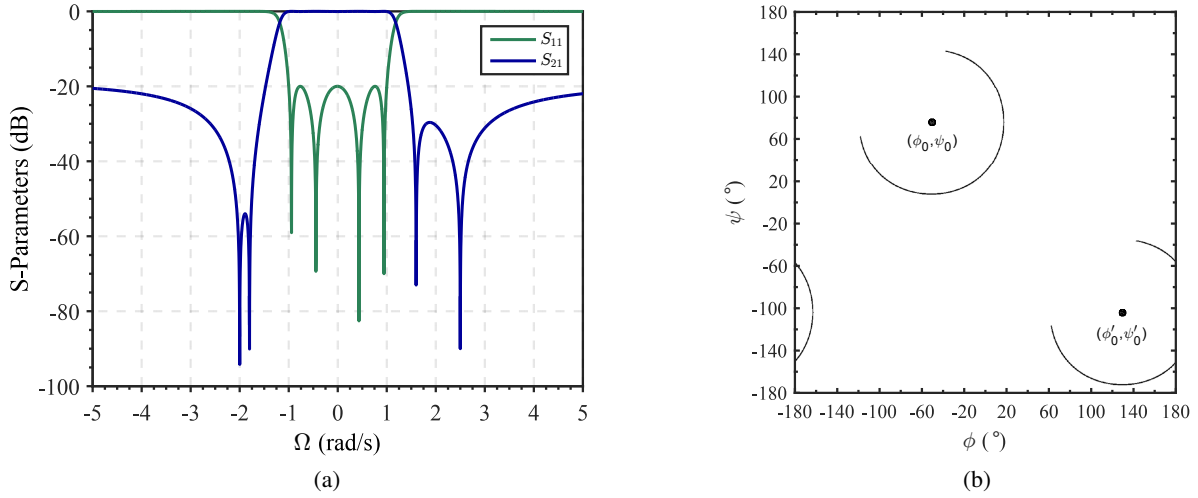
Figure 4.8: (a) S-parameters of the network with Ω_{Ek} TZs and (b) the phase map of the ellipse with a sweep between $\pm 180°$.

consider a 4th-order fully canonical filter with a TZs $\Omega_{Ek} = \{-1.8, 1.6, -2, 2.5\}$ rad/s and $RL = 20$ dB, with the network parameters in Table 4.5 and S-parameters in Figure 4.8a. The synthesis yields $J_k = \{1, -1, \; 1, -1, \; 1.1593\}$. The result of the sweep reveals the ellipses in Figure 4.8b.

Although being different from the hyperbola, the origin location at ψ_0 and ϕ_0 is determined with (4.11) likewise, and it can also be observed periodicity in the ellipse every $\pm 180°$ in both axis, ψ and ϕ. The origin in this case is located at ($\psi_0 = -50.3462°$, $\phi_0 = 75.7811°$). However, unlike the odd-order filters, the even-order do not show any variation in shape.

Besides, it can be noted that the black trace in Figure 4.8b never cuts $\psi = 0°$. That is, even-order filters may be susceptible not to have any output additive phase term ϕ that can provide a unitary admittance inverter $|J_{N+1}|$ without modifying the input phase. In consequence, it may be network configurations in which the admittance redistribution method is not applicable either.

The ellipse can be completely characterized by three parameters: the center location, the major radius and minor radius. To keep coherence with the rest of the text, the radii will be referred as r_ψ and r_ϕ, in function of the axis in which they are defined, instead of their length from the center. The general ellipse equation is

$$\frac{(\phi - \phi_0)^2}{r_\phi^2} - \frac{(\psi - \psi_0)^2}{r_\psi^2} = 1. \tag{4.15}$$
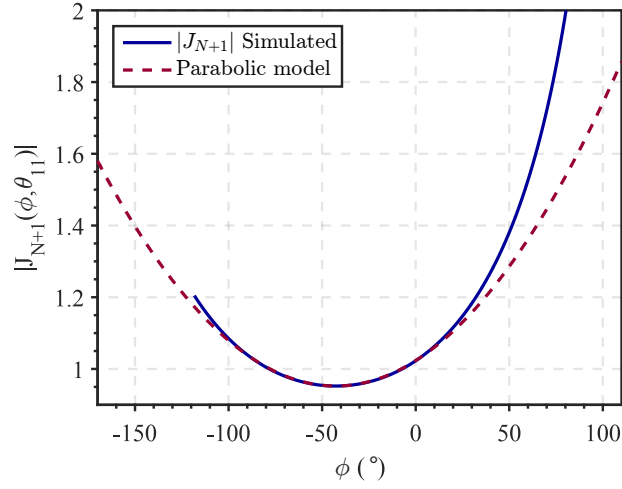
Figure 4.9: Comparison between the phase sweep in ϕ for filter with Ω_{tz1} TZs and the parabolic estimation model.

4.4   Fast Estimation of the Phase Maps

Performing a phase map for every network is a time-consuming task, doing a sweep from $-180°$ to $180°$ in both ψ and ϕ with a good precision requires about 10^6 full extractions. In this section, a method to obtain an accurate model for both shapes, the hyperbola and the ellipse is described. The proposed methods are generic with the intention to make unnecessary the phase exploration each time, enabling to arrive into a proper solution directly with a low computational cost.

4.4.1   Hyperbolic Model Estimation

As mentioned earlier, four parameters are required: the hyperbola type (horizontal or vertical), the two slant asymptotes, the origin locus and the distance from it to the vertex of one branch. All of them are obtained from the network parameters except the vertices. The vertex is the point at each branch closest to the center. In order to find its value, an indirect approach has been employed.

Since both vertices belong to the hyperbola, they will provide $|J_{N+1}| = 1$. A phase sweep has been carried out along the transverse axis, the line going from one vertex to the other. If it is a vertical hyperbola, the transverse axis is defined in ϕ axis, being also the sweeping parameter. Meanwhile, ψ is fixed and set to $\psi_0 = \theta_{11}$. In the horizontal hyperbola case, ψ is the sweeping parameter and $\phi_0 = \theta_{22}$. The traced curve is accurately described by a geometric parabolic function that is continuous within the range of interest given by (4.16) and (4.17) for the vertical and horizontal hyperbola case, respectively.

$$\phi = \pm(180° - |\theta_{11}|), \tag{4.16}$$

$$\psi = \pm(180° - |\theta_{22}|). \tag{4.17}$$

The parabola and hyperbola vertices have been denoted as V_p and V_h, respectively to avoid confusion. For the vertical hyperbola case, the parabola vertex is identified by $V_p(\phi_0, |J_{N+1}(\phi_0, \psi_0)|)$. At equal distance to the vertex, there are two $|J_{N+1}|$ values that are unitary; these points meet with the hyperbola vertices. Although the curve is not exactly a parabola, the approximation is valid for range close to the vertex V_p because it is where the solution usually is, and V_p does not takes values far from one. The equation is defined as follows:

$$(\phi - \phi_0)^2 = 4p(|J_{N+1}(\phi, \psi_0)| - |J_{N+1}(\phi_0, \psi_0)|), \tag{4.18}$$

where p is a constant that controls the parabola steepness. It can be obtained by

$$p = \frac{(\phi - \phi_0)^2}{4(|J_{N+1}(\phi, \psi_0)| - |J_{N+1}(\psi_0, \phi_0)|)}. \tag{4.19}$$

The ϕ value for calculating p should be chosen close to the vertex V_p to achieve an accurate approximation to the curve steep. Obviously, higher polynomial fit can be successfully used to increase the range and accuracy of the approximation, but based in the conducted experiments, the parabolic model is computationally faster, accurate enough and facilitates the understanding. The hyperbola vertices can be obtained from (4.18) by setting $|J_{N+1}(\phi, \psi_0)| = 1$ and solving for ϕ that are the angles where the vertices are located.

$$\phi = \phi_0 \pm 2\sqrt{p(1 - |J_{N+1}(\phi_0, \psi_0)|)} \tag{4.20}$$

Using equation (4.20), the vertices points of a vertical hyperbola are $V_h(\phi_0 \pm \alpha, \psi_0)$, where α is defined as

$$\alpha = 2\sqrt{p(1 - |J_{N+1}(\phi_0, \psi_0)|)}. \tag{4.21}$$

Considering the filter used in the previous section with TZs Ω_{tz1}, the vertices are located at $\phi = \theta_{22} \pm 35.04°$ and $\psi_0 = \theta_{11}$. As seen in Figure 4.9, the approximation is accurate around the parabola vertex. Analogously, when the hyperbola is horizontal, the parabola function equations are calculated, as follows:

$$(\psi - \psi_0)^2 = 4p(|J_{N+1}(\phi_0, \psi)| - |J_{N+1}(\phi_0, \psi_0)|), \tag{4.22a}$$

$$p = \frac{(\psi - \psi_0)^2}{4(|J_{N+1}(\phi_0, \psi)| - |J_{N+1}(\phi_0, \psi_0)|)}, \tag{4.22b}$$

$$\psi = \psi_0 \pm \alpha. \tag{4.22c}$$

Finally, the vertices points are defined as $V_h(\phi_0, \psi_0 \pm \alpha)$.

4.4.2 Illustrative Synthesis Example

A Chebyshev 7th-order fully canonical filter with an asymmetric TZs distribution is presented to demonstrate the accuracy of the proposed method. The transmission zeros are $\Omega_{tz} = \{2.4, -2.1, 1.7, -1.8, 2, -1.7, 1.5\}$ rad/s and $RL = 18$ dB. All characteristic polynomials are listed in Table 4.6.

The lowpass prototype filter resulting from the network synthesis is like the one depicted in Figure 4.1 with $N = 7$. The extracted parameters are shown in Table 4.7, leading to the transmission and reflection response in the lowpass domain depicted in Figure 4.10. In this example, the extracted uneven admittance inverter is $|J_{N+1}| = 1.2405$, meaning that the hyperbola is horizontal as shown in Figure 4.11a. The center of the hyperbola, obtained with (4.11), is located in $C(\phi = -83.6889°, \psi = -45.814°)$, θ_{22} and θ_{11}, respectively.

Table 4.6: Synthesized characteristic polynomial coefficients

	Initial characteristic polynomials			
Degree	$P(s)$	$E(s)$	$F_{11}(s)$	$F_{22}(s)$
7	1	1	1	1
6	$2.0000j$	$1.7997 - 0.3115j$	$-0.3115j$	$-0.3115j$
5	10.7200	$3.4792 - 0.5680j$	1.8598	1.8598
4	$20.7380j$	$3.6860 - 1.0261j$	$-0.5080j$	$-0.5080j$
3	37.6407	$3.3274 - 1.0378j$	1.0165	1.0165
2	$70.4446j$	$1.9944 - 0.8376j$	$-0.2183j$	$-0.2183j$
1	43.3847	$0.8449 - 0.4246j$	0.1470	0.1470
0	$78.6542j$	$0.1852 - 0.1290j$	$-0.0161j$	$-0.0161j$
	Modified polynomials by $\phi = -83.6889°$, $\psi = -36.6610°$			
Degree	$E_m(s)$	$F_{11m}(s)$	$F_{22m}(s)$	
7	$0.4974 + 0.8675j$	$0.9170 + 0.3990j$	$0.9169 + 0.3989j$	
6	$1.1653 + 1.4064j$	$0.1243 - 0.2856j$	$0.1242 - 0.2855j$	
5	$2.2232 + 2.7359j$	$1.7053 + 0.7420j$	$1.7053 + 0.7420j$	
4	$2.7234 + 2.6874j$	$0.2027 - 0.4658j$	$0.2026 - 0.4658j$	
3	$2.5552 + 2.3705j$	$0.9321 + 0.4056j$	$0.9321 + 0.4055j$	
2	$1.7186 + 1.3137j$	$0.0871 - 0.2001j$	$0.0870 - 0.2001j$	
1	$0.7885 + 0.5218j$	$0.1348 + 0.0586j$	$0.1347 + 0.0586j$	
0	$0.2040 + 0.0965j$	$0.0064 - 0.0147j$	$0.0064 - 0.0147j$	
	Modified polynomials by $\phi = -53.51°$, $\psi = -14.18°$			
Degree	$E_m(s)$	$F_{11m}(s)$	$F_{22m}(s)$	
7	$0.8305 + 0.5569j$	$0.9417 + 0.3365j$	$0.9416 + 0.3365j$	
6	$1.6682 + 0.7436j$	$0.1048 - 0.2933j$	$0.1048 - 0.2932j$	
5	$3.2060 + 1.4660j$	$1.7513 + 0.6259j$	$1.7513 + 0.6258j$	
4	$3.6328 + 1.2007j$	$0.1710 - 0.4784j$	$0.1709 - 0.4783j$	
3	$3.3415 + 0.9912j$	$0.9572 + 0.3421j$	$0.9572 + 0.3420j$	
2	$2.1230 + 0.4152j$	$0.0734 - 0.2055j$	$0.0734 - 0.2055j$	
1	$0.9382 + 0.1179j$	$0.1384 + 0.0495j$	$0.1384 + 0.0494j$	
0	$0.2257 - 0.0040j$	$0.0054 - 0.0151j$	$0.0054 - 0.0151j$	
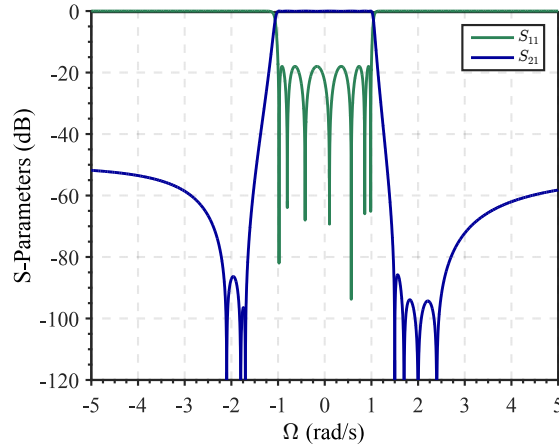
Figure 4.10: Lowpass transmission and reflection response of the extracted network.

(a)   (b)
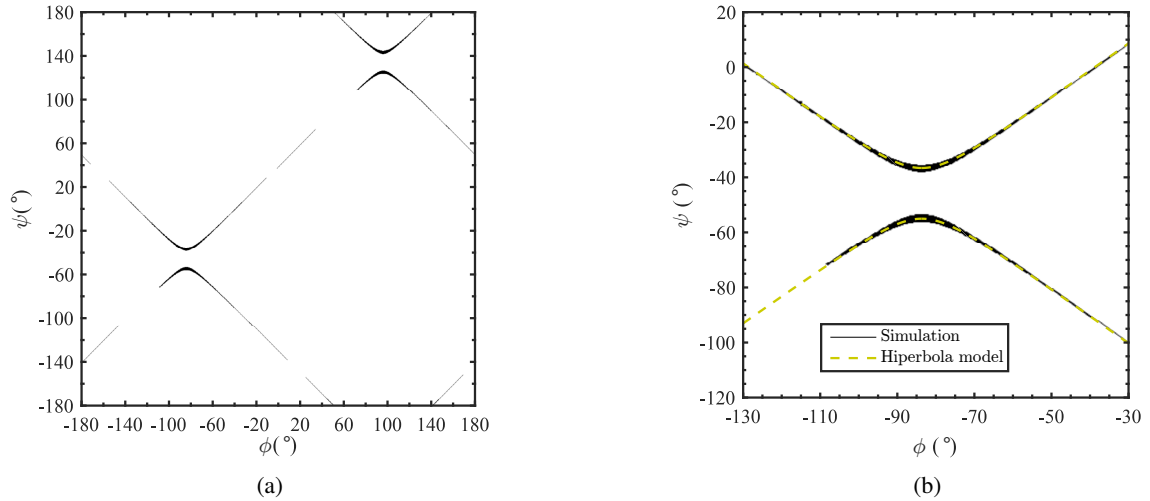
Figure 4.11: Hyperbola representation of the 7th-order filter: (a) the black trace represent those combinations of ψ, ϕ that yields $|J_{N+1}| = 1$, and (b) a comparison between the modeled and simulated hyperbola. For illustration purpose, all $|J_{N+1}|$ values that fit in 1 ± 0.001 have been plotted.

The vertices must be provided to characterize the hyperbola. Considering its nature, V_h has to be calculated using the expressions in (4.22). The parabolic steepness parameter $p = 6.6294 \times 10^3$ is obtained using $\phi = \phi_0 + 45°$. Then, the distance from the center to the vertices is $\alpha = 9.2096°$. The hyperbola modeled with (4.12) using the estimated parameters, matches the simulation accurately enough in those points in which $|J_{N+1}|$ is unitary as seen in the comparison in Figure 4.11b.

The filter, with the same set of TZs and RL, has been re-synthesized applying the proper polynomial modification in (4.6) and (4.7) using the vertex point $\phi = -83.6889°$ and $\psi = \theta_{11} + \alpha = -36.6610°$. The coefficients of the modified polynomials are found in Table 4.6. Since the allocation of the TZs has not been modified, the polynomial $P(s)$ remains the same. The values of the different extracted parameters are listed in Table 4.8. The value of the last admittance inverter results in $J_{N+1} = -0.99996 \approx -1$.

Table 4.7: Lowpass elements of the synthesized 7th-order ladder filter.

	B_k	b_k	J_{Rk}
Res. 1	-2.0663	-2.4	2.1118
Res. 2	2.9706	2.1	2.4151
Res. 3	-2.4493	-1.7	2.0115
Res. 4	2.7822	1.8	2.2187
Res. 5	-2.9497	-2.0	2.4700
Res. 6	2.2032	1.7	1.7362
Res. 7	-1.3197	-1.5	1.0718
Source	-0.4226		
Load	-0.8955		

Table 4.8: Lowpass elements of the synthesized 7th-order ladder filter with phase correction $\phi = -83.6889°, \psi = -36.6610°$.

	B_k	b_k	J_{rk}
Res. 1	-2.0794	-2.4	2.2853
Res. 2	2.5367	2.1	2.2317
Res. 3	-2.8683	-1.7	2.1767
Res. 4	2.3758	1.8	2.0502
Res. 5	-3.4543	-2.0	2.6728
Res. 6	1.8815	1.7	1.6044
Res. 7	-0.6499	-1.5	1.1598
Source	-0.0800		
Load	-		

Table 4.9: Lowpass elements of the synthesized 7th-order ladder filter with phase correction $\phi = -53.51°, \psi = -14.18°$.

	B_k	b_k	J_{rk}
Res. 1	-2.1254	-2.4	2.2058
Res. 2	2.7228	2.1	2.3122
Res. 3	-2.6722	-1.7	2.1010
Res. 4	2.5501	1.8	2.1241
Res. 5	-3.2181	-2.0	2.5799
Res. 6	2.0194	1.7	1.6622
Res. 7	-0.8568	-1.5	1.1195
Source	-0.2833		
Load	-0.2696		

It should be noted that in this particular case, the coefficient $\phi = \theta_{22}$. Therefore, the output phase after correcting polynomial $F_{22m}(s)$ becomes zero. That is, the load element is null. On the other hand, if the filter is re-synthesized with other suitable phases pair like $\phi = -53.51°, \psi = -14.18°$, the non-even admittance inverter is $J_{N+1} = -0.99968$, but now none of the loading elements are null as seen in Table 4.9.

The precision of both synthesis examples results demonstrates the effectiveness of the method convincingly. A complementary analysis shows a significant variation of the network parameters B_k, J_{rk} and the external elements in function of ψ and ψ. This circumstance is a double-edged sword. It may be useful to force values convenient for a design, but it must be considered that some phase pair may yield a good lowpass prototype that turns to be a non-feasible for acoustic wave technology.

4.4.3 Ellipsoidal Model Estimation

For even-order filters, the characterization of the ellipse only requires three parameters: the center loca-
tion and the major radius and minor radius. The radii are the only parameters that can not be obtained
from the network specifications or extracted elements.

The radii length must be obtained using a similar approach to the one described in Section 4.4.1. In
contrast to the vertex estimation, the radii are the furthest point from the center in both ψ and ϕ axes.
As depicted in Figure 4.12a, two parabolic estimations must be used to obtain their values. The parabola
for r_ψ is defined in the plane $(|J_{N+1}|, \psi)$ given by the equation (4.22a) with a steepness p (4.22b) in the
range stated by (4.17). The radius is the distance from the center to a crossing point in ψ between the
ellipse and the parabola that yields $|J_{N+1}| = 1$. Its value can be computed as

$$r_\psi = \psi_0 \pm 2\sqrt{p(1 - |J_{N+1}(\phi_0, \psi_0)|)}. \tag{4.23}$$

In the complementary case, the parabola that helps to estimate r_ϕ is in the plane $(|J_{N+1}|, \phi)$, and it is
defined by (4.22a). The steepness p is calculated with (4.19), within a range delimited by (4.16). The
radius is calculated as

$$r_\phi = \phi_0 \pm 2\sqrt{p(1 - |J_{N+1}(\phi_0, \psi_0)|)}. \tag{4.24}$$

Let us consider the 4th-order fully canonical filter with a TZs Ω_{Ek}, which network parameters are listed
in Table 4.5. The origin of the ellipse is located at $(\psi_0 = -50.3462°, \phi_0 = 75.7811°)$. The sweep shows
the ellipses in Figure 4.8b. Using the proposed method, the calculated radii are $r_\psi = 67.9811°$ and
$r_\phi = 68.4862°$. In Figure 4.12b it can be seen the result of ellipsoidal model in (4.15) over the simulated
ellipse from the phase map. Like the hyperbola, the ellipsoidal shape is incomplete in some parts.
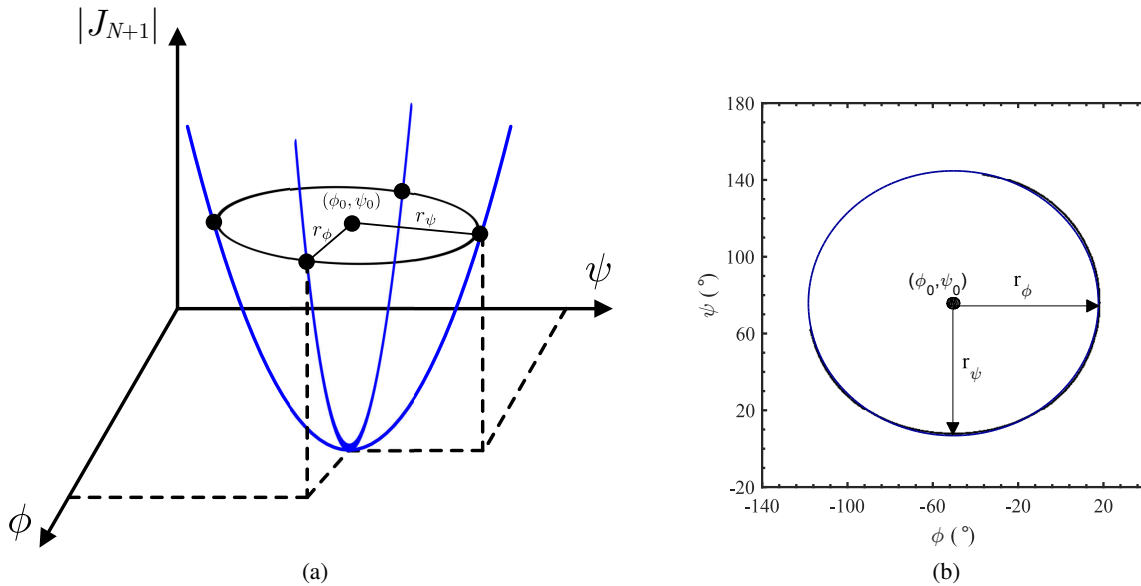
Figure 4.12: (a) Illustrative representation of the double parabolic estimation for the ellipsoidal model,
and (b) the result of applying it to the filter with Ω_{Ek} (blue trace) superimposed to the phase map (black
trace).

4.5 Experimental Validation

In order to validate the proposed methodology, a $N = 5$ order filter has been synthesized using the procedure described in Chapter 3, with the usual polynomial definition, $RL = 20$ dB, and allocation of the transmission zeros in the lowpass domain $\Omega_{tzk} = \{1.7342, -1.8170, 1.2350, -2.2460, 2.4673\}$ rad/s. The extracted elements of the lowpass prototype are shown in Table 4.10. The elements with subscript a correspond to those obtained directly from the synthesis procedure. In this case, the last inverter $J_{N+1} = -0.8936$, from the phase point of view, Figure 4.13 shows that $\theta_{11}(s) = \theta_{22}(s)$, as expected since symmetric polynomials have been used.

Table 4.10: Lowpass elements of the synthesized 5th-order ladder filter without phase correction before and after J_{N+1} redistribution.

	B_{ka}	b_{ka}	J_{rka}	B_{kb}	b_{kb}	J_{rkb}
Res. 1	-1.0043	1.7342	1.1104	-1.0043	1.7342	1.1104
Res. 2	2.6867	-1.8170	2.0959	2.6867	-1.8170	2.0959
Res. 3	-1.0426	1.2350	0.9444	-1.0426	1.2350	0.9444
Res. 4	3.6246	-2.2460	2.8412	3.6246	-2.2460	2.8412
Res. 5	-1.5172	2.4673	1.8313	-1.6887	2.4673	1.8313
Source	-0.7737			-0.7737		
Load	-0.4575			-0.7133		
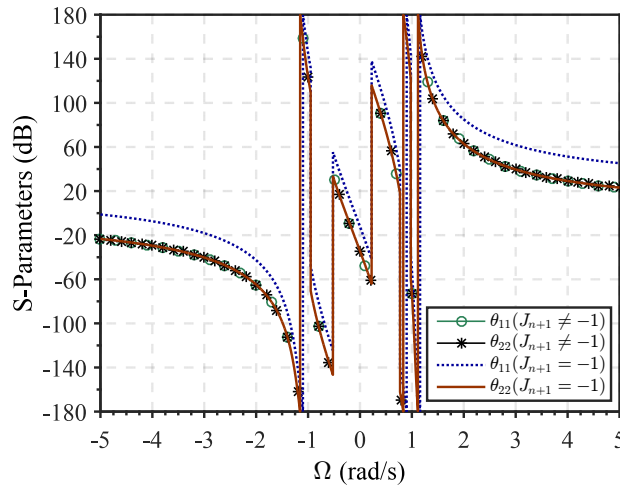
Figure 4.13: Input and output reflection coefficient phase $\theta_{11}(s)$ and $\theta_{22}(s)$.

The dangling resonator can only be serialized if the side inverters are equal with opposite sign. As it was previously discussed, a possible solution consists of applying a redistribution of the values of the last three elements of the network, the last two FIRs and the admittance inverter coupling them, to turn the last admittance inverter into unity. This is seen in the elements with subscript b in Table 4.10, where the FIR B_{kb} for resonator 5 and the load element have been modified. Now, the last inverter is $J_{N+1} = -1$, so

the serialization is possible. However, a phase shift of $-11.05°$ in the main-line is required for the exact and complete synthesis. The lack of such phase shift entails that the new phase terms $\theta'_{11}(s) \neq \theta'_{22}(s)$ because $\theta'_{22}(s) = \theta_{22}(s) + 22.1°$ and $\theta'_{11}(s) = \theta_{11}(s)$.

For clarity, the nodal representation of the directly synthesized network in Figure 4.15 is compared with the network after the element transformation is carried out to achieve the $J_{N+1} = -1$. Thereby, the presence of the phase shifter in the main-line path is mandatory to have a perfect equivalence between both networks. The admittance redistribution only introduces an additive term in $\theta_{22}(s)$ to correct the admittance inverter.
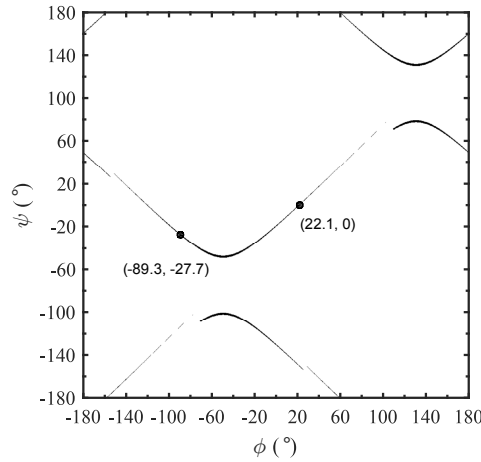
Figure 4.14: Hyperbola of the 5th-order filter in which the point (-89.3, -27.7) is the phase term used in the manufactured filter. The additive phase term applied after the circuital transformation is (22.1, 0).
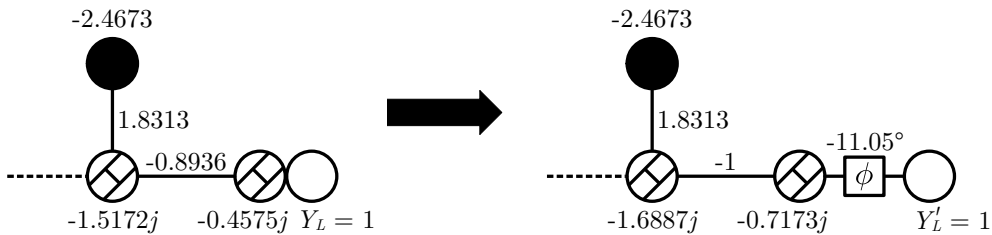
Figure 4.15: Nodal network representation with the direct synthesis of the elements resulting in $J_{N+1} \neq -1$ (left), and after the network transformation done to achieve $J_{N+1} = -1$ (right).

In other words, it is equivalent to synthesize the network with $\psi = 0°$ and $\phi = 22.1°$ as shown in the phase map in Figure 4.14. In order to have an exact and complete synthesis of the filter, the proposed phase correction method has been applied with $\phi = -89.3°$ and $\psi = -27.7°$ which locus in the phase map can be seen in Figure 4.14. In this case, the resulting last inverter $J_{N+1} = -1$ as expected. The transformation to the bandpass domain is the BVD equivalent circuit as shown in Figure 4.16a, where the values for the elements are summarized in Table 4.11. The frequency transformation has been done considering $f_0 = 245$ MHz, and BW$= 100$ MHz.

Table 4.11: Bandpass elements of the 5th-order filter with phase correction $\phi = -89.3°, \psi = -27.7°$.

	L_a (nH)	C_a (pF)	C_0 (pF)
Res. 1	53.18	7.35	13.28
Res. 2	81.14	8.90	15.13
Res. 3	135.24	2.68	11.03
Res. 4	48.83	16.59	18.33
Res. 5	41.63	14.86	6.65
Source	73.3 nH		
Load	4.74 pF		

(a)

(b)
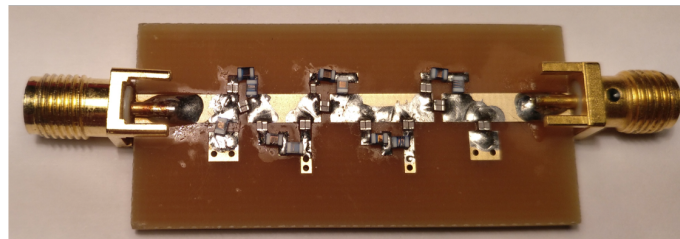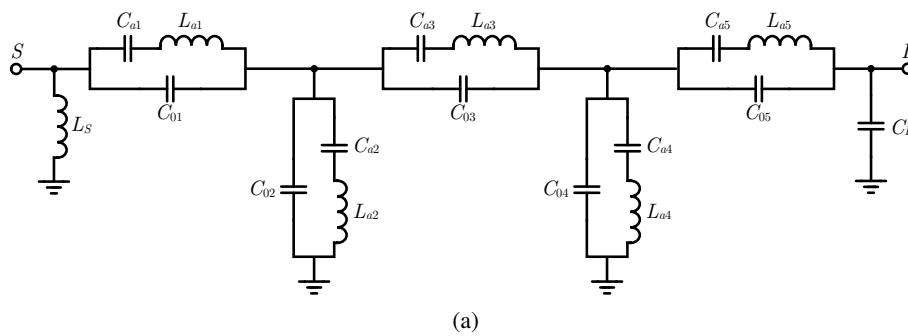
Figure 4.16: Implemented filter: (a) equivalent electric circuit using the Butterworth-Van Dyke model for the designed filter, (b) fabricated prototype using lumped elements.
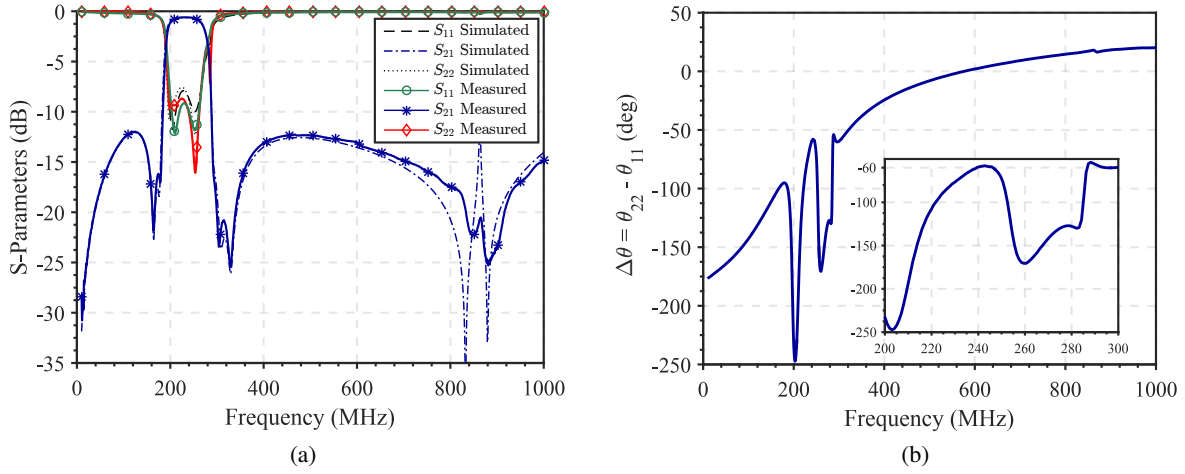
Figure 4.17: Filter response: (a) measured and simulated filter transmission response and input/output reflection coefficient, (b) difference between measured reflection coefficient phase $\Delta\theta = \theta_{22} - \theta_{11}$.

As a proof of concept and for rapid prototyping, the filter was fabricated using Wirewound High-Q Chip Inductors and Multi-layer High-Q Capacitors from Johanson Technology. The estimated Q factor for inductors and capacitors are respectively $Q_L = 45$ and $Q_C = 800$. The measured transmission response, as well as the input/output reflection coefficient, are shown in Figure 4.17a. The insertion losses are -0.6 dB as expected, taking into account the finite Q factor of the lumped components. The tolerances in the used commercial values of the components are also responsible for the detuning of the upper TZ closest to the bandpass, which at the same time results in a certain degradation of the RL and achieved BW.

On the other hand, Figure 4.17b shows the measured difference between the phase of the input and output reflection coefficient at f_0 $\Delta\theta = \theta_{22} - \theta_{11} = -58.73°$. The response is in a very good agreement with the specifications of the filter where the theoretical difference at f_0 is $\phi - \psi = \theta_{11} - \theta_{22} = -61.6°$. It has to be highlighted that, unlike the method based on the redistribution of the network, no phase shifters are required for the serialization of resonators by modifying the input and output phases.

4.6 Chapter Summary

In this chapter, the necessity of asymmetric polynomials for networks with asymmetric transmission zeros distribution in order to overcome phase offsets when using Chebyshev polynomials has been presented. To equalize all the admittance inverters in the main-line path to the same value, a method for the phase correction of the characteristic polynomials has been described for inline networks. A suitable pair of phase values can be accurately estimated using the developed hyperbolic and ellipsoidal models, whose main parameters are obtainable from the transmission zeros and reflection scattering parameters. The proposed method has been compared with the usual circuital transformation and has been demon-

strated that it is a particular case in the hyperbolic and ellipsoidal phase maps. The phase modifications are useful for stand-alone filters in order to eliminate input/output reactive elements, equalize the value of the admittance inverters, and also in multiplexers to provide a balanced input port by means of phase adjustment to avoid loading effects. To obtain all phase pair values, it has been proposed a fast estimation method that provides a low computational cost that models both conic sections. Finally, a ladder-type filter has been fabricated and measured to validate the proposed methodology.

Synthesis of Mixed-Topology Filters

Filters based on acoustic wave technology play an essential role in solving the complex challenges in present and next-generation of wireless devices. The ladder topology, with either SAW or BAW technology, is the most widely adopted solution by the market. One of the major drawbacks of ladder-type filters is related to their achievable bandwidth, limited by the effective electromechanical coupling constant of the AW resonators. Moreover, the required alternation of series and shunt resonators in this topology, or equivalently transmission zeros above and below the passband, may impose some limitations to obtain even greater out-of-band rejection levels. Despite the utility of the ladder topology, the quantity of TZs in each side of the passband is fixed by this condition. For example, some applications may require higher OoB or a steeper roll-off. The only option to achieve such performance in ladder networks is increasing the order filter while keeping the alteration between resonators. Consequently, the network complexity, the die area and insertion losses increase significantly.

Moreover, the resonance frequency of each resonator matches a TZ implemented by the filter. Thus, the parameters of the resonator are defined by them. That means that there exists low flexibility to decide the physical characteristics of the resonators. This fact may imply having some restrictions on the feasibility if some requirements can not be satisfied because of technological restrictions. Alternatively, the filtering function be can de modified to provide a realizable filter, but its performance may not meet the frequency masks.

In this regard, mixed-topology networks may represent a suitable alternative. For the synthesis of these kinds of networks, some general methods have already been developed. Specifically, in [86], it is described a particular method where the filter is created by cascading different two-port blocks: the outer blocks are synthesized with extracted-pole topology, while the inner block is obtained with a cross-coupled configuration. In [87, 88], the method starts building a canonical coupling matrix for the filter, which is based on a set of characteristic polynomials with complex coefficients to generate extracted-pole

sections at the source and load directly. Then, a specific matrix rotation sequence is introduced to reduce the filter to a more practical configuration.

In both, higher flexibility to the filter design process is introduced, where cross-coupled structures and extracted-pole sections are combined. These techniques expand the range of configurations that can be implemented. However, the cited synthesis methodologies can be impractical in many cases. The ladder-type structure with dangling resonators is not directly considered by the cross-coupled inner block in [86], which results in a non-suitable configuration for AW topology. Although in [87], the inner block can be configured as a set of dangling resonators, the result is just a conventional ladder.

The proposed topologies in this chapter are partially based on a cross-coupled lowpass prototype or transversal network. Unlike the fully canonical ladder filters, the resonance frequencies are not necessarily tied to the prescribed TZs of the filtering function. That is, the TZs are not individual contributions of series or parallel resonances of each resonator, but generated by the whole sub-network. This property provides higher flexibility to deal with the effective electro-mechanical coupling coefficient for better accommodation of the technology constraints. By disassociating TZs from their resonances, it is possible to achieve higher bandwidths by sorting the parameters with alternative topologies.

The aim of this chapter is to introduce a general synthesis method for fully canonical filters based on mixed-topology networks, which has been created to accommodate AW technology for new configurations beyond the classic ladder network. The proposed methodology enables the synthesis of filters with more flexible TZs assignation to the resonators, for instance, maximizing an arbitrary number of TZs in the above or below the passband. This characteristic is very useful to achieve a higher out-of-band rejection and steeper roll-off at the same time. Using the fundamentals of the synthesis method, the procedure to define two different topology families are described. Additionally, a detailed explanation to orient the extraction process to achievable networks in AW technology is provided. Finally, several examples have been included to validate the proposed methodology. Part of the content in this chapter is published by the author in [89–91].

5.1   Transversal Networks

The synthesis of inline ladder network has already been detailed in Chapter 3. Before moving to the synthesis mixed-topologies, the basic theory of transversal networks in [74] is briefly described in this section for a better understanding of the methodology developed later in this chapter.

The networks of interest are fully canonical, and its general form is depicted in Figure 5.1. It consists of a set of resonator nodes connected in parallel between the source and load terminations, but not to each other. A direct coupling from source to load J_{SL} is included to allow the realization of fully canonical filtering functions, otherwise J_{SL} is zero. The minimum path rule [92] states that the maximum number of TZs at finite frequencies realizable by a network is $N - n_{min}$, where n_{min} is the number of
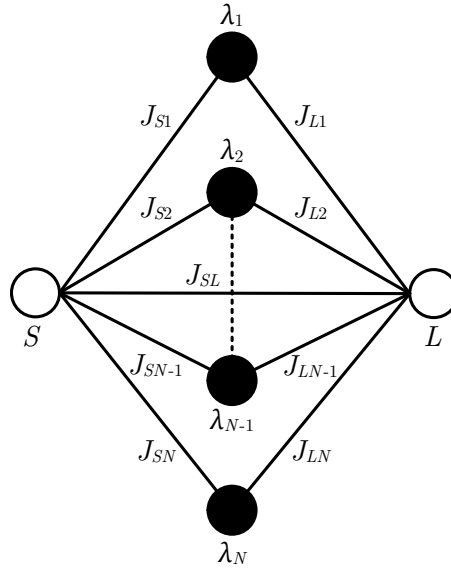
Figure 5.1: General Nth-order fully canonical transversal network.

resonator nodes in the shortest path between source and load nodes. In fully canonical networks, the maximum number of TZs $n_{fzmax} = N$. That is, it can implement as many TZs as the degree of the network. The transversal network may be synthesized from the admittance matrix $[Y]$, built from the characteristic polynomials, which may be associated with the general diagram scheme using the partial fraction expansions as follows:

$$[Y] = \frac{1}{y_d(s)} \begin{bmatrix} y_{11n}(s) & y_{12n}(s) \\ y_{21n}(s) & y_{22n}(s) \end{bmatrix} = j \begin{bmatrix} B_S & J_{SL} \\ J_{SL} & B_L \end{bmatrix} + \sum_{i=1}^{N} \frac{1}{(s - j\lambda_i)} \begin{bmatrix} r_{11i} & r_{21i} \\ rJ_{12i} & r_{22i} \end{bmatrix}$$

$$= j \begin{bmatrix} B_S & J_{SL} \\ J_{SL} & B_L \end{bmatrix} + \sum_{i=1}^{N} \frac{1}{(sC_i - jB_i)} \begin{bmatrix} J_{Si}^2 & J_{Si}J_{Li} \\ J_{Si}J_{Li} & J_{Li} \end{bmatrix}, \quad (5.1)$$

where $y_{11n}(s)$, $y_{12n}(s)$, $y_{21n}(s)$ and $y_{22n}(s)$ refer to the numerator polynomials of their respective Y-matrix polynomials, while $y_d(s)$ is the common denominator polynomial, which roots $j\lambda_i$ are the eigenvalues or resonance of the resonating nodes. Note that the expression $sC_i - jB_i$ is the circuital equivalent of the resonator node as depicted in Figure 3.2a, where $C_i = 1$ and $B_i = \lambda_i$.

The extraction of the source-load coupling J_{SL} must be carried out in first place to reduce the degree of polynomial y_{21n} by one and prepare the extraction of the couplings J_{Si} and J_{Li} by subtracting the frequency-independent term. The value is found by

$$J_{SL} = \lim_{s \to \infty} \frac{y_{21n}(s)}{y_d(s)}. \quad (5.2)$$

Note that in terms of ABCD polynomials, $y_{21n}(s) = jP(s)/\varepsilon$ and $y_d(s) = B_n(s)$. The updated polynomial $y'_{21n}(s)$ is calculated as

$$y'_{21n}(s) = y_{21n}(s) - jJ_{SL}y_d(s). \quad (5.3)$$

The elements B_S and B_L are the FIRs at source and load terminals, respectively. They are evaluated at $s = j\infty$ as

$$jB_S = \lim_{s \to \infty} \frac{y_{11n}(s)}{y_d(s)}, \tag{5.4a}$$

$$jB_L = \lim_{s \to \infty} \frac{y_{22n}(s)}{y_d(s)}. \tag{5.4b}$$

The polynomials y'_{11n} and y'_{22n} are updated with the following expressions:

$$y'_{11n}(s) = y_{11n}(s) - jB_S y_d(s), \tag{5.5a}$$

$$y'_{22n}(s) = y_{22n}(s) - jB_L y_d(s). \tag{5.5b}$$

Normally, $y_{11n}(s)$ and $y_{22n}(s)$ is one degree lower than $y_d(s)$, so B_S and B_L are expected to be zero. Now, all the frequency-independent terms have been extracted. The network is ready to calculate the couplings J_{Si} and J_{Li}. They are related to the residues directly by:

$$J_{Li} = \sqrt{r_{22i}}, \tag{5.6a}$$

$$J_{Si} = \frac{r_{21i}}{\sqrt{r_{22i}}}. \tag{5.6b}$$

Having N couplings from input and output, the transversal network topology seems to be impractical to realize in AW technology, but it can be transformed to a more convenient configuration. The use of this topology is developed in the following sections.

5.2 Class I Mixed-Topology Filters Made of an Inner Parallel-Connected Structures

The proposed synthesis combines transversal networks and the extracted-pole technique to create mixed-topology fully canonical filters with dangling resonators. Figure 5.2 describes the general scenario where the network is made of input and output inline sections connected to a central transversal network. The equivalent scheme in AW technology is depicted in Figure 5.3. There exist two ways to integrate the inline sections with the transversal structure. The first of them is to join them at the NRN of the last dangling resonator as shown in the left inline section in Figure 5.2. In practice, it means this AW resonator will be shunt. In the second option, an FIR is created at the transversal structure side, coupling to the inline section through an admittance inverter, as can be seen in the right inline section. The FIR will be transformed into a reactive element in shunt configuration and connected to ground like Figure 5.3 shows. That means, the AW resonator before the parallel-connected structure will be series.

The extraction procedure starts from the outside in, moving further from source and load nodes, until reaching the transversal section. In the following, it is described the extraction and reconfiguration stages that must be considered for the network synthesis, starting first with the inline sections and moving to the parallel-connected structure afterward.
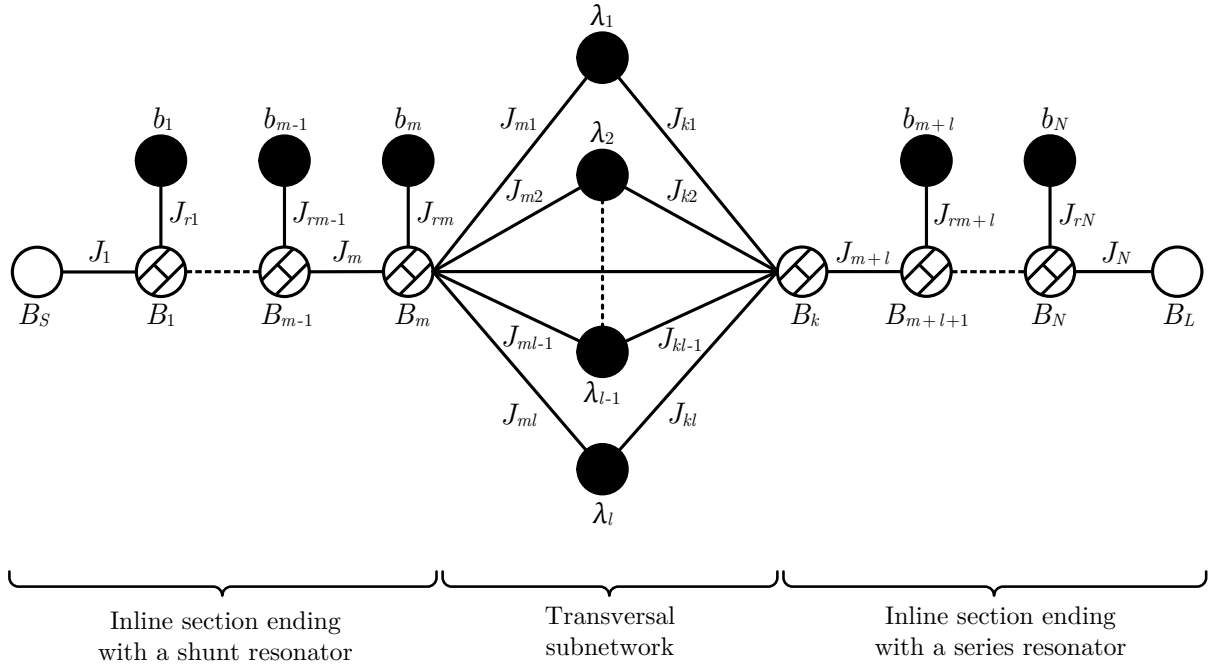
Figure 5.2: General Nth-order mixed-topology class I filter. The network is divided in three parts, two inline sections flanking the center part made of fully canonical transversal structure with l dangling resonators.

5.2.1 Inline Sections

The extraction procedure is done by an iterative process from the ABCD transfer matrix with the method described in Chapter 3. As mentioned before, the extraction process is done from the outside in. Beginning from the source node and using the general scheme in Figure 5.2, the extraction process is carried out as usual until the mth resonator (see Figure 5.4). Once the transversal section has been reached, the extraction of the junction node has to be done. If the dangling resonator m is meant to be a shunt AW resonator, only B_m is necessary to extract it with (5.7).

$$B_m = \frac{D_1(s_i)}{B_1(s_i)} \tag{5.7}$$

The polynomials $D_1(s_i)$ and $B_1(s_i)$ belongs to the matrix $ABCD_1$ in Figure 5.4. The frequency variable s_i should be one of the TZs not already assigned to the resonators in the inline sections. For simplicity, it could be taken as $s_i = j\Omega_{m+1}$, although any of the TZs that remain to be annihilated from $P(s)$ are eligible. Next, the process is repeated from load node to the closest resonator to the transversal subnetwork, extracting the junction in the same manner as in the previous case. If the resonator is intended to be implemented as a series AW, an additional admittance inverter is required for its serialization, like in Figure. 5.5. However, the standalone FIR will implement a reactive element. To accommodate the inline section in phase with the transversal one, only a fraction of the partial extraction is assigned to the NRN
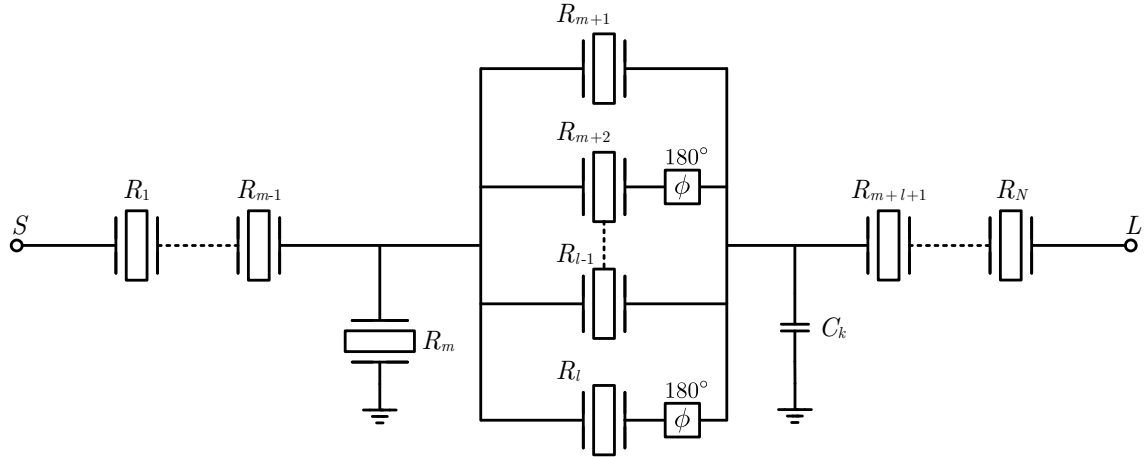
Figure 5.3: General Nth-order mixed-topology transversal array with N TZs in AW technology. The network is divided in three parts, the inline parts are formed by extracted-pole sections, and the center part is a fully canonical transversal structure generating l TZs. In a real design, part of the resonators in the transversal structure will require a $180°$ phase shift.
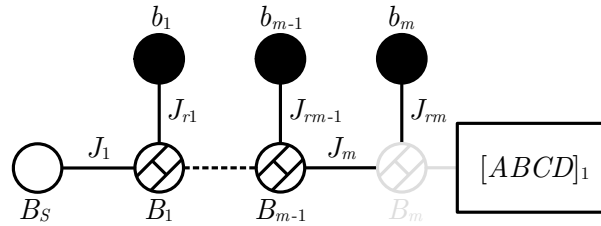
Figure 5.4: Nodal scheme of the network extracted from source node to the mth resonator. The FIR B_m in grey color is the next element to be extracted that, at this point it is part of the remaining $[ABCD]_1$.

B_k as follows:

$$B_k = \alpha \frac{D_2(s_i)}{B_2(s_i)}, \tag{5.8}$$

where α is the setting factor for the portion assigned to B_k that can be any arbitrary percentage. The polynomials $D_2(s_i)$ and $B_2(s_i)$ belong to the matrix $ABCD_2$ in Figure 5.4. The ABCD network has to be updated with (3.34). Finally, a unitary admittance inverter is extracted with (3.35). The non-extracted portion of B_k will be in the remaining ABCD network, and it will appear in the central transversal structure. The final aspect of the network at this stage of the process is represented in Figure 5.6, where both inline sections have been completely extracted.

5.2.2 Parallel-Connected Sections

The matrix $[ABCD]_{rem}$ is implemented as a fully canonical transversal network before being transformed into a parallel-connected structure. To be synthesized, the ABCD matrix is converted to an ad-
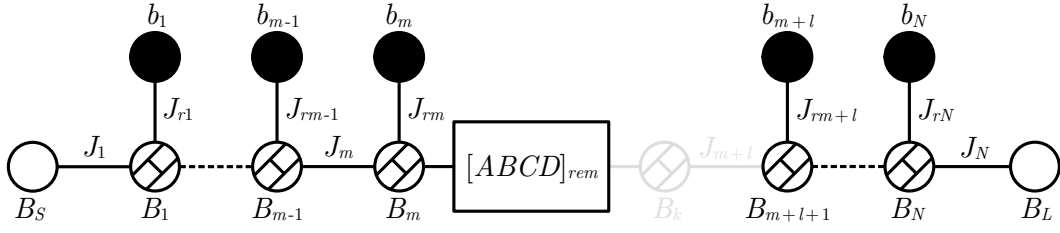
Figure 5.5: Nodal scheme of the network extracted from load node to resonator $m + l + 1$. The FIR B_k and admittance inverter J_{m+l} in grey color are the next elements to be extracted, but at this point, they are part of the remaining network $[ABCD]_2$.
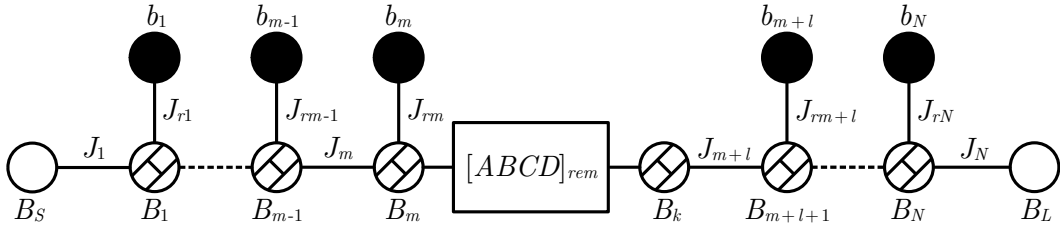
Figure 5.6: Nodal scheme of the network after the extraction of both inline sections. The remaining network in $[ABCD]_{rem}$ is the central transversal sub-network.

mittance matrix $[Y_{rem}]$ using the classical conversion formulas for two-port networks [93]. It can be expressed in terms of its residues in a similar form to (5.1) by

$$[Y_{rem}] = \frac{1}{y_d(s)} \begin{bmatrix} y_{11n}(s) & y_{12n}(s) \\ y_{21n}(s) & y_{22n}(s) \end{bmatrix} = j \begin{bmatrix} B_m & J_{mk} \\ J_{mk} & B_k \end{bmatrix} + \sum_{i=1}^{l} \frac{1}{(s - j\lambda_i)} \begin{bmatrix} r_{11i} & r_{12i} \\ r_{21i} & r_{22i} \end{bmatrix}, \qquad (5.9)$$

where the order of the sub-network is $l = k - m$. That is, the number of resonators between resonator m and k in Figure 5.2.

To transform this section into a parallel-connected configuration, the transversal sub-network must be split in as many branches as eigenvalues; they will be used to form a dangling resonator between admittance inverters by circuital transformation where each resonator resonates a finite frequency. The basic structure to carry out the transformation is named singlet, along with the dangling resonator, it is capable of producing TZ at finite frequency. It is made of three nodes: a resonant node and the outer FIRs at the input and output terminals. The nodes are coupled to each other by admittance inverters, two connect the resonant node to the other two, and the third inverter is a direct coupling between input and output nodes. The equivalence of the singlet and the dangling resonator is depicted in Figure 5.7.

Together with the eigenvalues, the input-to-output coupling J_{mk} plays an important role in the definition of the resonance frequency of the resonators in each branch. In order to implement them, a direct source-to-load path at each branch is required. A good follow-up strategy to assign a specific portion of J_{mk} to each split is to compute it from the desired normalized resonance frequencies of the dangling resonator b_i. Using the equations in Appendix B, that relates the singlet and dangling structures between admittance inverters, the mathematical expression of the input-output coupling can be defined for all l
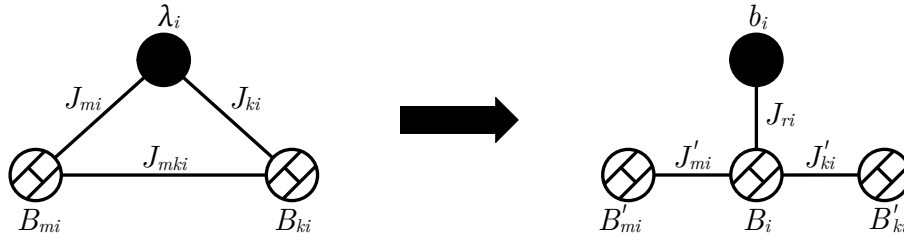
Figure 5.7: Equivalent nodal scheme of a singlet and a dangling resonator structure.

branches as

$$J_{mki} = -\frac{J_{mi}J_{ki}}{(b_i - \lambda_i)}. \tag{5.10}$$

Notice that b_i can be set arbitrarily. The equation not only establishes a relationship between eigenvalues and resonance frequencies but allows to disassociate the resonators from the TZs generated by the whole filter. However, not every resonance frequency can be chosen freely. In order to not alter the network, up to $(l-1)$ resonance frequencies can be determined with (5.10). Otherwise, the sum of all J_{mki} would not equal to J_{mk}. Because of that, the coupling assigned to the lth resonator must be the remaining coupling after subtracting the sum of the rest. The value of this input-to-output coupling can be computed as follows:

$$J_{mkl} = J_{mk} - \sum_{i=1}^{l-1} J_{mki}. \tag{5.11}$$

In turn, J_{mki} is directly related to the NRN of the resonators $m + 1$ to l, as can be seen in (5.12).

$$B_i = -\frac{J_{mi}/J_{ki}}{J_{mki}} \tag{5.12}$$

The admittance matrix for each branch is defined as

$$[Y_i] = j \begin{bmatrix} B_{mi} & J_{mki} \\ J_{mki} & B_{ki} \end{bmatrix} + \frac{1}{(s - j\lambda_i)} \begin{bmatrix} r_{11i} & r_{12i} \\ r_{21i} & r_{22i} \end{bmatrix}. \tag{5.13}$$

Every $[Y]_i$ matrix is turned into an $[ABCD]_i$ matrix using the classical two-port network conversion equations. Then, they are extracted as inline networks using the process described in Chapter 3. The roots of polynomials $P_i(s)$ determines the resonance frequency of the resonators at each branch, which meets with the b_i selected in (5.10). After all individual extractions have been carried out, the final form of the central section is depicted in Figure 5.8. As last step, all branches are merged together from their input and output nodes. Then, they are joint to the rest of the network to form the whole filter. To validate the synthesis methodology, a numerical example is provided in Section 5.4. In addition, a experimental validation is provided in Appendix C.
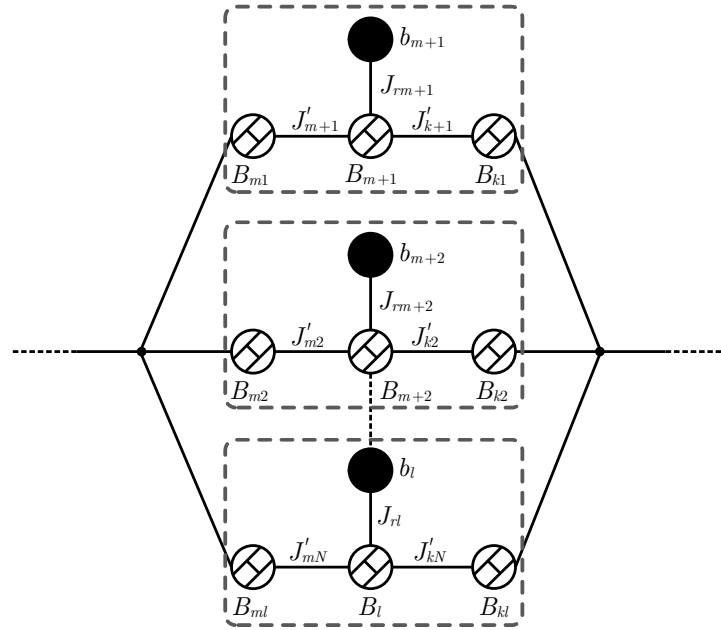
Figure 5.8: Central transversal sub-network after the transformation to dangling resonators between admittance inverters of each eigenvalue.

5.3 Considerations for the Design of Feasible Class I Filters in AW Technology

In this section, the different aspects to be taken into account in order to produce a lowpass network that could be turned into a realizable filter with acoustic wave technology are discussed.

5.3.1 Selection of Resonance Frequencies for the Parallel-Connected Sub-Network

As mentioned previously, the TZs implemented by the transversal network do not necessarily meet the resonance frequency of the resonators implemented by the parallel-connected section. According to (5.10), they can be chosen without restriction to meet the design requirements. One of the stated advantages of the proposed method is precisely the freedom to choose both the TZs and the resonance frequencies of the resonators that form the parallel-connected structure. Nevertheless, those dangling resonators between admittance inverters are going to be implemented as series AW resonators.

The electrical branch of AW resonators can be modeled with a static capacitor. In the lowpass prototype, the equivalent dangling resonator between admittance inverters requires a negative NRN value upon the circuital transformation if they are to be the static capacitance of a BVD resonator afterward. To force that parameter to be negative, the NRN B_i value is computed with (5.12), where J_{SLi} depends directly on the eigenvalue λ_i and the desired resonance frequency in (5.10). To always assure a negative NRN value, the denominator in equation (5.10), $(b_i - \lambda_i)$ must be negative.
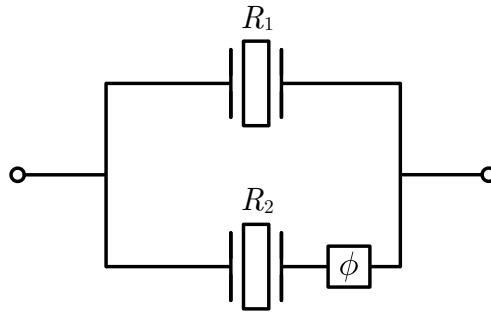
Figure 5.9: An all pole 2nd-order AW filter with a phase shift in the lower branch.

The source-to-load admittance inverter is inversely proportional to the difference between the resonance b_i (roots of $P(s)$) and the eigenvalue λ_i (roots of $B(s)$). However, strong couplings mean resonance frequencies moved far away from the center frequency. The narrow-band characteristic of the frequency transformation implies that the further a resonance frequency is from the center one, the impact of the transformation deviations is more significant. In any case, the sign of the J_{SLi} coupling must be positive in series resonator in order to obtain a negative NRN. Evidently, how the overall source-to-load coupling is shared will impact all the resonators, requiring more effort for a whole tune. Adjusting it, the static capacitance can also be tuned. This means that, by extension, the NRN is also related to the electromechanical coupling coefficient k_{eff}^2 of an AW resonator, so it should be chosen carefully.

5.3.2   Serialization of the Parallel-Connected Resonators

This circuital transformation requires the dangling resonators, in the parallel-connected branch, to be placed between two admittance inverters with the same value and opposite sign (see Chapter 4). The sign is dependent upon the associated residues to an eigenvalue within the transversal network. Such alternation is only achieved if the residues also show that characteristic. The eigenvalues represent the odd and even modes of the transversal coupling matrix. The even-mode eigenvalues associated residues are of equal sign. Meanwhile, odd-mode eigenvalues present alternation in sign. Generically, an Nth order transversal network possesses the same quantity of even-odd eigenvalues pairs if the N is an even number, or $(N + 1)/2$ odd modes and $(N - 1)/2$ even modes, in case of an odd order filter.

Therefore, not all dangling resonators created in the parallel-connected section can be directly turned into AW series resonators. The physical implementation of those created from even-mode eigenvalues will require a $180°$ phase shift. In AW technology, this structure is one of the filtering networks that has been defined in the patent proposal [94], where its authors propose a phase shift made of metamaterials and a microstrip delay line as possible solutions. This can be seen in Figure 5.11, where the response of a 2nd-order filter in Figure 5.9 with a phase shift in the lower branch is depicted. The filter provides a response without TZs at finite frequencies with 48 MHz bandwidth and return loss $RL = 13$ dB.
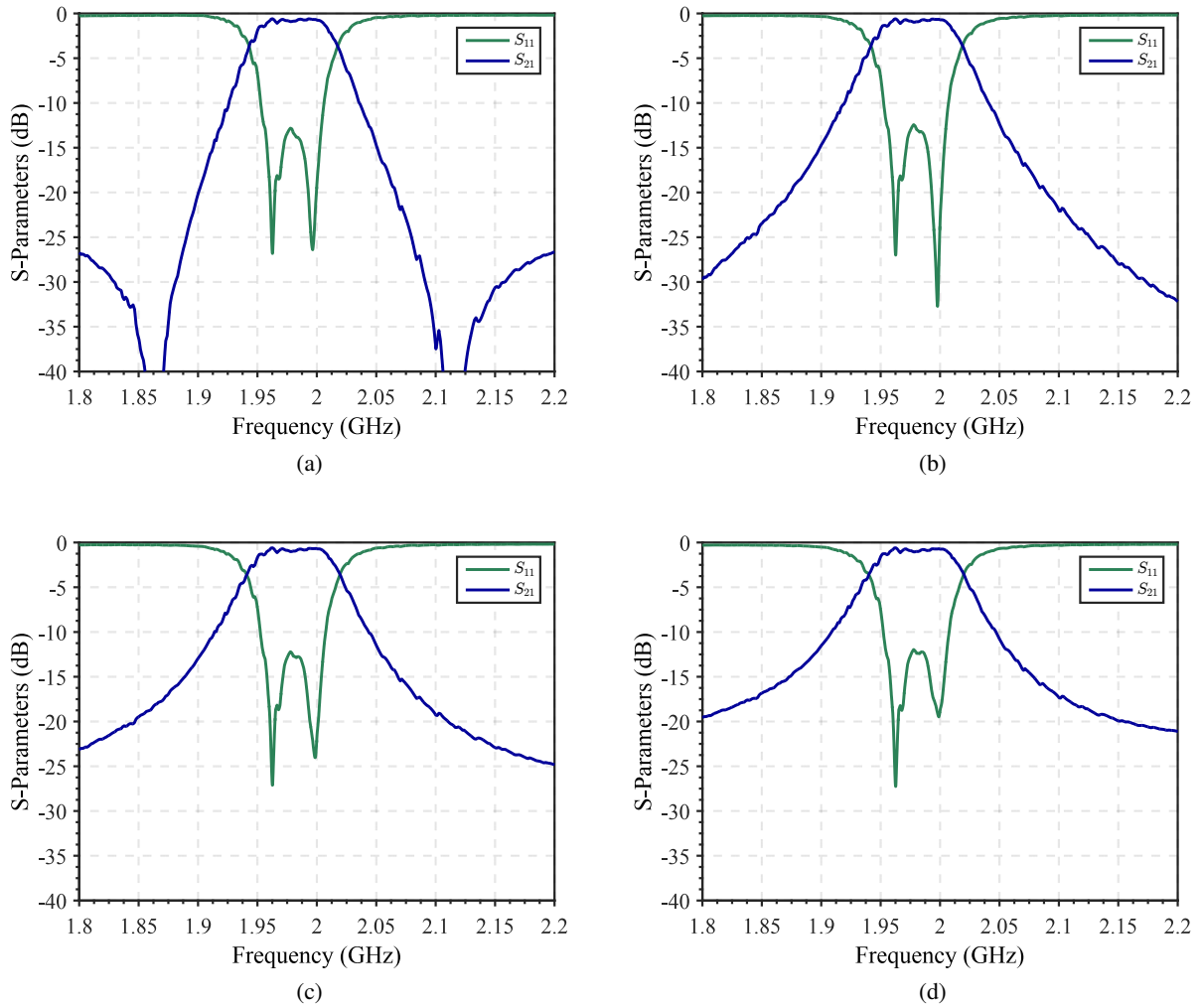
Figure 5.10: Response of a 2nd-order filter with four different ideal phase shifts: (a) 170°, (b) 180°, (c) 185° and (d) 190°.

The resonators employed are BAW-SMR using AlN as a piezoelectric material. The first resonator shows a resonance and anti-resonance frequency $f_{r1} = 1.962$ GHz and $f_{a1} = 2.018$ GHz, respectively. The resonance frequencies of the second resonator are $f_{r2} = 1.908$ GHz and $f_{a2} = 1.962$ GHz. An even-mode and odd-mode eigenvalues form this network. Therefore, when both are directly connected in a transversal configuration, the network is not fully synthesized. A 180° phase shift is required in the lower branch for proper implementation of the filter in Figure 5.9.

The network is very sensitive to phase deviations in any of its branches. In Figure 5.10, four scenarios are considered for the 2nd-order filter, an ideal phase shift with values 170°, 180°, 185° and 190°. In Figure 5.10a, it can be appreciated the appearance of two TZs by just a 10° difference from the filter with a 180° phase shift in Figure 5.10b. The cases in Figures 5.10c and 5.10d shows a worse OoB rejection level at both sides of the band and a slight deterioration of the RL.
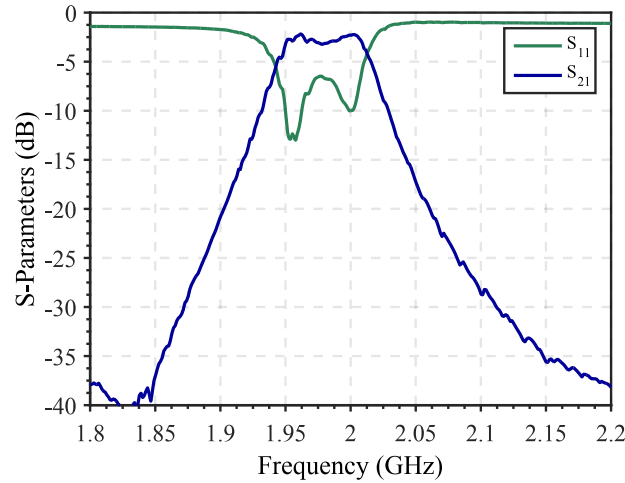
Figure 5.11: 2nd-order filter response with a phase shift implemented with the commercial balun model HHM1534.

These results suggest that even a small deviation from the nominal value may be very damaging for the filter response, but adjusting it could be useful to tune the location of the TZs in further stages of the design process. Nevertheless, these cases consider ideal phase shifts that introduce a constant phase over all frequency spectrum. Using a commercial balun having a $180°$ phase shift does not assure a perfectly matched filter either. Figure 5.11 shows the same filter but implementing the phase shift with a balun HHM1534 by TDK that shows an IL= 0.5 dB, a $5°$ phase balance and amplitude balance of 0.7 dB within a frequency range between 1.700 MHz to 2.300 MHz. The phase unbalance introduces an evident response deterioration in comparison with the ideal phase shift. Although it can be considered adequate for illustration purposes, the phase error within the bandwidth range should be considered due to the high sensitivity of the network.

5.3.3   Junction Nodes

By choosing a shunt resonator as the last one before the parallel-connected structure, the NRN can assimilate the FIR. Hence, no reactive element is necessary. For example, the NRN B_m value in Figure 5.2 is the combination of the initially extracted B_m and the sum of all series dangling in parallel from the central structure. This situation can be seen in Figure 5.12, where the FIRs in the left colored area is at the same node. Therefore, the FIR B_m is computed by

$$B_m = B'_m + B_{m1} + B_{m2} + \cdots + B_{mN}. \tag{5.14}$$

However, when the adjacent resonator to the parallel-connected structure is series, the extraction of an admittance inverter is required. Consequently, an new FIR to ground appears in the common node of the parallel-connected resonators.
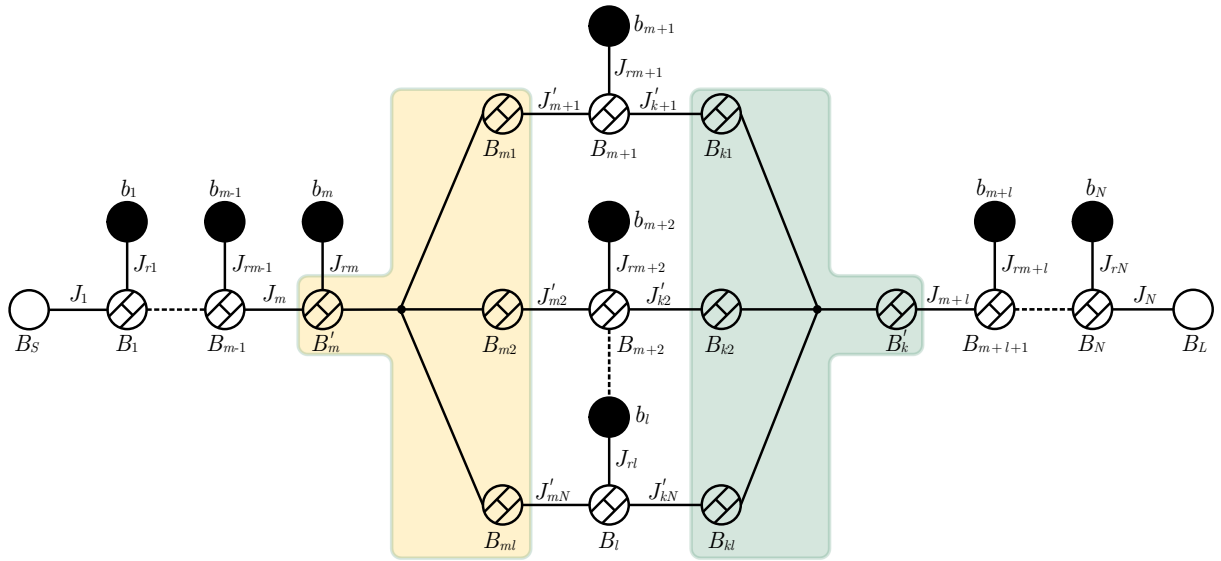
Figure 5.12: An inline section in the left, joint to the parallel-connected structure directly to the NRN of the last dangling resonator. On the right side, the inline section is connected to a junction element. The FIRs in the colored areas at the same node, the inside black lines that do not possess a label, are just connecting lines instead of admittance inverters.

Such case can be observed in the right colored area in Figure 5.12, wherein the junction node B_k is computed by

$$B_k = B'_k + B_{k1} + B_{k2} + \cdots + B_{kN}. \tag{5.15}$$

Figure 3.10 illustrates that if such element is positive, it may be implemented as a capacitor, or an inductor otherwise. Despite being necessary for an exact network synthesis, the inclusion of this element may introduce more difficulties in the fabrication process by increasing the physical network complexity. In case of requiring a series resonator, the FIR could be possibly eliminated during the design by selecting an adequate splitting factor α (5.8) to turn its value to zero. Although it may not be affordable in some situations, it could be minimized enough to make it negligible. Alternatively, a phase correction of the polynomial phase, as proposed in Chapter 4, can be employed to overcome this limitation, although no predictable model or conic section resemblance has been found for this kind of topologies.

5.4 Numerical Example

To validate the synthesis methodology, a numerical example is provided in this section. Additionally, the requirements exposed in Section 5.3 are also discussed. The network is a 5th-order Chebyshev fully canonical filter with 2 TZs in the lower passband and 3 TZs in the upper side of the passband. The transmission zeros of the filtering function are $\Omega_{tz} = \{2, 1.5, -2, -1.6, 2.5\}$ rad/s and $RL = 20$ dB. The lowpass prototype filter configuration is depicted in Figure 5.13.
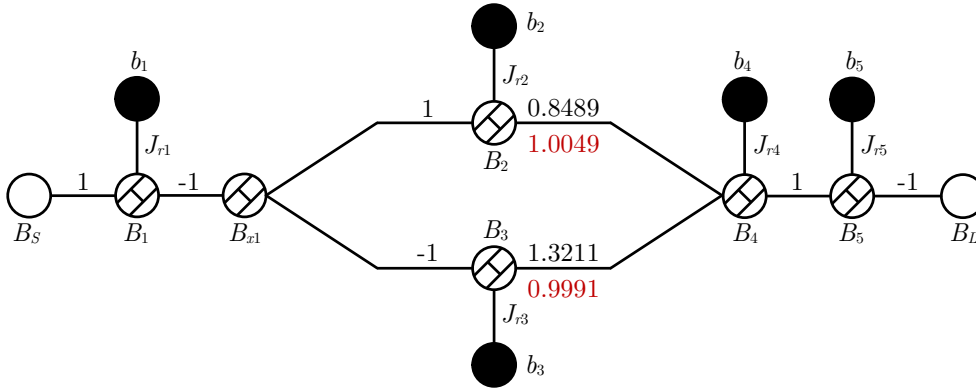
Figure 5.13: 5th-order mixed-topology fully canonical filter. The admittance inverter values are in black, the values after the phase adjustment in resonator 3 and 4 are displayed in red.

Table 5.1: Synthesized characteristic polynomial coefficients of the 5th-order filter.

Degree	$F(s)$	$E(s)$	$P(s)$
5	1	1	j
4	$-0.2397j$	$1.9991 - 0.2431j$	2.4
3	1.3354	$3.3383 - 0.4907j$	$6.65j$
2	$-0.2631j$	$3.2599 - 0.8020j$	15.6
1	0.3788	$2.2170 - 0.6671j$	$10.6j$
0	$-0.0433j$	$0.8497 - 0.4462j$	24

The parallel-connected section comprises resonators 2 and 3. These are the ones in which resonance frequency can be selected independently from the TZs set. The left inline section is made of a single resonator between admittance inverters with the same value and opposite sign that will implement a series AW resonator. The resonator is connected to the central section by an FIR B_{x1}. Finally, the right section is conformed by two resonators with no extra elements. The characteristic polynomials are listed in Table 5.1.

The synthesis begins from source node to the junction element after resonator 1. Then, the second inline section is extracted from load to resonator 4. After this step, all elements in the inline sections have been obtained. The remaining part of the filter is implemented as a transversal sub-network that contains two eigenvalues (an even-mode and a single odd-mode), and its respective couplings. This sub-network is split in two branches to implement dangling resonators $k = 2, 3$. It can be seen in Table 5.2 that those resonators present a negative FIR value B_k, in agreement with the capacitive nature of the element for acoustic wave technology since they will be serialized. The junction element $B_{x1} = 1.8098$ has been chosen by setting $\alpha = 0.316$. It is a positive value. Therefore, it will turn into a shunt capacitor to ground.

The input-to-output coupling of the transversal network is divided in two using equations (5.10) and (5.11) for resonators 2 and 3, respectively. The resonance frequency of the upper branch resonator is denoted by the constant susceptance $s = -jb_2$. In this example, the value has been arbitrarily chosen

to be $b_2 = -0.5$. Since only one can be set freely, the lower branch resonance frequency is indirectly determined by the one in the upper branch. For resonator 3 is $s = -jb_3$. The rest of the extracted elements are provided in Table 5.2. As shown in Figure 5.13, the admittance inverters associated to resonator 2 are 1 and 0.84896. Meanwhile, the admittance inverters of resonator 3 are 1 and 1.3211.

Table 5.2: 5th-order lowpass filter elements made with a central parallel-connected section between resonators 2 and 3.

	$\psi = \phi = 0°$			$\psi = 14.68°, \phi = 68.96°$		
	B_k	b_k	J_{rk}	B_k	b_k	J_{rk}
Res. 1	-0.6451	-2.0000	1.4530	-0.2300	-2.0000	0.6893
Res. 2	-5.1024	-0.5000	2.8312	-4.1365	-0.5000	2.4437
Res. 3	-3.9877	-1.2922	1.8477	-2.2479	-1.2852	1.2946
Res. 4	1.6713	1.6000	1.5105	1.8779	1.6000	1.6174
Res. 5	-1.7608	-2.5000	2.0722	-1.6551	-2.5000	1.9353
B_S	-0.6181			-2.2674		
B_L	-0.4531			-0.6179		
B_{x1}	0.5909			1.8098		
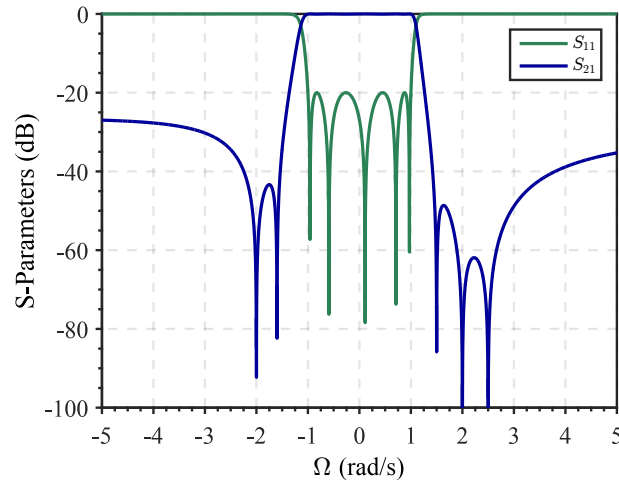
Figure 5.14: 5th-order filter lowpass response made with a parallel-connected section between resonators 2 and 3.

Note that resonator 2 is created from an even-mode eigenvalue, and it will require a $180°$ phase shift. Moreover, none of the resonators are placed between unitary admittance inverters. To equalize them, a phase correction can be applied to the characteristic polynomials using the asymmetric polynomial definition. The new values are 1.0049 and 0.9991. The final network scheme is depicted in Figure 5.13. Now, they are sufficiently equalized to not affect the filter response significantly. The network elements with the phase correction are listed in Table 5.2. Finally, the response of the filter is shown in Figure 5.14.

5.5   Class II Mixed-Topology Filters Made of Source-Load Parallel-Connected Structures

The second topology class consists in the transversal network to create a parallel-connected structure that represents the filter in Figure 5.15. The proposed synthesis begins directly with the lowpass Nth-order transversal network, as shown in Figure 5.1. It is split in two main branches, one will be used to implement a classical ladder topology, and the second will form a transversal sub-network. In the latter, each resonant node (eigenvalues) will be employed to implement a set of series AW resonators in parallel-connected configuration. An illustrative diagram of the whole synthesis procedure is illustrated in Figure 5.16. The general admittance function of the filter can be expressed in a matrix format using the partial fraction expansions like in (5.1).
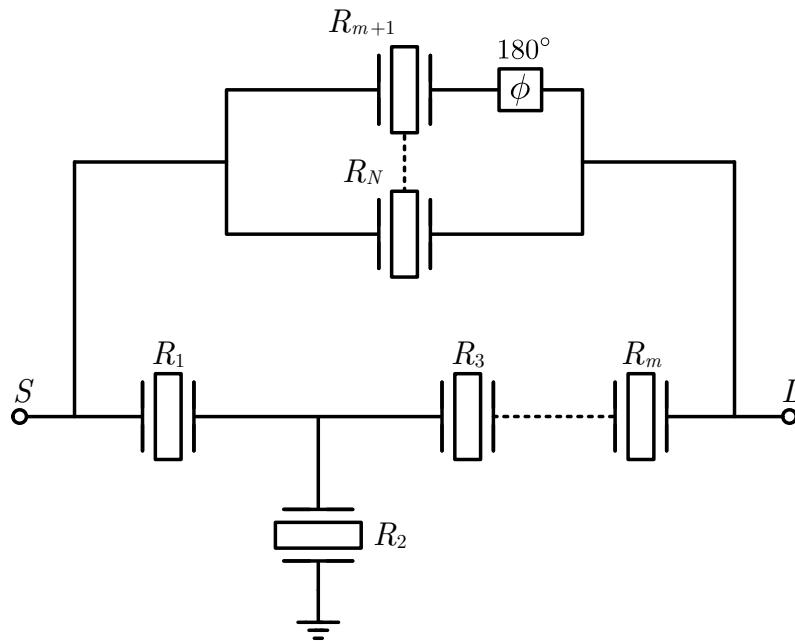
Figure 5.15: General scheme of a Nth-order mixed-topology filter in AW technology, made of m resonators in ladder configuration and $N - m$ array of transversal.

5.5.1   Series Resonators in Parallel Configuration

After splitting the transversal network, one branch configures an inline ladder sub-network with m eigenvalues. The remaining are allocated to implement single dangling resonators in parallel to each other. To configure them, the equivalent singlet requires a source-to-load path, the mathematical expression of the input-to-output coupling for each singlet J_{SLi} is the same as (5.11). As in the previous topology, b_i can be set arbitrarily too.
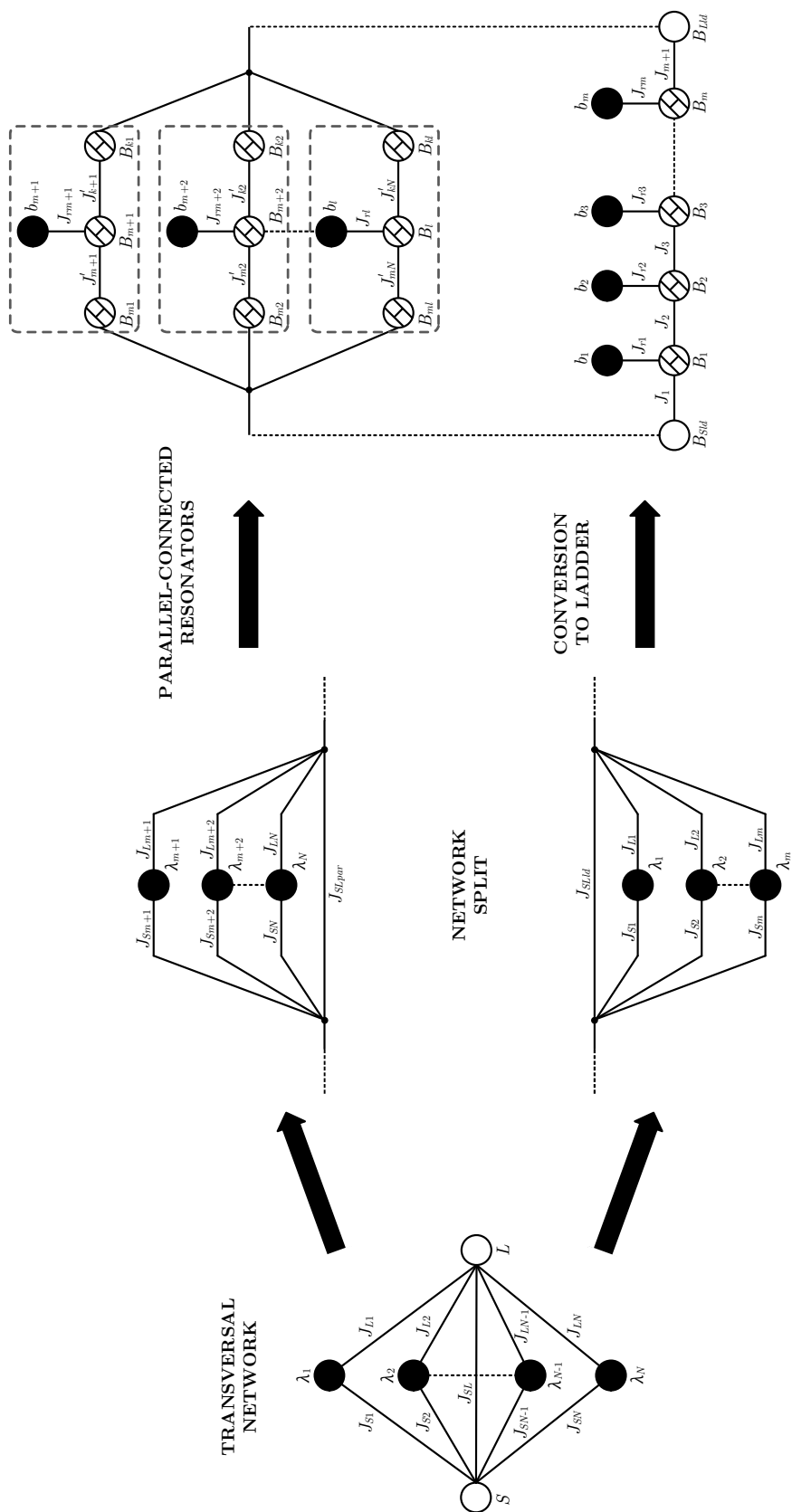
Figure 5.16: Overview of the Class II topology synthesis procedure.

5.5.2   Synthesis of the Inline Lower Branch

The elements of the transversal network used to form parallel-connected series resonators are subtracted from the admittance matrix expression (5.9). The remaining input-to-output coupling and the elements from the transversal coupling matrix are assigned to the ladder sub-network, forming the matrix Y_{ld}. The coupling is computed as follows:

$$J_{SL_{ld}} = J_{SL} - J_{SLpar}, \tag{5.16}$$

where J_{SLpar} is the input-to-output coupling that results from the combination of all calculated partial couplings of the parallel-connected resonators conforming the transversal sub-network:

$$J_{SLpar} = \sum_{i=m+1}^{N} J_{SLi}, \tag{5.17}$$

being J_{SLi} the individual couplings required by the $N - m$ resonators in parallel. Next, the admittance matrix of the ladder sub-network Y_{ld} is defined as follows:

$$[Y_{ld}] = j \begin{bmatrix} 0 & J_{SL_{ld}} \\ J_{SL_{ld}} & 0 \end{bmatrix} + \sum_{i=1}^{m} \frac{1}{(s-j\lambda_i)} \begin{bmatrix} r_{11i} & r_{12i} \\ r_{21i} & r_{22i} \end{bmatrix}. \tag{5.18}$$

Once it is created, the inline network elements are extracted with the synthesis procedure in Chapter 3 as usual. Finally, each branch of the filter has its own input and output elements, required for a perfect phase matching. As the branches are joint from those nodes, the final network is assembled by merging into one the values of the individual parameters. To validate the synthesis methodology, a numerical example is provided in Section 5.7.

5.6   Considerations for the Design of Realizable Class II Filters in AW Technology

The topics discussed in Section 5.3 apply to this topology class too. However, in this context, the eigenvalues of the transversal network have to be distributed carefully among the different branches. In configurations like the described in Figure 5.16, a part of the network is used to implement a set of dangling resonators in parallel to each other. The ladder branch is built from the remaining values. Therefore, the extracted parameters of this sub-network cannot be controlled arbitrarily, and it may result in a network not suitable for AW technology. For instance, some eigenvalues configuration could require the ladder sub-network to synthesize a complex resonant frequency instead of purely imaginary, which cannot be physically implemented.

However, with a meticulous design, it is possible to find eigenvalue combinations that produce purely imaginary resonant frequencies. When more than one eigenvalue has to be gathered in the same group, it is recommended to assort the eigenvalues and their associated input-to-output couplings in complementary pairs within each group [46], in order to avoid complex roots. That is, if an odd eigenvalue and their couplings are selected to be part of one group, there should be an even eigenvalue in the same group.
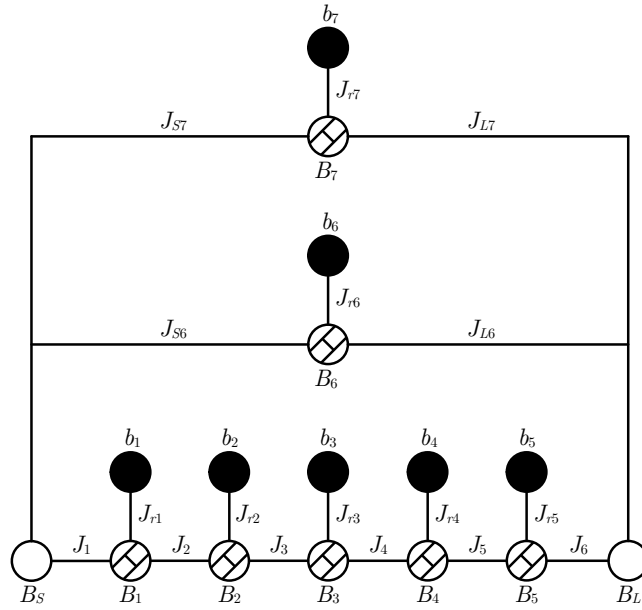
Figure 5.17: 7th-order mixed-topology fully canonical filter with two dangling resonator in a parallel-connected configuration from source to load nodes.

Alternatively, if the scenario cannot be avoided, the synthesis method described in Section 6.2 to realize complex resonance frequencies can be used, where a cross-coupling is introduced within the ladder network to turn the complex resonance frequencies to purely imaginary again without changing the TZs generated by the sub-network.

5.7 Numerical Example of a Class II Topology

In this section, an example is presented to demonstrate the capabilities of the method described for class II topologies. The design requirements exposed in Section 5.6 are discussed. The filter corresponds to a 7th-order Chebyshev fully canonical network. The transmission zeros are $\Omega_{tz} = \{-3, -2, 1.2, 1.2, 2.5, 1.8, 4\}$ rad/s and $RL = 20$ dB. The resonators from 1 to 5 are in ladder configuration. Meanwhile, resonators 6 and 7 are configured as series resonators in parallel. As shown, we configure five series resonators but only two parallel resonators. The nodal scheme of the lowpass prototype is depicted in Figure 5.17. The characteristic polynomials are listed in Table 5.3.

First, we obtain the transversal network elements, which values are shown in Table 5.4. Resonators 6 and 7 have been created using eigenvalues λ_3 and λ_4, respectively. Meanwhile, The rest are assigned to the ladder section. The input-to-ouput admittance inverter calculated with (5.10) for both parallel resonators are $J_{SL6} = -0.2371$ and $J_{SL7} = 0.1707$, using Ω_3 and Ω_4, respectively. The remaining coupling for the ladder branch is $J_{SL_{ld}} = -0.1709$. Notice that λ_4 is an even-mode. Therefore, resonator 7 will require a $180°$ phase shift.

Table 5.3: Synthesized characteristic polynomial coefficients.

Degree	$P(s)$	$E(s)$	$F(s)$
7	j	1	1
6	5.7000	$1.9715 - 1.2729j$	$-1.2729j$
5	$4.4400j$	$3.0906 - 2.5573j$	1.1471
4	69.0680	$2.7690 - 4.3707j$	$-1.8024j$
3	$-77.3520j$	$1.4517 - 4.3675j$	0.1130
2	145.8720	$0.0776 - 3.1505j$	$-0.6032j$
1	$-317.0880j$	$-0.4715 - 1.3350j$	-0.0848
0	-155.5200	$-0.2433 - 0.2235j$	$-0.0233j$

Table 5.4: Transversal elements of the 7th-order network.

i	λ_i	J_{Si}	J_{Li}
1	-0.1919	0.4875	0.4875
2	0.5235	-0.4106	0.4106
3	0.9066	0.2848	0.2848
4	-0.9436	-0.4730	0.4730
5	1.0874	-0.3133	0.3133
6	1.0958	0.2774	0.2774
7	-1.2048	0.3155	0.3155
J_{SL}	0.0011		

Table 5.5: Lowpass elements of the synthesized 7th-order filter.

Parameters	B_i	b_i	J_{ri}
Res1	-0.4139	-1.2000	0.2554
Res2	8.1785	0.6594	2.1787
Res3	-0.0843	-1.1376	0.4509
Res4	0.1357	2.0635	5.4688
Res5	-0.0741	-0.8330	0.0885
Res6	-3.6182	-1.2000	1.0303
Res7	-9.5797	-1.2000	4.5316
B_S	-2.4524		
B_L	-0.5272		
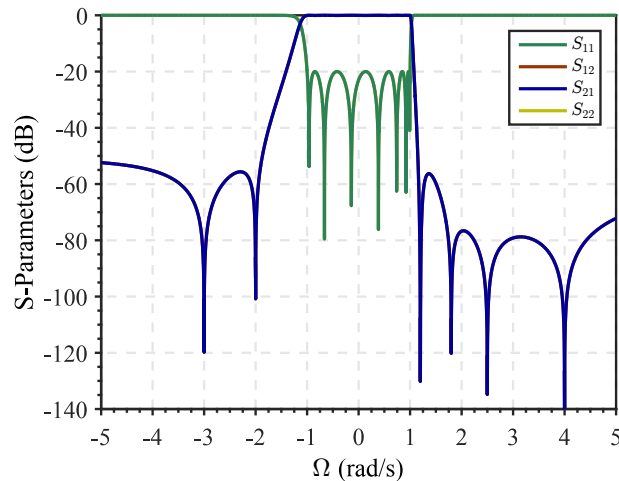
Figure 5.18: Lowpass response of the 7th-order filter.

After defining the expressions of each branch, the ladder section is extracted by synthesis, and the series resonators in parallel are obtained using the circuital transformation. The network elements are listed in Table 5.5. Notice that the resonance frequencies of resonators 6 and 7 have been chosen to meet with Ω_3 and Ω_4. However, the resonance frequencies of the resonators in the ladder branch are not the remaining prescribed TZs anymore. They are fully determined by the $P(s)$ polynomial of the ABCD matrix defined for the ladder sub-network.

From the filter response shown in Figure 5.18, it is confirmed that the TZs are created at their prescribed location despite the aforementioned different resonance frequencies. It can also be noticed that five TZs have been generated on the upper side of the band, thus achieving a good OoB rejection. Finally, the denormalization and bandpass transformation will follow the same procedure laid out in [77].

5.8   Chapter Summary

The use of mixed-topology improves the flexibility in filters design. This chapter presents a synthesis method that combines inline and parallel-connected structures to create ladder-like fully canonical filters based on acoustic wave technology. Two topologies classes have been presented, one consists of a parallel-connected section flanked by two inline ladder sections. The other is made of two branches, one implemented as a parallel-connected sub-network and the other as a classic ladder network.

The parallel-connected section of the filters provides a degree of freedom by disassociating the resonance frequency of a dangling resonator from the TZs of the filtering function. This kind of topology allows implementing filter responses with steeper roll-off in one of the sides of the passband than a ladder filter of the same order. Also, the degree of freedom to select the resonance frequency independently can be useful to find suitable parameters to accommodate the technology constraints. A guidance to orient the synthesis of the lowpass network toward a feasible filter in AW technology has been provided. To illustrate the synthesis method, the extraction process of two filters has been detailed.

Synthesis of Ladder Filters with Multiple Cross-couplings

Once the synthesis technique for the design of ladder-type filters has been introduced in Chapter 3. The design of AW filters has moved a step forward by presenting the synthesis of mixed-topology filters based on acoustic resonators. The new topologies in Chapter 5 describe filters that combines ladder and transversal network by organizing the AW resonators in a non-conventional way. In contrast, this chapter focus only on a ladder topology with cross-coupling configurations. These filters consists of circuits with bypassing couplings between non-contiguous resonators or coupled with reactive elements.

In bandpass filters, external elements like inductors and capacitors are added to the network in order to achieve a better performance, and also for better accommodation of the technology constraints. Without a general method, these elements are not extracted during the synthesis but added to the synthesized network afterward. Consequently, the original filter response is degraded up to a certain extent. Recovering the original characteristics and maintaining the advantages introduced by the additional elements requires a time-consuming optimization process with a high computational cost.

There are some structures that have been proved to be useful for which a systematic synthesis method has not yet been developed, specifically those shown in Figure 6.1. They are a sample of two generic types of configuration, filters with Ground-Loop Inductor (GLI) couplings, and filters with L-C inter-resonator couplings (LCC). Both types of structures were issued in the patent [95].

Direct addition of reactive cross-couplings may cause a negative impact to the filters like TZs detuning and in-band return losses degradation. However, the reactive elements help to introduce an additional TZ in a region far away from the passband without introducing an extra pole. The immediate effect is a significant improvement of the rejection level, attaining higher levels of isolation between bands in case of multiplexers.
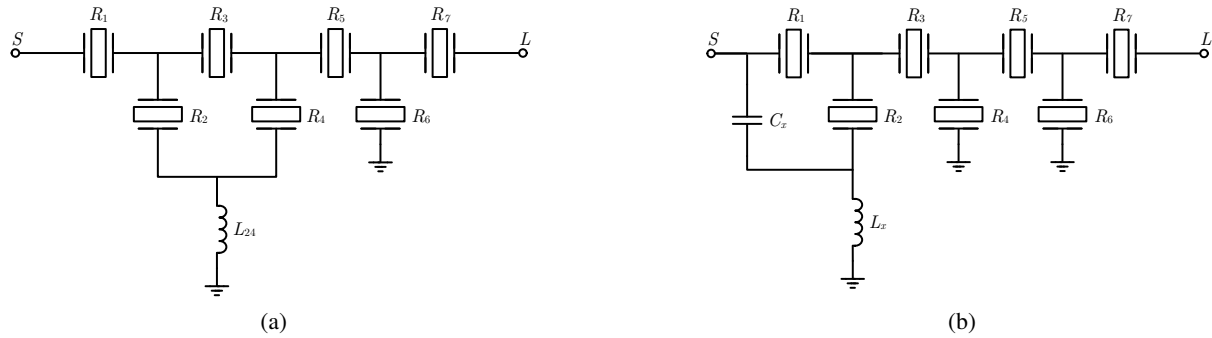
Figure 6.1: Examples of cross-coupled networks. The filter (a) represents a GLI and (b) is a filter with a LCC coupling.

These effects can be seen clearly in Figure 6.2, where three simulation cases are presented to illustrate them. Figure 6.2a shows the S-parameter comparative of a classic ladder filter with seven TZs and the same filter with an additional 0.15 nH inductor, coupling resonators 2 and 4 to ground like in Figure 6.1a. This element produces the detuning of the TZs at each side of the passband. Those above are moved toward the same frequency, and those located below are moved away from each other. Nevertheless, it can be noted that a new TZ appears at 2.24 GHz, improving the rejection level in the OoB region above the passband more than 20 dB. The second case in Figure 6.2b corresponds to an LCC in which a capacitor $C_X = 0.3$ pF and an inductor $L_X = 0.8$ nH between source and the second resonator like in the scheme shown in Figure 6.1b. The effects, in this case, are again the TZs detuning and the appearance of a new TZ at 2.26 GHz. The achieved level in the OoB region above the passband is below -80 dB. The TZs detuning on both sides of the passband also increases the rejection level in the lower side. In both cases, GLI and LCC, there is a slight degradation of the in-band return losses band, but the gain obtained in terms of rejection level is far superior.

The cross-coupled topologies can also be useful to model and explain the origin of undesired couplings like an electromagnetic feedthrough bypassing the package ports in the design of filter based on acoustic wave resonators which may cause a severe limitation of cross-isolation levels in multiplexers, a degraded response and transmission zeros vanishing in standalone filters. This phenomenon has been well documented in [18, 59, 80, 96].

The limiting factors can be classified in two types of signal leakage: one occurs via the main signal path due to the finite impedance of the RX filter in the TX band in a duplexer; the second one is due to ElectroMagnetic Feedthrough (EMF), electromagnetic couplings or imperfect grounding.

The aim of this chapter is to take advantage of the capabilities of the synthesis techniques described in Chapter 3 and 5, to obtain the exact lowpass prototype network ready to implement three types cross-coupled standalone filter structures in a general way without requiring optimization. The cross-coupled topology that models the EMF derives directly from the synthesis method for cross-coupled filters described in Chapter 3. However, the developed procedure for GLI and LCC topologies addresses the
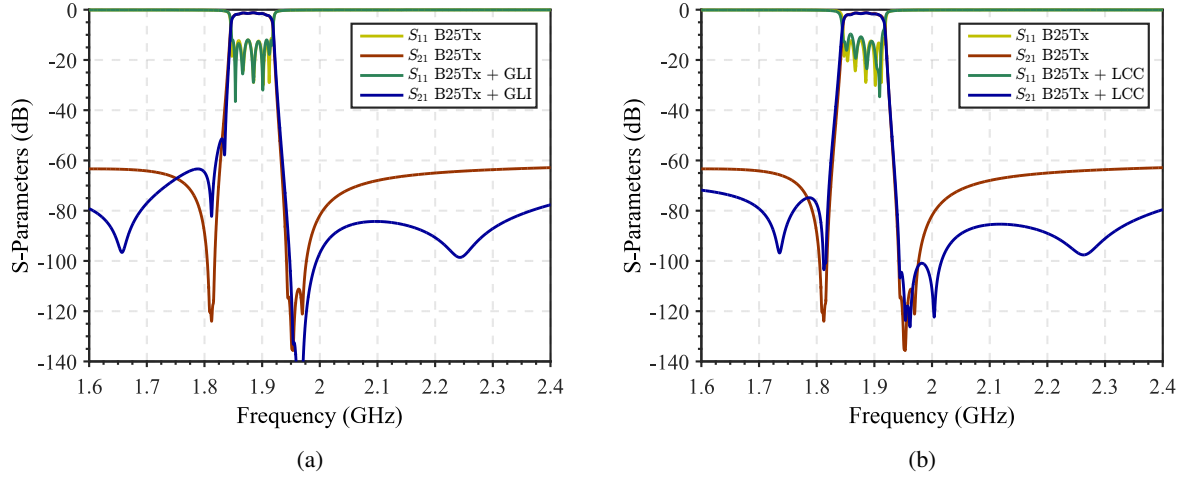
Figure 6.2: Simulation of the 7th-order filter with three different configurations: a plain ladder, the same filter in GLI configuration with an additional inductor $L_{24} = 0.15$ nH coupling resonators 2 and 4 (see Figure 6.1a) (a), and the ladder filter with in LCC configuration (b) with a capacitor $C_X = 0.3$ pF and an inductor $L_X = 0.8$ nH between source and resonator 2 like in Figure 6.1b.

synthesis of prototypes filters based on a mixed-topology extraction. The basic principle is the same described in Chapter 5, where it was used to define new topologies. But for this case, it is applied to generate cross-coupled filters that retain their ladder structure while aggregating reactive elements to the network. Part of the content in this chapter has been published by the author in [97].

6.1 Filters with Reactive Element Cross-Couplings

In this section is proposed a systematic methodology to obtain the exact lowpass prototype configuration of GLI and LCC structure types in a general way. The developed procedure is based on the theory described in Chapter 5, which combines inline ladder networks with parallel-connected structures. The methodology provides the exact resonator parameters required to maintain the frequency position of TZs for ladder acoustic wave filters while generating the reactive elements within the network.

6.1.1 General Synthesis Procedure

The general scenario is similar to the class I topology in Section 5.2, where the network is made of a central transversal network connected to inline sections at each side. For this specific case, the junction nodes are FIRs at both sides, as depicted in Figure 6.3. The extraction will also start from the outside in, moving further from source nodes until reaching the transversal section at resonator $m - 1$, and concluding with the extraction of J_m and B_{m-1}. The last two elements are obtained by means of partial extractions using (5.8).
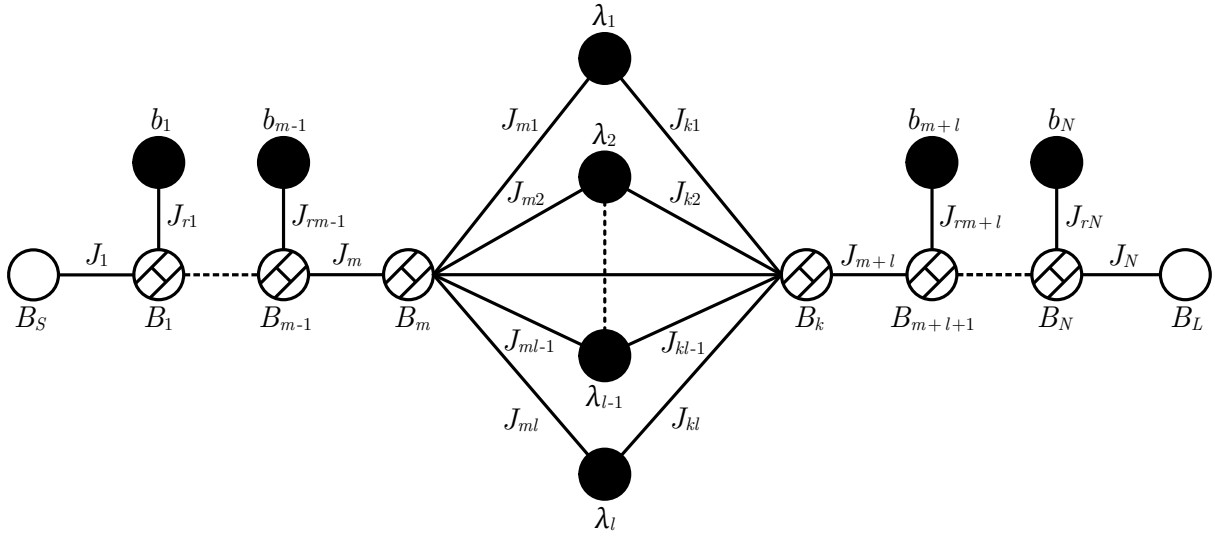
Figure 6.3: General Nth-order mixed-topology transversal array with N TZs.

Continuing from the load terminal, the extraction process is carried out up to resonator $m + l + 1$ and finishes after the extraction of J_{m+l} and B_k. At this point, the rest of the network is implemented as a transversal structure like the central section of Figure 6.3. The remaining ABCD matrix for the transversal network is converted into an admittance matrix $[Y_{rem}]$ that can be expressed in terms of its residues by partial fraction expressions like in (5.1):

$$[Y_{rem}] = \frac{1}{y_d(s)} \begin{bmatrix} y_{11n}(s) & y_{12n}(s) \\ y_{21n}(s) & y_{22n}(s) \end{bmatrix} = j \begin{bmatrix} B_m & J_{mk} \\ J_{mk} & B_k \end{bmatrix} + \sum_{i=1}^{h} \frac{1}{(s-j\lambda_i)} \begin{bmatrix} r_{11i} & r_{12i} \\ r_{21i} & r_{22i} \end{bmatrix}, \tag{6.1}$$

where the order of the sub-network is $h = m - k$, the number of resonators between resonator m and k.

To transform the transversal sub-network to the parallel-connected configuration, it must be split in two branches, upper and lower, in order to obtain two fully-canonical networks. Moreover, the eigenvalues of the transversal sub-network must also be distributed between the branches in a specific way. In the previous chapter, it was stated that there must be complementary pairs of eigenvalues and their associated residues between B_k and B_m nodes within each branch in case of having a more than one eigenvalue in a group. For example, in a structure with three eigenvalues, there are two odd-mode and a one even-mode, one group should be made of even-odd pair, instead of two odd-modes.

Both branches require a part of the input-to-output coupling J_{mk}, the distribution of the parameter between them must be done accordingly. Following the proposal in Section 5.2.2 and reformulating (5.10) and (5.11), the coupling for the upper and lower branches J_{mkup} and J_{mklo} are calculated as

$$J_{mkup} = \sum_{i=1}^{h} -\frac{J_{mi}J_{ki}}{(b_i - \lambda_i)}, \tag{6.2}$$

$$J_{mklo} = J_{mk} - J_{mkup}. \tag{6.3}$$
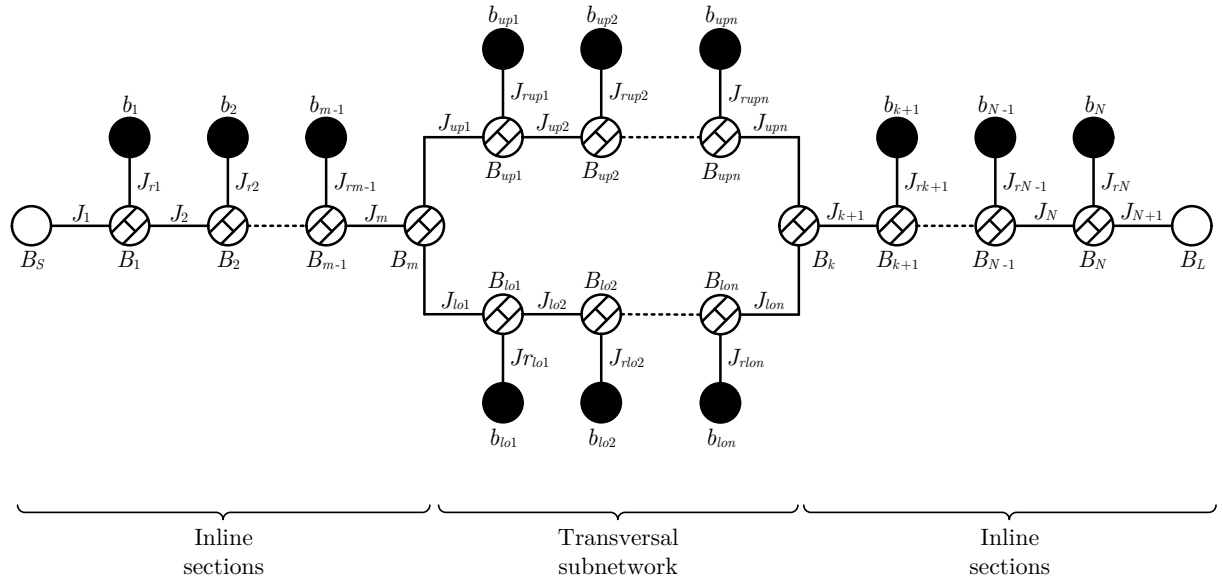
Figure 6.4: General Nth-order mixed-topology fully canonical filter. The network is divided in three parts: The inline sections are formed by extracted-pole resonators, and the center part is a parallel-connected structure made of two branches of extracted-pole inline sections that generate $m - k$ TZs.

where b_i represents the resonant frequencies implemented by the resonators in the upper branch, and λ_i the eigenvalues that will be used to form it. The rest are assigned to the lower branch. The admittance matrices for both parts are defined as follows:

$$[Y_{up}] = j \begin{bmatrix} 0 & J_{mkup} \\ J_{mkup} & 0 \end{bmatrix} + \sum_{i=1}^{n_{up}} \frac{1}{(s - j\lambda_i)} \begin{bmatrix} r_{11i} & r_{12i} \\ r_{21i} & r_{22i} \end{bmatrix}, \tag{6.4}$$

$$[Y_{lo}] = j \begin{bmatrix} 0 & J_{mklo} \\ J_{mklo} & 0 \end{bmatrix} + \sum_{i=n_{up}+1}^{h} \frac{1}{(s - j\lambda_i)} \begin{bmatrix} r_{11i} & r_{12i} \\ r_{21i} & r_{22i} \end{bmatrix}. \tag{6.5}$$

where n_{up} is the array number with the desired parameters in the upper branch.

Both matrices, $[Y_{up}]$, $[Y_{lo}]$, are turned into $[ABCD_{up}]$ and $[ABCD_{lo}]$, respectively. Then, they can be extracted as inline networks. The roots of polynomials $P_{up}(s)$ and $P_{lo}(s)$ determines the resonance frequencies of the resonators at each branch. Like in the previous chapter, they may not be the prescribed TZs anymore, because the TZs are implemented by the whole structure and not as the individual contribution of each resonator.

Finally, both upper and lower branches are merged and joint to the rest of the network to form the whole filter. After applying this step, the generic scheme of the final network is shown in Figure 6.4. The procedure to achieve the filter structures shown in Figure 6.1 using the general method described detailed in the next sections.

6.1.2 Ground-Loop Inductor Coupling

In this section, an example procedure for the synthesis of GLI couplings is detailed. Let us consider a 5th-order lowpass fully canonical filter to illustrate the method. The GLI coupling synthesis yields a network topology shown in Figure 6.5, which equivalent in AW technology is like the filter in Figure 6.1a but lower order. FIRs B_{x2} and B_{x4} are the junction nodes that connect every network part, while B_{24} is the lowpass equivalent of the coupling inductor.
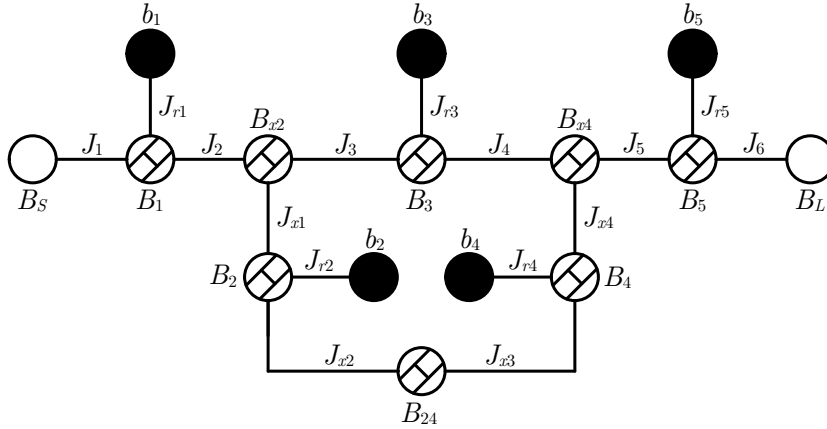
Figure 6.5: Nodal scheme of a 5th-order filter with a GLI coupling between resonators 2 and 4.

The TZs set, corresponding with the five roots of $P(s)$, is $j\{\Omega_1, \Omega_2, \Omega_3, \Omega_4, \Omega_5\}$. The inductor is coupling resonators 2 and 4. Thus, the inline sections are formed by resonators 1 and 5. The parallel-connected section is created with resonators 2, 3 and 4. The reactive element, modeled as an FIR, is introduced in the lower branch that is made up of resonators 2 and 4. The upper branch is composed of resonator 3, which contributes with the TZ $j\Omega_3$.

At the first step, the parameters of resonators 1 and 5 are extracted. In the first iteration, the values of B_S, J_{r1} and b_1 are obtained, and after the second extraction iteration, the values of B_L, J_{r5} and b_5 are computed too. The resonant frequencies for resonator 1 and 5 are $b_1 = \Omega_1$ and $b_5 = \Omega_5$, respectively.

After two iterations, every parameter from both resonators has been determined completely, except the NRN nodes B_1, B_5, and their respective admittance inverters J_2 and J_5, which couple them to the internal network. The NRNs values are computed by means of a partial extractions at the next TZ i.e. $s_2 = j\Omega_2$ for B_1 and $s_4 = j\Omega_4$ for B_5. To accommodate in phase the inline with the transversal sections, only a fraction of the partial extraction is assigned to the NRNs. B_1 is extracted sequentially as follows:

$$B_1 = \alpha_1 \left.\frac{D_1(s)}{B_1(s)}\right|_{S=j\Omega_2},\tag{6.6}$$

where α_1 is the setting factor for the reactance portion assigned to B_1 that can be set arbitrarily in a range $\alpha_1 = [0, 1]$. Polynomials $D_1(s)$ and $B_1(s)$ use subindex 1 to differentiate the original ABCD

polynomials from the updated matrix after the extraction that has already taken place. After extracting B_1, the updated matrix used subindex 2. Then, the adjacent admittance inverter is also extracted. The process is repeated in for resonator 5, B_5 is extracted as follows:

$$B_5 = \alpha_5 \left. \frac{D_2(s)}{B_2(s)} \right|_{S=j\Omega_2}, \tag{6.7}$$

where α_5 is the equivalent factor for the reactance portion assigned to B_5 that can be set arbitrarily within the same range as α_1. Finally, the adjacent admittance inverter is extracted, the network matrix is updated to $[ABCD]_{rem}$ in the scheme shown in Figure 6.6.
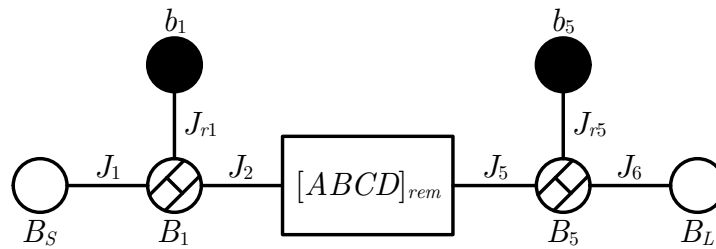
Figure 6.6: Status of the network after complete extraction of resonators 1 and 5 flanking the remaining ABCD matrix.

The network will be synthesized as 3rd-order fully canonical transversal network. First, the ABCD matrix is converted into an admittance matrix $[Y_{rem}]$ that can be expressed by

$$[Y_{rem}] = j \begin{bmatrix} B_{x2} & J_{SL} \\ J_{SL} & B_{x4} \end{bmatrix} + \sum_{i=1}^{h} \frac{1}{(s - j\lambda_i)} \begin{bmatrix} r_{11i} & r_{12i} \\ r_{21i} & r_{22i} \end{bmatrix}, \tag{6.8}$$

where the order of the network is $h = 3$. The nodal scheme is shown in Figure 6.7. Next, the parameters B_{x2} and B_{x4} are extracted with (5.4) prior to splitting the transversal network in two branches.
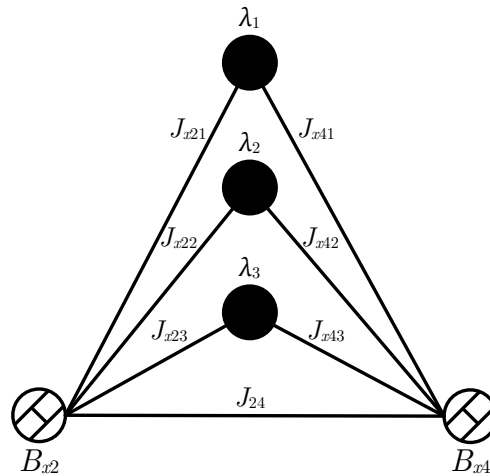
Figure 6.7: Transversal nodal diagram of a 3rd-order filter.

The upper branch is intended to form a single dangling resonator between unitary inverters, as the case of resonator 3 in Figure 6.5, using a single odd-mode eigenvalue. On the other hand, the lower branch will be a two-dangling resonator configuration in series, coupled by an FIR using the other odd-mode and the single even-mode eigenvalue available.

Upper Branch

The upper branch can be implemented directly employing a circuit transformation to dangling resonator from a singlet (see Appendix B). To carry out the aforementioned transversal network splitting, the input-to-output coupling must be divided in two for the upper and lower branches respectively. Otherwise would not be possible to implement the network as extracted-pole sections. The admittance matrix of the upper branch $[Y_{up}]$ expressed in terms of its residues is

$$[Y_{up}] = j \begin{bmatrix} B_{x2up} & J_{24up} \\ J_{24up} & B_{x4up} \end{bmatrix} + \frac{1}{j\,(\Omega_3 - \lambda_1)} \begin{bmatrix} r_{111} & r_{121} \\ r_{211} & r_{221} \end{bmatrix}. \tag{6.9}$$

Particularizing equations (6.2) and (6.3), that relates eigenvalue to the desired transmission zero for J_{24up} and J_{24lo}, the split results in

$$J_{24up} = -\frac{J_{x21}J_{x41}}{(\Omega_3 - \lambda_1)}, \tag{6.10}$$

$$J_{24lo} = J_{24} - J_{24up}. \tag{6.11}$$

Note that J_{24up} has been computed using the transmission zero Ω_3. Forcing $b_3 = -\Omega_3$, assures that the resonator 3 is tuned to the frequency that was meant to be in the classic ladder network. The parameters, B_3 and J_{r3}, can be derived from the same equations in Appendix B:

$$B_3 = -\frac{J_{x21}/J_{x41}}{J_{24up}}, \tag{6.12}$$

$$J_{r1} = |J_{x21}B_3|. \tag{6.13}$$

Besides the dangling resonator parameters, other pair of input and output NRN elements appear, B_{x2up}, B_{x4up}. They have to be added to B_{x2} and B_{x4}, respectively. The equations to calculate these elements are defined as follows:

$$B_{x2} = \frac{J_{x21}^2}{B_3}, \tag{6.14}$$

$$B_{x4} = \frac{J_{x41}^2}{B_3}. \tag{6.15}$$

Lower Branch

The lower branch is formed by the elements from the transversal coupling matrix not already used for the upper branch, and it is synthesized as an inline network. Before any extraction, it is necessary to define its admittance matrix $[Y_{lo}]$ by subtracting the upper branch matrix $[Y_{up}]$ from $[Y_{rem}]$ in (6.16) and then, convert it into a ABCD matrix.

$$[Y_{lo}] = [Y_{rem}] - [Y_{up}] = j \begin{bmatrix} B_{x2lo} & J_{24lo} \\ J_{24lo} & B_{x4lo} \end{bmatrix} + \sum_{i=2}^{3} \frac{1}{(b_i - j\lambda_i)} \begin{bmatrix} r_{11i} & r_{12i} \\ r_{21i} & r_{22i} \end{bmatrix} \tag{6.16}$$

The $P_{lo}(s)$ roots determine the resonance frequencies in the lower branch. They may be different from any of the roots of $P(s)$. The extraction procedure yields a 2nd-order fully canonical network of dangling resonators shown in Figure 6.8.
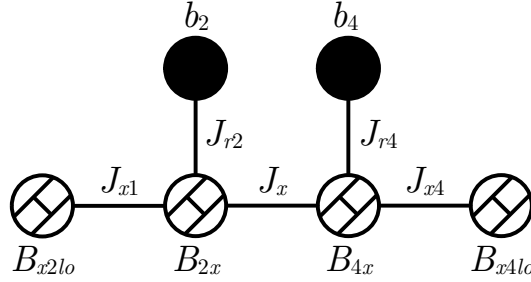
Figure 6.8: Lower branch circuit configuration nodal scheme.

It must also be noticed that if b_3 in the upper branch is chosen from the prescribed TZs of the filter, one root of $P_{lo}(s)$ will be the value assigned to b_3 too. When the filter is evaluated at one of the finite TZ frequencies, the source-to-load path is blocked. If that occurs at a TZ of the filtering function, the lower branch path must also be blocked for that TZ to be generated. Thus, it becomes evident that the $P(s)$ polynomials from both branches ought to share a common root in this particular case.

For the generation of B_{24} (Figure 6.9), the FIR to implement the reactive element, a circuit transformation is applied to the admittance inverter J_x, B_{2x} and B_{4x} (see Appendix D). The value of the final parameters are

$$B_{24} = \frac{J_{x2}J_{x3}}{J_x}, \tag{6.17a}$$

$$B_2 = B_{x2} - \frac{J_{x2}}{J_{x3}}J_x, \tag{6.17b}$$

$$B_4 = B_{x4} - \frac{J_{x3}}{J_{x2}}J_x. \tag{6.17c}$$
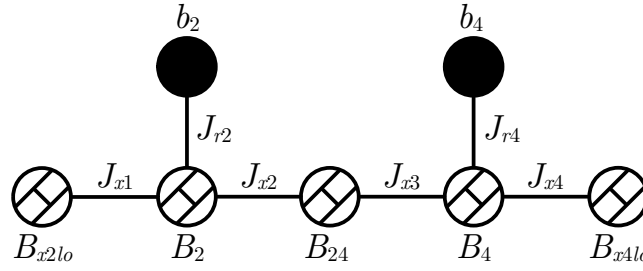
Figure 6.9: Lower branch circuit with the FIR B_{24} generated by circuit transformation.

Network Assembling

In the last step, the sub-networks are connected in parallel between the input and output terminations, combining the input and output parameters of each branch.

6.1.3 Ground-Loop Inductor Numerical Example

Considering a 5th-order fully canonical filter as in Figure 6.5 with a $RL = 20$ dB and $\Omega_{tz} = \{1.3, -2.4, 2.6, -1.3, 2\}$ rad/s, yields the response in Figure 6.10. The normalized TZs exhibits a asymmetric distribution. Resonators 1 and 5 are extracted as dangling resonators and the values of their elements are $B_S = -11.2957$, $B_L = -0.6112$, $b_1 = -1.3$, $b_5 = -2$, $J_{r1} = 0.0686$, $J_{r5} = 0.5614$. The NRNs of the resonators are $B_1 = -0.0449$ and $B_5 = -0.1245$ using $\alpha_1 = 0.5$ and $\alpha_5 = 0.8$.
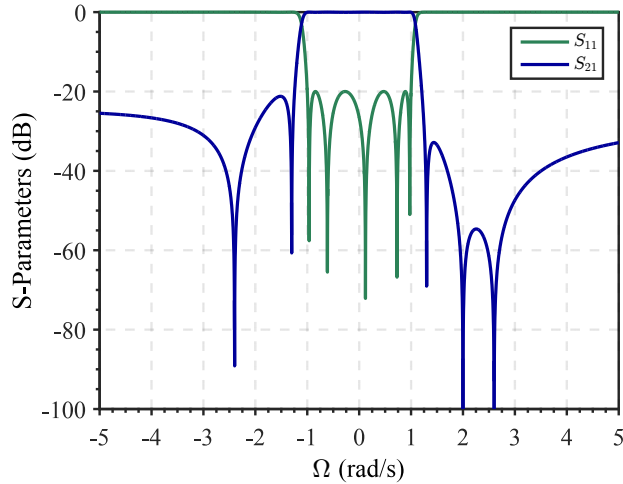
Figure 6.10: Lowpass response of the 5th-order filter with a GLI between resonators 2 and 4.

Next, the transversal coupling matrix element values are calculated and shown in Table 6.1. The transversal sub-network is divided in two to generate upper and lower branches. The upper branch resonator is desired to resonate at $\Omega_3 = 2.6$ using λ_1, J_{x21} and J_{x41}. Therefore, using (6.2) and (6.3), the input-to-output coupling for each branch is $J_{24up} = 0.2519$, $J_{24lo} = -0.1375$.

Table 6.1: Transversal sub-network parameters of GLI-coupled filter.

i	λ_i	J_{x2i}	J_{x4i}
1	-1.1917	0.5163	-0.2293
2	-0.9067	0.5821	1.0165
3	0.4900	0.4511	-1.1782
J_{24}	0.1144		
B_{x2}	-0.9664		
B_{x4}	-0.2634		

Table 6.2: Final lowpass elements of the extracted 5th-order filter with a GLI coupling.

	B_k	b_k	J_{rk}
Res. 1	-0.0449	-1.3000	0.0686
Res. 2	-3.2357	-2.6000	3.3770
Res. 3	-1.5201	-2.6000	1.7909
Res. 4	-0.0047	1.2564	0.0469
Res. 5	-0.1245	-2.0000	0.5615
B_S	-11.2957	B_{x02}	20.1045
B_L	-0.6112	B_{x04}	42.7268
		B_{L24}	-30.1798

The upper branch element values in a dangling configuration are $B_{x2up} = -1.6243$, $B_{x4up} = -0.3598$, $B_3 = -1.5201$, $J_{r3} = 1.7909$ and $b_3 = -2.6$. The lower branch elements are extracted as represented in Figure 6.9, the values of the input and output FIRs are are, $B_{x2lo} = 21.7287$, $B_{x4lo} = 6.6225$. After joining both branches, the FIRs connecting the parallel-connected to the inline section are $B_{x2} = 20.1045$ and $B_{x4} = 42.7268$. The rest of parameter of the filter are listed in Table 6.2.

6.1.4 Inter-Resonator L-C Coupling

The coupling described in this section is made of an inductor that couples a shunt resonator to ground, and a series capacitor that couples a series resonator to the inductor and the shunt resonator. Figure 6.1b shows a sample configuration. In this particular case, the second resonator is coupled to ground through L_X and a capacitor C_X connects the first resonator from the source port to the inductor and shunt resonator R_2. The equivalent nodal scheme is depicted in Figure 6.11. The nodes B_{Cx}, B_{Lx} play the role of C_X and L_X in the lowpass prototype, respectively.
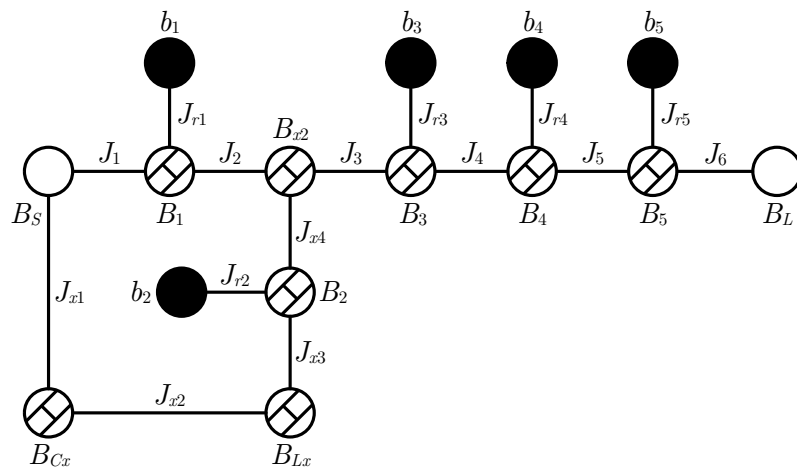
Figure 6.11: Nodal Scheme of a 5th-order filter with a LCC coupling.
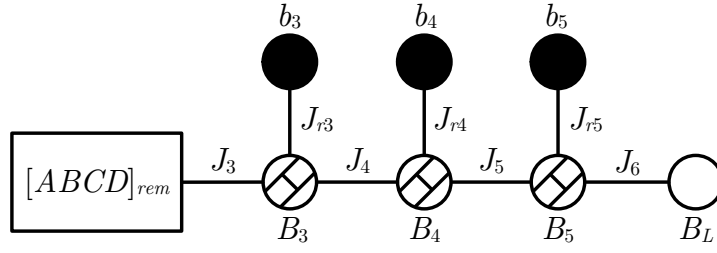
Figure 6.12: Network nodal scheme after the extraction from the resonator 5 to 3.

In the same way that it was done for the case of the GLI coupling, the extraction is carried out in two steps. First, we need to isolate the parallel-connected section, comprised of resonators 1 and 2, from the rest of the network. Then, the extraction will be carried out from the load until resonator 3, resulting in the structure shown in Figure 6.12.

The remaining matrix $[ABCD_{rem}]$ implements as a 2nd-order fully canonical transversal network. Again, to reconfigure this sub-network in the parallel-connected, it must be divided in two branches, upper and lower. Each branch is made of a single eigenvalue and a coupling to input and load nodes. For the network splitting, we also need to divide the input-to-output coupling in two using the expressions (6.2) and (6.3). Once divided, the upper branch is implemented as explained in the previous case.

The FIRs B_{Cx} and B_{Lx} are in the lower branch. Before extracting them, the admittance matrix of the lower branch $[Y_{lo}]$ must be built and turned in an ABCD matrix. The lower branch is obtained as an inline network by synthesis, which nodal scheme can be found in Figure 6.13, being the resonance frequency $s = -jb_2$ the root of $P_{lo}(s)$. First, B_{Lx} and B_{Cx} are obtained by evaluating polynomial $D(s)$ and $B(s)$ at the single root of $P_{lo}(s)$ as follows:

$$jB = \left.\frac{D(s)}{B(s)}\right|_{S=jb_2} \tag{6.18}$$

The parameter is computed but not immediately extracted from the matrix. B is distributed with the expressions (6.19a) and (6.19b), where factor α can be set arbitrarily between 0 and 1.

$$B_{x1lo} = B(1-\alpha) \tag{6.19a}$$

$$B'_{Cx} = B\alpha \tag{6.19b}$$

Next, the matrix $ABCD_1$ is updated with the removal of B_{x1lo}. The process continues by extracting sequentially a unitary admittance inverter, J'_{x1} and B'_{Cx}. The remaining parameters in the lower branch are extracted as usual. The FIR B_{Lx} is created by circuital transformation in Appendix D which set the final values of each element, yielding the network shown in Figure 6.13. Finally the parallel-connected sub-network is assembled by joining both branches between source and load ports where $B_S = B_{Sup} + B_{Slo}$ and $B_{02} = B_{Lup} + B_{Llo}$.
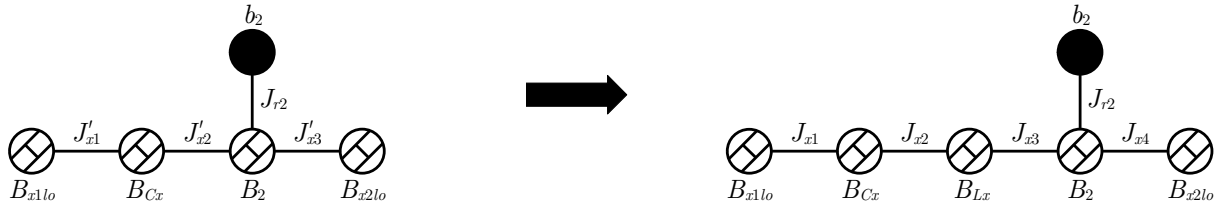
Figure 6.13: Lower branch nodal scheme of the LCC coupling configuration with only B_C (left), and the complete lower branch after generating B_L (right).

6.1.5 Numerical Examples

In this section, two realization examples are presented to validate the synthesis methodology. During the extraction process, the values of admittance inverters J_i are set to ± 1 over the main and secondary paths.

5th-Order Fully Canonical Filter with a LCC Between Source and Resonator 2

The filter design considered in this example is a fully canonical 5th-order filter which TZs are $\Omega_{tz} = \{2.7, -2.8, 1.5, -1.3, 2.1\}$ rad/s and $RL = 18$ dB. Its nodal scheme can be seen in Figure 6.11. Following the procedure described in Section 6.1.4, the inline part of the network is extracted from load node to resonator 3, while the parallel-connected section is defined between source node and resonator 2. Thus, the transversal structure is a 2nd-order network, which parameters are provided in Table 6.3.

Table 6.3: Transversal sub-network parameters of the 5th-order LCC coupled filter.

i	λ_i	J_{x1i}	J_{x2i}
1	-0.9578	-0.3801	0.6184
2	0.7473	0.3507	0.7294
J_{12}	-0.0667		
B_{x1}	0.0029		
B_{x2}	0.6260		

Table 6.4: Final lowpass elements of extracted 5th-order filter with a LCC coupling.

	B_k	b_k	J_{rk}
Res. 1	-0.8509	-1.2000	0.6207
Res. 2	-5.0208	0.4860	0.5967
Res. 3	-0.1539	-1.5000	0.7914
Res. 4	7.5358	1.5000	2.9082
Res. 5	-0.6313	-2.1000	-0.8138
B_S	-2.3098	B_{x2}	0.2083
B_L	-2.1190	B_{Cx}	-5.4539
		B_{Lx}	-0.4178

The sub-network is split in two. The upper branch is formed to have a resonator which resonant frequency is $s = -jb_1 = j1.2$, using λ_2 together with its associated couplings $J_{x12} = 0.3507$ and $J_{x22} = 0.7294$. The input-to-output coupling J_{12} is separated in two, resulting in $J_{12up} = -0.5650$ and $J_{12lo} = 0.4983$. The remaining eigenvalue λ_1 and its associated coupling are used for the lower branch. Next, the individual matrices for the upper and lower branches are created by building $[Y_{up}]$ and $[Y_{lo}]$, respectively. Subsequently, they are converted to ABCD matrices. The upper branch is extracted with the procedure described in Chapter 3.
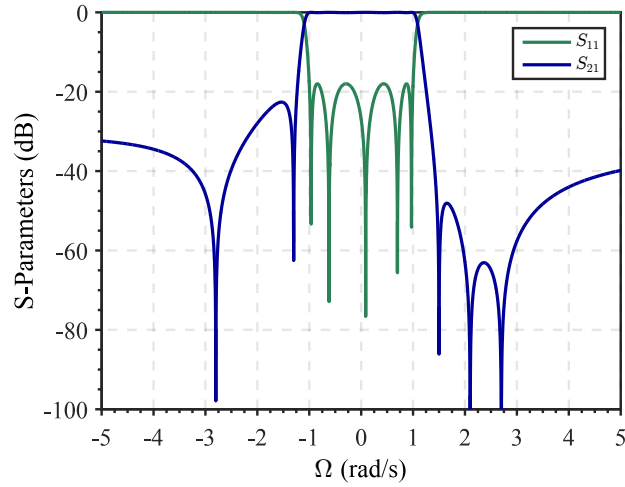
Figure 6.14: Lowpass response of the 5th-order filter with a LCC between resonators 1 and 2.

The extraction of the lower branch is carried out as explained in the previous section. To assign a value to B_{Cx} and B_{x1lo}, the sharing factor is $\alpha = 0.6$, yielding $B_{Cx} = -5.4539$ and $B_{Lx} = -0.4178$. The value of all extracted elements is provided in Table 6.4. The resonance frequency in the lower branch resonator is $s = -jb_3 = -j0.48$. That is, it is located within the in-band range. Finally, the filter response is shown in Figure 6.14.

7th-order Fully Canonical Filter with a LCC Between Source and Resonator 4

For this example a fully canonical order filter with TZs $\Omega_{tz} = \{\, 3.8,\ 2,\ -2.5,\ 2.7,\ 1.6,\ -1.5,\ 1.3 \,\}$ rad/s and $RL = 23$ dB is used. In this configuration, five of the TZs are generated above the passband, while only two of them are located below. For this case, the cross-coupling is created between source node and resonator 4. Its nodal scheme can be seen in Figure 6.15, and the filter response is shown in Figure 6.16.
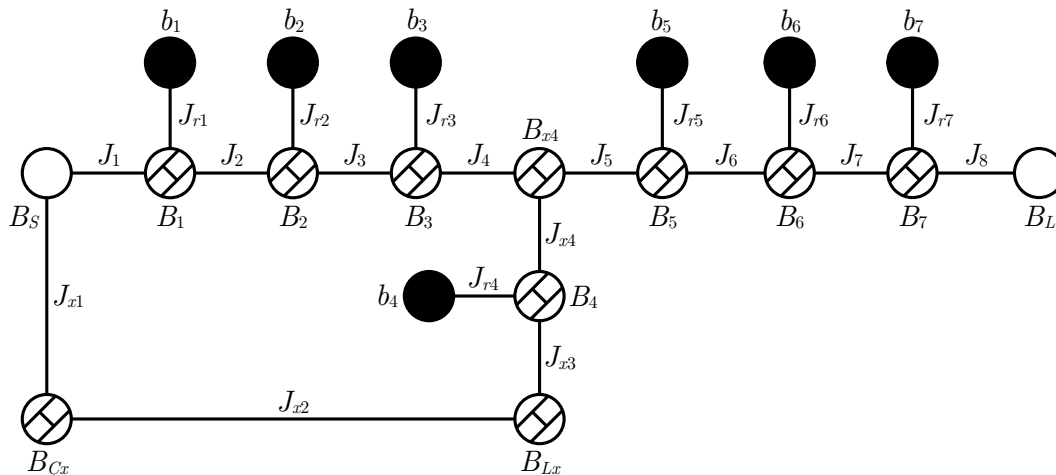
Figure 6.15: Transversal nodal diagram of a 7th-order filter with a LCC between source and resonator 4.

The extraction begins from the inline section from load until resonator 5. The rest is reconfigured as a 4th-order transversal network, which parameters are listed in Table 6.5. The LCC coupling embraces three resonators. Upon the sub-network split, the upper branch requires three eigenvalues. Meanwhile, the lower branch only needs one. To facilitates the splitting step, the transversal network is divided by fixing the resonance frequency of the lower branch resonator with $b_4 = -1.342$, created with λ_3 and its associated couplings J_{x13} and J_{x13}. The input-to-output coupling is distributed between both branches, resulting in $J_{14up} = -0.2994$ and $J_{14lo} = 0.2927$.

Next, matrices $[Y_{up}]$ and $[Y_{lo}]$ are created to be converter to ABCD matrices, afterwards. The extraction of the lower branch is carried out as an inline network, the sharing factor is $\alpha = 0.9$, yielding $B_{Cx} = -1.3968$ and $B_{Lx} = -1.2828$.

The resonance frequencies in the upper branch are determined by the roots of polynomial $P_{up}(s)$. When it is made of more than one resonator, it is necessary to determine the extraction order of each root. In this case, the upper branch is extracted as a 3rd-order fully canonical network. The first and third resonators will be implemented in series configuration. Normally, they require to have a resonance frequency above the passband, thus, a positive root in the lowpass domain. In order to synthesize a feasible filter, the extraction procedure must be realized alternating the sign of the $P_{up}(s)$ roots in each iteration.

In this example, the roots of polynomial $P_{up}(s)$ are $j\{1.4420, -1.4027, 0.4346\}$. The extraction procedure has been done using the given order, yielding the elements in Table 6.6. It should be noticed that this is another degree of freedom. With different root sorting, it is possible to achieve other values for the network elements. Ultimately, it must be decided which roots extraction order produces the most convenient result.
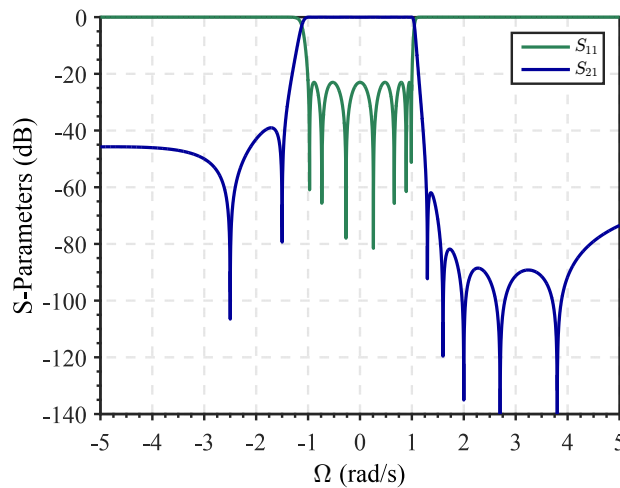
Figure 6.16: Lowpass response of the 7th-order filter with a LCC between source and resonator 4.

Table 6.5: Transversal parameter's values of the 4th-order inner parallel-connected section.

i	λ_i	J_{x1i}	J_{x4i}
1	-1.1438	0.3385	0.5403
2	-0.3813	-0.7169	0.5529
3	0.5805	0.4532	0.4917
4	1.1240	-0.0952	0.5106
J_{14}	-0.0067		
B_{x1}	-		
B_{x4}	2.1485		

Table 6.6: Lowpass elements of the synthesized 7th-order ladder filter with a LCC between source and resonator 4.

	B_k	b_k	J_{rk}
Res. 1	-0.5097	-1.4420	0.6071
Res. 2	1.9195	1.4027	1.2575
Res. 3	-1.7072	-0.4346	1.2721
Res. 4	-6.7856	-1.3420	1.9554
Res. 5	-0.3662	-1.6000	-1.1578
Res. 6	4.2523	1.5000	-1.8582
Res. 7	-0.3540	-1.3000	-0.3808
B_S	-3.0378	B_{x4}	0.8782
B_L	-1.7588	B_{Cx}	-1.3968
		B_{Lx}	-1.2828

6.2 Synthesis-Based Modeling of Electromagnetic Feedthrough

In AW devices, there are some effects that can distort the desired response of a filter. One of them is the electromagnetic feedthrough, which is due to direct coupling between the input and output ports of the device, bypassing any acoustic response [21, 98]. This effect is minimized by proper design, mounting, bonding, and packaging. Even so, there are situations in which it may be too punishing for the design.

The presence of electromagnetic feedthrough between package ports may cause degraded isolation levels and transmission zeros vanishing. It was demonstrated in [59, 80], that by means of a phase and amplitude-adjusting block, added at the Rx port, some leakage is canceled out, leading to a significant improvement in the Tx band isolation of the duplexer. Although it is an effective remedy, they do not broach the problem with a rigorous explanation of the involved effect. Other techniques, such as the one used in [99] eliminates the main-line leakage by an additional intentionally well-designed path with proper phase and amplitude, achieving a high attenuation at an arbitrary frequency. Other authors have presented circuital models to take parasitic elements into account [100–104]. However, none of them has tried to solve it from the synthesize approach.

The EMF phenomenon can be observed in Figure 6.17, where a co-simulation of a B1Tx 5th-order filter with three different feedthrough levels is presented. It is noticeable that a higher leakage level implies lower isolation. The effect of an input-to-output cross-coupling is equivalent to detune the resonance frequency of all resonators. Under weak couplings, the network can keep the TZs allocation practically unaltered, but some of the them may become complex with strong couplings [66, 82]. It is known that acoustic technology is only capable of synthesizing pure imaginary resonant frequencies. In such cases, the implemented filter would be partially synthesized and, therefore, the network response will be severely degraded. This is more evident in the region above the passband in Figure 6.17a, where even some TZs vanishes for -50 dB and -40 dB couplings.
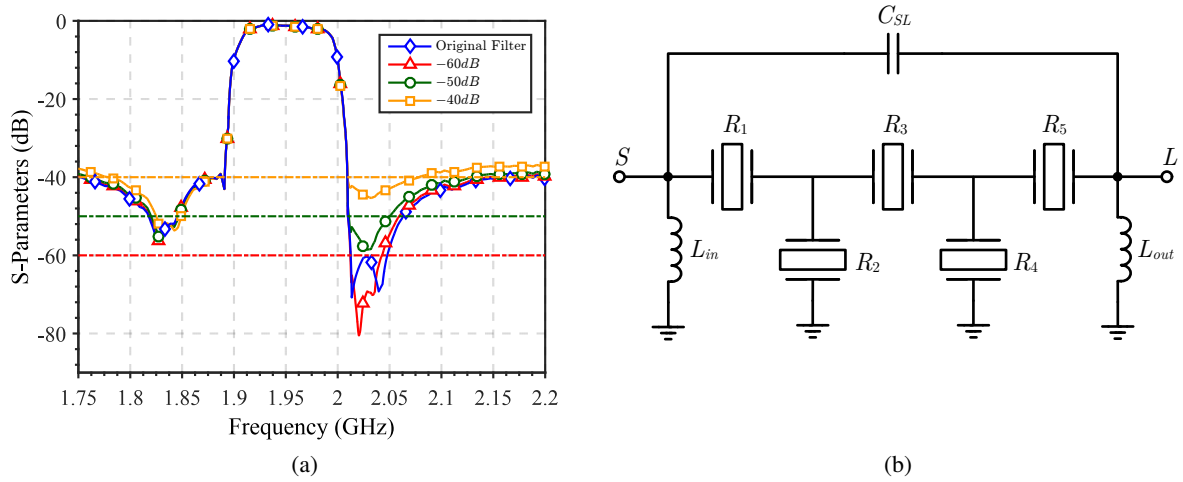
Figure 6.17: Co-simulation of a measured transmission response with three different feedthrough levels and its equivalent bandpass circuit scheme.
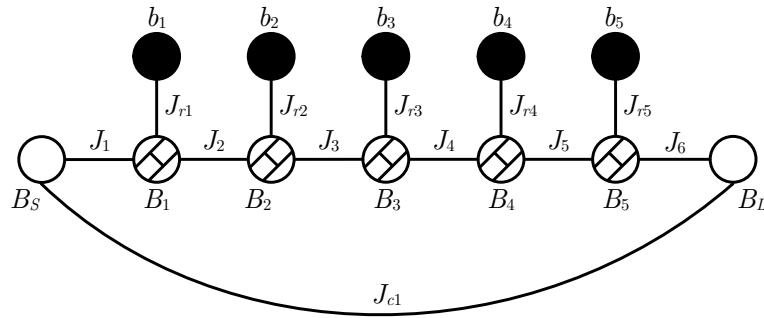
Figure 6.18: 5th-order filter scheme with a source-to-load coupling.

6.2.1 EMF Model

To address the EMF from the synthesis point of view, it is necessary to establish an equivalence between the bandpass filter and the lowpass prototype. In general, all circuital models in the cited works include a series capacitor between input and output nodes. Figure 6.17b models the EMF as a capacitor C_{SL}.

The ladder networks design with bypassing cross-couplings is directly based on the extraction of the cross inverter J_{ck} at finite frequencies (see Chapter 3). If there exist leakage paths, the synthesis methodology may provide the exact resonator parameters in order to maintain the position of TZs for ladder acoustic wave filters and prevent the existence of complex transmission zeros.

The equivalent lowpass prototype is depicted in Figure 6.18. The cross inverter can be realized as an ideal lumped elements with a Pi-network configuration like in Figure 6.19. The admittances Y_A can be combined with the FIR in the input and output nodes B_S and B_L, respectively. The relationship between

EMF may be modeled with the capacitor C_{SL} (Y_B), and the cross-coupling is defined as

$$C_{SL} = -\frac{J_{c1}}{\omega Z_0}, \tag{6.20}$$

where Z_0 is the characteristic impedance used to normalize the lowpass source and load nodes. It should be noticed that J_{c1} must be negative to be obtained a capacitive coupling. It also worth to mention that the realization works in a relatively narrow frequency range $\omega \pm \Delta\omega_0$.
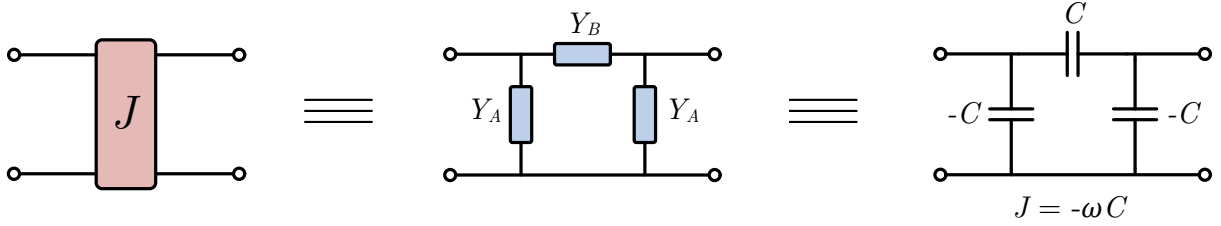
Figure 6.19: An equivalent circuit for admittance inverters.

6.2.2   Cross-Coupling Extraction Procedure

The extraction theory of the cross-inverter follows the procedure described in Section 3.3.3. It states that upon an extraction at an arbitrary frequency that differs from the prescribed TZs of the filtering function that remains to be extracted, a cross inverter is required to keep the filter response unchanged.

For modeling the preexisting EMF, the given definition must be interpreted backward. That is, to take into account the parasitic coupling, a cross inverter should be generated between the involved nodes. Therefore, for a given cross inverter J_{ck} the ABCD transfer matrix polynomials $P_{(k+1)}(s)$ and $C_{(k+1)}(s)$ must be updated by

$$P_{(k+1)}(s) = P_k(s) + J_{SL}B_k(s), \tag{6.21a}$$

$$C_{(k+1)}(s) = C_k(s) + 2J_{SL}P_k(s) + J_{SL}^2 B_k(s). \tag{6.21b}$$

Because the $P_{(k+1)}(s)$ polynomial is updated, the remaining roots do not correspond to the original TZs implemented by the filter. In other words, the resonators have to resonate at different frequencies to keep the transmission response completely unaffected, but their value can be controlled with the polynomial updating procedure.

6.2.3   Complex Transmission Zeros

The new singularities of the updated polynomial $P_{(k+1)}(s)$, may remain pure imaginary or appear in complex conjugate pairs [46]. In order to exemplify how complex TZs arise after a cross-coupling extraction between source and load, let us consider a 5th-order lowpass filter with $RL = 12$ dB. The TZs set, corresponding with the five roots $j\Omega_1^i$ ($i = 1..5$), obtained from the numerator of the transmission response $P_1(s)$ are shown in first row of Table 6.7. The result is an inline network is shown in Figure 6.20.
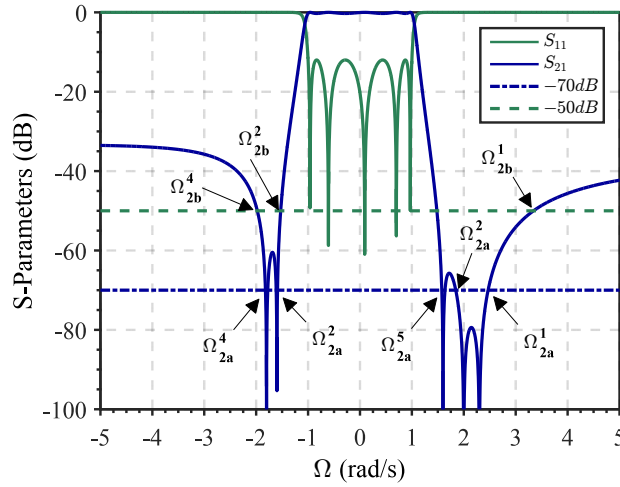
Figure 6.20: Lowpass response of the 5th-order filter. The dash lines represent two degrees of coupling, -70 dB (green trace) and -50 dB (blue trace).

Table 6.7: Lowpass resonance frequencies of each resonator.

	Ω_k^1	Ω_k^2	Ω_k^3	Ω_k^4	Ω_k^5
$P_1(s)$	2.30	-1.60	1.60	-1.80	2.00
$P_{2a}(s)$	2.46	-1.59	1.63	-1.82	1.86
$P_{2b}(s)$	3.31	-1.54	$1.59 + 0.21j$	-1.96	$1.59 - 0.21j$

To illustrate the effects of the source-to-load coupling, two cases will be detailed hereafter, one with a -70 dB and another with a -50 dB leakage (case a and b, respectively). The coupling level has been included as a design parameter during the synthesis.

Let us consider first the leakage between source load ports of -70 dB. The extraction process returns a cross-coupling between source and load, $J_{c1} = 0.0001584$. The updated $P_{(k+1)}(s)$ for case a will define a new set of resonance frequencies (Ω_{2a}^i) which are the roots of polynomial $P_{2a}(s)$, listed in the second row of Table 6.7. The roots of this updated polynomial are not the prescribed TZs anymore, and all resonators embraced by the cross-coupling resonate at different resonance frequencies.

It can be seen that for each resonance frequency, i.e., roots of $P_{2a}(s)$, the signal from source to load is blocked through the inline resonator path and the unique available path is through the cross-coupling. Therefore, at any resonance frequency, the transmission level of the network has to reach the value of -70 dB. It can be observed in Figure 6.20 that the resonance frequencies are detuned to those frequencies where the source-to-load coupling transmission level intersect with the transmission response. That is to say, the frequency detuning is related to the coupling strength. But, despite being shifted from its original location, they continue being purely imaginary and they can be implemented with acoustic resonators.
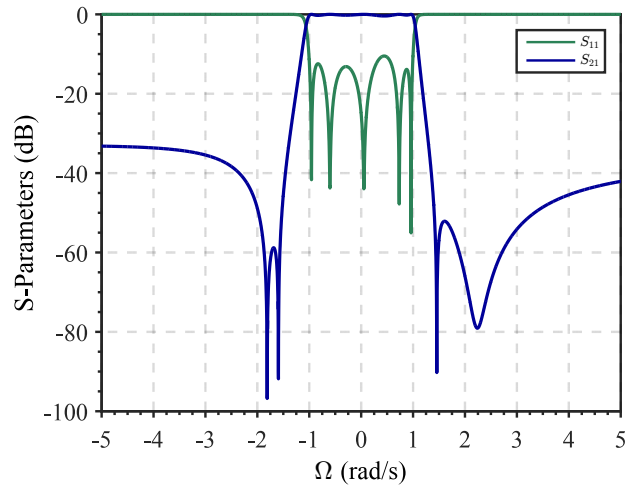
Figure 6.21: Synthesized lowpass filter response with a -50 dB source-to-load coupling.

In the second example, a -50 dB coupling strength is considered. As done in the previous case, we obtain a cross-coupling $J_{c1} = 0.0016$ between source and load ports. The roots (Ω_{2b}^i) of the updated polynomial, $P_{2b}(s)$, are listed in third row in Table 6.7. Notice that third and fifth resonant frequencies became a conjugate complex pair.

Given that an acoustic wave resonator is unable to implement complex singularities, the network does not synthesize the response correctly. The filter is not ready to accommodate the transmission response, Figure 6.21 clearly shows the return loss and OoB rejection significantly degraded. The outcome is comparable to the filter co-simulation in Figure 6.17 where the arising complex singularities cannot be implemented by AW resonators, producing a great impact on the isolation at the counter-band region.

The results of these two cases expose cross-couplings effects and the existence of complex transmission zeros. Although they do not show when pure imaginary roots become complex. For such purpose, we have carried out a source-to-load leakage swept with a coupling strength ranging from -70 dB up to -50 dB. The updated polynomial is just referred as $P_2(s)$. It can be observed in Figure 6.22 how third and fifth resonance frequency (Ω_2^3 and Ω_2^5) from the roots of $P_2(s)$ in Table 6.7 move towards the meeting point where both have the same imaginary value and then, turns into a conjugated complex pair. When the real part of the complex roots is small, the effect on the filter response is negligible, but the degradation is more severe as the coupling level becomes higher because, as mentioned before, pure imaginary TZs can be implemented by NRN-RN pairs, but we cannot implement complex TZs in acoustic technology.

6.2.4 Complex Roots Realization

In this section, it will be shown how the method is also capable of annihilating complex singularities. The methodology can provide the allocation and nature of further cross-couplings enabling the complex
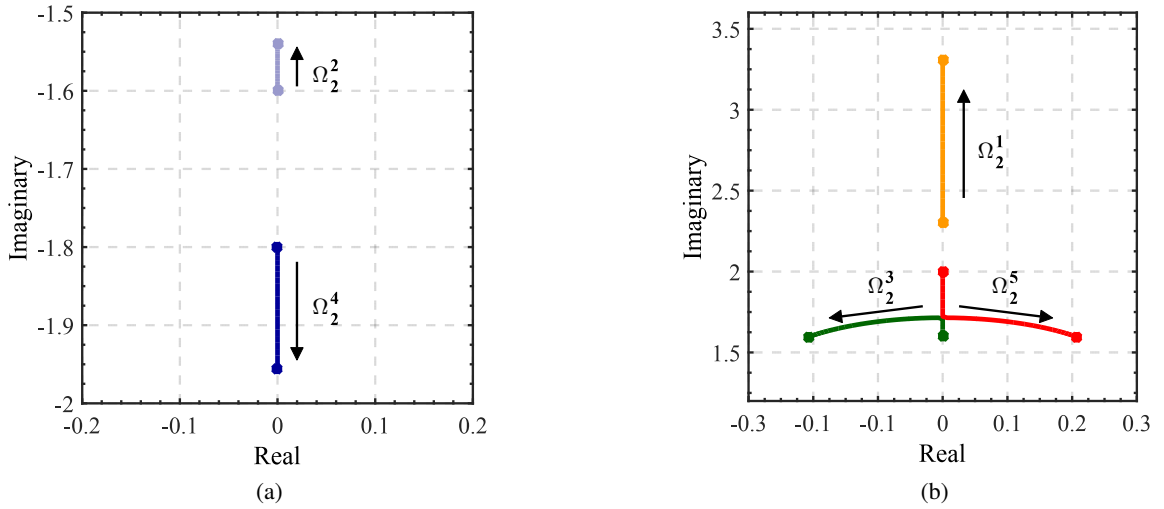
Figure 6.22: $P_{k+1}(s)$ root loci depicted for a source-to-load coupling strength sweep from -70 dB to -50 dB. The roots located below and above the passband are separated in figures (a) and (b), respectively.

roots to become pure imaginary again. That is, additional cross-couplings must be extracted, modifying for a second time the $P_{(k+1)}(s)$ singularities.

To validate the proposed method, the original filter response shown in Figure 6.17 has been compared with two test cases: (i) the original filter considering a -50 dB EMF leakage and (ii) a solution considering a synthesized filter with a -50 dB coupling and with a second cross-coupling at -40 dB from the second resonator to load. The nodal representation of the topology is found in Figure 6.23. The transmission response of the original filter with blue trace in Figure 6.24. The synthesized network with a coupling strength of -50 dB ($J_{c1} = 0.0016$) yields a polynomial $P_2(s)$ which roots are listed in Table 6.8 , requiring a conjugated complex pair: $1.41 \pm 0.15j$ for resonators 3 and 5. The transmission response partially synthesized is shown in Figure 6.24 with green trace. The degradation arises from the impossibility of synthesizing the complex singularity. Therefore, an extra -40 dB cross-coupling is considered to convert the complex roots into pure imaginary by $J_{c2} = 0.005$. The five $P_3(s)$ roots become purely imaginary, and the transmission response is improved to almost its original OoB rejection level as seen in Figure 6.24 with red trace. Although the response is restored, some resonance frequencies have been moved far away from the passband, like the 4th root of $P_3(s)$ (third row in Table 6.8).

Moreover, arrangements with asymmetric resonances distributions are more prone to happen with cross-couplings due to the roots of $P_{(k+1)}(s)$ are detuned in such way. Consequently, one of the admittance inverter at main-line positions gets a non-unitary value when the phase shift is neglected the transmission response is not properly synthesized. To revert this undesired situation, the phase correction method described in Chapter 4 allows obtaining realizable networks by providing homogeneous values for main-line couplings.
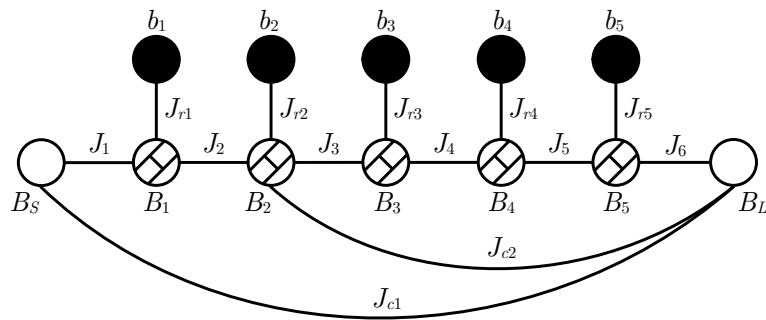
Figure 6.23: Lowpass filter with two cross-coupling, between source and load nodes, and between the second resonator and load nodes.
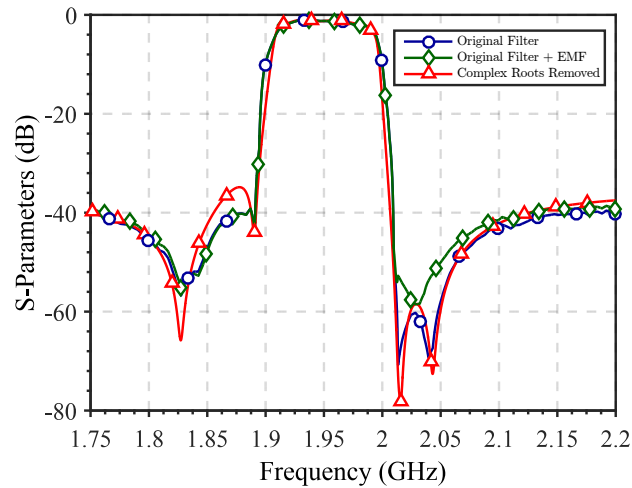
Figure 6.24: Comparison between the original B1Tx filter without cross-coupling (blue), the filter when the cross-coupling is present (green), and when the second cross-coupling is included to convert complex singularities to pure imaginary (red).

For instance, let us consider a filter with TZs $P_1(s) = \{2.3, -1.6, 1.6, -1.8, 2\}$ from Table 6.7 and $RL = 12$ dB. If we apply a -55 dB source-to-load coupling, the updated roots are $P_1'(s) = \{2.92, -1.56, 1.65 + 0.16j, -1.89, 1.65 - 0.16j\}$. By introducing a -45 dB between resonator 2 and load node (Figure 6.23), the roots of the updated polynomial $P_1''(s) = \{2.92, -1.56, 1.6, -1.91, 1.76\}$. Without modifying the input and output phases, the admittance inverters are $J_k = \{1, -1, 1, -1, 1, -1.159\}$. By applying $\psi = 18.74°$ and $\phi = -33.86°$ and performing the extraction procudure again, the last admittance inverter J_6 is equalized to -1.

The additive phase terms also change slightly the values of extracted elements, including the resonance frequencies of the resonators. The roots of the updated polynomial are now $P_1''(s) = \{2.90, -1.57, 1.56, -1.90, 1.77\}$. The result from both extraction procedure yields can be compared in Table 6.9. The filter response coincides with Figure 6.20.

Table 6.8: $P(s)$ roots at each step of the complex TZ removal

	Ω_k^1	Ω_k^2	Ω_k^3	Ω_k^4	Ω_5^k
$P_1(s)$	2.05	-1.49	1.5	-3.42	1.49
$P_2(s)$	2.61	-1.48	$1.41 + 0.15j$	-3.92	$1.41 - 0.15j$
$P_3(s)$	2.61	-1.48	1.52	-4.27	1.40

Table 6.9: Lowpass elements of the synthesized 5th-order ladder filter with two cross-couplings to load, before and after the phase correction.

	$\psi = \phi = 0°$			$\psi = 18.74°, \phi = -33.86°$		
	B_k	b_k	J_{rk}	B_k	b_k	J_{rk}
Res. 1	-3.5455	-2.92	3.2291	-3.3129	-2.90	3.0391
Res. 2	1.6443	1.56	1.4658	1.8442	1.57	1.5574
Res. 3	-2.9224	-1.60	2.1365	-2.5908	-1.56	2.0050
Res. 4	1.9673	1.91	1.8889	2.1862	1.90	1.9812
Res. 5	-2.4389	-1.76	1.8390	-1.8574	-1.77	1.7457
B_S	-0.2463			-0.4302		
B_L	-0.6399			-0.2902		

6.3   Chapter Summary

In this chapter, a synthesis methodology for the design of filters with cross-couplings has been presented. This approach is intended to be a step forward in the process to define arbitrary cross-couplings in ladder-type networks for acoustic wave resonators.

First, two topologies provide a robust mathematical procedure for filter synthesis. The technique is based on the combination of inline network along with parallel-connected structures. A general method has been described in other to obtain networks that provide the exact lowpass structure required and the parameter's values. The method has been applied for two specific cases, ground-loop inductor structures and L-C coupling between resonators. Through two different synthesis examples, the method has been rigorously proved and assets the capability to be used to implement a myriad of filters topologies based on the two types of cross-couplings proposed considering adjacent and non-adjacent resonators.

Secondly, it has been proposed a method that provides the network parameters to consider leakage paths different than the main signal as a design parameter. It has been demonstrated that electrical cross-couplings will convert some pure imaginary resonant frequencies into complex if it is strong enough. In this case, the OoB rejection will be degraded since AW technology is not able to construct such complex singularities. However, the transmission response can be recovered by adding a second cross-coupling in the proper allocation. Despite converting some of the resonance frequencies into purely imaginary again, their values are not the originally prescribed. Some may be detuned far away from the center frequency, causing inaccuracies with the bandpass transformation because it is a narrow-band approximation.

Conclusions and Future Work

7.1 Conclusions

The already in deployment 5G telecommunication network for commercial use and the ever-increasing stringent requirements of filters for mobile communication is spurring all manufactures to provide better filtering solutions for the new generation set of bands. The technological improvements make possible to achieve higher levels of performance, wider bandwidth, smaller chip size and better reliability. Although the technology delimits the maximum achievable performance, having the right synthesis techniques is crucial to obtain the best results from it. The objective of this research has focused on the theoretical analysis of general synthesis techniques for the design of filters based on acoustic wave technology which main goal was to explore new topologies beyond the widely used classic ladder filter.

Chapter 2 gives an overview of the acoustic wave technology, their capabilities, strengths and weaknesses. At the present time, Acoustic wave technology is the only one that can satisfy the current and forthcoming requirements of the mobile communication standards, the most recent type of resonators like I.H.P. SAW, LLSAW and XBAR represent a significant improvement that may help to overcome the limits of the already mature technologies.

The filters design begins with the definition of the filtering function and the lowpass prototype extraction. The basic building blocks of an acoustic filter are the resonators. To establish a link between the physical resonator and the network prototype is necessary to create an accurate mathematical model. For this purpose, the BVD equivalent circuit models the acoustic wave resonator reasonably good. This helps to simulate and analyze the network in the first stages of the design process.

Even at this level in which electromagnetic behavior of the physical resonator is not considered, some technological constraints can be taken into account to orient the synthesis toward a realizable filter with

121

a good performance. The most important parameter of the resonator like electromechanical coupling coefficient, quality factor, insertion loss, and power handling have been discussed.

To design a filter from the most elemental specifications, TZs, network order, and return losses, a robust method is required. In Chapter 3, a general class of Chebyshev filtering function has been introduced. The outcome of the function synthesis is the characteristic polynomials that define the transmission and reflection response of the network. They have been connected to the lowpass inline topology. Its parameters are entirely determined by a general synthesis procedure in which every parameter is obtained through a recursive extraction method. The versatility of the synthesis methodology described in this work is capable of providing different topologies, especially the realization of fully canonical filters, which lowpass prototype is directly linked to the ladder filter used in acoustic wave technology.

To analyze the lowpass prototype, the coupling matrix arrangement of the network in his nodal scheme in both lowpass and bandpass is a fast and easy to use representation tool for the simulation and analysis of the network. The coupling matrix is flexible enough to support the same functionality for other types of topologies like cross-coupled explored in the chapters 5 and 6.

The synthesis methodology provides the exact parameters to reproduced the filtering function. However, there is no guarantee that the result is realizable by acoustic wave technology. In ladder networks, the series resonators are modeled as a dangling resonator flanked by admittance inverters with the same value at opposite sign. Each resonator resonates at one of the frequencies of the prescribed TZs. When they are arranged symmetrically along the topology, all the main-line admittance inverter posses the necessary values. With other configurations, one of the admittance inverters takes a different value than the rest during the extraction procedure. This occurs because the filtering function assumes a symmetric response in the sense that the input and output phases of the S-parameters are the same. Taking the central resonator as a pivot or 'center of symmetry', the network that produces a non-evenly distributed inverters lacks such symmetry.

To overcome this situation, in Chapter 4 is proposed a method to amend the phase correction of the characteristic polynomials unequivocally. Analyzing the pattern traced by the combination of the input and output additive phase terms, two differentiated geometrical models have been elaborated for even- and odd-order filters. The method can address two important aspects during the synthesis at the same time: the homogenization of the admittance inverters in the main-line, and it also helps to provide a balanced input port in multiplexers through phase adjustment to avoid loading effects and to have all the filters with a uniform value of admittance inverters. A previous solution to achieve similar results suggested a circuital transformation of part of the network to equalize the inverters. However, that solution does not apply to every situation. The input and output phase correction described in this work is a general method that provides a better understanding of the previous solution and enables to obtain all possible combinations.

The ladder network is one of the most employed topologies for acoustic wave technology. Despite

being a useful and well-established solution, it presents some drawbacks, the required alternation of TZs above and below the passband set a limitation to obtain greater out-of-band (OoB) rejection levels. The Chapters 5 and 6 address a different approach than the ladder, creating a new paradigm that moves away extracted-pole technique in which the prescribed TZs of the filtering function meets with the resonance frequencies to a new space of mixed-topologies where the whole structure provides the TZs. This approach expands the maximum number of achievable configurations for the same filtering function, providing more flexibility to define the resonator parameters like the K_{eff}^2. Therefore, it creates more options to accommodate the synthesized network to the acoustic wave technology. In addition to the already mentioned characteristics, the methodology enables the filter synthesis with a more flexible assignation of TZs to the resonators, for instance, maximizing an arbitrary number of TZs in the above or below the passband.

In Chapter 5, the general synthesis method for fully canonical filters based on mixed-topology networks has been presented. Using the fundamentals of the synthesis method, the procedure to define two different topologies have been described. The first allows to implement a central section of an arbitrary number of dangling resonators in a parallel configuration with a classic inline section at both sides. While the outer sections are conventional ladder sub-networks in which the resonance frequencies meet with the TZs, the central section grants a more free selection of the resonance frequencies. In the second topology, a ladder section is in parallel with an arbitrary number of resonators stuck above the inline sub-network. In this case, none of the resonance frequencies meet with the TZs, and those dangling resonators in parallel-connected configurations have not restrictions to choose a convenient value.

Regardless of the advantages of this new method, the production of suitable networks for acoustic wave technology can be achieved only by a thoughtful selection of the network parameters. At the end of the chapter, a detailed explanation to guide the extraction process to achievable networks has been provided, in which the selection of resonance frequencies, serialization of resonators, eigenvalue grouping, and the management of junction nodes (external reactive elements), are discussed.

Chapter 6 has used the same methodology to create a systematic method for cross-coupled filters with reactive elements that are in use for current filter design, but no synthesis method has been developed. The GLI topology consists of two shunt resonators coupled to each other and connected to ground through a common inductor. When they are added after the network synthesis, it introduces an additional TZ in a region far away of the passband (above or below), detuning in the process the TZs at each side of the passband. Both effects improve the rejection level in the OoB region where the TZ is introduced but at the expense of deteriorating the filtering function. A different topology, the LCC, is made of an inductor that couples a shunt resonator to ground and a series capacitor that couples a series resonator to the inductor. The effects on the filtering function are similar to the one shown by the GLI. It requires two external elements, but the impact is more notorious with lower values of the reactive elements.

The proposed method has proved to be capable of generating, by synthesis, the requires parameters to create the lowpass equivalent topology that generally is obtained by optimization. Not only produce the

required topology but also with the exact elements for the lowpass structure ready for a direct bandpass transformation. It also provides the designer with an understating of how what should be added to the network in order to obtain the initial response without degrading the filter performance.

Additionally, the synthesis methodology described in Chapter 3 has been used to solve and explain the effects of undesired couplings like electromagnetic feedthrough bypassing the package ports in AW filter. Such couplings may cause a severe limitation of cross-isolation levels in multiplexers, a degraded response and transmission zeros vanishing in standalone filters. The proposed synthesis technique considers these leakage paths as a design parameter to avoid its negatives effects, adapting the network to them.

The theory presented in this document has the intention of pushing forward the synthesis techniques for the design of acoustic wave filters beyond the classic ladder filter. During the Ph.D. program, different software tools have been created. They allow the design of each topology proposed in every step, from the definition of the filter specifications to the bandpass transformation of the network. They are an agile tool for the design of diverse solutions to find the filtering network that can satisfy the mask specifications and the technological constraints.

7.2 Future Work

This dissertation is an attempt to expand the design possibilities for filters in acoustic wave technology, new topologies that aim to improve the performance and help designers to find feasible the filters to deal effectively with the requirements of 4G and 5G network standards. However, there are still some open challenges that need to be addressed. Some possible future work on this field include the following:

1. New 5G standards require filters with great bandwidths like bands n77, n78 and n79, that have FBW over 11%. This is a great challenge to address their requirements, especially in AW technology. Large bandwidths require strong k_{eff}^2 that to the date none commercial acoustic technology is able to provide. Recently, one XBAR n79 filter prototype has been presented [42]. Although it is a remarkable achievement, having resonators with $k_{eff}^2 \simeq 24\%$. Commercial AW devices can achieve a maximum k_{eff}^2 about 9%. With the synthesis techniques described in this document, it is possible to attain large bandwidths with coupling factors that can be manufactured in current commercial AW technology. For example, the class I 7th-order network in Figure 7.1b implements a n79 band filter with a $k_{eff}^2 \simeq 6.6\%$. Resonator 4 needs to adjust its k_{eff}^2, but this can be fixed with an external capacitor C_{ext} shown in the network scheme. The prototype elements are provided in Table 7.1.

   Further research can be conducted to delimit the applicability of mixed-topology networks to create filters with arbitrary k_{eff}^2. Thus the technology constraints can be fulfilled more effectively from the synthesis point of view.
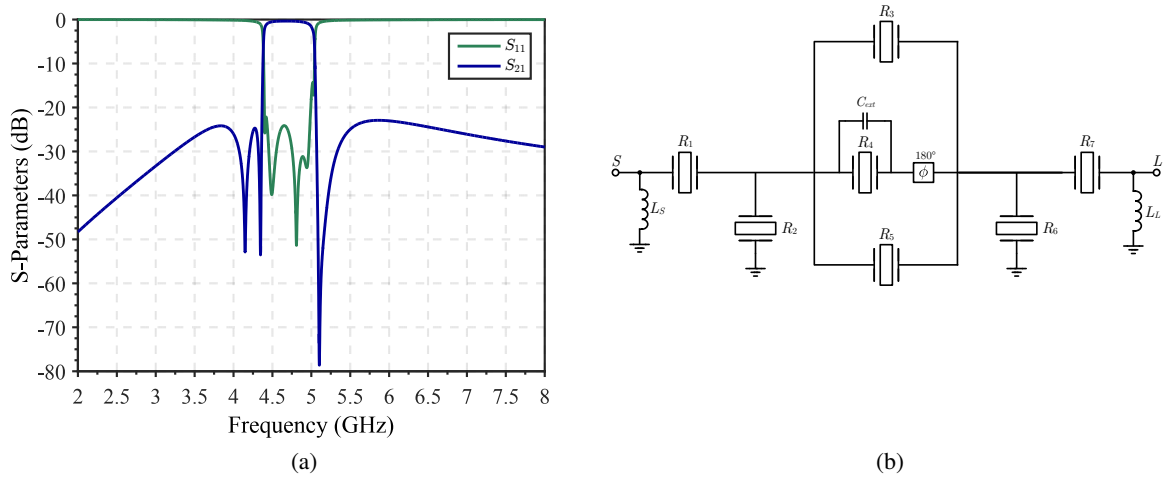
Figure 7.1: AW scheme of the n79 filter with a phase shifter in resonator 4, and the S-parameters simulation using the BVD model.

Table 7.1: Bandpass elements of the synthesized n79 filter with a $180°$ phase shift.

	L_a (nH)	C_a (fF)	C_0 (pF)	$k_{eff}^2(\%)$
Res 1&7	5.30	193.18	3.41	6.59
Res 2&6	22.66	59.48	1.04	6.64
Res 3	57.20	22.81	0.40	6.62
Res 4	17.55	67.29	0.44	6.6
Res 5	57.16	18.03	0.32	6.59
Source	0.78 nH			
Load	0.78 nH			
C_{ext}	0.28 pF			

2. It has been observed that the software tools developed show accuracy issues for high order filters during the extraction procedure. The numerical instabilities appear due to the finite numerical representation of the network parameters. The deviation from the exact parameter value at some point during the extraction procedure provokes accumulative errors that grow exponentially, making the lowpass prototype response to losing resemblance with original filtering function or producing no realizable parameters. For fully canonical networks, the created software tools show applicability limitations in 12th-order and higher using standard double-precision arithmetic. In case of a network that combines extracted-pole sections (at finite frequency) with resonating node extractions (at infinite frequency), the instability has been observed at 9th-order filters. In this regard, a research could be conducted to solve the discretization errors and reduce the instability of the iterative method to increase the highest order filter achievable.

3. The mixed-topology synthesis techniques shown in this thesis used the transversal networks to create dangling resonators. The distribution of the eigenvalues and its associated couplings impact directly on the parameters of the resonators. Depending on how the eigenvalue dedicated for each

branch are grouped, complex resonance frequencies may appear, resulting in a non-feasible resonator in acoustic wave technology. A precise analysis of the resonance frequency formation from the arbitrary grouping of part of the eigenvalues can provide more accurate control of the synthesis procedure.

4. In this work, the used of parallel-connected and cross-coupled topologies has been introduced. To simulate such complex networks, a coupling matrix representation in both lowpass and bandpass domain has been proposed. The adaptation of the losses from the mBVD to a nodal scheme network representation will provide a more realistic simulation of the filter and a fast calculation of the energy stored by individual resonators. This will dramatically increase the coupling matrix size. However, a first estimation of the energy will help the designer to know if the resonator multiplicity is necessary, giving the possibility to reconfigure the filter in the lowpass domain to obtain a better energy distribution over the resonators.

5. In this dissertation, the filters are assumed to be two-port networks terminated with real reference impedances at both ends. Nevertheless, there are some situations in with the filters in the RF chain are connected devices with a complex impedance value, like the impedance of an antenna port or the input/output impedance of a power amplifier [105–107]. In such cases is required to design matching networks to fulfill the design requirement. Some works explore synthesis with complex load impedances [108–110]. Complementing the methodology of the topologies presented in this works with complex terminated network synthesis, they could be applied to more diverse and complex designs.

Lowpass-to-Bandpass Transformation of the Coupling Matrix Elements

The coupling matrix elements transformation from lowpass to bandpass domain can be done by comparing the admittance expression of the lowpass and bandpass circuits. Although the lowpass model of AW resonators is the same for series and shunt resonators, they are covered separately. As the resonator is described with three elements, we require unless three equations to determine them completely. For such purpose, the first and second derivate, with respect to ω, of each admittance expression is provided.
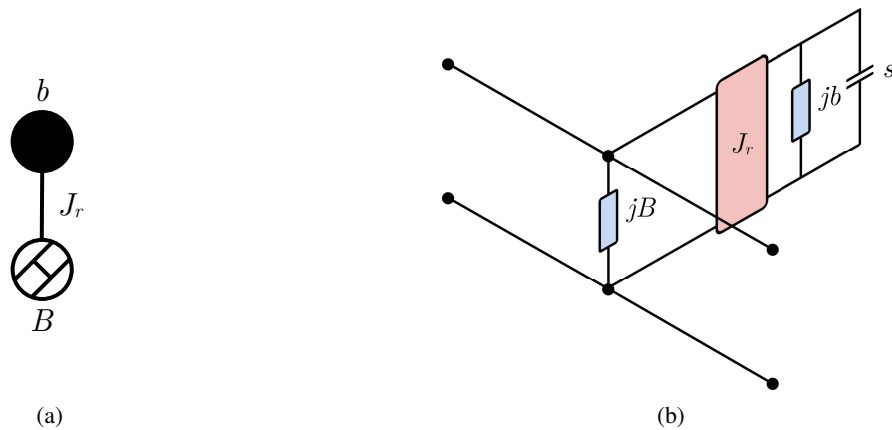
Figure A.1: Nodal resonator model (a) and its equivalent circuital lowpass prototype. (b).

A.1   Lowpass Equivalent Model

The lowpass resonator can be modeled by a dangling resonator coupled to an NRN as depicted in Figure A.1. The admittance of the resonator is expressed as

$$Y_{LP} = jB + \frac{J_r^2}{j\Omega + jb},$$ (A.1)

where the normalized frequency Ω is defined as

$$\Omega = FBW\left(\frac{\omega}{\omega_0} - \frac{\omega_0}{\omega}\right).$$ (A.2)

The first derivative is

$$\frac{\partial Y_{LP}}{\partial \omega} = -\frac{jJ_r^2 FBW\left(\frac{\omega}{\omega_0^2} + \frac{1}{\omega_0}\right)}{\left[jb + jFBW\left(\frac{\omega}{\omega_0} - \frac{\omega_0}{\omega}\right)\right]^2},$$ (A.3)

and the second derivative is

$$\frac{\partial^2 Y_{LP}}{\partial \omega^2} = j^2 \frac{2J_r^2 FBW^2\left(\frac{\omega}{\omega_0^2} + \frac{1}{\omega_0}\right)^2}{\left[jb + jFBW\left(\frac{\omega}{\omega_0} - \frac{\omega_0}{\omega}\right)\right]^3} + j\frac{2J_r^2 FBW\omega_0}{\omega^3\left[jb + jFBW\left(\frac{\omega}{\omega_0} - \frac{\omega_0}{\omega}\right)\right]^2}.$$ (A.4)

By evaluating equations (A.1), (A.3) and (A.4) at the center frequency $\omega = \omega_0$, the result is:

$$Y_{LP}(\omega = \omega_0) = jB - j\frac{J_r^2}{b},$$ (A.5a)

$$Y_{LP}'(\omega = \omega_0) = j\frac{2J_r^2 FBW}{b^2\omega_0},$$ (A.5b)

$$Y_{LP}''(\omega = \omega_0) = -jJ_r^2\frac{8FBW^2 + 2bFBW}{b^3\omega_0^2}.$$ (A.5c)

A.2   Bandpass Equivalent Model

The lowpass acoustic resonator can be modeled similarly like the lowpass model, but we can distinguish different configurations for series and shunt resonators.

A.2.1   Series Resonator

The series resonator admittance in bandpass domain can be expressed as

$$Y_{BP} = \frac{-j}{\omega B_x} + \frac{J_r^2}{j\omega C_x + \frac{1}{j\omega b_x}}.$$ (A.6)

(a)   (b)
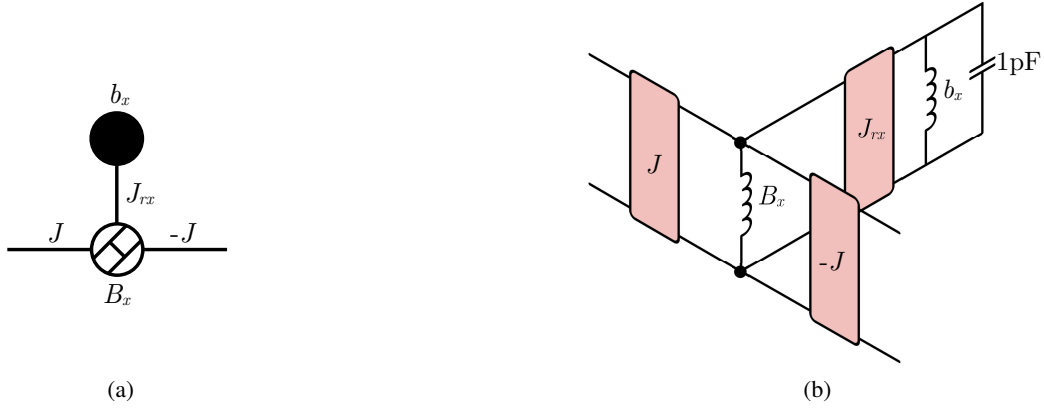
Figure A.2: Nodal series resonator model (a) in lowpass domain and (b) its equivalent circuital bandpass prototype.

The first derivative is given by

$$\frac{\partial Y_{BP}}{\partial \omega} = \frac{j}{\omega^2 B_x} - \frac{J_{rx}^2 \left(jC_x - \frac{1}{jb_x\omega^2} \right)}{\left(jC_x\omega + \frac{1}{jb_x\omega} \right)^2}, \tag{A.7}$$

and the second derivative is

$$\frac{\partial^2 Y_{BP}}{\partial \omega^2} = -\frac{2j}{\omega^3 B_x} + \frac{2J_{rx}^2 \left(jC_x - \frac{1}{jb_x\omega^2} \right)^2}{\left(jC_x + \frac{1}{jb_x\omega} \right)^3} + j\frac{2J_{rx}^2}{b_x\omega^3 \left(jC_x\omega + \frac{1}{jb_x\omega} \right)^2}. \tag{A.8}$$

By evaluating equations (A.6), (A.7) and (A.8) at the center frequency $\omega = \omega_0$ the result is

$$Y_{BP}(\omega = \omega_0) = jB_x\omega_0 - j\frac{J_{rx}^2 b_x \omega_0}{\omega_0^2 C_x b_x - 1}, \tag{A.9a}$$

$$Y'_{BP}(\omega = \omega_0) = jB_x + j\frac{J_{rx}^2 b_x \left(\omega_0^2 C_x b_x + 1 \right)}{\left(\omega_0^2 C_x b_x - 1 \right)^2}, \tag{A.9b}$$

$$Y''_{BP}(\omega = \omega_0) = -j\frac{2J_{rx}^2 b_x \left(\left(\omega_0^2 C_x b_x + 1 \right)^2 + \left(\omega_0^2 C_x b_x - 1 \right) \right)}{\omega_0 \left(\omega_0^2 C_x b_x - 1 \right)^3}. \tag{A.9c}$$

A.2.2 Shunt Resonator

The shunt resonator admittance in bandpass can be expressed as

$$Y_{BP} = j\omega B_x + \frac{J_r^2}{j\omega C_x + \frac{1}{j\omega b_x}}. \tag{A.10}$$
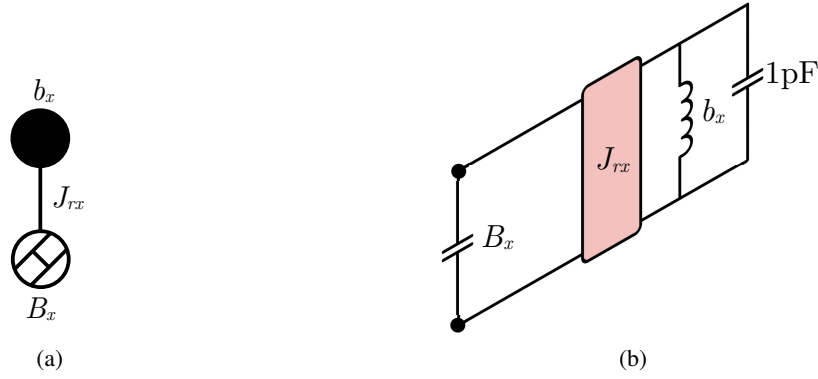
Figure A.3: Nodal shunt resonator model (a) in lowpass domain and its equivalent circuital bandpass prototype. (b).

The first derivative is given by

$$\frac{\partial Y_{BP}}{\partial \omega} = jB_x - \frac{J_{rx}^2\left(jC_x - \frac{1}{jb_x\omega^2}\right)}{\left(jC_x + \frac{1}{jb_x\omega}\right)^2},$$ (A.11)

and the second derivative is

$$\frac{\partial^2 Y_{BP}}{\partial \omega^2} = \frac{2J_{rx}^2\left(jC_x - \frac{1}{jb_x\omega^2}\right)^2}{\left(jC_x + \frac{1}{jb_x\omega}\right)^3} + j\frac{2J_{rx}^2}{b_x\omega^3\left(jC_x\omega + \frac{1}{jb_x\omega}\right)^2}.$$ (A.12)

By evaluating equations (A.10), (A.11) and (A.12) at $\omega = \omega_0$ the result is

$$Y_{BP}(\omega = \omega_0) = jB_x\omega_0 - j\frac{J_{rx}^2 b_x\omega_0}{\omega_0^2 C_x b_x - 1},$$ (A.13a)

$$Y'_{BP}(\omega = \omega_0) = jB_x + j\frac{J_{rx}^2 b_x\left(\omega_0^2 C_x b_x + 1\right)}{\left(\omega_0^2 C_x b_x - 1\right)^2},$$ (A.13b)

$$Y''_{BP}(\omega = \omega_0) = -j\frac{2J_{rx}^2 b_x\left(\left(\omega_0^2 C_x b_x + 1\right)^2 + \left(\omega_0^2 C_x b_x - 1\right)\right)}{\omega_0\left(\omega_0^2 C_x b_x - 1\right)^3}.$$ (A.13c)

A.3   Lowpass-to-Bandpass Transformation

To calculate the equivalence between the lowpass and bandpass nodal parameters, the admittance expressions and their respective derivatives in (A.9) and (A.13) must be equal.

A.3.1 Series Resonator

The first element to determine is b_x, and the process begins setting the lowpass and bandpass admittances equal to each other. The following variable substitution for series resonators has been used to simplify the expression:

$$
\begin{aligned}
\Phi &= \omega_0^2 C_x b_x - 1, \\
\Gamma &= \omega_0^2 C_x b_x + 1, \\
\alpha &= \frac{Bb - J_r^2}{b}, \\
\lambda &= \frac{2J_r^2 FBW}{b^2}, \\
\xi &= J_r^2 \frac{4FBW^2 + bFBW}{b^3}.
\end{aligned}
\tag{A.14}
$$

By equating $Y_{LP}(\omega_0) = Y_{BP}(\omega_0)$ for the series resonator, the expression results in:

$$
\frac{1}{B_x \omega_0} = -\left(\alpha + \frac{J_{rx}^2 b_x \omega_0}{\Phi}\right).
\tag{A.15}
$$

Next, the same operation is done with the first derivative $Y'_{LP}(\omega_0) = Y'_{BP}(\omega_0)$.

$$
\frac{1}{B_x \omega_0} = \lambda - \frac{J_{rx}^2 b_x \Gamma \omega_0}{\Phi^2}.
\tag{A.16}
$$

The two equations, (A.15) and (A.16), are equated to each other and the expression solved for $J_{rx}^2 b_x$.

$$
J_{rx}^2 b_x = \frac{\Phi^2}{\omega_0} \frac{\lambda + \alpha}{\Gamma - \Phi}
\tag{A.17}
$$

In third place, the second derivatives are equated: $Y''_{LP}(\omega_0) = Y''_{BP}(\omega_0)$.

$$
\frac{\xi}{\omega_0} = \frac{1}{B_x \omega_0^2} + \frac{J_{rx}^2 b_x (\Gamma^2 + \Phi)}{\Phi^3}
\tag{A.18}
$$

The term $\frac{1}{B_x \omega_0}$ from (A.15) is substituted in the either equations and the expression is simplified.

$$
\frac{\xi - \lambda}{\omega_0} = \frac{J_{rx}^2 b_x (\Gamma^2 + \Phi - \Gamma\Phi)}{\Phi^3}
\tag{A.19}
$$

The parameters $J_{rx}^2 b_x$ from (A.16) are substituted in the equation and the operating continue to determine b_x.

$$
\frac{\xi - \lambda}{\lambda + \alpha} = \frac{2\Gamma + \Phi}{2\Phi}
\tag{A.20}
$$

For further simplification, the following variable substitution is carried out:

$$
\begin{aligned}
x &= \omega_0^2 C_x b_x, \\
\Phi &= x - 1, \\
\Gamma &= x + 1, \\
\eta_{se} &= \frac{\xi - \lambda}{\lambda + \alpha}.
\end{aligned}
\tag{A.21}
$$

The equation (A.20) is rewritten as

$$\eta_{se} = \frac{2(x+1) + x - 1}{2(x-1)} \rightarrow \eta_{se} = \frac{3x+1}{2(x-1)}. \tag{A.22}$$

Now, we can solve for b_x as

$$x = \frac{1 + 2\eta_{se}}{2\eta_{se} - 3} \rightarrow b_x = \frac{1 + 2\eta_{se}}{2\eta_{se} - 3} \frac{1}{\omega_0^2 C_x}. \tag{A.23}$$

Finally, the equations to determine J_{rx} and B_x can be obtained as

$$J_{rx} = \left(\frac{1 + 2\eta_{se}}{2\eta_{se} - 3} - 1 \right) \sqrt{\frac{(\lambda + \alpha)(2\eta_{se} - 3)\omega_0 C_x}{2(1 + 2\eta_{se})}}, \tag{A.24a}$$

$$B_x = \frac{1}{\omega_0} \frac{2\eta_{se} - 3}{\alpha(1 - 2\eta_{se}) - 2\lambda}. \tag{A.24b}$$

A.3.2   Shunt Resonator

The first element to determine is b_x, and the process begins by setting the lowpass and bandpass admittances equal to each other. By equating $Y_{LP}(\omega_0) = Y_{BP}(\omega_0)$ for the shunt resonator, the expression results in

$$j\alpha = jB_x\omega_0 - j\frac{J_{rx}^2 b_x \omega_0}{\Phi},$$
$$B_x = \frac{\alpha}{\omega_0} + \frac{J_{rx}^2 b_x}{\Phi}. \tag{A.25}$$

Next, the same operation is done with the first derivatives $Y'_{LP}(\omega_0) = Y'_{BP}(\omega_0)$.

$$j\frac{\lambda}{\omega_0} = jB_x + j\frac{J_{rx}^2 b_x \Gamma}{\Phi^2},$$
$$B_x = \frac{\lambda}{\omega_0} - \frac{J_{rx}^2 b_x \Gamma}{\Phi^2}. \tag{A.26}$$

The resulting equations (A.25) and (A.26) are equated to each other, and it is solved for $J_{rx}^2 b_x$.

$$\frac{\alpha}{\omega_0} + \frac{J_{rx}^2 b_x}{\Phi} = \frac{\lambda}{\omega_0} - \frac{J_{rx}^2 b_x \Gamma \omega_0}{\Phi^2},$$
$$J_{rx}^2 b_x = \frac{\lambda - \alpha}{\omega_0} \frac{\Phi^2}{\Phi + \Gamma}. \tag{A.27}$$

In third place, the second derivatives are equated: $Y''_{LP}(\omega_0) = Y''_{BP}(\omega_0)$.

$$-2j\frac{\xi}{\omega_0^2} = -2j\frac{J_{rx}^2 b_x \left(\Gamma^2 + \Phi \right)}{\omega_0 \Phi^3}. \tag{A.28}$$

Now, $J_{rx}^2 b_x$ from (A.27) is substituted into the equation to determine b_x and then, the expression is simplified.

$$\frac{\xi}{\lambda - \alpha} = \frac{\Gamma^2 + \Phi}{\Phi(\Phi + \Gamma)} \tag{A.29}$$

For further simplification, the following variable substitution is carried out:

$$\eta_{sh} = \frac{\xi}{\lambda - \alpha}, \tag{A.30}$$

using (A.21) and (A.30), equation (A.29) can be rewritten as

$$\eta_{sh} = \frac{(x+1)^2 + x - 1}{(x-1)(x+1+x-1)} = \frac{x+3}{2(x-1)}. \tag{A.31}$$

Finally, b_x is defined by

$$x = \frac{3 + 2\eta_{sh}}{2\eta_{sh} - 1} \rightarrow b_x = \frac{3 + 2\eta_{sh}}{2\eta_{sh} - 1} \frac{1}{\omega_0^2 C_x}. \tag{A.32}$$

Now, the parameters J_{rx} and B_x can be obtained with the following expressions:

$$J_{rx} = \left(1 - \frac{2\eta - 1}{3\eta + 2}\right)\sqrt{\frac{\omega_0 Cx(\lambda - \alpha)}{2}}, \tag{A.33a}$$

$$B_x = \frac{1}{\omega_0}\left[\alpha + \frac{\lambda - \alpha}{2}\left(1 - \frac{2\eta_{sh} - 1}{3\eta_{sh} + 2}\right)\right], \ or \tag{A.33b}$$

$$B_x = \frac{1}{\omega_0}\left[\lambda - \frac{\lambda - \alpha}{2}\left(1 + \frac{2\eta_{sh} - 1}{3\eta_{sh} + 2}\right)\right]. \tag{A.33c}$$

A.4 Bandpass-to-Lowpass Transformation

To calculate the lowpass nodal parameters from the bandpass parameters, the admittance expressions and their derivatives in (A.9) and (A.13) must be equated as it has been done in the previous section.

A.4.1 Series Resonator

The first element to determine is the constant susceptance b, and the process begins setting the lowpass and bandpass admittances equal to each other. To simplify the expressions, the following variable substitution for series resonators has been used:

$$\begin{aligned}
\Phi &= \omega_0^2 C_x b_x - 1, \\
\Gamma &= \omega_0^2 C_x b_x + 1, \\
\theta &= B_x \Phi^2 + J_{rx}^2 b_x \Gamma, \\
\sigma &= \Phi^2 + J_{rx}^2 b_x B_x \Gamma \omega_0^2, \\
T &= \Phi^3 + J_{rx}^2 (\Gamma^2 + \Phi) B_x b_x \omega_0^2.
\end{aligned} \tag{A.34}$$

The first step is to equate $Y_{LP}(\omega_0) = Y_{BP}(\omega_0)$ for the series resonator and solve for B, the expression results in

$$jB - \frac{J_r^2}{b} = -\frac{1}{jB_x\omega_0} - j\frac{J_{rx}^2 b_x \omega_0}{\Phi},$$

$$B = \frac{J_r^2}{b} - \frac{\Phi + J_{rx}^2 B_x b_x \omega_0^2}{\Phi B_x \omega_0}. \tag{A.35}$$

Next, the same operation is done with the first derivatives $Y'_{LP}(\omega_0) = Y'_{BP}(\omega_0)$.

$$j\frac{2J_r^2 FBW}{b^2\omega_0} = \frac{1}{jB_x\omega_0^2} + j\frac{J_{rx}^2 b_x \Gamma}{\Phi^2},$$

$$J_r^2 = \frac{b^2\sigma}{2FBW\Phi^2 B_x\omega_0}. \tag{A.36}$$

In third place, the lowpass and bandpass second derivatives are set equal to each other.

$$-2jJ_r^2\frac{4FBW^2 + bFBW}{b^3\omega_0^2} = \frac{-2j}{B_x\omega_0^3} - 2j\frac{J_{rx}^2 b_x\left(\Gamma^2 + \Phi\right)}{\omega_0\Phi^3},$$

$$\frac{J_r^2\left(4FBW^2 + bFBW\right)}{b^3} = \frac{\Phi^3 + J_{rx}^2(\Gamma^2 + \Phi)B_x b_x\omega_0^2}{\Phi^3 B_x\omega_0}. \tag{A.37}$$

Now, the parameter J_r^2 from (A.36) is substituted into (A.37), and we can proceed to solve for b as

$$\frac{b^2\sigma}{2FBW\Phi^2 B_x\omega_0}\frac{J_r^2\left(4FBW^2 + bFBW\right)}{b^3} = \frac{T}{\Phi^3 B_x\omega_0},$$

$$\frac{\sigma}{2FBW}\frac{J_r^2\left(4FBW^2 + bFBW\right)}{b} = \frac{T}{\Phi}. \tag{A.38}$$

$$\sigma\Phi\left(2FBW + b\right) = 2Tb.$$

$$b = \frac{4FBW\sigma\Phi}{2T - \sigma\Phi}.$$

After obtaining the first parameter, the equations to determine J_r is

$$J_r^2 = \left[\frac{4FBW\sigma\Phi}{2T - \sigma\Phi}\right]^2\frac{b^2\sigma}{2FBW\Phi^2 B_x\omega_0},$$

$$J_r = \frac{\sigma}{2T - \sigma\Phi}\sqrt{\frac{8FBW}{B_x\omega_0}}. \tag{A.39}$$

Finally, the expression for B is obtained by substituting J_r^2 from (A.39) in (A.35).

$$B = \frac{b^2\sigma}{2FBW\Phi^2 B_x\omega_0}\frac{1}{b} - \frac{\Phi + J_{rx}^2 B_x b_x\omega_0^2}{\Phi B_x\omega_0} \tag{A.40}$$

By substituting b from (A.38) and using the substitutive expressions in (A.34), B can be further simplified to

$$B = \frac{2\sigma^2}{B_x\left(2T - \sigma\Phi\right)\omega_0} - \frac{\Phi + J_{rx}^2 B_x b_x\omega_0^2}{\Phi B_x\omega_0}. \tag{A.41}$$

A.4.2   Shunt Resonator

The process to determine the equations is done by setting the lowpass and bandpass admittances equal to each other, as in the previous cases. Let us start with the admittance expressions and solve for B.

$$jB - \frac{J_r^2}{b} = jB_x\omega_0 - j\frac{J_{rx}^2 b_x\omega_0}{\Phi},$$

$$B = \frac{J_r^2}{b} + \omega_0\left(\frac{B_x\Phi - J_{rx}^2 b_x}{\Phi}\right). \tag{A.42}$$

Next, the same operation is done with the first derivative $Y'_{LP}(\omega_0) = Y'_{BP}(\omega_0)$.

$$
\begin{aligned}
j\frac{2J_r^2 FBW}{b^2\omega_0} &= jB_x + j\frac{J_{rx}^2 b_x \Gamma}{\Phi^2}, \\
J_r^2 &= \frac{b^2\omega_0}{2FBW}\frac{\theta}{\Phi^2}.
\end{aligned}
\tag{A.43}
$$

In third place, the lowpass and bandpass second derivatives are set equal to each other.

$$
\begin{aligned}
-2jJ_r^2\frac{4FBW^2 + bFBW}{b^3\omega_0^2} &= -2j\frac{J_{rx}^2 b_x\left(\Gamma^2 + \Phi\right)}{\omega_0\Phi^3}, \\
J_r^2\frac{4FBW^2 + bFBW}{b^3\omega_0} &= \frac{J_{rx}^2 b_x\left(\Gamma^2 + \Phi\right)}{\Phi^3}.
\end{aligned}
\tag{A.44}
$$

Now, the parameter J_r^2 from (A.43) is substituted into (A.44) and procedure continues solving for b.

$$
\begin{aligned}
\frac{b^2\omega_0}{2FBW}\frac{\theta}{\Phi^2}\frac{4FBW^2 + bFBW}{b^3\omega_0} &= \frac{J_{rx}^2 b_x\left(\Gamma^2 + \Phi\right)}{\Phi^3}, \\
\frac{\theta}{2b}\left(4FBW + b\right) &= \frac{J_{rx}^2 b_x\left(\Gamma^2 + \Phi\right)}{\Phi}, \\
b &= \frac{4FBW\,\Phi\theta}{2J_{rx}^2 b_x\left(\Gamma^2 + \Phi\right) - \Phi\theta}.
\end{aligned}
\tag{A.45}
$$

After finding the expression for b, the parameters J_r and B can be obtained substituting (A.45) in (A.43),

$$
J_r = \frac{\sqrt{8FBW\theta^3}}{\left[2J_{rx}^2 b_x\left(\Gamma^2 + \Phi\right) - \Phi\theta\right]}.
\tag{A.46}
$$

Finally, B can be determined by substituting b from (A.45) and J_r^2 from (A.46) in (A.42).

$$
B = \frac{\omega_0}{\Phi}\left[\frac{2\theta^2}{2J_{rx}^2 b_x\left(\Gamma^2 + \Phi\right) - \Phi\theta} + B_x\Phi - J_{rx}^2 b_x\right].
\tag{A.47}
$$

Network Transformation from Singlet to Dangling

The lowpass prototype of a BVD resonator model can be represented with two different configurations, the singlet trisection and the dangling resonator. The first consists of three nodes coupled to each other, as shown in Figure B.1a. The equivalent dangling resonator is made of three elements, a resonant node made of a unit capacitor in parallel with a constant reactance b, an NRN B, and an admittance inverter J_r coupling each node. This structure is coupled to two nodes by admittance inverters as depicted in Figure B.1b. The transformation procedure to obtain one structure from the other is described in [111]. In this appendix, the transformation is particularized to the generation of the dangling resonator with unitary admittance inverters from the singlet structure.

Figure B.1: Equivalent nodal scheme of (a) a singlet and (b) a dangling resonator structure.

For both networks to be equivalent, they must have the same node equations from their respective admittance matrices as in [111]. The matrix equation, considering the coupling between nodes for the nodal scheme in Figure B.1a is

$$\begin{bmatrix} B_A & J_A & J_{AB} \\ J_A & \omega + j\lambda & J_B \\ J_{AB} & J_B & B_B \end{bmatrix} \begin{bmatrix} V_1 \\ V_2 \\ V_3 \end{bmatrix} = \begin{bmatrix} e_1 \\ e_2 \\ e_3 \end{bmatrix},$$ (B.1)

where ω is the normalized frequency, λ is the frequency shift of the resonator, the vector $\vec{V} =$

137

$\{V_1, V_2, V_3\}$ is the node voltages and $\vec{e} = \{e_1, e_2, e_3\}$ is the external excitation at the nodes. For the dangling resonator in Figure B.1b, the matrix equation is defined with four equations as

$$
\begin{bmatrix}
B_1 & 0 & 0 & J_1 \\
0 & \omega + jb & 0 & J_r \\
0 & 0 & B_2 & J_2 \\
J_1 & J_r & J_2 & B
\end{bmatrix}
\begin{bmatrix}
V_1 \\
V_2 \\
V_3 \\
V_4
\end{bmatrix}
=
\begin{bmatrix}
e_1 \\
e_2 \\
e_3 \\
0
\end{bmatrix}.
\tag{B.2}
$$

where b is the normalized frequency shift of the dangling. In this equation system, $V4$ is the voltage of the internal node B and it is not externally excited, therefore, $e_4 = 0$.

To find the equivalence between both resonators, the equation system in (B.2) must be reduced to three equations system using the fourth row to eliminate the voltage $V4$. The new equation matrix is

$$
\begin{bmatrix}
B_1 - \dfrac{J_1^2}{B} & \dfrac{J_1 J_r}{B} & \dfrac{J_1 J_2}{B} \\
\dfrac{J_1 J_r}{B} & (\omega + b) - \dfrac{J_r^2}{B} & \dfrac{J_2 J_r}{B} \\
\dfrac{J_1 J_2}{B} & \dfrac{J_2 J_r}{B} & B_2 - \dfrac{J_2^2}{B}
\end{bmatrix}
\begin{bmatrix}
V_1 \\
V_2 \\
V_3
\end{bmatrix}
=
\begin{bmatrix}
e_1 \\
e_2 \\
e_3
\end{bmatrix}.
\tag{B.3}
$$

The singlet elements, in function of the dangling parameters, are

$$
B_A = B_1 - \frac{J_1^2}{B},
\tag{B.4}
$$

$$
B_B = B_A - \frac{J_2^2}{B}.
\tag{B.5}
$$

The admittance inverters are calculated as

$$
J_A = J_1 \frac{J_r}{B},
\tag{B.6}
$$

$$
J_B = J_2 \frac{J_r}{B}.
\tag{B.7}
$$

The input-to-output coupling J_{AB} and the eigenvalue λ are

$$
J_{AB} = -\frac{J_1 J_2}{B},
\tag{B.8}
$$

$$
\lambda = b - \frac{J_r^2}{B}.
\tag{B.9}
$$

To express the dangling parameters exclusively in function of the singlet elements, we need to operate the previous equations so that J_{AB} is linked to λ and b. First, equations (B.6) and λ from (B.9) have to be solved for B and set equal to each other.

$$
J_r \frac{J_A}{J_1} = \frac{J_r^2}{b - \lambda}
\tag{B.10}
$$

Hence, J_r is defined as

$$
J_r = \frac{J_1}{J_A} (b - \lambda).
\tag{B.11}
$$

By substituting (B.11) in (B.7) and solving for B, the NRN can be obtained.

$$B = \left(\frac{J_1 J_2}{J_A J_B} \right) (b - \lambda) \tag{B.12}$$

In the dangling resonator, the admittance inverters J_1 and J_2 are required to be unitary with alternated sign. Thus, they must satisfy the following condition:

$$J_1 J_2 = \frac{J_1}{J_2} = \frac{J_A}{J_B}. \tag{B.13}$$

Hence, the coupling J_{AB} is

$$J_{AB} = -\frac{J_A J_B}{b - \lambda}. \tag{B.14}$$

Solving (B.8) for B and using the condition in (B.13), the NRN can be defined only by parameters from the singlet trisection as

$$B = -\frac{J_1 J_2}{J_{AB}} = -\frac{J_A/J_B}{J_{AB}}. \tag{B.15}$$

And the RN-to-NRN coupling can be calculated using the following expression:

$$J_r = \left(\frac{J_A}{J_1} \right) \frac{1}{B} = |J_A B|. \tag{B.16}$$

Once, the NRN and J_r are defined, the admittance inverters are given by

$$J_1 = J_A \frac{B}{J_r} \quad \text{and} \quad J_2 = J_B \frac{B}{J_r}. \tag{B.17}$$

Finally, the input and output FIRs are defined as

$$B_1 = B_A + \frac{J_1^2}{B} \quad \text{and} \quad B_2 = B_B + \frac{J_2^2}{B}. \tag{B.18}$$

Mixed-Topology Class I: Experimental Validation

(a)

(b)
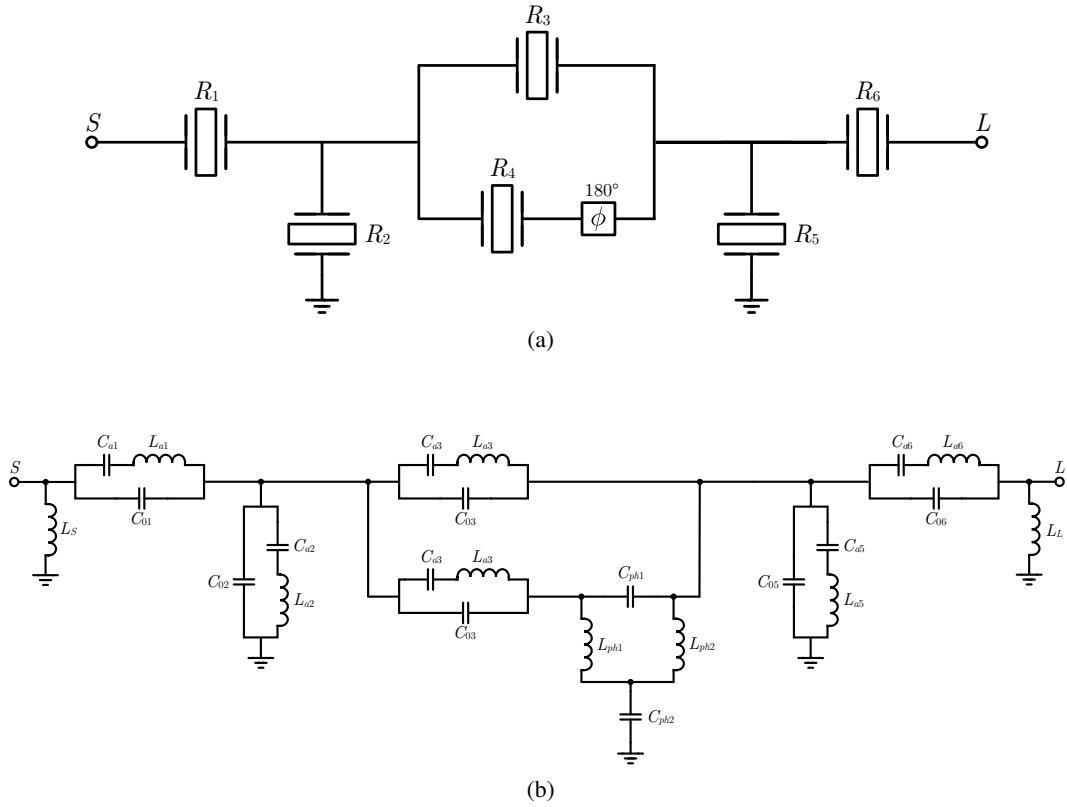
Figure C.1: 6th-order mixed-topology filter scheme with (a) AW resonators and its equivalent circuit using (b) the BVD model, where the 180° is implemented as an all pass network.

In order provide validation of the proposed methodology in Chapter 5, a $N = 6$ order filter has been synthesized with $RL = 25$ dB. The transmission zeros in the lowpass domain have been allocated at $\Omega_{tz} = \{1.85, -1.8, 2, 2.4, -1.8, 1.85\}$ rad/s. The parallel-connected section is created for resonators 3 and 4 and their resonance frequencies are at $\Omega_{r3} = 2.1$ and $\Omega_{r4} = 2.09$, respectively. The design does not require junction elements.
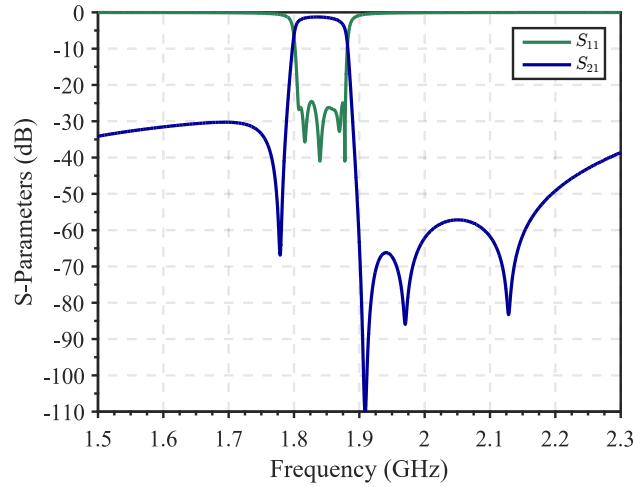
Figure C.2: Simulated transmission response and input/output reflection coefficient of the B3Rx filter.

Resonator 4 is created from an even-mode eigenvalue, and the resulting dangling resonator is between admittance inverter with the same value and sign. Therefore, a phase inverter will be needed to be fully synthesized after serialization. The equivalent network with AW resonators would be like the one shown in Figure C.1a. The transformation to the bandpass domain results in the BVD equivalent circuit as shown in Figure C.1b. A bandpass simulation considering a frequency transformation for the B3Rx band using the BVD is shown in Figure C.2. As demonstrated in [78], this kind of simulation method shows a very good agreement between the simulation and the fabricated filter.

The phase shift in the lower branch of the parallel-connected structure has been implemented as an all-pass filter, as described in [112]. The network is based on Pi-topology in which the inductors are connected to ground through a capacitor. The value for all the elements, including the phase shift, are summarized in Table C.1. The proposed synthesis methodology results in a network configuration composed of acoustic resonators with uniform electromagnetic coupling constant $K_{eff}^2 = 6\%$ except resonator 3 with $K_{eff}^2 = 12.1\%$. In this case, as shown in [78], external reactive elements can be used to accommodate this technological constraint.

Although the scheme proposed in Figure C.1b is meant for AW, the architecture of the filter is independent of the technology. Given the difficulty to manufacture filter prototypes in AW and the generality of the method described in this work, a rapid-prototyping proof of concept has been constructed with a dummy lumped element filter by employing the BVD model to provide a physical validation. This solution allows us to demonstrate more effectively the possibilities of the synthesis methodology. The fabricated filter scheme is depicted in Figure C.1b, it has the same TZs and RL than the previous one except the resonators 3 and 4 in the parallel-connected section which resonance frequencies are $\Omega_{r3} = 4$ and $\Omega_{r4} = 6.4375$, respectively. The frequency transformation has been done considering $f_0 = 236.64$ MHz, and BW = 80 MHz. The prototype filter is shown in Figure C.3a. It has been fabricated using Multi-layer High-Q Capacitors from Johanson Technology with an estimated $Q_C = 800$.

Table C.1: Bandpass elements of the synthesized B3Rx filter with a $180°$ phase shift.

	L_a (nH)	C_a (fF)	C_0 (pF)	$k^2_{eff}(\%)$
Res. 1	67.80	107.78	2.08	6.0
Res. 2	31.15	257	4.92	6.1
Res. 3	144.88	527	0.48	12.1
Res. 4	512.55	14.14	0.27	6.0
Res. 5	31.15	257	4.92	6.1
Res. 6	67.80	107.78	2.08	6.0
Source	4.9 nH			
Load	4.9 nH			
$L_{ph1,2}$	4.41 nH			
C_{ph1}	0.88 pF			
C_{ph2}	3.53 pF			

Table C.2: Bandpass elements of the fabricated filter with a $180°$ phase shift.

	L_a (nH)	C_a (pF)	C_0 (pF)
Res 1	72.28	5.15	15
Res 2	78.99	8.18	22
Res 3	105.34	3.69	1.78
Res 4	371.62	0.3	0.83
Res 5	102.96	8.95	29.26
Res 6	53.11	6.78	15.88
Source	34.62 nH		
Load	42.43 nH		
$L_{ph1,2}$	36.38 nH		
C_{ph1}	8.2 pF		
C_{ph2}	24 pF		
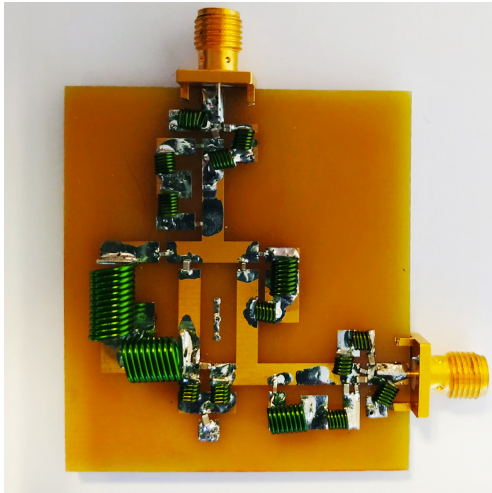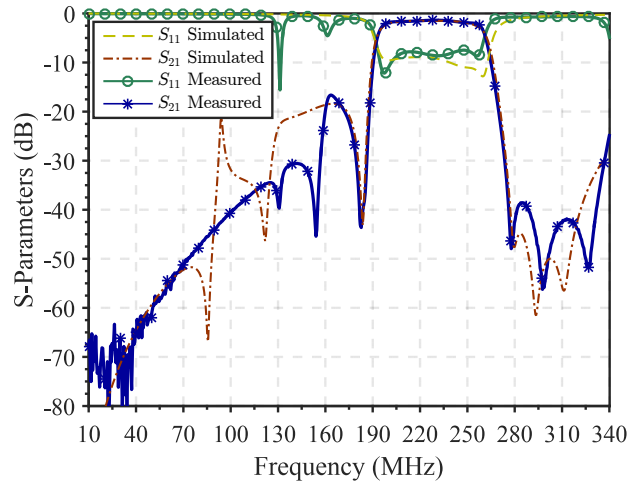
(a)   (b)

Figure C.3: Fabricated prototype using lumped elements and the measured transmission response and input/output reflection coefficient. The result includes a comparison with the simulation.

The employed inductors are HighQ Air core from Coil Craft, with estimated Q factor $Q_L = 100$. The network elements can be found in Table C.2.

The measured transmission response, as well as the input/output reflection coefficient, are shown in Figure C.3b. The result has been compared to the electromagnetic simulation of the whole structure, the real models of the lumped elements were not considered in the EM simulation and the S_{21} parameter at lower frequencies below the passband shows discordance with the simulation. Yet, considering the Q factor of the lumped components, it shows a good agreement between both simulated and measured

filters. The tolerances in the used commercial values of the components and the limited bandwidth of the implemented phase shift are responsible for the detuning of the TZs allocation above the passband and degradation of the RL.

FIR Generation by Network Transformation

The synthesis of mixed-topology filters with cross-coupling implemented by reactive elements, requires an FIR that models such element. This extra node can be created by circuital transformation from a two-node structure coupled by an admittance inverter like the depicted in Figure D.1.

(a) (b)

Figure D.1: Nodal scheme of (a) a two-node network coupled by an admittance inverter and (b) an equivalent three-nodes network.

For both networks to be equivalent, they must have the same node equations from their respective admittance matrices. The matrix equation for the nodal scheme in Figure D.1a is

$$\begin{bmatrix} B_A & J_{AB} \\ J_{AB} & B_B \end{bmatrix} \begin{bmatrix} V_1 \\ V_2 \end{bmatrix} = \begin{bmatrix} e_1 \\ e_2 \end{bmatrix},$$

(D.1)

where the vector $\vec{V} = \{V_1, V_2\}$ is the node voltages and $\vec{e} = \{e_1, e_2\}$ is the external excitation at the nodes. For the three-node network in Figure B.1b, the matrix equation is given by

$$\begin{bmatrix} B_1 & 0 & J_1 \\ 0 & B_3 & J_2 \\ J_1 & J_2 & B_2 \end{bmatrix} \begin{bmatrix} V_1 \\ V_3 \\ V_2 \end{bmatrix} = \begin{bmatrix} e_1 \\ 0 \\ e_2 \end{bmatrix}.$$

(D.2)

To find the equivalence between both networks, the equation system in (D.2) must be reduced to two equations using the third row to eliminate the voltage $V3$. The new equation matrix is

$$\begin{bmatrix} B_1 - \dfrac{J_1^2}{B_3} & -\dfrac{J_1 J_2}{B_3} \\ -\dfrac{J_1 J_2}{B_3} & B_2 - \dfrac{J_2^2}{B_3} \end{bmatrix} \begin{bmatrix} V_1 \\ V_2 \end{bmatrix} = \begin{bmatrix} e_1 \\ e_2 \end{bmatrix}.$$

(D.3)

Thus, the transformation equations for the three-node network are

$$B_3 = -\frac{J_1 J_2}{J_{AB}},$$ (D.4)

where the admittance inverters J_1 and J_2 values can be assigned arbitrarily. The other two nodes are calculated as

$$B_1 = B_A - \frac{J_1}{J_2} J_{AB} \quad \text{and} \quad B_2 = B_B - \frac{J_2}{J_1} J_{AB}.$$ (D.5)

Bibliography

[1] Ericsson, "Ericsson mobility report," Available: https://www.ericsson.com/en/mobility-report, 2019, Accessed: 2020-01-08.

[2] J. Rodriguez, *Fundamentals of 5G Mobile Networks*, Wiley, 2015.

[3] J. M. Khurpade, D. Rao, and P. D. Sanghavi, "A Survey on IOT and 5G Network," in *Proc. Int. Conf. Smart City and Emerging Technology (ICSCET)*, Jan. 2018, pp. 1–3.

[4] N. A. Mohammed, A. M. Mansoor, and R. B. Ahmad, "Mission-Critical Machine-Type Communications: An Overview and Perspectives towards 5G," *IEEE Access*, p. 1, 2019.

[5] A. Ahad, M. Tahir, and K. A. Yau, "5G-based Smart Healthcare Network: Architecture, Taxonomy, Challenges and Future Research Directions.," *IEEE Access*, p. 1, 2019.

[6] A. Gonzalez-Plaza, J. Moreno, I. Val, A. Arriola, P. M. Rodriguez, F. Jimenez, and C. Briso, "5G communications in high speed and metropolitan railways," in *Proc. 11th European Conf. Antennas and Propagation (EUCAP)*, Mar. 2017, pp. 658–660.

[7] A. Gupta and R. K. Jha, "A Survey of 5G Network: Architecture and Emerging Technologies," *IEEE Access*, vol. 3, pp. 1206–1232, 2015.

[8] M. Shafi, A. F. Molisch, P. J. Smith, T. Haustein, P. Zhu, P. De Silva, F. Tufvesson, A. Benjebbour, and G. Wunder, "5G: A Tutorial Overview of Standards, Trials, Challenges, Deployment, and Practice," *IEEE Journal on Selected Areas in Communications*, vol. 35, no. 6, pp. 1201–1221, June 2017.

[9] R. Vannithamby and S. Talwar, *Towards 5G: Applications, Requirements and Candidate Technologies*, Wiley, 2017.

[10] Resonant, "RF Innovation and the Transition to 5G Wireless Technology," Tech. Rep., Resonant Inc., October 2016.

[11] D. C. Malocha, "SAW/BAW acoustoelectronic technology for filters and communication systems," in *Proc. IEEE 11th Annual Wireless and Microwave Technology Conf. (WAMICON)*, Apr. 2010, pp. 1–7.

[12] C. C. W. Ruppel, "Acoustic Wave Filter Technology: A Review," *IEEE Transactions on Ultrasonics, Ferroelectrics, and Frequency Control*, vol. 64, no. 9, pp. 1390–1400, Sep. 2017.

[13] S. Mahon, "The 5G Effect on RF Filter Technologies," *IEEE Transactions on Semiconductor Manufacturing*, vol. 30, no. 4, pp. 494–499, Nov. 2017.

[14] R. Aigner, "SAW and BAW technologies for RF filter applications: A review of the relative strengths and weaknesses," in *Proc. IEEE Ultrasonics Symp*, Nov. 2008, pp. 582–589.

[15] R. Aigner, "Filter technologies for converged RF-frontend architectures: SAW, BAW and beyond," in *Proc. Topical Meeting Silicon Monolithic Integrated Circuits in RF Systems (SiRF)*, Jan. 2010, pp. 136–139.

[16] V. Chauhan, C. Huck, A. Frank, W. Akstaller, R. Weigel, and A. Hagelauer, "Enhancing RF Bulk Acoustic Wave Devices: Multiphysical Modeling and Performance," *IEEE Microwave Magazine*, vol. 20, no. 10, pp. 56–70, Oct. 2019.

[17] Phil Warder and David Schnaufer, "Temperature-Compensated Filter Technologies Solve Crowded Spectrum Challenges," *Microwave Journal*, vol. 11, November 2014.

[18] T. Bauer, C. Eggs, K. Wagner, and P. Hagn, "A Bright Outlook for Acoustic Filtering: A New Generation of Very Low-Profile SAW, TC-SAW, and BAW Devices for Module Integration," *IEEE Microwave Magazine*, vol. 16, no. 7, pp. 73–81, Aug 2015.

[19] T. Takai, H. Iwamoto, Y. Takamine, T. Fuyutsume, T. Nakao, M. Hiramoto, T. Toi, and M. Koshino, "I.H.P. SAW technology and its application to microacoustic components (Invited)," in *Proc. IEEE Int. Ultrasonics Symp. (IUS)*, Sept. 2017, pp. 1–8.

[20] A. Hagelauer, G. Fattinger, C. C. W. Ruppel, M. Ueda, K. Hashimoto, and A. Tag, "Microwave Acoustic Wave Devices: Recent Advances on Architectures, Modeling, Materials, and Packaging," *IEEE Transactions on Microwave Theory and Techniques*, vol. 66, no. 10, pp. 4548–4562, Oct 2018.

[21] D. Morgan, *Surface Acoustic Wave Filters: With Applications to Electronic Communications and Signal Processing*, Studies in Electrical and Electronic Engineering. Elsevier Science, 2010.

[22] K. Hashimoto, *RF Bulk Acoustic Wave Filters for Communications*, Artech House microwave library. Artech House, 2009.

[23] T. E. Parker and M. B. Schulz, "Temperature Stable Surface Acoustic Wave Delay Lines with SiO_2 Film Overlays," in *1974 Ultrasonics Symposium*, Nov 1974, pp. 295–298.

[24] M. Kadota, T. Nakao, N. Taniguchi, E. Takata, M. Mimura, K. Nishiyama, T. Hada, and T. Komura, "SAW duplexer for PCS in US with excellent temperature stability," in *Proc. IEEE Symp. Ultrasonics*, Oct. 2003, vol. 2, pp. 2105–2109 Vol.2.

[25] G. Kovacs, W. Ruile, M. Jakob, U. Rosler, E. Maier, U. Knauer, and H. Zoul, "A SAW duplexer with superior temperature characteristics for US-PCS," in *Proc. IEEE Ultrasonics Symp*, Aug. 2004, vol. 2, pp. 974–977 Vol.2.

[26] M. Kadota, T. Nakao, N. Taniguchi, E. Takata, M. Mimura, K. Nishiyama, T. Hada, and T. Komura, "SAW substrate for Duplexer with Excellent Temperature Characteristics and Large Reflection Coefficient realized by using Flattened SiO$_2$ Film and Thick Heavy Metal Film," in *Proc. IEEE MTT-S Int. Microwave Symp. Digest*, June 2006, pp. 382–385.

[27] H. Nakamura, H. Nakanishi, T. Tsurunari, K. Matsunami, and Y. Iwasaki, "6E-1 A Small-Sized SAW Duplexer on a SiO$_2$/IDT/LiNbO$_3$ Structure for Wideband CDMA Application," in *Proc. IEEE Ultrasonics Symp*, Oct. 2007, pp. 488–491.

[28] Joji Fujiwara Hiroyuki Nakamura, Hidekazu Nakanishi and Tetsuya Tsurunari, "A Review of SiO$_2$ Thin Film Technology for Temperature Compensated SAW Devices," in *Proceedings of International Chiba Symposium on Acoustic Wave Devices*, Chiba/Japan, Nov. 2015.

[29] B. Abbott, A. Chen, T. Daniel, K. Gamble, T. Kook, M. Solal, K. Steiner, R. Aigner, S. Malocha, C. Hella, M. Gallagher, and J. Kuypers, "Temperature compensated SAW with high quality factor," in *Proc. IEEE Int. Ultrasonics Symp. (IUS)*, Sept. 2017, pp. 1–7.

[30] Fumiya Matsukura, Masato Uematsu, Keiko Hosaka, and S Kakio, "Longitudinal-Type Leaky Surface Acoustic Wave on LiNbO$_3$ with High-Velocity Thin Film," *Japanese Journal of Applied Physics*, vol. 52, 07 2013.

[31] T. Kimura, M. Omura, Y. Kishimoto, and K. Hashimoto, "Comparative Study of Acoustic Wave Devices Using Thin Piezoelectric Plates in the 3-5 GHz Range," *IEEE Transactions on Microwave Theory and Techniques*, vol. 67, no. 3, pp. 915–921, Mar. 2019.

[32] T. Kimura, M. Omura, Y. Kishimoto, and K. Hashimoto, "Applicability Investigation of SAW Devices in the 3 to 5 GHz range," in *Proc. IEEE/MTT-S Int. Microwave Symp. - IMS*, June 2018, pp. 846–848.

[33] A. Ansari, "Single Crystalline Scandium Aluminum Nitride: An Emerging Material for 5G Acoustic Filters," in *Proc. IEEE MTT-S Int. Wireless Symp. (IWS)*, May 2019, pp. 1–3.

[34] M. Park, Z. Hao, D. G. Kim, A. Clark, R. Dargis, and A. Ansari, "A 10 GHz Single-Crystalline Scandium-Doped Aluminum Nitride Lamb-Wave Resonator," in *Proc. Actuators and Microsystems Eurosensors XXXIII (TRANSDUCERS EUROSENSORS XXXIII) 2019 20th Int. Conf. Solid-State Sensors*, June 2019, pp. 450–453.

[35] K. M. Lakin, K. T. McCarron, and R. E. Rose, "Solidly mounted resonators and filters," in *Proc. An Int. Symp. 1995 IEEE Ultrasonics Symp*, Nov. 1995, vol. 2, pp. 905–908 vol.2.

[36] R. Ruby, "11E-2 Review and Comparison of Bulk Acoustic Wave FBAR, SMR Technology," in *Proc. IEEE Ultrasonics Symp*, Oct. 2007, pp. 1029–1040.

[37] R. Ruby, "A Snapshot in Time: The Future in Filters for Cell Phones," *IEEE Microwave Magazine*, vol. 16, no. 7, pp. 46–59, Aug. 2015.

[38] R. Ruby, "The 'how & why' a deceptively simple acoustic resonator became the basis of a multi-billion dollar industry," in *Proc. IEEE 30th Int. Conf. Micro Electro Mechanical Systems (MEMS)*, Jan. 2017, pp. 308–313.

[39] R. Strijbos, A. Jansman, J. Lobeek, N. X. Li, and N. Pulsford, "Design and Characterisation of High-Q Solidly-Mounted Bulk Acoustic Wave Filters," in *Proc. 57th Electronic Components and Technology Conf. 2007*, May 2007, pp. 169–174.

[40] V. Plessky, S. Yandrapalli, P. J. Turner, L. G. Villanueva, J. Koskela, and R. B. Hammond, "5 GHz laterally-excited bulk-wave resonators (XBARs) based on thin platelets of lithium niobate," *Electronics Letters*, vol. 55, no. 2, pp. 98–100, 2019.

[41] V. Plessky, S. Yandrapalli, P. J. Turner, L. G. Villanueva, J. Koskela, M. Faizan, A. De Pastina, B. Garcia, J. Costa, and R. B. Hammond, "Laterally excited bulk wave resonators (XBARs) based on thin Lithium Niobate platelet for 5 GHz and 13 GHz filters," in *Proc. IEEE MTT-S Int. Microwave Symp. (IMS)*, June 2019, pp. 512–515.

[42] P. J. Turner, B. Garcia, V. Yantchev, G. Dyer, S. Yandrapalli, L. G. Villanueva, R. B. Hammond, and V. Plessky, "5 GHz Band n79 wideband microacoustic filter using thin lithium niobate membrane," *Electronics Letters*, vol. 55, no. 17, pp. 942–944, 2019.

[43] K. M. Lakin, K. T. McCarron, J. Belsick, and J. F. McDonald, "Thin film bulk acoustic wave resonator and filter technology," in *Proceedings RAWCON 2001. 2001 IEEE Radio and Wireless Conference (Cat.No.01EX514)*, Aug 2001, pp. 89–92.

[44] M. H. Memon, Z. Khan, M. H. Memon, S. Chen, and F. Lin, "Film Bulk Acoustic Wave Resonator in RF Filters," in *Proc. 15th Int. Computer Conf. Wavelet Active Media Technology and Information Processing (ICCWAMTIP)*, Dec. 2018, pp. 237–240.

[45] R. Baum, "Design of Unsymmetrical Band-Pass Filters," *IRE Transactions on Circuit Theory*, vol. 4, no. 2, pp. 33–40, June 1957.

[46] R.J. Cameron, C.M. Kudsia, and R.R. Mansour, *Microwave Filters for Communication Systems: Fundamentals, Design, and Applications*, Wiley, 2018.

[47] Mercedes Jiménez Blasco, *A coupling matrix vision for mobile filtering devices with micro-acoustic wave technologies. A systematic approach*, Ph.D. thesis, Universitat Autónoma de Barcelona, [Barcelona], 2015.

[48] H. Bell, "Transformed-variable synthesis of narrow-bandpass filters," *IEEE Transactions on Circuits and Systems*, vol. 26, no. 6, pp. 389–394, June 1979.

[49] J. D. Rhodes and R. J. Cameron, "General Extracted Pole Synthesis Technique with Applications to Low-Loss TE_{011} Mode Filters," *IEEE Transactions on Microwave Theory and Techniques*, vol. 28, no. 9, pp. 1018–1028, Sept. 1980.

[50] G. Macchiarella, M. Oldoni, F. Seyfert, and S. Amari, "Synthesis of Microwave Filters with "Reactive" Nodes," in *2012 42nd European Microwave Conference*, Oct 2012, pp. 467–470.

[51] S. Amari and G. Macchiarella, "Synthesis of inline filters with arbitrarily placed attenuation poles by using nonresonating nodes," *IEEE Transactions on Microwave Theory and Techniques*, vol. 53, no. 10, pp. 3075–3081, Oct 2005.

[52] H. Bhugra and G. Piazza, *Piezoelectric MEMS Resonators*, Microsystems and Nanosystems. Springer International Publishing, 2017.

[53] K. Uchino, "Chapter 1 - The Development of Piezoelectric Materials and the New Perspective," in *Advanced Piezoelectric Materials (Second Edition)*, Kenji Uchino, Ed., Woodhead Publishing in Materials, pp. 1 – 92. Woodhead Publishing, second edition edition, 2017.

[54] T. Takai, H. Iwamoto, Y. Takamine, T. Fuyutsume, T. Nakao, M. Hiramoto, T. Toi, and M. Koshino, "High-Performance SAW Resonator With Simplified $LiTaO_3/SiO_2$ Double Layer Structure on Si Substrate," *IEEE Transactions on Ultrasonics, Ferroelectrics and Frequency Control*, vol. 66, no. 5, pp. 1006–1013, May 2019.

[55] K.Y. Hashimoto, *Surface Acoustic Wave Devices in Telecommunications: Modelling and Simulation*, Engineering online library. Springer Berlin Heidelberg, 2000.

[56] J. D. Larson, P. D. Bradley, S. Wartenberg, and R. C. Ruby, "Modified Butterworth-Van Dyke circuit for FBAR resonators and automated measurement system," in *2000 IEEE Ultrasonics Symposium. Proceedings. An International Symposium (Cat. No.00CH37121)*, Oct 2000, vol. 1, pp. 863–868 vol.1.

[57] P. Warder and A. Link, "Golden Age for Filter Design: Innovative and Proven Approaches for Acoustic Filter, Duplexer, and Multiplexer Design," *IEEE Microwave Magazine*, vol. 16, no. 7, pp. 60–72, Aug. 2015.

[58] M. Wagner, T. Gossmann, J. Tomasik, R. Weigel, and A. Hagelauer, "Simulations of a New Design Concept for Hybrid Ladder Filters," in *Proc. IEEE 20th Wireless and Microwave Technology Conf. (WAMICON)*, Apr. 2019, pp. 1–5.

[59] J. Tsutsumi, S. Inoue, M. Iwaki, M. Hara, H. Nakamura, K. Matsumoto, M. Ueda, and Y. Satoh, "A design technique to enhance isolation of duplexer in single-ended and differential modes," in *2011 IEEE International Ultrasonics Symposium*, Oct 2011, pp. 1833–1836.

[60] R. Ruby, R. Parker, and D. Feld, "Method of Extracting Unloaded Q Applied Across Different Resonator Technologies," in *Proc. IEEE Ultrasonics Symp*, Nov. 2008, pp. 1815–1818.

[61] D. A. Feld, R. Parker, R. Ruby, P. Bradley, and S. Dong, "After 60 years: A new formula for computing quality factor is warranted," in *Proc. IEEE Ultrasonics Symp*, Nov. 2008, pp. 431–436.

[62] O. Wunnicke, P. J. van der Wel, R. C. Strijbos, and F. de Bruijn, "Thermal behavior of BAW filters at high RF power levels," *and Frequency Control IEEE Transactions on Ultrasonics, Ferroelectrics*, vol. 56, no. 12, pp. 2686–2692, Dec. 2009.

[63] J. Costa, S. McHugh, N. Rice, P. J. Turner, B. A. Willemsen, N. O. Fenzi, R. B. Hammond, J. D. Ha, C. H. Lee, and T. Sato, "Design and characterization of SAW filters for high power performance," in *Proc. IEEE Int. Ultrasonics Symp. (IUS)*, Sept. 2017, pp. 1–4.

[64] A. Tajic, R. Aigner, M. Al Joumayly, F. Vetelino, P. Stokes, F. Dumont, M. Fattinger, and G. Fattinger, "No-drift^TM BAW-SMR: Over-moded reflector for temperature compensation," in *Proc. IEEE Int. Ultrasonics Symp. (IUS)*, Sept. 2016, pp. 1–4.

[65] R. Aigner, G. Fattinger, M. Schaefer, K. Karnati, R. Rothemund, and F. Dumont, "BAW Filters for 5G Bands," in *2018 IEEE International Electron Devices Meeting (IEDM)*, Dec 2018, pp. 14.5.1–14.5.4.

[66] Alfred Raul Giménez Bonastre, *RF filters and multiplexers based on acoustic wave technologies with ladder-type and cross-coupled topologies : designing under a systematic strategy*, Ph.D. thesis, Universitat Autónoma de Barcelona, [Barcelona], 2016.

[67] J. D. Rhodes and S. A. Alseyab, "The generalized chebyshev low-pass prototype filter," *International Journal of Circuit Theory and Applications*, vol. 8, no. 2, pp. 113–125, 1980.

[68] J.S.G. Hong and M.J. Lancaster, *Microstrip Filters for RF / Microwave Applications*, Wiley Series in Microwave and Optical Engineering. Wiley, 2004.

[69] F. Kuo, *Network Analysis and Synthesis, 2nd Edition*, Wiley India Pvt. Limited, 2006.

[70] R. J. Cameron, "General coupling matrix synthesis methods for Chebyshev filtering functions," *IEEE Transactions on Microwave Theory and Techniques*, vol. 47, no. 4, pp. 433–442, April 1999.

[71] R. J. Cameron, "Fast generation of Chebyshev filter prototypes with asymmetrically-prescribed transmission zeros," *ESA Journal*, vol. 6, no. 1, pp. 83–95, Jan 1982.

[72] S. Tamiazzo and G. Macchiarella, "Synthesis of Cross-Coupled Prototype Filters Including Resonant and Non-Resonant Nodes," *IEEE Transactions on Microwave Theory and Techniques*, vol. 63, no. 10, pp. 3408–3415, Oct 2015.

[73] S. Amari and M. Bekheit, "Physical Interpretation and Implications of Similarity Transformations in Coupled Resonator Filter Design," *IEEE Transactions on Microwave Theory and Techniques*, vol. 55, no. 6, pp. 1139–1153, June 2007.

[74] R. J. Cameron, "Advanced coupling matrix synthesis techniques for microwave filters," *IEEE Transactions on Microwave Theory and Techniques*, vol. 51, no. 1, pp. 1–10, Jan 2003.

[75] A. Sivadas, Ming Yu, and R. Cameron, "A simplified analysis for high power microwave bandpass filter structures," in *2000 IEEE MTT-S International Microwave Symposium Digest (Cat. No.00CH37017)*, June 2000, vol. 3, pp. 1771–1774 vol.3.

[76] R.A.H.C.R. Johnson, *Matrix Analysis, Second Edition*, Cambridge University Press, 2012.

[77] J. Verdú, I. Evdokimova, P. de Paco, T. Bauer, and K. Wagner, "Synthesis methodology for the design of acoustic wave stand-alone ladder filters, duplexers and multiplexers," in *2017 IEEE International Ultrasonics Symposium (IUS)*, Sep. 2017, pp. 1–4.

[78] A. Giménez, J. Verdú, and P. De Paco Sánchez, "General Synthesis Methodology for the Design of Acoustic Wave Ladder Filters and Duplexers," *IEEE Access*, vol. 6, pp. 47969–47979, 2018.

[79] A. Triano, P. Silveira, J. Verdú, and P. de Paco, "Phase Correction of Asymmetrical Chebyshev Polynomials for Extracted-Pole Fully Canonical Filters," in *2019 IEEE MTT-S International Microwave Symposium (IMS)*, June 2019, pp. 838–841.

[80] J. Tsutsumi and K. Matsumoto, "Super-Isolation Duplexer Aiming for Removing Rx Inter-stage Filter in W-CDMA Handsets," in *2008 38th European Microwave Conference*, Oct 2008, pp. 1066–1069.

[81] A. Gimenez and P. de Paco, "Involving source-load leakage effects to improve isolation in ladder acoustic wave filters," in *2016 IEEE MTT-S International Microwave Symposium (IMS)*, May 2016, pp. 1–4.

[82] A. Triano, J. Verdú, P. de Paco, T. Bauer, and K. Wagner, "Relation between electromagnetic coupling effects and network synthesis for AW ladder type filters," in *2017 IEEE International Ultrasonics Symposium (IUS)*, Sept 2017, pp. 1–4.

[83] Y. He, G. Wang, and L. Sun, "Direct Matrix Synthesis Approach for Narrowband Mixed Topology Filters," *IEEE Microwave and Wireless Components Letters*, vol. 26, no. 5, pp. 301–303, May 2016.

[84] J.R. Fanchi, *Math Refresher for Scientists and Engineers*, Wiley - IEEE. Wiley, 2006.

[85] H.V. Lundsgaard, *Shadows Of The Circle: Conic Sections, Optimal Figures And Non-euclidean Geometry*, World Scientific Publishing Company, 1998.

[86] G. Macchiarella, M. Oldoni, and S. Tamiazzo, "Narrowband Microwave Filters With Mixed Topology," *IEEE Transactions on Microwave Theory and Techniques*, vol. 60, no. 12, pp. 3980–3987, Dec 2012.

[87] L. Sun Y. He G. Wang and G. Rushingabigwi, "Coupling matrix and admittance function synthesis for mixed topology filters," in *2016 IEEE MTT-S International Microwave Symposium (IMS)*, May 2016, pp. 1–3.

[88] Y. He, G. Wang, X. Song, and L. Sun, "A Coupling Matrix and Admittance Function Synthesis for Mixed Topology Filters," *IEEE Transactions on Microwave Theory and Techniques*, vol. 64, no. 12, pp. 4444–4454, Dec 2016.

[89] A Triano, J. Verdú, and P. de Paco, "Novel Synthesis Technique of Mixed-Topology Extracted-Pole Resonators with Parallel-Connected Structures for Ladder-Type Acoustic Filters," in *2019 IEEE MTT-S International Microwave Symposium (IMS)*, June 2019, pp. 1019–1022.

[90] A. Triano, J. Verdú and P. de Paco, "Synthesis of Acoustic Filters Based On Mixed-Topology With Parallel-Connected Structures," in *2019 European Microwave Conference in Central Europe (EuMCE)*, May 2019, pp. 120–123.

[91] A. Triano, J. Verdú, and P. de Paco Sánchez, "A General Synthesis Technique of Mixed-Topology Including Parallel-Connected Structures for Fully Canonical Ladder-Type Acoustic Filters," *IEEE Transactions on Microwave Theory and Techniques*, pp. 1–8, 2019.

[92] S. Amari, "On the maximum number of finite transmission zeros of coupled resonator filters with a given topology," *IEEE Microwave and Guided Wave Letters*, vol. 9, no. 9, pp. 354–356, Sept. 1999.

[93] D.M. Pozar, *Microwave Engineering, 4th Edition*, Wiley, 2011.

[94] J. Lue and Maha Achour, "Electro-Acoustic Filter," *Patent Number US8576024 B2*, Nov 2013.

[95] P. Bradly and Y. She, "Resonator filter with multiple cross-couplings," *Patent Number US8902020 A1*, Dec 2011.

[96] R. E. Jones, C. Ramiah, T. Kamgaing, S. K. Banerjee, Chi-Taou Tsai, H. G. Hughes, A. P. De Silva, J. Drye, Li Li, W. Blood, Qiang Li, C. R. Vaughan, R. Miglore, D. Penunuri, R. Lucero, D. R. Frear, and M. F. Miller, "System-in-a-package integration of SAW RF Rx filter stacked on a transceiver chip," *IEEE Transactions on Advanced Packaging*, vol. 28, no. 2, pp. 310–319, May 2005.

[97] A. Triano, P. Silveira, J. Verdú, and P. de Paco, "Synthesis Methodology for Mixed-topology Acoustic Wave Filters," in *Proc. IEEE Int. Ultrasonics Symp. (IUS)*, Oct. 2019, pp. 2568–2571.

[98] C.Dorf Richard, *The Electrical Engineering Handbook*, CRC Press, 1999.

[99] M. Iwaki, J. Tsutsumi, Y. Endo, H. Nakamura, and Y. Satoh, "An attenuation improvement technology for ladder SAW/FBAR filters and duplexers employing cancellation circuit," in *2011 41st European Microwave Conference*, Oct 2011, pp. 751–754.

[100] F. Moller and W. Buff, "Electromagnetic feedthrough in Si/ZnO-SAW-devices," in *IEEE 1992 Ultrasonics Symposium Proceedings*, Oct 1992, pp. 245–248 vol.1.

[101] G. Fischerauer, D. Gogl, R. Weigel, and P. Russer, "Investigation of parasitic effects in multi-transducer SAW RF filters," in *1994 Proceedings of IEEE Ultrasonics Symposium*, Oct 1994, vol. 1, pp. 241–244 vol.1.

[102] T. Makkonen, V. P. Plessky, S. Kondratiev, and M. M. Salomaa, "Electromagnetic modeling of package parasitics in SAW-duplexer," in *1996 IEEE Ultrasonics Symposium. Proceedings*, Nov 1996, vol. 1, pp. 29–32 vol.1.

[103] H. Yatsuda, "Modeling of parasitic effects for flip-chip SAW filters," in *1997 IEEE Ultrasonics Symposium Proceedings. An International Symposium (Cat. No.97CH36118)*, Oct 1997, vol. 1, pp. 143–146 vol.1.

[104] P. Dufilie and J. Desbois, "Modeling of feedthrough and ground loops in SAW filters," in *1993 Proceedings IEEE Ultrasonics Symposium*, Oct 1993, pp. 223–226 vol.1.

[105] C. Chuang and S. Chung, "Synthesis and Design of a New Printed Filtering Antenna," *IEEE Transactions on Antennas and Propagation*, vol. 59, no. 3, pp. 1036–1042, Mar. 2011.

[106] K. Chen, J. Lee, W. J. Chappell, and D. Peroulis, "Co-Design of Highly Efficient Power Amplifier and High-Q Output Bandpass Filter," *IEEE Transactions on Microwave Theory and Techniques*, vol. 61, no. 11, pp. 3940–3950, Nov. 2013.

[107] P. Silveira, A. Triano, J. Verdú, and P. d. Paco, "Complex Terminating Impedance for AW Filters: the Key for Power Amplifier Co-design," in *Proc. IEEE Int. Ultrasonics Symp. (IUS)*, Oct. 2019, pp. 2580–2583.

[108] K. Wu and W. Meng, "A Direct Synthesis Approach for Microwave Filters With a Complex Load and Its Application to Direct Diplexer Design," *IEEE Transactions on Microwave Theory and Techniques*, vol. 55, no. 5, pp. 1010–1017, May 2007.

[109] M. Meng and K. Wu, "Direct synthesis of general Chebyshev bandpass filters with a frequency variant complex load," in *Proc. IEEE MTT-S Int. Microwave Symp*, May 2010, pp. 433–436.

[110] C. Guo, X. Shang, M. J. Lancaster, J. Xu, J. Powell, H. Wang, B. Alderman, and P. G. Huggard, "A 135-150-GHz Frequency Tripler With Waveguide Filter Matching," *IEEE Transactions on Microwave Theory and Techniques*, vol. 66, no. 10, pp. 4608–4616, Oct. 2018.

[111] S. Amari, "Direct Synthesis of Cascaded Singlets and Triplets by Non-Resonating Node Suppression," in *2006 IEEE MTT-S International Microwave Symposium Digest*, June 2006, pp. 123–126.

[112] X. Tang and K. Mouthaan, "Design Considerations for Octave-Band Phase Shifters Using Discrete Components," *IEEE Transactions on Microwave Theory and Techniques*, vol. 58, no. 12, pp. 3459–3466, Dec 2010.